

# Constraining New Physics with Atmospheric Neutrinos at INO-ICAL

by

**Amina Khatun**

Enrollment Number : PHYS01201404001

Bhabha Atomic Research Centre, Mumbai

*A thesis submitted to the  
Board of studies in Physical Sciences*

*In partial fulfillment of the requirements  
for the Degree of*

**DOCTOR of PHILOSOPHY**

*of*

**HOMI BHABHA NATIONAL INSTITUTE**

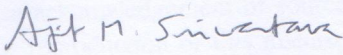
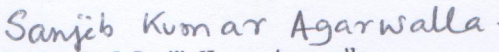
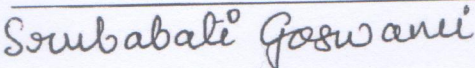
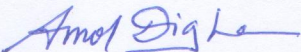
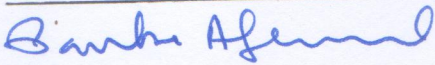
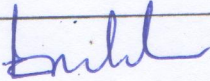


**December 2018**

## Homi Bhabha National Institute

### Recommendations of the Viva Voce Committee

As members of the Viva Voce Committee, we certify that we have read the dissertation prepared by Amina Khatun entitled "Constraining New Physics with Atmospheric Neutrinos at INO-ICAL" and recommend that it may be accepted as fulfilling the thesis requirement for the award of Degree of Doctor of Philosophy.

 Chairman - Prof. Ajit M Srivastava	28-5-19 Date:
 Guide - Prof. Sanjib Kumar Agarwalla	28/5/2019 Date:
 Examiner - Prof. Srubabati Goswami	28.5.19 Date:
 Member 1 - Prof. Amol Dighe	28.5.19 Date:
 Member 2 - Prof. Pankaj Agrawal	28.5.19 Date:
 Member 3 - Prof. Lalit Mohan Pant	28.5.19 Date:

Final approval and acceptance of this thesis is contingent upon the candidate's submission of the final copies of the thesis to HBNI.

I hereby certify that I have read this thesis prepared under my direction and recommend that it may be accepted as fulfilling the thesis requirement.

Date: 28/5/2019


Place: Bhubaneswar

Sanjib Kumar Agarwalla.  
(Prof. Sanjib Kumar Agarwalla)

## STATEMENT BY AUTHOR

This dissertation has been submitted in partial fulfilment of requirements for an advanced degree at Homi Bhabha National Institute (HBNI) and is deposited in the Library to be made available to borrowers under rules of the HBNI.

Brief quotations from this dissertation are allowable without special permission, provided that accurate acknowledgement of source is made. Requests for permission for extended quotation from or reproduction of this manuscript in whole or in part may be granted by the Competent Authority of HBNI when in his or her judgement the proposed use of the material is in the interests of scholarship. In all other instances, however, permission must be obtained from the author.

  
Amina Khatun 28/05/2019

## DECLARATION

I, hereby declare that the investigation presented in the thesis has been carried out by me. The work is original and has not been submitted earlier as a whole or in part for a degree / diploma at this or any other Institution / University.

*Amina Khatun*  
28/05/2019  
Amina Khatun

## LIST OF PUBLICATIONS (Included in this thesis)

1. **Indirect Searches of Galactic Diffuse Dark Matter in INO-MagICAL Detector**  
Amina khatun, Ranjan Laha, and Sanjib Kumar Agarwalla  
*JHEP* 1706, 057 (2017), arXiv:1703.10221
2. **Can INO be Sensitive to Flavor-Dependent Long-Range Forces?**  
Amina Khatun, Tarak Thakore, and Sanjib Kumar Agarwalla,  
[JHEP 1804 \(2018\) 023](#), arXiv:1801.00949

## LIST OF PUBLICATIONS (Not included in this thesis)

1. “Physics Potential of the ICAL detector at the India-based Neutrino Observatory (INO)”  
ICAL collaboration, [Pramana 88 \(2017\) no.5, 79](#), arXiv:1505.07380

## LIST OF CONFERENCE PROCEEDINGS

1. “Constraining Non-Standard Interactions of Neutrino using ICAL detector at INO”, **Amina Khatun**, Sabya Sachi Chatterjee, Tarak Thakore, and Sanjib Kumar Agarwalla, [Springer Proc.Phys. 203 \(2018\) 289-292](#)
2. “Looking for Galactic Diffuse Dark Matter in INO-MagICAL Detector” **Amina Khatun**, Ranjan Laha, and Sanjib Kumar Agarwalla, [PoS NuFact2017 \(2017\)](#), arXiv:1703.10221

## CONFERENCE ATTENDED

1. PANE-2018, 25th May - 1st June 2018, ICTP, Trieste, Italy
2. NuHorizon-2018, 21 - 23 February, 2018, HRI, Allahabad, India
3. WHEEP XV, 14-23 December, 2017, IISER Bhopal, India
4. XXII DAE-BRNS HEP Symposium 2016, December 2016, DU, Delhi, India
5. INSS 2016, 21-27 August 2016, ICISE, Vietnam
6. SANGAM@HRI 2016, February, 2016, HRI, Allahabad, India
7. SERC THEP 2015, December 2015, BITS-Pilani, India
8. Crash Course on GEANT4, May 2015, TIFR, Mumbai, India
9. XXI DAE-BRNS HEP Symposium 2014, December 2014, IIT Guwahati, India
10. IX SERC SCHOOL 2013 on experimental high energy physics , December 2013, IIT Madras, India

## SEMINARS PRESENTED

1. *Long-Range Forces in Atmospheric neutrinos*, PANE, 2018, ICTP, Trieste, Italy.
2. *Search for New Physics at INO-ICAL*, WHEEP XV, 14-23 December, 2017, IISER Bhopal, Bhopal, India
3. *Indirect Searches of Dark matter in ICAL detector of INO experiment*, August, 2017, Harish Chandra Research Institute (HRI), Allahabad, India.
4. *The effect of Non-Standard Interactions on the measurements of the neutrino parameters at the INO-ICAL detector*, XXII DAE-BRNS HEP symposium, December, 2016, Delhi University, Delhi, India.
5. *Study of Non-standard Interaction (NSI) of Neutrino at the ICAL Detector of INO Experiment*, XXI DAE-BRNS HEP symposium, 2014, IIT Guwahati, India.

Amina Khatun  
28/03/2019

Amina Khatun

**Dedicated to**

**My Parents**



## ACKNOWLEDGMENTS

*My thesis would not have been possible without continuous help and supports from many people, and now, I take this opportunity to acknowledge them.*

*First and foremost, I express my sincere gratitude to my supervisor Prof. Sanjib Kumar Agarwalla for his valuable guidance. His intellectual ideas, motivative discussions immensely helped in my research work. I express appreciation from the bottom of my heart for his patience and supports in my difficult time. I would like to thank my collaborators Dr. Ranjan Laha, Dr. Tarak Thakore, and Dr. Sabya Sachi Chatterjee for their great effort during the works.*

*I am thankful to my thesis committee members Prof. Ajit M Srivastava, Prof. Amol Dighe, Prof. Lalit M. Pant, and Prof. Pankaj Agrawal for their kind evaluation and useful suggestions on my research work. I sincerely thank the director of Institute of Physics Bhubaneswar (IOPB) Prof. Sudhakar Panda for allowing me to come to IOPB and for providing me the facilities for my research works. I am thankful to administration staffs at TIFR and also at IOPB.*

*I acknowledge the INO collaborations for all kinds of help throughout my Ph.D. life. I am grateful to Prof. Naba K. Mandal, Prof. Vivek Datar, Prof. Srubabati Goswami, Prof. D. Indumathi, Prof. Gobinda Majumder, Prof. Amitava Raychaudhuri, Prof. M V N Murthy, Dr. B. Satyanarayana for their continuous supports and suggestions for my work.*

*I thank my friends at INO, Lakshmi, Moon Moon, Daljeet, Deepak, Chandan, Apoorva, Neha, Dhruv, Roni, Nizam, Anil, Honey, and Jaydeep. I am fortunate to get the company of Sarama, Somen, Sudipta, Supbhadip, Sazim, Anjan, Manimala di, Tapoja, Soumya, Masoom during my stay at IOPB.*

*Last but not least, I am largely indebted to my parents, my brother, and my sister. They are the source of my energies and motivations to move forward.*

*Amina Khatun*  
28/05/2019

Amina Khatun



# Summary

Neutrino physics is an intense and exciting field of research having wide range of implications in elementary-particle physics, nuclear physics, nuclear and particle astrophysics, and cosmology. Active attempts are being made to unravel the fundamental properties of neutrinos like their masses, mixings, interactions, Dirac vs. Majorana nature, and so on. The path-breaking discovery of neutrino oscillation at the Super-Kamiokande experiment using atmospheric neutrinos and the confirmation of the same from solar, accelerator, and reactor experiments have given a tremendous boost to the research in neutrino physics. One of the most important properties which we have learned from the observation of flavor-induced neutrino oscillation is that neutrinos are massive and their different flavors mix among each other. However, in the basic Standard Model (SM) of particle physics, neutrinos are massless. Therefore, the phenomena of neutrino oscillation is the first experimental proof for physics beyond the SM. To explain the small neutrino masses and relatively large neutrino mixing as indicated by the neutrino oscillation data, various neutrino mass-models extending the basic SM have been proposed. These models also give rise to interesting new physics signatures in neutrino oscillation experiments. In this thesis, we have made a sincere attempt to explore few such new physics scenarios using the atmospheric neutrino data, which will be available in the proposed Iron CALorimeter (ICAL) detector at the India-based Neutrino Observatory (INO) facility.

The ambitious INO project has plans to build a 50 kiloton (kt) magnetized ICAL detector to observe atmospheric neutrinos and antineutrinos separately over a wide range of energies and baselines. By performing a detailed research and development study and publishing several high-quality research papers over the last few years, the INO Collaboration has convinced the community that the upcoming 50 kt magnetized ICAL detector has immense potential to address some of

the outstanding issues in neutrino oscillation physics using atmospheric neutrinos. In this thesis, we have studied the capabilities of this experimental set-up to probe various new physics scenarios beyond the SM which I describe now.

One of the key findings of our research work is that the ICAL detector can play an important role in the indirect searches of Galactic diffuse dark matter in the neutrino and antineutrino mode separately. We find that the ICAL detector will be able to set competitive constraints on the velocity-averaged self-annihilation cross-section ( $\langle\sigma v\rangle$ ) and decay lifetime ( $\tau$ ) of dark matter  $\chi$  having mass in the multi-GeV range. Assuming no excess over the conventional atmospheric neutrino and antineutrino fluxes at the INO site, we obtain the limits,  $\langle\sigma v\rangle \leq 1.87 \times 10^{-24} \text{ cm}^3 \text{ s}^{-1}$  for  $\chi\chi \rightarrow \nu\bar{\nu}$  and  $\tau \geq 4.8 \times 10^{24} \text{ s}$  for  $\chi \rightarrow \nu\bar{\nu}$  at 90% C.L. (1 d.o.f.) for  $m_\chi = 10 \text{ GeV}$ , assuming the NFW as dark matter density profile and using 500 kt-yr exposure.

In another work, we study the impact of flavor violating neutral current non-standard interaction (NSI) parameter  $\varepsilon_{\mu\tau}$  in the oscillations of atmospheric neutrinos and antineutrinos separately using the 500 kt-yr exposure of ICAL. We find that  $\nu_\mu \rightarrow \nu_\mu$  and  $\bar{\nu}_\mu \rightarrow \bar{\nu}_\mu$  vacuum oscillation probabilities at higher energies and longer baselines through matter of the Earth get modified due to non-zero  $\varepsilon_{\mu\tau}$ . In case of no-show, the expected limit on the NSI parameter  $\varepsilon_{\mu\tau}$  at 90% C.L. is  $-0.01 < \varepsilon_{\mu\tau} < 0.01$  considering reconstructed muon energy ( $E_\mu \in [1, 21] \text{ GeV}$ ), muon zenith angle ( $\cos\theta_\mu \in [-1, 1]$ ), and hadron energy ( $E'_{\text{had}} \in [0, 25] \text{ GeV}$ ) as observables.

Towards the end of this thesis, we explore in detail the possible influence of the long-range flavor-diagonal neutral current interactions due to  $L_e - L_\mu$  and  $L_e - L_\tau$  symmetries (one at-a-time) in the context of 50 kt magnetized ICAL detector. For an example, the electrons inside the Sun can generate a flavor-dependent long-range potential at the Earth surface, which can enhance  $\nu_\mu$  and  $\bar{\nu}_\mu$  survival probabilities over a wide range of energies and baselines in atmospheric neutrino experiments. Combining the information on muon momentum and hadron energy on an event-by-event basis, ICAL would be sensitive to long-range forces at 90% ( $3\sigma$ ) C.L. if the effective gauge coupling of this new abelian symmetry  $\alpha_{e\mu/e\tau} > 1.2 \times 10^{-53}$  ( $1.75 \times 10^{-53}$ ).

# List of Figures

- 1.1 Left plot: a schematic diagram of production of atmospheric neutrinos and antineutrinos. Right plot: the flux ratio of atmospheric muon neutrinos to electron neutrinos as calculated for the Kamioka site [88]. . . . . 7
  
- 1.2 The solar neutrino flux calculated on the basis of the Standard Solar Model. The solid lines present solar neutrinos produced in  $pp$  chain, and dashed lines are for neutrinos generated in CNO cycle. The unit of flux in y-axis is  $\text{cm}^{-2} \text{s}^{-1} \text{MeV}^{-1}$  and  $\text{cm}^{-2} \text{s}^{-1}$  for continuum and line fluxes respectively. The fluxes are taken from the website <http://www.sns.ias.edu/~jnb/>. . . . . 9
  
- 1.3 Measured values of the double ratio  $\mathcal{R} = (N_\mu/N_e)_{data}/(N_\mu/N_e)_{MC}$  from different atmospheric neutrino experiments are shown here. This figure is taken from Ref. [120]. . . . . 15
  
- 1.4 Number of the observed multi-GeV ( $E_{vis} > 1.3 \text{ GeV}$ ) electron-like (left panel) and muon-like (right panel) events as a function of zenith angle using the data sample of 414 days collected by the Super-Kamiokande experiment. This figure is taken from Ref. [8]. . . . . 15
  
- 1.5 Statistical significance ( $\chi^2$ ) in the Super-Kamiokande for fitting the atmospheric neutrino data with different  $L/E^n$  with  $n$  as a variable as shown in x-axis. This figure is taken from Ref. [122]. . . . . 16

- 2.1 The survival probability of  $\bar{\nu}_e$  as a function of baseline  $L$  with neutrino energy 3 MeV. The black line presents the results in  $3\nu$  oscillation framework, whereas the red and blue lines are in the  $2\nu$  framework corresponding to mass-squared differences  $\Delta m_{21}^2 = 7.5 \times 10^{-5} \text{ eV}^2$  and  $\Delta m_{31}^2 = 2.5 \times 10^{-3} \text{ eV}^2$  respectively. Other oscillation parameters are  $\theta_{12} = 34^\circ$ ,  $\theta_{13} = 8.5^\circ$ . . . . . 25
- 2.2 Feynman diagrams depicting neutrino scatterings inside the matter. Left panel shows CC interactions, whereas right panel describes NC processes. . . . . 28
- 2.3 The allowed region in the plane of  $[\sin^2 \theta_{12}, \Delta m_{21}^2]$  obtained from the analysis of solar, KamLAND, and KamLAND + solar (global) data are shown with black lines, blue lines, and colored regions respectively.  $\theta_{13}$  is marginalized according to its latest measurement in reactor experiments. This figure is taken from Ref. [171]. 34
- 2.4 The parameter space at 90% C.L. in the plane of  $\sin^2 \theta_{23}$  vs.  $\Delta m_{32}^2$  obtained from the atmospheric experiments Super-Kamiokande (SK) [172], DeepCore/IceCube [174], accelerator-based experiments T2K [36], NO $\nu$ A [38], and MINOS/MINOS+ [30]. . . . . 36
- 2.5 The variation of  $T_0$ ,  $T_1$ ,  $T_2$ , and  $P_{\mu\mu}$  (Eq. 2.6.2) with neutrino energy ( $E$ ) for a baseline of 5000 km through the Earth for neutrino (left panel) and antineutrino (right panel) with NH. The line-averaged constant matter density for the 5000 km baseline through the Earth is taken as  $3.9 \text{ g/cm}^3$  based on the PREM profile [158] of the Earth matter density. The values of oscillation parameters are taken as  $\Delta m_{31}^2 = 2.5 \times 10^{-3} \text{ eV}^2$ ,  $\theta_{23} = 45^\circ$ , and  $\theta_{13} = 8.5^\circ$ . . . . . 45
- 3.1 A pictorial representation of the proposed ICAL detector at the INO facility. . . . 49
- 3.2 The layout of a glass Resistive Plate Chamber. . . . . 50
- 3.3 The magnetic field as obtained from a simulation study with one iron plate of dimension  $16 \text{ m} \times 16 \text{ m} \times 5.6 \text{ cm}$ . This figure is taken from Ref. [200]. . . . . 51

- 3.4 The variation of reconstruction (left panel) and charge identification (right panel) efficiencies with true muon energy  $P_{\text{in}}$  and true muon angle  $\cos \theta$ . These figures are taken from Ref. [202]. . . . . 53
- 3.5 The muon energy and angular resolutions at the ICAL detector are shown in left and right panels respectively as a function of true muon energy  $P_{\text{in}}$  and true muon angle  $\cos \theta$ . These figures are taken from Ref. [202]. . . . . 54
- 3.6 Left panel: The charged pion energy resolution at the ICAL detector. Right Panel: The hadron energy resolution obtained from the simulation with neutrino events that are generated using the NUANCE neutrino event generator. These figures are taken from Ref. [204]. . . . . 55
- 3.7 The relation between total number of hits registered in the ICAL detector due to hadrons and the total true energy of those hadrons ( $E'_{\text{had}} = E_{\nu} - E_{\mu}$ ). The black dots are mean, and the error bars denote  $\sigma$  of the Vavilov fits. This figure is taken from [204]. . . . . 57
- 3.8 The event distributions for  $\mu^{-}$  (left panel) and  $\mu^{+}$  (right panel) as a function of reconstructed  $\cos \theta_{\mu}$  at ICAL with an exposure of 500 kt-yr. Here, the events are summed over the reconstructed  $E_{\mu} \in [4, 6]$  GeV. The black and red lines show events without and with oscillation respectively. In case of oscillation, we take  $\theta_{12} = 33.2^{\circ}$ ,  $\theta_{13} = 8.5^{\circ}$ ,  $\theta_{23} = 45^{\circ}$ ,  $\Delta m_{21}^2 = 7.5 \times 10^{-5} \text{ eV}^2$ ,  $\Delta m_{32}^2 = 2.36 \times 10^{-3} \text{ eV}^2$ , and  $\delta_{\text{CP}} = 0^{\circ}$ . Note that the y-axis ranges in left and right panels are different. 59
- 3.9 The  $\mu^{-}$  (left panel) and  $\mu^{+}$  (right panel) event spectra as a function of reconstructed  $\cos \theta_{\mu}$  with mass hierarchy as NH (blue line) and IH (red line) using 500 kt-yr of ICAL exposure. Here, the reconstructed  $E_{\mu}$  is in the range of  $[4, 5]$  GeV. We use  $\theta_{12} = 33.2^{\circ}$ ,  $\theta_{13} = 8.5^{\circ}$ ,  $\theta_{23} = 45^{\circ}$ ,  $\Delta m_{21}^2 = 7.5 \times 10^{-5} \text{ eV}^2$ , and  $|\Delta m_{\text{eff}}^2| = 2.4 \times 10^{-3} \text{ eV}^2$ , and  $\delta_{\text{CP}} = 0^{\circ}$ . Note that the y-axis ranges in left and right panels are different. 60

- 3.10 For different values of  $\theta_{23}$ , the expected  $\mu^-$  (left panel) and  $\mu^+$  (right panel) event spectra as a function of reconstructed  $\cos \theta_\mu$  at the ICAL detector with 500 kt-yr exposure. The blue, red, and green lines are for  $\theta_{23} = 40^\circ, 45^\circ$ , and  $50^\circ$  respectively. Here, the events are summed over reconstructed  $E_\mu \in [4, 5]$  GeV. Other oscillation parameters are taken as  $\theta_{12} = 33.2^\circ$ ,  $\theta_{13} = 8.5^\circ$ ,  $\theta_{23} = 45^\circ$ ,  $\Delta m_{21}^2 = 7.5 \times 10^{-5} \text{ eV}^2$ ,  $\Delta m_{32}^2 = 2.36 \times 10^{-3} \text{ eV}^2$ , and  $\delta_{\text{CP}} = 0^\circ$ . Note that the y-axis ranges in left and right panels are different. . . . . 62
- 3.11 For different values of  $\Delta m_{32}^2$ , the expected  $\mu^-$  (left panel) and  $\mu^+$  (right panel) event spectra as a function of reconstructed  $\cos \theta_\mu$  at the ICAL detector with 500 kt-yr exposure. The blue, red, and green lines are for  $\Delta m_{32}^2 = 2.26 \times 10^{-3} \text{ eV}^2$ ,  $2.36 \times 10^{-3} \text{ eV}^2$ , and  $2.46 \times 10^{-3} \text{ eV}^2$  respectively. Here, the events are summed over reconstructed  $E_\mu \in [4, 5]$  GeV. Other oscillation parameters are taken as  $\theta_{12} = 33.2^\circ$ ,  $\theta_{13} = 8.5^\circ$ ,  $\theta_{23} = 45^\circ$ ,  $\Delta m_{21}^2 = 7.5 \times 10^{-5} \text{ eV}^2$ , and  $\delta_{\text{CP}} = 0^\circ$ . . . . . 63
- 4.1 (a) Distribution of the dark matter density in the Milky Way galaxy for the NFW (black solid line) and Burkert profiles (green dashed line). The observational bounds on local dark matter density ( $\rho_{sc}$ ) and the solar radius ( $R_{sc}$ ) and their  $2\sigma$  uncertainties are indicated [214, 264]. (b) A schematic diagram of some part of the Milky Way dark matter halo. The Galactic center (GC) is denoted by O and  $R_{sc}$  is the distance between the Earth and the GC. The parameter  $l$  is the distance between point P and the Earth. The angle made at the Earth by points P and O and the corresponding solid angle are denoted by  $\psi$  and  $\Delta\Omega$  respectively. . . . . 68
- 4.2 The value of  $\mathcal{J}^{ann}(\psi)$  (see Eq. 4.2.3) and its average ( $\mathcal{J}_{\Delta\Omega}^{ann}(\psi)$ ) over solid angle  $\Delta\Omega = 2\pi(1 - \cos \psi)$  (see Eq. 4.2.5) are shown in left and right panels. In both the panels, black solid and green dashed lines present the corresponding quantities for the NFW and Burkert profiles respectively. We use  $\mathcal{J}_{\Delta\Omega}^{ann}(\psi = 180^\circ)$  for the diffuse dark matter analysis, which has values 3.33 and 1.6 for the NFW and Burkert profiles respectively. . . . . 70

- 4.3 Line of sight integral for dark matter decay,  $\mathcal{J}^{dec}(\psi)$ , (see Eq. 4.2.9) vs.  $\psi$  and the average value of  $\mathcal{J}^{dec}(\psi)$  over solid angle  $\Delta\Omega$ , i.e.,  $\mathcal{J}_{\Delta\Omega}^{dec}(\psi)$  (see Eq. 4.2.10) for the decay process are shown in left and right panels respectively. In both the panels black solid and green dashed lines present the corresponding quantities for the NFW and the Burkert profiles respectively. We use the value of  $\mathcal{J}_{\Delta\Omega}^{dec}(\psi = 180^\circ)$  in our analysis, which are given by 2.04 and 1.85 for the NFW and Burkert profiles respectively. . . . . 71
- 4.4 Total per nucleon charged current cross-section for neutrino (left panel) and antineutrino (right panel) as a function of neutrino energy. These cross-sections are for an isoscalar target. These plots are taken from Ref. [276]. Note that the y-axis ranges in left and right panels are different. . . . . 73
- 4.5 Event spectra of atmospheric  $\nu_\mu$  (denoted by ATM) are shown by the black solid lines. The predicted event distributions coming from atmospheric  $\nu_\mu$  and dark matter originated neutrino (ATM + DM) are shown in red dotted lines for different  $\cos\theta$  ranges using 500 kt·yr exposure of the MagICAL detector. The signal (DM) is coming from 30 GeV annihilating DM particles here. The mass ordering is taken as NO. The  $\chi\chi \rightarrow \nu\bar{\nu}$  cross-section is arbitrarily chosen to  $\langle\sigma v\rangle = 3.5 \times 10^{-23} \text{ cm}^3 \text{ s}^{-1}$  to have visual clarity. . . . . 78
- 4.6 (a) The upper limit on self-annihilation cross-section of DM particle ( $\chi\chi \rightarrow \nu\bar{\nu}$ ) at 90% C.L. (1 d.o.f.) as a function of DM mass  $m_\chi$  using 500 kt·yr exposure of the MagICAL detector. The bound calculated with only  $\nu_\mu$  ( $\bar{\nu}_\mu$ )-induced events is shown with red dashed (blue dot-dashed) line as MagICAL can distinguish  $\nu_\mu$  from  $\bar{\nu}_\mu$ . The upper bound obtained by combining these two channels is also shown by the black solid line in the figure. We take the NFW as DM profile. (b) The upper bounds on the self-annihilation cross-section ( $\chi\chi \rightarrow \nu\bar{\nu}$ ) of dark matter are presented for the NFW (black solid) and Burkert (green dashed) profiles combining the information coming from  $\nu_\mu$  and  $\bar{\nu}_\mu$ . For both (a) and (b), the choice of mass ordering is NO. . . . . 79



- 4.7 The event distribution of atmospheric  $\nu_\mu$  (denoted as ATM) and the predicted  $\nu_\mu$  event spectra in presence of decay of 30 GeV dark matter particles (denoted as ATM + DM) in different  $\cos \theta_\nu$  ranges using 500 kt-yr exposure of the MagICAL detector. Black solid (red dotted) line represents the ATM (ATM + DM). The mass ordering is taken as NO. The lifetime of dark matter is arbitrarily chosen ( $4.7 \times 10^{24}$  s) for sake of visual clarity. . . . . 81
- 4.8 (a) The lower bound on the decay lifetime of dark matter ( $\chi \rightarrow \nu\bar{\nu}$ ) as a function of DM mass  $m_\chi$  at 90% C.L. (1 d.o.f.) obtained using only  $\nu_\mu$  and only  $\bar{\nu}_\mu$  data using 500 kt-yr exposure of MagICAL. The red dashed (blue dot-dashed) line shows the sensitivity coming from  $\nu_\mu$  ( $\bar{\nu}_\mu$ )-induced events. The black solid line represents the same combining  $\nu_\mu$  and  $\bar{\nu}_\mu$  events at  $\chi^2$  level. We take NO as mass ordering. (b) The constraints on the decay lifetime of dark matter ( $\chi \rightarrow \nu\bar{\nu}$ ) assuming the NFW (black solid line) and Burkert (green dashed line) profiles using 500 kt-yr of MagICAL exposure. Here the results are shown combining  $\nu$  and  $\bar{\nu}$  (see Sec. 4.5 for detail). . . . . 82
- 4.9 (a) Current bounds at 90% C.L. (1 d.o.f.) on self-annihilation cross-section which are obtained from the first three phases of Super-Kamiokande [231] (blue long-dashed line), the four phases of Super-Kamiokande [285] (blue long-dash-dotted line), IceCube [264, 286] (green dot-dashed and green triple-dot-dashed lines), and ANTARES [287, 288] (red dotted and red dashed lines) are shown. The future sensitivity of PINGU [188] with its 1 year of exposure is shown by green shaded region. We compare these limits with the bound obtained from 500 kt-yr MagICAL (black solid line) detector. For all the cases the NFW profile is used. (b) Blue long-dashed line shows the current bound on decay lifetime of DM from the first three phases of Super-Kamiokande [231] using the NFW profile. We compare this limit with the performance of 500 kt-yr MagICAL detector (black solid line) using the same NFW profile. . . . . 83

- 4.10 The limit on (a)  $\nu_{e/\mu/\tau}$  and (b)  $\bar{\nu}_{e/\mu/\tau}$  flux produced from the dark matter in Milky Way galaxy at 90% C.L. (1 d.o.f.) by 500 kt-yr MagICAL detector. The blue filled and red empty triangles are for the annihilation and decay of dark matter particles respectively. . . . . 85
- 5.1 The oscillograms for  $\nu_\mu \rightarrow \nu_\mu$  ( $\bar{\nu}_\mu \rightarrow \bar{\nu}_\mu$ ) channel in  $E_\nu, \cos \theta_\nu$  plane are shown in top (bottom) panels for three different scenarios: i)  $\varepsilon_{\mu\tau} = -0.05$  (left panel), ii)  $\varepsilon_{\mu\tau} = 0.0$  (the SM case, middle panel), and iii)  $\varepsilon_{\mu\tau} = 0.05$  (right panel). Here, in all the panels, we assume NH. . . . . 92
- 5.2 The upper left panel shows the difference in  $\nu_\mu \rightarrow \nu_\mu$  oscillation channel between the SM case ( $\varepsilon_{\mu\tau} = 0$ ) and  $\varepsilon_{\mu\tau} = -0.05$ . In the top right panel, the difference is due to the SM case and  $\varepsilon_{\mu\tau} = 0.05$ . The lower panels are for  $\bar{\nu}_\mu \rightarrow \bar{\nu}_\mu$  oscillation channel. Here, in all the panels, we assume NH. . . . . 93
- 5.3 The distributions of  $\mu^-$  (upper panels) and  $\mu^+$  (lower panels) events for three different  $E_\mu$  ranges: [3, 4] GeV in left panel, [5, 11] GeV in middle panel, and [11, 21] GeV in right panel. In each panel, we consider three different cases: i)  $\varepsilon_{\mu\tau} = 0.05$  (blue line), ii)  $\varepsilon_{\mu\tau} = 0$  (the SM case, black line), and iii)  $\varepsilon_{\mu\tau} = -0.05$  (red line). Here, we sum over  $E'_{\text{had}}$  in its entire range of 0 to 25 GeV and show the results for 500 kt-yr exposure and assuming NH. . . . . 96
- 5.4 Distributions of  $\Delta\chi^2_{\text{ICAL-NSI}}$  (per unit area) from  $\mu^-$  events in reconstructed  $\cos \theta_\mu$  and  $E_\mu$  plane assuming non-zero  $\varepsilon_{\mu\tau}$  in the fit with a strength of 0.05. The top (bottom) panels are for the LE (HE) binning scheme. For a given binning scheme, left and right panels are obtained with  $[E_\mu, \cos \theta_\mu]$  and  $[E_\mu, \cos \theta_\mu, E'_{\text{had}}]$  respectively. In all the panels, we use 500 kt-yr exposure and assume NH in both data and theory. . . . . 101

- 5.5 Distributions of  $\Delta\chi^2_{\text{ICAL-NSI}}$  (per unit area) from  $\mu^+$  events in reconstructed  $\cos\theta_\mu$  and  $E_\mu$  plane assuming non-zero  $\varepsilon_{\mu\tau}$  in the fit with a strength of 0.05. The top (bottom) panels are for the LE (HE) binning scheme. For a given binning scheme, left and right panels are obtained with  $[E_\mu, \cos\theta_\mu]$  and  $[E_\mu, \cos\theta_\mu, E'_{\text{had}}]$  respectively. In all the panels, we use 500 kt-yr exposure and assume NH in both data and theory. . . . . 102
- 5.6 The sensitivity of the ICAL detector to set upper bounds on the NSI parameter  $\varepsilon_{\mu\tau}$  using 500 kt-yr exposure and assuming NH. as true mass hierarchy. Left (right) panel is with LE (HE) binning scheme. In each panel, the red solid line shows the sensitivity for the "3D" where we consider  $E_\mu, \cos\theta_\mu$ , and  $E'_{\text{had}}$  as observables. The black dashed line in each panel portrays the sensitivity for the 2D case considering  $E_\mu$  and  $\cos\theta_\mu$  as observables. These results are obtained after performing marginalization over  $\theta_{23}, \Delta m^2_{\text{eff}}$ , and both choices of mass hierarchy. . . . . 103
- 5.7 In each panel, the red solid (black dashed) line shows the expected sensitivity on  $\varepsilon_{\mu\tau}$  with (without) charge identification capability of ICAL. The left (right) panel is for the 2D:  $E_\mu, \cos\theta_\mu$  (3D:  $E_\mu, \cos\theta_\mu, E'_{\text{had}}$ ) mode assuming the HE binning scheme. We consider 500 kt-yr exposure and NH. Here, we keep all the oscillation parameters fixed in the fit (fixed parameter scenario). . . . . 104
- 5.8 90% C.L. (2 d.o.f.) allowed regions in  $\sin^2\theta_{23} - |\Delta m^2_{32}|$  plane for 500 kt-yr exposure of the ICAL detector assuming NH. The brown dot represents the true choices of  $\sin^2\theta_{23}$  and  $|\Delta m^2_{32}|$ . The solid lines show the results for the "SM" case, where we do not consider  $\varepsilon_{\mu\tau}$  in data and in fit. The dashed lines portray the results when we introduce  $\varepsilon_{\mu\tau}$  in the fit and marginalize over its  $\pm 10\%$  range. For other details, see text. . . . . 107
- 6.1 The variations in the effective mixing angles with the neutrino energy  $E$  in the presence of  $V_{CC}$  and  $V_{e\mu/e\tau}$ . The left, middle, and right panels show the effective value of  $\theta_{23}^m, \theta_{13}^m$ , and  $\theta_{12}^m$  respectively for  $L=5000$  km and NH. In each panel, the black solid line is for the SM case, whereas the blue dash-dotted and red dashed lines are for  $\alpha_{e\mu} = 10^{-52}$  and  $\alpha_{e\tau} = 10^{-52}$  respectively. . . . . 116

- 6.2 The variations in the  $\Delta m_{31,m}^2$  ( $\equiv m_{3,m}^2 - m_{1,m}^2$ , left panel) and  $\Delta m_{21,m}^2$  ( $\equiv m_{2,m}^2 - m_{1,m}^2$ , right panel) with the neutrino energy  $E$  in presence of  $V_{CC}$  and  $V_{e\mu/e\tau}$  for  $L=5000$  km and NH. We give plots for three different cases: i)  $\alpha_{e\mu} = \alpha_{e\tau} = 0$  (the SM case, black solid line), ii)  $\alpha_{e\mu} = 10^{-52}$ ,  $\alpha_{e\tau} = 0$  (blue dash-dotted line), and iii)  $\alpha_{e\mu} = 0$ ,  $\alpha_{e\tau} = 10^{-52}$  (red dashed line). . . . . 118
- 6.3  $\nu_e \rightarrow \nu_\mu$  ( $\bar{\nu}_e \rightarrow \bar{\nu}_\mu$ ) transition probability for 5000 km in upper left (right) panel assuming NH. In bottom left (right) panel, we show  $\nu_\mu \rightarrow \nu_\mu$  ( $\bar{\nu}_\mu \rightarrow \bar{\nu}_\mu$ ) survival probability. In all the panels, we compare our analytical expressions (solid curves) to the exact numerical results (dashed curves) for the SM and SM + LRF cases. For LRF, we consider  $\alpha_{e\tau} = 10^{-52}$ . Note that the y-axis ranges are different in the upper left and right panels. . . . . 119
- 6.4 The oscillograms for  $\nu_e \rightarrow \nu_\mu$  channel in  $E_\nu$ ,  $\cos \theta_\nu$  plane for three different scenarios: i)  $\alpha_{e\mu} = \alpha_{e\tau} = 0$  (the SM case, left panel), ii)  $\alpha_{e\mu} = 10^{-52}$ ,  $\alpha_{e\tau} = 0$  (middle panel), and iii)  $\alpha_{e\mu} = 0$ ,  $\alpha_{e\tau} = 10^{-52}$  (right panel). Here, in all the panels, we assume NH. . . . . 121
- 6.5 The oscillograms for  $\nu_e \rightarrow \nu_\mu$  channel in  $E_\nu$ ,  $\cos \theta_\nu$  plane for three different scenarios: i)  $\alpha_{e\mu} = \alpha_{e\tau} = 0$  (the SM case, left panel), ii)  $\alpha_{e\mu} = 3 \times 10^{-53}$ ,  $\alpha_{e\tau} = 0$  (middle panel), and iii)  $\alpha_{e\mu} = 0$ ,  $\alpha_{e\tau} = 3 \times 10^{-53}$  (right panel). Here, in all the panels, we assume NH. . . . . 121
- 6.6 The oscillograms for  $\nu_\mu \rightarrow \nu_\mu$  channel in  $E_\nu$ ,  $\cos \theta_\nu$  plane for three different scenarios: i)  $\alpha_{e\mu} = \alpha_{e\tau} = 0$  (the SM case, left panel), ii)  $\alpha_{e\mu} = 10^{-52}$ ,  $\alpha_{e\tau} = 0$  (middle panel), and iii)  $\alpha_{e\mu} = 0$ ,  $\alpha_{e\tau} = 10^{-52}$  (right panel). Here, in all the panels, we assume NH. . . . . 122
- 6.7 The oscillograms for  $\nu_\mu \rightarrow \nu_\mu$  channel in  $E_\nu$ ,  $\cos \theta_\nu$  plane for three different scenarios: i)  $\alpha_{e\mu} = \alpha_{e\tau} = 0$  (the SM case, left panel), ii)  $\alpha_{e\mu} = 3 \times 10^{-53}$ ,  $\alpha_{e\tau} = 0$  (middle panel), and iii)  $\alpha_{e\mu} = 0$ ,  $\alpha_{e\tau} = 3 \times 10^{-53}$  (right panel). Here, in all the panels, we assume NH. . . . . 122

- 6.8 The distributions of  $\mu^-$  (upper panels) and  $\mu^+$  (lower panels) events for three different  $E_\mu$  bins: 1 to 5 GeV in left panel, 5 to 11 GeV in middle panel, and 11 to 21 GeV in right panel. In each panel, we consider three different cases: i)  $\alpha_{e\mu} = \alpha_{e\tau} = 0$  (the SM case, black solid line), ii)  $\alpha_{e\mu} = 10^{-52}$ ,  $\alpha_{e\tau} = 0$  (blue dash-dotted line), and iii)  $\alpha_{e\mu} = 0$ ,  $\alpha_{e\tau} = 10^{-52}$  (red dashed line). Here, we sum over  $E'_{\text{had}}$  in its entire range of 0 to 25 GeV and show the results for 500 kt-yr exposure and assuming NH. . . . . 123
- 6.9 The distributions of  $\mu^-$  (upper panels) and  $\mu^+$  (lower panels) events for three different  $E_\mu$  bins: 1 to 5 GeV in left panel, 5 to 11 GeV in middle panel, and 11 to 21 GeV in right panel. In each panel, we consider three different cases: i)  $\alpha_{e\mu} = \alpha_{e\tau} = 0$  (the SM case, black solid line), ii)  $\alpha_{e\mu} = 3 \times 10^{-53}$ ,  $\alpha_{e\tau} = 0$  (blue dash-dotted line), and iii)  $\alpha_{e\mu} = 0$ ,  $\alpha_{e\tau} = 3 \times 10^{-53}$  (red dashed line). Here, we sum over  $E'_{\text{had}}$  in its entire range of 0 to 25 GeV and show the results for 500 kt-yr exposure and assuming NH. . . . . 124
- 6.10 Distributions of  $\Delta\chi^2_{\text{ICAL-LRF}}$  (per unit area) in  $E_\mu$  and  $\cos\theta_\mu$  plane. The left (right) panels are for  $\mu^-$  ( $\mu^+$ ) events. In upper (lower) panels, we assume non-zero  $\alpha_{e\mu}$  ( $\alpha_{e\tau}$ ) in the fit with a strength of  $10^{-52}$ . In all the panels, we use 500 kt-yr exposure and assume NH in both data and theory. . . . . 127
- 6.11 Sensitivity of ICAL to set upper limits on  $\alpha_{e\mu}$  (blue dashed line) and  $\alpha_{e\tau}$  (red dash-dotted line) using 500 kt-yr exposure and assuming NH as true choice. . . . 128
- B.1  $\nu_e \rightarrow \nu_\mu$  ( $\bar{\nu}_e \rightarrow \bar{\nu}_\mu$ ) transition probability for 5000 km in upper left (right) panel assuming NH. In bottom left (right) panel, we show  $\nu_\mu \rightarrow \nu_\mu$  ( $\bar{\nu}_\mu \rightarrow \bar{\nu}_\mu$ ) survival probability. In all the panels, we compare our analytical expressions (solid curves) to the exact numerical results (dashed curves) for the SM and SM + LRF cases. For LRF, we consider  $\alpha_{e\mu} = 10^{-52}$ . Note that the y-axis ranges are different in the upper left and right panels. . . . . 141

# List of Tables

2.1	The best-fit values of oscillation parameters and their $3\sigma$ ranges as obtained in Ref. [14] from the global fit of world neutrino oscillation data. The results from other global fit studies [15, 16] are almost similar to these best-fit values and ranges.	41
3.1	The specifications of the ICAL detector.	49
3.2	Number of $\mu^-$ (left panel) and $\mu^+$ (right panel) events at ICAL with an exposure of 500 kt·yr. We sum over all the directions and reconstructed $E_\mu$ in the range of 1 GeV to 21 GeV. In case of oscillation, we use $\theta_{12} = 33.2^\circ$ , $\theta_{13} = 8.5^\circ$ , $\theta_{23} = 45^\circ$ , $\Delta m_{21}^2 = 7.5 \times 10^{-5} \text{ eV}^2$ , and $\Delta m_{32}^2 = 2.36 \times 10^{-3} \text{ eV}^2$ .	58
3.3	Total number of $\mu^-$ (left table) and $\mu^+$ (right table) events expected at ICAL with NH (IH) is given in 2nd (3rd) column. We sum over all the directions and reconstructed $E_\mu$ in the range of 1 GeV to 21 GeV and consider an exposure of 500 kt·yr. We take $\theta_{12} = 33.2^\circ$ , $\theta_{13} = 8.5^\circ$ , $\theta_{23} = 45^\circ$ , $\Delta m_{21}^2 = 7.5 \times 10^{-5} \text{ eV}^2$ , $ \Delta m_{\text{eff}}^2  = 2.4 \times 10^{-3} \text{ eV}^2$ , and $\delta_{\text{CP}} = 0^\circ$ .	60
3.4	Total number of $\mu^-$ (left panel) and $\mu^+$ (right panel) events expected for different values of atmospheric mixing angle $\theta_{23}$ . The numbers in 2nd, 3rd, and 4th columns are for $\theta_{23} = 40^\circ$ , $45^\circ$ , and $50^\circ$ respectively. We sum over all the directions and reconstructed muon energy ( $E_\mu$ ) in the range of 1 GeV to 21 GeV and consider ICAL exposure of 500 kt·yr. We use other oscillation parameters as $\theta_{12} = 33.2^\circ$ , $\theta_{13} = 8.5^\circ$ , $\Delta m_{21}^2 = 7.5 \times 10^{-5} \text{ eV}^2$ , $\Delta m_{32}^2 = 2.36 \times 10^{-3} \text{ eV}^2$ , and $\delta_{\text{CP}} = 0^\circ$ .	61

4.1	The value of parameters associated with the NFW and Burkert profiles are listed here. They are same as in Ref. [264]. . . . .	68
4.2	The detector characteristics used in the simulations. We use the same detector properties for $\mu^-$ and $\mu^+$ events. . . . .	72
4.3	The binning scheme adopted for the reconstructed $E_\nu$ and $\cos \theta_\nu$ for each muon polarity. The last column depicts the total number of bins considered for each observable. . . . .	74
5.1	Expected number of $\mu^-$ and $\mu^+$ events for 500 kt-yr exposure of the ICAL detector considering low-energy (LE) and high-energy (HE) binning schemes. We present the event rates for the following three cases: i) $\varepsilon_{\mu\tau} = 0.05$ , ii) $\varepsilon_{\mu\tau} = 0$ (the SM case), and iii) $\varepsilon_{\mu\tau} = -0.05$ . Apart from showing the total $\mu^-$ event rates, we also give the estimates of individual event rates coming from $\nu_\mu \rightarrow \nu_\mu$ ( $P_{\mu\mu}$ ) disappearance channel and $\nu_e \rightarrow \nu_\mu$ ( $P_{e\mu}$ ) appearance channel. For $\mu^+$ events also, we separately show the contributions from $\bar{\nu}_\mu \rightarrow \bar{\nu}_\mu$ ( $P_{\bar{\mu}\bar{\mu}}$ ) disappearance channel and $\bar{\nu}_e \rightarrow \bar{\nu}_\mu$ ( $P_{\bar{e}\bar{\mu}}$ ) appearance channel. Here, we consider NH and assume the benchmark values of the oscillation parameters as mentioned in Sec. 5.4. . . . .	95
5.2	The low-energy (LE) binning scheme considered for different reconstructed observables ( $E_\mu, \cos \theta_\mu, E'_{\text{had}}$ ) associated with each of the muon polarities. The total number of bins for each of these observables are given in 5th column. . . . .	98
5.3	The high-energy (HE) binning scheme considered for different reconstructed observables ( $E_\mu, \cos \theta_\mu, E'_{\text{had}}$ ) associated with each of the muon polarities. The total number of bins for each of these observables are given in 5th column. . . . .	98
5.4	The expected bound on $\varepsilon_{\mu\tau}$ for four different choices of binning schemes and observables at $3\sigma$ and 90% C.L. obtained using 500 kt-yr exposure of the ICAL detector. We give results for the both choices of true mass hierarchy. To obtain these constraints, we marginalize over $\theta_{23}$ , $\Delta m_{\text{eff}}^2$ , and both the choices of mass hierarchy in the fit. . . . .	103



- 5.5 The mass hierarchy sensitivity of the ICAL detector using 500 kt·yr exposure. For the “SM” case (third column), we do not consider  $\varepsilon_{\mu\tau}$  in data and in fit. For the “SM +  $\varepsilon_{\mu\tau}$ ” case (fourth column), we introduce  $\varepsilon_{\mu\tau}$  in the fit and marginalize over it in the range of  $[-0.1, 0.1]$  along with oscillation parameters  $\theta_{23}$  and  $\Delta m_{\text{eff}}^2$ . Last column shows how much the mass hierarchy sensitivity deteriorates in presence of  $\varepsilon_{\mu\tau}$  as compared to the SM case. We present our results for various choices of binning schemes and observables assuming both true NH and true IH. . . . . 106
- 6.1 The values of  $\Delta m_{31}^2/2E$  (third column),  $V_{CC}$  (fourth column), and  $V_{e\mu/e\tau}$  (fifth column) for our benchmark choices of  $E$ ,  $L$ , and  $\alpha_{e\mu/e\tau}$ . We take  $\Delta m_{31}^2 = 2.524 \times 10^{-3} \text{ eV}^2$ . Based on the PREM profile, the line-averaged constant Earth matter densities for 2000 km, 5000 km, and 8000 km baselines are 3.46 g/cm<sup>3</sup>, 3.9 g/cm<sup>3</sup>, and 4.26 g/cm<sup>3</sup> respectively. The parameter  $\theta_\nu$  is the zenith angle for a given baseline. 113
- 6.2 The binning scheme considered for the reconstructed observables  $E_\mu$ ,  $\cos \theta_\mu$ , and  $E'_{\text{had}}$  for each muon polarity. In last column, we give the total number of bins taken for each observable. . . . . 125



# 1

# Introduction

## Contents

---

<b>1.1 Neutrinos in the Standard Model . . . . .</b>	<b>3</b>
<b>1.2 Neutrino Sources . . . . .</b>	<b>6</b>
1.2.1 Natural Sources of Neutrinos	6
1.2.2 Man-made Sources of Neutrinos	11
<b>1.3 The Detection of Neutrinos and Anomalies. . . . .</b>	<b>12</b>
1.3.1 Solar Neutrino Anomaly	13
1.3.2 Atmospheric Neutrino Anomaly	14
<b>1.4 A Brief Motivation and Plan of the Thesis . . . . .</b>	<b>17</b>

---

Neutrino physics is an important area of research having interesting implications in elementary-particle physics, nuclear physics, nuclear and particle astrophysics, and cosmology [1–3]. Active attempts are being made to unravel the fundamental properties of neutrinos like their masses, mixings, interactions, Dirac vs. Majorana nature, and so on [4]. This year, we are celebrating the twentieth anniversary of discovery of atmospheric neutrino oscillation by the world class Super-Kamiokande experiment [5]. In the year 1998, the famous Super-Kamiokande experiment addressed the long-standing atmospheric neutrino anomaly [6, 7] using their first 414 live days (25 kiloton-year) of data, and showed that half of the muon neutrinos ( $\nu_\mu$ ) oscillated into tau neutrinos ( $\nu_\tau$ ) while passing through the Earth [5]. They established the phenomena of neutrino flavor oscillation at high confidence level ( $6.2\sigma$ ) by observing the zenith angle dependence of multi-GeV atmospheric neutrinos in their detector [8]. Later in the year 2002, the solar neutrino experiment SNO measured the total active neutrino flux coming from the Sun by observing the neutral

current (NC) events in the detector [9]. The global fit of SNO and other solar neutrino data finally led to the solution of the long-standing solar neutrino anomaly suggesting the flavor-induced neutrino conversion. The KamLAND [10–13] reactor antineutrino experiment established the oscillation hypothesis by observing the disappearance of  $\bar{\nu}_e$  and restricted the mixing parameters to the so-called LMA-MSW solution [4]. All the neutrino oscillation data available so far can be accommodated in the standard three-flavor oscillation picture of neutrinos [14–16], except few anomalous results obtained at very-short-baseline experiments (for recent reviews see [17, 18]), which point towards oscillations with substantially large mass-squared difference ( $\Delta m^2 \sim 1 \text{ eV}^2$ ) in comparison to the well-known solar and atmospheric mass splittings. The theory of neutrino oscillation demands that neutrinos are massive and should have non-zero mixings suggesting that leptonic flavors are not symmetries of Nature. But, in the simplest form of the Standard Model (SM), neutrinos are massless fermions. Therefore, the discovery of neutrino oscillation provides an exclusive evidence for physics beyond the Standard Model. For the discovery of neutrino oscillation, Professor Takaaki Kajita and Professor Arthur B. McDonald were jointly awarded the Nobel prize for physics in the year 2015.

The marvelous data [19–41] have revealed that the flavor mixing angles are large in the neutrino sector, and neutrinos have tiny masses. These observed properties of neutrino are speculated to be consequences of some phenomena which happen at very high energies. Therefore, neutrino facilities pursuing the study of neutrino oscillation are complementary to high energy colliders and really important candidates for the next-generation world-class experiments in the field of particle physics. Neutrino physics has now entered into the precision era, where the main aim is to gain a detailed understanding of the structure of neutrino mass matrix. There is no doubt that an accurate reconstruction of neutrino mass matrix would certainly help us to know the underlying new physics that gives rise to the neutrino masses and mixings.

Several high-precision neutrino oscillation experiments are currently running and refining our knowledge about the oscillation parameters day-by-day. In the future neutrino road map, a number of ambitious large-scale next-generation oscillation experiments are under construction, whose mission will be to resolve the remaining fundamental unknowns in the neutrino sector. The proposed Iron CALorimeter (ICAL) detector at the India-based Neutrino Observatory (INO) facility is going to play an important role along this direction. The 50 kiloton magnetized ICAL detector

is being designed to observe atmospheric neutrinos and antineutrinos separately over a wide range of energies and baselines [42, 43]. The main aim of this experiment is to explore the Earth matter effect [44–46] by studying the energy and zenith angle<sup>1</sup> dependence of the atmospheric neutrinos in the multi-GeV range. It will enable the ICAL detector to address some of the fundamental issues in neutrino oscillation physics. Preliminary studies have already shown that the INO-ICAL experiment has immense potential to determine the neutrino mass hierarchy and to improve the precision on atmospheric neutrino mixing parameters [42, 47–52]. This facility can also offer an unparalleled window to probe the new physics beyond the Standard Model [53–64]. In this thesis, we have studied in detail a few interesting new physics scenarios which can be tested in the upcoming INO-ICAL facility.

This chapter is organized as follows. We start Sec. 1.1 with a brief history of how neutrinos appeared into the field of particle physics. Then, we provide a short description of the Standard Model of particle physics and the properties that neutrinos possess in the SM. Sec. 1.2 provides a discussion on various sources of neutrinos and antineutrinos. In Sec. 1.3, we discuss the detection of the solar and atmospheric neutrinos which led to the solar and the atmospheric neutrino anomalies respectively. Then, we focus on the contributions of the Sudbury Neutrino Observatory (SNO) and the Super-Kamiokande experiments to resolve these anomalies. Sec. 1.4 provides a brief motivation of the work that we have done in this thesis. In Sec. 1.4, we give the layout of the thesis.

## 1.1 Neutrinos in the Standard Model

The journey of neutrinos began with a letter sent by Professor Wolfgang Pauli to a group of “radioactive” scientists in December 1930. In his thoughtful letter, Professor Pauli proposed that an electrically neutral, spin-half particle gets emitted when a radioactive nucleus transforms into a lighter nucleus with the emission of an electron through beta-decay. The beta-decay, at that time,

---

<sup>1</sup>Zenith angle,  $\theta$ , and baseline,  $L$ , of atmospheric neutrino in terrestrial experiment are related by the following equation:

$$\cos \theta = \frac{(R + l)^2 - (R - h)^2 - L^2}{2L(R - h)}, \quad L = \sqrt{(R + l)^2 - (R - h)^2 \sin^2 \theta} - (R - h) \cos \theta, \quad (1.0.1)$$

where  $R$ ,  $l$ , and  $h$  denote radius of Earth, atmospheric height ( $\sim 15$  km), and depth of the location where the detector is situated respectively.

was thought to be a two-body process (a daughter nucleus and an electron in the final state), and thus the laws of energy and momentum conservation demanded for the electron to have a discrete energy. However, in experiments, the energy spectrum of electrons from beta-decay was found to be continuous. This contradiction puts the laws of conservation of energy and momentum in jeopardy. After Professor Pauli proposed that a third particle gets emitted in the final state of beta-decay and shares the total available energy in the final state with electron, the tension over conservation of energy and momentum got removed [65]. In 1934, Professor Enrico Fermi proposed “neutrino” as the name for Pauli’s postulated particle and formulated a quantitative theory of weak particle interactions in which neutrinos play an important role [66, 67]. B. Pontecorvo took Fermi’s theory of beta-decay to another level by introducing the idea of the existence of a Universal weak interaction which includes  $e\text{-}\nu$  and  $\mu\text{-}\nu$  pairs [68]. Later, the idea of  $\mu\text{-}e$  Universality was proposed by Puppi [69], Klein [70], and Yang and Tiomno [71]. However, for about two decades, the actual nature of the Universal Fermi interaction was not known.

Until the first half of twentieth century, parity was thought to be a symmetry of Nature since it was found to be conserved in all the strong and electromagnetic interactions. However, the observation of  $K^+$  decay (a weak interaction) through two modes of opposite parity, the  $\tau - \theta$  puzzle, led to the question whether the weak interaction is symmetric under the parity transformation. Lee and Yang were the first to invoke the concept of the parity violation in weak interaction [72]. The observed asymmetric distribution of electron from beta-decay of polarized Cobalt nuclei ( $^{60}\text{Co}$ ) in the experiment performed by Madame Wu proved that the parity was indeed violated in beta-decay [73]. On the basis of the results of Wu’s experiment, Lee and Yang realized the left-handedness of neutrino and the right-handedness of antineutrino. Later, Goldhaber et al. measured the helicity of  $\nu_e$  in the process  $e^- + ^{152}\text{Eu} \rightarrow ^{152}\text{Sm}^*(^{152}\text{Sm} + \gamma) + \nu_e$  and confirmed that neutrinos are left-handed particle and no right-handed neutrinos exist in Nature [74]. This observation supports the two-component theory of massless neutrino [75] and more importantly the V–A (V: vector and A: axial vector) [76–78] structure of the coupling of weak interactions, which has been embedded in the Standard Model of particle physics.

The Standard Model of particle physics successfully describes the three fundamental interactions of elementary particles which are strong, weak, and electromagnetic with the help of a local gauge group  $SU(3)_C \times SU(2)_L \times U(1)_Y$  [79–82]. Here, the subscripts  $C$ ,  $L$ , and  $Y$  stand for color, weak

isospin, and weak hypercharge respectively. In the Standard Model, there are total twelve elementary particles which are all spin-half fermions. They are categorized as leptons and quarks, each of them having six particles, and paired in three generations, the lightest and stable particles belong to first generation, whereas the heavier and unstable ones are part of second and third generations. Neutrinos are grouped with their charged lepton partner, such as, electron neutrino ( $\nu_e$ ) with electron, muon neutrino ( $\nu_\mu$ ) with muon, and tau neutrino ( $\nu_\tau$ ) with tau. All these fermions in the Standard Model can be written as the combination of left ( $\psi_L$ ) and right ( $\psi_R$ ) chiral fields such as,

$$\psi = \psi_L + \psi_R, \quad \text{where } \psi_R = \frac{1}{2}(1 + \gamma_5)\psi \text{ and } \psi_L = \frac{1}{2}(1 - \gamma_5)\psi. \quad (1.1.1)$$

The V–A structure of the weak interaction invokes  $\psi_L$  to be weak isospin doublets and all the  $\psi_R$  to be singlets under the weak isospin transformation. Total twelve generators of the SM gauge group correspond to eight massless gluons which are the mediators of strong interactions, three massive gauge bosons as the force carrier of weak interaction, and one massless photon as the mediator of electromagnetic interaction. One of the successes of the SM is the prediction of weak neutral current which was discovered in the bubble chamber experiment Gargamelle using the Proton Synchrotron in 1973 [83]. The Standard Model also predicted the existence of the weak gauge bosons  $W^\pm$  ( $\sim 80$  GeV) and  $Z$  ( $\sim 91$  GeV) which were discovered by the experiments UA1 [84] and UA2 [85] respectively at CERN in 1983.

An important ingredient of the Standard Model is the Higgs Mechanism which explains the mass of fermions as well as the gauge bosons through spontaneous symmetry breaking. In the Standard Model, fermionic fields acquire their masses through the Yukawa couplings with the Higgs doublet and physical states are the excitations of the Higgs field above the vacuum. The last piece of confirmation for the validity of the Standard Model comes from the discovery of Higgs boson around 125 GeV, the neutral component of Higgs doublet, by the CMS and ATLAS detectors at the LHC [86, 87]. The mass term for any fermion is given by  $m\bar{\psi}\psi$  which can be rewritten as follows using Eq. 1.1.1,

$$m\bar{\psi}\psi = m(\bar{\psi}_L\psi_R + \bar{\psi}_R\psi_L). \quad (1.1.2)$$

As there is only left-handed neutrino and its right-handed part does not exist, thus neutrino does not have mass in the SM. As far as the interactions of the SM fermions are concerned, quarks



interact via all the three fundamental interactions, while charged leptons take part in weak and electromagnetic interactions. On the other hand, neutrinos interact via only weak interactions because they are electrically neutral and colorless. Since neutrinos are associated with the charged lepton in the SM, therefore, neutrinos take part in charged current (CC) weak interactions which are given by

$$- \mathcal{L}_{CC} = \frac{g}{\sqrt{2}} \sum_I \bar{\nu}_{LI} \gamma^\mu l_{LI}^- W_\mu^+ + h.c.. \quad (1.1.3)$$

The NC interactions of neutrino are given by

$$- \mathcal{L}_{NC} = \frac{g}{2 \cos \theta_W} \sum_I \bar{\nu}_{LI} \gamma^\mu \nu_{LI} Z_\mu^0. \quad (1.1.4)$$

Eq. 1.1.3 and 1.1.4 describe all the interactions of neutrino in the Standard Model. Next, we will discuss various sources of neutrinos.

## 1.2 Neutrino Sources

Neutrinos, produced from a variety of sources, natural as well as man-made, are different in the context of their energies and flavor composition. Here, we discuss different sources of neutrinos and their importance in the neutrino experiments.

### 1.2.1 Natural Sources of Neutrinos

- **Earth's Atmosphere:** Atmospheric neutrinos are produced in interaction of primary cosmic particles with nuclei in the Earth's atmosphere. The primary cosmic particles are composed of mainly protons ( $\sim 89\%$ ) apart from a small amount of helium nuclei ( $\sim 10\%$ ) and heavier nuclei ( $\sim 1\%$ ). We do not have the exact knowledge about origin and production mechanism of these primary cosmic rays. When these primary cosmic rays pass through the Earth's atmosphere, they interact with atmospheric nuclei (mostly nitrogen) and produce kinematically allowed hadrons and their decay products. The secondary cosmic particles are abundant with the charged pions which decay with 99.9% branching ratio in the follow-

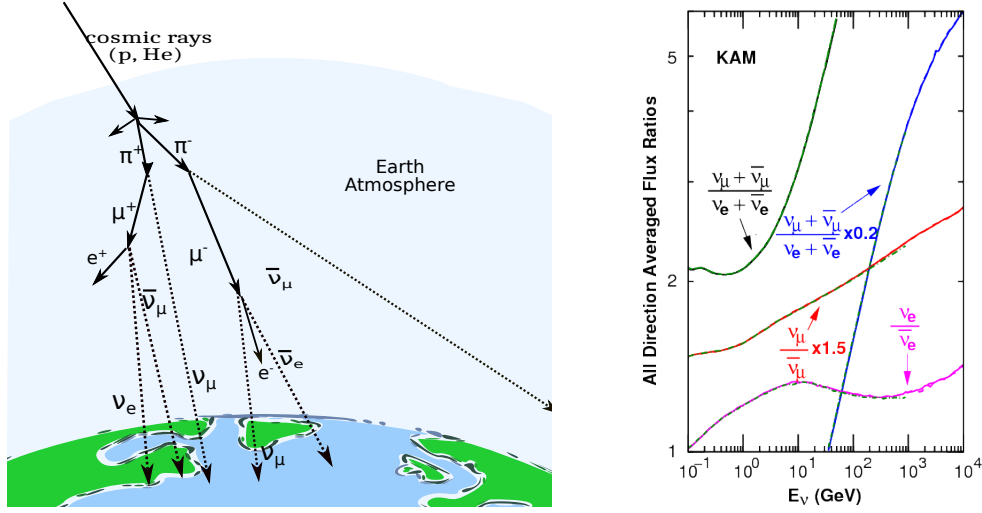


**Figure 1.1.** Left plot: a schematic diagram of production of atmospheric neutrinos and antineutrinos. Right plot: the flux ratio of atmospheric muon neutrinos to electron neutrinos as calculated for the Kamioka site [88].

ing way,

$$\pi^- \rightarrow \mu^- + \bar{\nu}_\mu, \quad \pi^+ \rightarrow \mu^+ + \nu_\mu. \quad (1.2.1)$$

The decay of  $\mu^-$  ( $\mu^+$ ) gives rise to one electron antineutrino (neutrino) and one muon neutrino (antineutrino) in the following fashion,

$$\mu^- \rightarrow e^- + \nu_\mu + \bar{\nu}_e, \quad \mu^+ \rightarrow e^+ + \bar{\nu}_\mu + \nu_e. \quad (1.2.2)$$

The left plot of Fig. 1.1 presents a schematic diagram of neutrino production in the Earth atmosphere. From Eqs. 1.2.1 and 1.2.2, we can see that the total flux of muon type neutrino ( $\nu_\mu$ ) and antineutrino ( $\bar{\nu}_\mu$ ) is approximately double of the total flux of electron type neutrino ( $\nu_e$ ) and antineutrino ( $\bar{\nu}_e$ ),

$$\frac{\Phi(\nu_\mu) + \Phi(\bar{\nu}_\mu)}{\Phi(\nu_e) + \Phi(\bar{\nu}_e)} \approx 2, \quad (1.2.3)$$

if all the muons decay in flight before they reach to the surface of Earth. However, at high energies ( $E > 1$  GeV), the decay lifetime of muon gets dialated and it is possible that a large fraction of muons hit the surface of the Earth before they decay. As a result, the flux ratio of muon neutrino to electron neutrino increases with neutrino energy as can be seen in the right panel of Fig. 1.1.

In the interaction of high energy primary cosmic particles, kaons are also produced, which contribute to the atmospheric  $\nu_e$ ,  $\bar{\nu}_e$ ,  $\nu_\mu$ , and  $\bar{\nu}_\mu$  flux spectra. At  $E > 1$  TeV, the three-body decays of charged and neutral kaons are the main source for atmospheric  $\nu_e$  and  $\bar{\nu}_e$  fluxes. The contribution of the charmed meson in the high energy part of neutrino spectra is not well known, and active research being pursued on this topic. The atmospheric neutrinos cover a wide range of energy, few MeV to few thousands of TeV, however, neutrino flux falls rapidly with energy since it has a power law dependence of  $\sim E^{-3}$ . The Kolar Gold Field (KGF) experiment in India [89] and the underground experiment in South Africa [90] are the first to detect atmospheric neutrinos in 1960.

- **The Sun:** In thermonuclear fusion reactions at the core of Sun, electron neutrinos are produced with energy in the range of 0.8 MeV to 15 MeV. Since neutrinos interact weakly, they reach the surface of the Sun much before the light. Therefore, solar neutrino is a perfect tool to learn about the activities inside core of the Sun. The neutrino spectra from the Sun are shown in Fig. 1.2. There are eight different types of solar neutrinos, three ( $^{13}\text{N}$ ,  $^{15}\text{O}$ ,  $^{17}\text{F}$ ) of which are produced in the CNO cycle, and other five are generated in the  $pp$  chain inside core of the Sun. In 1970, solar neutrinos were first detected in the Homestake experiment which was performed by R. Davis and his group [91]. Later, Kamiokande did the first real-time measurement of solar neutrinos and achieved the neutrino image of the Sun [92].
- **Earth's Crust:** Earth is a natural source of radioactive isotopes. The composition models of Earth predict that the total radiogenic power generated in the decay of these isotopes (16 TW) is around half of the measured rate of total heat dissipated by the Earth ( $44.2 \pm 1.0$  TW). The amount of total radioactive isotopes inside the Earth can be estimated by detecting geoneutrinos, the electron antineutrinos produced in the beta-decay of these radioisotopes inside the Earth. The typical energy of geoneutrinos lies in the range of 0.1 MeV to 3 MeV. A major part of the geoneutrinos are created in the decay chain of  $^{238}\text{U}$ ,  $^{232}\text{Th}$ , and  $^{40}\text{K}$ :

$$^{238}\text{U} \rightarrow ^{206}\text{Pb} + 8\alpha + 8e^- + 6\bar{\nu}_e + 51.7 \text{ MeV}, \quad (1.2.4)$$

$$^{232}\text{Th} \rightarrow ^{208}\text{Pb} + 6\alpha + 4e^- + 4\bar{\nu}_e + 42.7 \text{ MeV}, \quad (1.2.5)$$

$$^{40}\text{K} \rightarrow ^{40}\text{Ca} + e^- + \bar{\nu}_e + 1.31 \text{ MeV}. \quad (1.2.6)$$

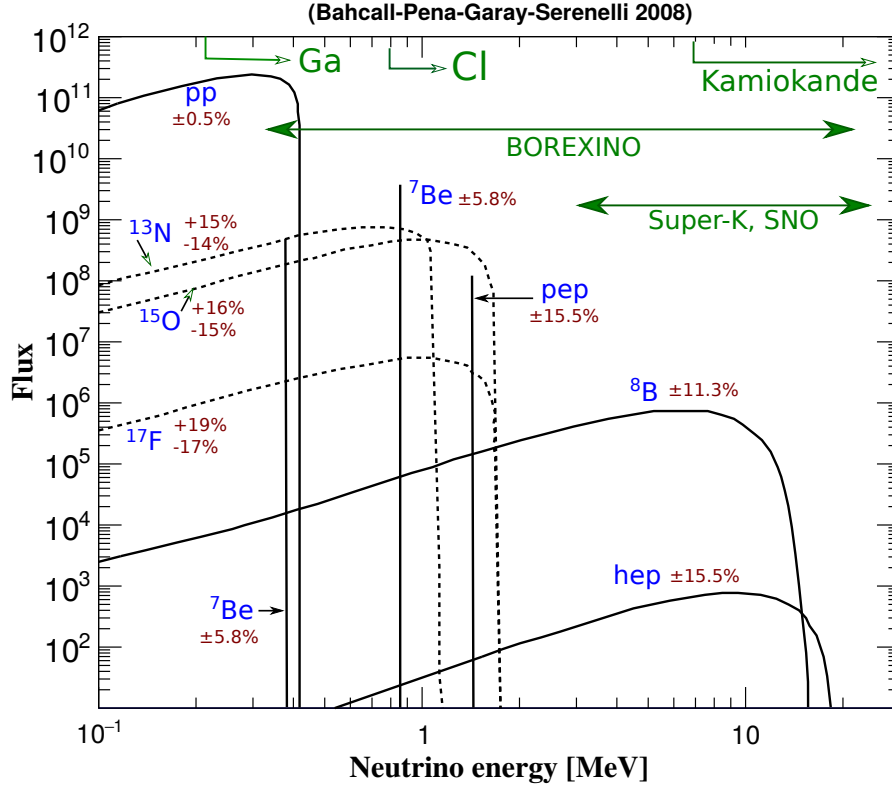


**Figure 1.2.** The solar neutrino flux calculated on the basis of the Standard Solar Model. The solid lines present solar neutrinos produced in  $pp$  chain, and dashed lines are for neutrinos generated in CNO cycle. The unit of flux in y-axis is  $\text{cm}^{-2} \text{s}^{-1} \text{MeV}^{-1}$  and  $\text{cm}^{-2} \text{s}^{-1}$  for continuum and line fluxes respectively. The fluxes are taken from the website <http://www.sns.ias.edu/~jnb/>.

The geoneutrinos were first detected in the KamLAND experiment [93]. In the recent observation, KamLAND detected total  $116^{+28}_{-27}$  geoneutrinos which corresponded to a flux of  $[3.4 \pm 0.8] \times 10^6 \text{ cm}^{-2} \text{s}^{-1} \bar{\nu}_e$  [13]. Another antineutrino detector, Borexino, observed total  $23.7^{+6.5}_{-5.7} (\text{stat})^{+0.9}_{-0.6} (\text{sys})$  geoneutrinos from its 2056 days of data [94]. The combined analysis of geoneutrino data collected by KamLAND and Borexino experiments showed that the total heat produced from  $^{238}\text{U}$  and  $^{232}\text{Th}$  decay chains inside the Earth was around  $20^{+8.8}_{-8.6} \text{ TW}$ , and confirmed that the primordial heat supply has not been exhausted yet [95].

- **High Energy Astrophysical Neutrino Sources:** Various astrophysical sources like active galactic nuclei (AGN) and gamma-ray bursts (GRB) can produce ultra-high energetic ( $\gg \text{TeV}$ ) astrophysical neutrinos. They can reach to the Earth without being affected by the interstellar magnetic field. Therefore, the detection of astrophysical neutrinos is useful in the study of the astrophysical objects. It is widely believed that high energy cosmic particles are produced in the AGN and/or GRB, and interact with the ambient photons in that object

to produce high energy astrophysical neutrinos. Thus, the detection of these neutrinos plays an important role to understand the sources of cosmic particles. The IceCube, an ice-based neutrino detector at the South Pole, detected in three years around 37 neutrino events with deposited energy in the range of 30 TeV to 2000 TeV, and excluded the assumption of pure atmospheric origin for these events by  $5.7\sigma$  confidence level [96]. In the data collected by the IceCube experiment over six years of exposure, a total of 82 events with deposited energy greater than 30 TeV were observed [97]. Very recently, the IceCube detector detected a high-energy neutrino having spatial and temporal coincidence with the gamma flaring from a blazar TXS 0506+056 at the Northern Hemisphere [98,99]. This is the breakthrough discovery of a source of high energy astrophysical neutrinos and a possible source of cosmic particles.

- **The Galactic Supernova:** In a supernova of type II, the core of a massive star (mass  $\geq 8M_{\odot}$ ) collapses from thousands of kilometers to tens of kilometers in a fraction of second if mass of the core reaches to a critical value after it runs out of nuclear fuel. In the process of collapse, an immense amount of gravitational binding energy ( $\sim 3 \times 10^{53}$  erg) is released. Almost 99% of the released energy is carried out by neutrino and antineutrino of all three flavors. The energy of supernova neutrino lies in the range of 10 MeV to 30 MeV. Supernova neutrinos can reach the terrestrial neutrino detectors from the core of the collapsed star unimpeded. Therefore, supernova neutrinos play an important role in understanding the supernova mechanism.

So far, neutrinos from one supernova, SN 1987A in the Large Magellanic Cloud, were observed. The Kamiokande II (11 events) [100], the IMB (8 events) [101], and the BAKSAN (5 events) [102] experiments detected total 24 supernova neutrino events on 23rd of February in 1987 approximately three hours before the lights were visible from the supernova. Despite the small statistics, these supernova neutrino events were useful to confirm many predictions of supernova theory and to study the neutrino emission mechanism inside the supernova [103–107]. One of the main channels for the detection of supernova neutrinos is the inverse beta-decay process,  $\bar{\nu}_e + p \rightarrow n + e^+$ , in the water Cherenkov detector.

- **The Big Bang:** The relic neutrinos which form the cosmic neutrino background were produced in the Big Bang nucleosynthesis process. At the early stage of the Universe, neutrinos

were in thermal equilibrium with the hot plasma of the Universe. As the Universe expanded, the interaction rate of various processes became smaller than the expansion rate, and particles got decoupled (freeze-out) from the thermal bath. Since neutrinos interact through weak interaction, they got decoupled very quickly when the Universe was  $\sim 1$  second old. It is worthwhile to note that the relic neutrino might carry the imprint of the Universe at the time of their decoupling. The present temperature of relic neutrino is 1.95 Kelvin which corresponds to the energy of 0.00017 eV. Although the relic neutrinos are the second abundant particles in the Universe, detecting them in experiments is still an open problem because the energy of these neutrinos is too small.

### 1.2.2 Man-made Sources of Neutrinos

- **Nuclear Reactors:** Many countries including India have nuclear power plants to generate electricity using the nuclear fission processes of radioactive elements. Mainly, four radioactive isotopes are used, viz.  $^{235}\text{U}$ ,  $^{238}\text{U}$ ,  $^{239}\text{Pu}$ , and  $^{241}\text{Pu}$ , which decay through normal beta-decay chain and produce reactor antineutrinos ( $\bar{\nu}_e$ ) in a large number. The energy of the reactor antineutrino lies in the range of 0.1 to 10 MeV. In each fission process, on an average, six antineutrinos are generated, and a total energy of about 200 MeV is released<sup>2</sup>. Therefore, a nuclear reactor having 1 GW thermal power emits a flux of electron antineutrinos of around  $2 \times 10^{20}$ /per second.

The reactor antineutrinos are extensively used in the measurement of the neutrino oscillation parameters. The value of the smallest mixing angle  $\theta_{13}$  was measured in Daya Bay [108], RENO [109], and Double Chooz [110] experiments by detecting  $\bar{\nu}_e$  from reactors. The KamLAND experiment, a long-baseline reactor antineutrino oscillation experiment, played an important role to establish that the solar neutrino anomaly could be explained by the so-called LMA-MSW solution.

- **Particle Accelerators:** A high intensity neutrino beam can be produced using the pion ( $\pi$ ) decay in a lab. In a particle accelerator, a bunch of protons are accelerated to the desired energy, and then directed to impinge on a target to produce pions. These  $\pi^-$  ( $\pi^+$ ) are focused

---

<sup>2</sup>Roughly 4.5% of the total released energy in one fission process ( $\sim 200$  MeV) is carried away by six antineutrinos, whereas rest of the energy ( $\sim 95.5\%$ ) is retained as heat in the core.

by the magnetic horn and are left to decay in a decay pipe to produce  $\mu^-$  ( $\mu^+$ ) and  $\bar{\nu}_\mu$  ( $\nu_\mu$ ). The neutrinos generated from a particle accelerator have been vastly used in the study of fundamental properties of neutrino. An advantage of the accelerator-based neutrino experiment is that the neutrino energy can be tuned as per the need of study.

The K2K, a long-baseline neutrino experiment, sent the  $\nu_\mu$  beam produced at the KEK accelerator to the water Cherenkov detector of the Super-Kamiokande experiment, and confirmed the disappearance of  $\nu_\mu$  as observed in the atmospheric neutrino experiments. The on-going neutrino oscillation experiments T2K and NOvA detect neutrinos produced at the accelerators in J-PARC, Japan and Fermilab, US respectively.

### 1.3 The Detection of Neutrinos and Anomalies

Neutrinos were not detected for more than two decades after their prediction because their interaction cross-section is very small. In 1956, two pioneering scientists Cowan and Reines detected the antineutrino coming from a nuclear reactor situated at the Savannah River Plant of U.S. [111]. They used two tanks of dissolved  $\text{CdCl}_2$  and three tanks of liquid scintillation detectors in alternate layers to observe the inverse beta-decay (IBD) process ( $\bar{\nu}_e + p \rightarrow n + e^+$ ) of antineutrino in the detector. The coincident measurement of two pulses<sup>3</sup> in a narrow time window of  $17 \mu\text{s}$  was the smoking gun signature of antineutrino events in the experiment by Cowan and Reins. Using 4200 litres of  $\text{CdCl}_2$ , they were able to detect the antineutrino coming from the Savannah River reactor in 1956. They observed that the number of neutrino interaction was dependent on the reactor power, and estimated the cross-section of the IBD process as  $\bar{\sigma} = 6.3 \times 10^{-44} \text{ cm}^2$  with  $\pm 25\%$  uncertainty [111]. In this experiment, the signal to background ratio was reported as 3:1 [111]. Later, the detection of solar and atmospheric neutrinos in several world-class experiments gave rise to the solar and the atmospheric neutrino anomalies respectively, which we will discuss now.

---

<sup>3</sup>The incoming antineutrino interacts with the protons of hydrogenous liquid scintillator through the inverse beta-decay (IBD) process  $\bar{\nu}_e + p \rightarrow n + e^+$ . The positron in final state annihilates an ambient electron in the detector, and produces two 511 keV photons. The first pulse in the detector occurs as a result of the energy deposition by these 511 keV photons in the scintillation detector. After a few  $\mu\text{s}$ , another pulse appears due to the photon produced in the neutron capture process of cadmium nuclei ( $^{113}\text{Cd}(n, \gamma) ^{114}\text{Cd}$ ).



### 1.3.1 Solar Neutrino Anomaly

In 1968, Raymond Davis performed an experiment to detect solar neutrino using 520 ton liquid tetrachloroethylene ( $\text{C}_2\text{Cl}_4$ ) with a 24% natural abundance of  $^{37}\text{Cl}$ . To reduce background from the cosmic particles, the detector was placed at a depth of about 1.5 km underground at the Homestake gold mine in South Dakota, USA [91]. A neutrino with energy higher than 814 keV interacts with a chlorine ( $^{37}\text{Cl}$ ) nuclei and produces an argon ( $^{37}\text{Ar}$ ) in the final state. The heart of this experiment was the system of counting the number of argon atoms, which determined the number of neutrino events, in a tank filled with mainly the chlorine. The  $^{37}\text{Ar}$  atoms were extracted from the tank once in around two months and were counted. Observations from 108 such extractions of  $^{37}\text{Ar}$  atoms in the detector provided an estimation of the solar neutrino flux as  $2.56 \pm 0.16$  SNU (solar neutrino unit =  $10^{-36}$  captures per target atom per second) [19]. However, the expected solar neutrino event was  $9.3 \pm 1.3$  SNU using the predicted flux from the Standard Solar Model (SSM) [112]. More than  $3\sigma$  discrepancy between the predicted and the measured solar neutrino events gave rise to the famous “solar neutrino problem”. Subsequently, the deficit in the observed solar neutrino events was confirmed by the gallium-based ( $^{71}\text{Ga}$ ) solar neutrino experiments, SAGE [20] and GALLEX [21, 113]. The real time measurement of the solar neutrinos in the Kamiokande [92] and the Super-Kamiokande [22, 24, 114] experiments obtained around one-thirds of the total events that was predicted by the SSM. The mystery of the two-thirds of the predicted solar neutrinos remained unresolved for almost 30 years until the heavy water Cherenkov detector in the SNO experiment brought the solution in light. The SNO could distinguish the NC interaction, participated by all  $\nu$  flavors, from the CC interaction, experienced by only  $\nu_e$  [115]. The SNO data confirmed that the total NC events agreed with the predicted number of events obtained on the basis of the SSM, however, the CC events ( $\nu_e$ ) were one-third of the predicted one [9]. These observations implied that the solar neutrino flux arriving at the Earth had the non-electron flavors and the two-third of  $\nu_e$  must had converted to  $\nu_\mu$  and  $\nu_\tau$ . It is worthwhile to mention that the Kamioka Liquid scintillator Anti-Neutrino Detector (KamLAND) observed the disappearance of reactor  $\bar{\nu}_e$  for the first time [10] and played an important role in measuring the solar neutrino oscillation parameters [11]. For more discussion on the solar neutrino oscillation, see Sec. 2.3.1. The neutrino flavor conversion was discovered in the atmospheric sector even before it was found in the solar neutrinos. Next, we

will discuss the epic story of how the first evidence of neutrino flavor oscillation was observed in the Super-Kamiokande experiment.

### 1.3.2 Atmospheric Neutrino Anomaly

By the end of twentieth century, the anomalous behavior of neutrino was observed not only in solar but also in atmospheric neutrino events. Precise estimations of atmospheric  $\nu$  and  $\bar{\nu}$  fluxes were required for proton decay searches as these  $\nu/\bar{\nu}$ -induced events contribute to the background in the detector. In Sec. 1.2, we have seen that the atmospheric  $\nu_\mu$  ( $\bar{\nu}_\mu$ ) flux is expected to be almost double of the  $\nu_e$  ( $\bar{\nu}_e$ ) flux. However, the experiments like Kamiokande [7], IMD [116], and Soudan-2 [117] found that the fluxes of atmospheric  $[\nu_e + \bar{\nu}_e]$  and  $[\nu_\mu + \bar{\nu}_\mu]$  were equal in number. On the contrary, two other proton decay experiments Frejus [118] and NUSEX [119] did not observe this anomaly in atmospheric neutrino although they had large uncertainties in their results. To unfold the puzzle, neutrino flux and cross-section calculations were verified by more than one groups independently. On the other hand, to verify the performance of the detector, Kamiokande collaboration performed a dedicated test beam study by shooting charged particles at the 1 kiloton water Cherenkov detector. This test beam experiment clearly showed that “electrons and muons were well separated by the applied particle identifications algorithms, and data and simulation were in very good agreement” [120].

Being inspired by the success of the Kamiokande experiment, the collaboration upgraded their detector to a bigger and more efficient one which is the Super-Kamiokande (SK) experiment. They reported the double ratio  $\mathcal{R} = (N_\mu/N_e)_{\text{data}}/(N_\mu/N_e)_{\text{MC}} = 0.61 \pm 0.03 \text{ (stat)} \pm 0.05 \text{ (sys)}$  using the sub-GeV event sample (visible energy  $E_{\text{vis}} < 1.3 \text{ GeV}$ ) [121] collected over an exposure of 414 days with 22.5 kiloton fiducial mass of the SK detector. The measured value of double ratio in SK was similar to the results as obtained in Kamiokande. Fig. 1.3 presents the double ratio measured in different experiments. We can see that all experiments except NUSEX and Frejus obtained the double ratio as almost 1/2, whereas its expected value was 1 [120].

The multi-GeV events ( $E_{\text{vis}} > 1.3 \text{ GeV}$ ) in 414 days of data in Super-Kamiokande clarified the reason for getting  $\mathcal{R} < 1$ . Having the separate zenith angle distributions for  $\nu_e$  and  $\nu_\mu$ -induced events (see Fig. 1.4), SK showed that the number of electron-like events matched with the expected

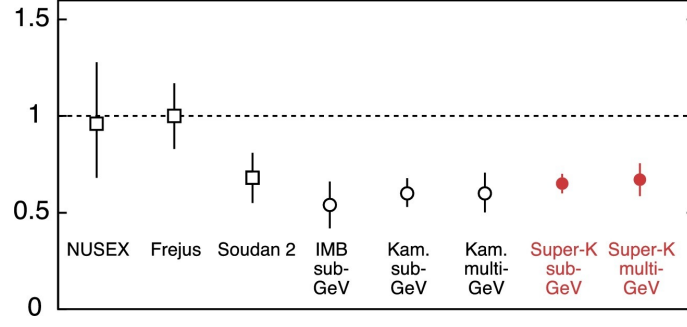


**Figure 1.3.** Measured values of the double ratio  $\mathcal{R} = (N_\mu/N_e)_{data}/(N_\mu/N_e)_{MC}$  from different atmospheric neutrino experiments are shown here. This figure is taken from Ref. [120].

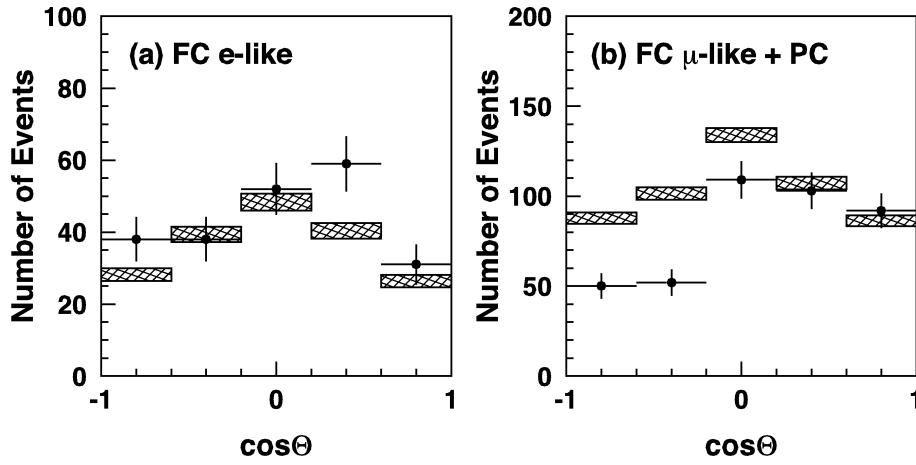


**Figure 1.4.** Number of the observed multi-GeV ( $E_{vis} > 1.3$  GeV) electron-like (left panel) and muon-like (right panel) events as a function of zenith angle using the data sample of 414 days collected by the Super-Kamiokande experiment. This figure is taken from Ref. [8].

tation, whereas the muon-like events were smaller in number than the expected one [8]. Most importantly, upward-going muon-like events ( $-1 < \cos\theta < 0$ ) exhibited the distinct distortion in zenith angle distribution, and downward-going ( $0 < \cos\theta < 1$ ) muon-like events matched with the predicted numbers. It is to be noted that the upward-going events traverse a long distance through the Earth matter before they reach the detector, while the downward-going events travel a small distance which is the height of the atmosphere above the Earth. With around 400 multi-GeV muon-like events, the up-down asymmetry was observed with greater than  $5\sigma$  confidence level [120]. The zenith angle distributions of sub-GeV and multi-GeV events revealed that the origin of anomaly in the double ratio was due to the disappearance of muon neutrino depending on their energies and the path lengths that they traversed [8].

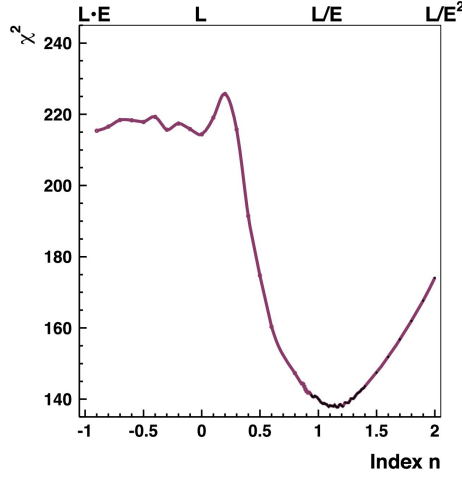


**Figure 1.5.** Statistical significance ( $\chi^2$ ) in the Super-Kamiokande for fitting the atmospheric neutrino data with different  $L/E^n$  with  $n$  as a variable as shown in x-axis. This figure is taken from Ref. [122].

There are many theoretical hypotheses which could explain the disappearance of  $\nu_\mu$  in the Super-Kamiokande experiment, such as, neutrino flavor induced oscillation [123, 124], neutrino decay [125–129], decoherence [130–132], Lorentz invariance violation [133, 134], and so on. These theories produce  $L/E^n$  oscillation patterns with different value of  $n$ , for example,  $n = -1$  indicates the violation of Lorentz invariance and equivalence principle,  $n = 0$  for CPT violation,  $n \neq 1$  is valid for non-standard neutrino oscillation, and  $n = 1$  is true for neutrino oscillation due to non-degenerate masses and flavor mixings. Fig. 1.5 illustrates the significance for fitting ( $\chi^2$ ) the data with varying parameter  $n$ , where  $n = 1$ , the standard oscillation, is the most favored [122]. The possibility of  $\nu_\mu \rightarrow \nu_{\text{sterile}}$  as a sole reason for  $\nu_\mu$  disappearance is disfavored with more than  $7\sigma$  confidence level [135–137]. The oscillation among active neutrinos  $\nu_\mu \rightarrow \nu_e$  results a poor fit with  $\chi^2 = 87.8/67$ . The best fit ( $\chi^2 = 65.2/67$ ) theory is  $\nu_\mu \rightarrow \nu_\tau$  with maximal mixing and mass-squared splitting as  $2.2 \times 10^{-3} \text{ eV}^2$  [5]. Other neutrino experiments, which are sensitive to the mass-squared splitting  $\sim 10^{-3} \text{ eV}^2$  like K2K [138], MINOS [139], T2K [140, 141], have confirmed the disappearance of  $\nu_\mu$  in the neutrino beam sent by the particle accelerators. The appearance of  $\nu_\tau$  in the beam of  $\nu_\mu$  is verified in the accelerator-based long-baseline neutrino experiment OPERA [142]. We will discuss more on the neutrino oscillation in Chapter 2.

## 1.4 A Brief Motivation and Plan of the Thesis

Starting from its prediction, neutrinos have surprised the particle physicists. The experimental evidences for the existence of only left-handed neutrino and absence of its right-handed partner make the neutrino massless in the Standard Model of particle physics. However, the solar and atmospheric neutrino anomalies unravel that neutrinos are massive and neutrino flavors mix with each other. The Standard Model provides the correct descriptions of the three fundamental interactions of elementary particles and can explain almost all the experimental results. Nevertheless, there are few experimental observations which cannot be explained within the basic SM, and neutrino oscillation is one of them. It is widely speculated that the SM is an effective theory at low energy, while the unresolved issues are consequences of the physics that exists at very high energy. Neutrino holds a property that can only be explained by extension of the Standard Model (BSM) theory, thus the attempts of finding the signal for new physics in the neutrino experiments are quite interesting and at the same time challenging too. All the on-going and proposed neutrino experiments have the parallel missions to explore BSM physics along with the standard oscillation measurements. Currently neutrino physics is going through the precision phase, and the presence of BSM physics at the sub-leading level can alter the outcome of an experiment. Therefore, the study of possible BSM theories in neutrino experiments can be helpful in unfolding some new flavors of Nature.

The main focus of the thesis is to study three different new physics scenarios that can arise in beyond the Standard Model framework. In chapter 2, we provide an overview of the theory of neutrino oscillation and highlight the important results from the past and currently-ongoing neutrino oscillation experiments. Chapter 3 discusses the main features of the 50 kiloton magnetized ICAL detector at the India-based Neutrino Observatory and its responses to muons and hadrons. In Chapter 4, we explore the indirect detection of the Galactic dark matter assuming its annihilation and decay to  $\nu\bar{\nu}$  pair, and estimate the sensitivity of the proposed ICAL detector to place the constraint on such dark matter interactions.

Chapter 5 is devoted to the study of a flavor changing neutral current (FCNC) non-standard interaction (NSI) of neutrinos with matter fermions ( $f$ ) as given by  $\nu_\mu + f \rightarrow \nu_\tau + f$  in a model independent way. In optimizing the sensitivity of the ICAL detector to NSI, we highlight the

importance of the high energy neutrino events and reconstructed hadron energy included in the analysis. We show that the ability to identify the charge of  $\mu^-$  and  $\mu^+$  in the ICAL detector is crucial to study the NSI of neutrino. Moreover, we estimate the sensitivity of the ICAL detector to determine the mass hierarchy and to measure the atmospheric oscillation parameters including NSI in the theory.

In Chapter 6, we consider the flavor-diagonal neutral current (FDNC) non-standard interactions of neutrino which appears in the minimal extension of the SM gauge group with an additional  $U(1)$  in an anomaly free way having  $L_e - L_\mu$  and  $L_e - L_\tau$  symmetries. The extra  $U(1)$  gives rise to a new force, and if the associated gauge boson is ultralight, then the force has long range. This new force with a range comparable to the Earth-Sun distance can produce an extra potential due to the NC forward elastic scattering between terrestrial neutrinos and solar electrons mediated by the new gauge boson. We produce the expected  $\nu$  and  $\bar{\nu}$  data in the ICAL detector including these extra potentials apart from the standard matter potential and perform a detailed analysis to estimate the sensitivity of the ICAL detector to long range forces of type  $L_e - L_\mu$  and  $L_e - L_\tau$  one at-a-time. Chapter 7 provides the summary and an outlook of the thesis.

# 2 Neutrino Flavor Oscillation

## Contents

---

<b>2.1 Neutrino Oscillation in Vacuum . . . . .</b>	<b>20</b>
<b>2.2 Neutrino Oscillation in Matter . . . . .</b>	<b>27</b>
<b>2.3 Experimental Results . . . . .</b>	<b>30</b>
2.3.1 Solar Oscillation Parameters ( $\theta_{12}, \Delta m_{21}^2$ )	30
2.3.2 Atmospheric Oscillation Parameters ( $\theta_{23}, \Delta m_{32}^2$ )	35
2.3.3 Discovery of non-zero $\theta_{13}$	39
<b>2.4 Current Status of Neutrino Oscillation Parameters . . . . .</b>	<b>40</b>
<b>2.5 Remaining Unsolved Issues in Neutrino Oscillation . . . . .</b>	<b>42</b>
<b>2.6 Relevant Oscillation Channels in Atmospheric Experiments . . . . .</b>	<b>43</b>

---

The idea of neutrino oscillation was first put forward by Bruno Pontecorvo as a quantum mechanical phenomenon analogous to the  $K^0 - \bar{K}^0$  meson oscillation [143, 144]. If the non-degenerate neutrino mass eigenstates, which propagate independently, and the flavor eigenstates, which are produced at the source and detected at the detector, are not identical, then the neutrino oscillation takes place. The theory of active neutrino flavor mixing was first postulated by Maki, Nakagawa, and Sakata [145] in 1962 just after the discovery of the second ( $\nu_e$  was already known) neutrino flavor (muon type) in the Brookhaven experiment [146]. Subsequent works saw a proliferation of the plane wave treatment of the two flavor mixing [147–151].

In this chapter, we describe the theory of neutrino oscillation and the current status of our understanding on neutrino mixing parameters. The oscillation of neutrinos in matter can be different from that of in vacuum due to the non-trivial effects of the matter potential that appears due to

the coherent forward elastic scattering of neutrinos with matter fermions. Secs. 2.1 and 2.2 are devoted to explain the neutrino oscillation in vacuum and matter respectively. Sec. 2.3 contains a summary of the relevant experimental results. In Sec. 2.4, we present the values of neutrino oscillation parameters obtained from the global analysis of neutrino oscillation data. In Sec. 2.5, we discuss remaining fundamental unsolved issues in neutrino oscillation physics. In Sec. 2.6, we highlight in context of the ICAL at INO a few important points of the oscillation channels that are relevant for the atmospheric  $\nu_\mu$  and  $\bar{\nu}_\mu$  induced events in detector.

## 2.1 Neutrino Oscillation in Vacuum

Neutrino oscillation in vacuum is an outcome of the pure quantum mechanical linear superposition of non-degenerate neutrino mass eigenstates. The mixing of  $N$  generations of neutrino is described with a unitary  $N \times N$  matrix, which is parameterized in terms of  $N(N - 1)/2$  mixing angles and  $N(N + 1)/2$  phases. However, if neutrinos are Dirac<sup>1</sup> type in Nature then  $2N - 1$  phases are not physical. Thus, we need  $(N - 1)(N - 2)/2$  physical phases to explain the oscillation phenomena. In general, the neutrino flavor state  $\nu_\alpha$  is a linear superposition of the neutrino mass eigenstates  $|\nu_i\rangle$ ,  $i = 1$  to  $N$ ,

$$|\nu_\alpha\rangle = \sum_{i=1}^N U_{\alpha i}^* |\nu_i\rangle, \quad (2.1.1)$$

where  $U$  is a unitary matrix representing the lepton mixing. The orthonormal mass eigenstates ( $\langle \nu_i, \nu_j \rangle = \delta_{ij}$ ) and the unitary nature of  $U$  ensure that the flavor eigenstates are orthonormal ( $\langle \nu_\alpha, \nu_\beta \rangle = \delta_{\alpha\beta}$ ). The Schrödinger equation for a neutrino mass eigenstate  $\nu_k(t)$  with energy  $E_k$  ( $\hbar = 1$ ) is given by

$$i \frac{d}{dt} |\nu_k(t)\rangle = E_k |\nu_k(t)\rangle, \quad (2.1.2)$$

which governs the time evolution of a massive neutrino as

$$|\nu_k(t)\rangle = e^{-iE_k t} |\nu_k\rangle. \quad (2.1.3)$$

---

<sup>1</sup>If neutrino is Majorana particle then  $N$  number of phases can be eliminated by rephasing charged lepton fields and there is no freedom to rephase neutrino fields. Thus, in Majorana case, the number of physical phases is  $N(N - 1)/2$ , out of which  $(N - 1)(N - 2)/2$  are Dirac phases and rest  $N - 1$  are the Majorana phases. Note that the Majorana phases do not come into the picture of neutrino oscillation.



Therefore, the time evolution of a flavor state is

$$|\nu_\alpha(t)\rangle = \sum_{i=1}^N U_{\alpha i}^* e^{-i E_i t} |\nu_i\rangle. \quad (2.1.4)$$

The transition amplitude for alteration of  $\nu_\alpha$  to another flavor state  $\nu_\beta$  is

$$A(t) = \langle \nu_\beta | \nu_\alpha(t) \rangle = \sum_{i=1}^N U_{\alpha i}^* U_{\beta i} e^{-i E_i t}. \quad (2.1.5)$$

If there is a pure beam of  $\nu_\alpha$  at  $t = 0$ , then the probability to get  $\nu_\beta$  at time  $t = T$  is the square of  $\nu_\alpha \rightarrow \nu_\beta$  transition amplitude, which can be written as

$$\begin{aligned} P_{\nu_\alpha \rightarrow \nu_\beta}(T) &= |A(T)|^2 = \sum_{i,j=1}^N U_{\alpha i}^* U_{\beta i} U_{\alpha j} U_{\beta j}^* e^{-i(E_i - E_j)T} \\ &= \sum_{i=j=1}^N |U_{\alpha i}|^2 |U_{\beta j}|^2 + \underbrace{\sum_{i>j=1}^N U_{\alpha i}^* U_{\beta i} U_{\alpha j} U_{\beta j}^* e^{-i(E_i - E_j)T}}_X + X^*. \end{aligned} \quad (2.1.6)$$

The cosmological observations reveal that the upper limit on the sum of all the neutrino mass eigenvalues ( $\sum_i m_i$ ) is around 0.23 eV at 95% C.L. [152] considering the WMAP polarization and baryon acoustic oscillation (BAO) measurements. Therefore, for the study of neutrino oscillation in current neutrino oscillation experiments where neutrino energy ( $E$ ) is of the order of MeV or more, we can safely take the ultra-relativistic assumption as follows. The energy of the mass eigenstate  $\nu_k$  with mass  $m_k$  and momentum  $p$  can be written as (in natural units,  $c = 1$ )

$$E_k = \sqrt{p^2 + m_k^2} \approx |p| + \frac{m_k^2}{2|p|}. \quad (2.1.7)$$

Therefore,

$$E_i - E_j = \frac{\Delta m_{ij}^2}{2|p|} \approx \frac{\Delta m_{ij}^2}{2E}, \quad (\Delta m_{ij}^2 = m_i^2 - m_j^2), \quad (2.1.8)$$

where the ultra-relativistic limit allows us to take  $|p| = E$  neglecting the mass of neutrino. Also, for ultra-relativistic neutrinos propagating with almost speed of light, we can consider the distance traversed by neutrino as  $L = T$  in natural units ( $c = 1$ ).

For any two complex numbers, let us say  $A$  and  $B$ , the following relation is valid,

$$AB + A^* B^* = 2 [\text{Re}(A) \text{Re}(B) - \text{Im}(A) \text{Im}(B)] = 2\text{Re}(AB). \quad (2.1.9)$$

Using Eqs. 2.1.8 and 2.1.9, and replacing  $T$  by  $L$  as discussed before, we can rewrite Eq. 2.1.6 as

$$\begin{aligned} P_{\nu_\alpha \rightarrow \nu_\beta}(L) &= \sum_{i=j=1}^N |U_{\alpha i}|^2 |U_{\beta j}|^2 + 2 \sum_{i>j=1}^N \text{Re}(U_{\alpha i}^* U_{\beta i} U_{\alpha j} U_{\beta j}^*) \cos \frac{\Delta m_{ij}^2 L}{2E} \\ &\quad + 2 \sum_{i>j=1}^N \text{Im}(U_{\alpha i}^* U_{\beta i} U_{\alpha j} U_{\beta j}^*) \sin \frac{\Delta m_{ij}^2 L}{2E} \\ &= \sum_{i=j=1}^N |U_{\alpha i}|^2 |U_{\beta j}|^2 + 2 \sum_{i>j=1}^N \text{Re}(U_{\alpha i}^* U_{\beta i} U_{\alpha j} U_{\beta j}^*) - 4 \sum_{i>j=1}^N \text{Re}(U_{\alpha i}^* U_{\beta i} U_{\alpha j} U_{\beta j}^*) \sin^2 \frac{\Delta m_{ij}^2 L}{4E} \\ &\quad + 2 \sum_{i>j=1}^N \text{Im}(U_{\alpha i}^* U_{\beta i} U_{\alpha j} U_{\beta j}^*) \sin \frac{\Delta m_{ij}^2 L}{2E}. \end{aligned} \quad (2.1.10)$$

Since  $U$  is a unitary matrix, we can write

$$\sum_j U_{\alpha j} U_{\beta j}^* = \delta_{\alpha\beta}. \quad (2.1.11)$$

Now, squaring the above equation, we get

$$\sum_{i=j=1}^N |U_{\alpha i}|^2 |U_{\beta j}|^2 + 2 \sum_{i>j=1}^N \text{Re}(U_{\alpha i}^* U_{\beta i} U_{\alpha j} U_{\beta j}^*) = \delta_{\alpha\beta}. \quad (2.1.12)$$

Therefore, we can write the expression for  $\nu_\alpha \rightarrow \nu_\beta$  transition probability as

$$P_{\nu_\alpha \rightarrow \nu_\beta}(L) = \delta_{\alpha\beta} - 4 \sum_{i>j=1}^N \text{Re}(U_{\alpha i}^* U_{\beta i} U_{\alpha j} U_{\beta j}^*) \sin^2 \frac{\Delta m_{ij}^2 L}{4E} + 2 \sum_{i>j=1}^N \text{Im}(U_{\alpha i}^* U_{\beta i} U_{\alpha j} U_{\beta j}^*) \sin \frac{\Delta m_{ij}^2 L}{2E}. \quad (2.1.13)$$

One can clearly see that the oscillation probability is a function of the mass-squared difference ( $\Delta m_{ij}^2$ ) rather than the absolute masses, and the phase of oscillation is proportional to  $L/E$ . Thus, the oscillation probability depends on the neutrino energy as well as the path length that a neutrino travels between its source and detector. Next, we discuss the neutrino oscillation in  $2\nu$  framework to understand the oscillation probability in a simplified fashion.

### • Oscillation in Two Neutrino Framework

The three-neutrino mixing has been firmly established by the data of neutrino oscillation experiments. Nevertheless, let us first discuss the oscillation probability in a two neutrino ( $2\nu$ ) framework to understand the neutrino oscillation phenomena in a simpler way. To explain the  $2\nu$  mixing, we need one mixing angle ( $\theta$ ), and therefore, for any two neutrino flavors,  $\nu_\alpha$  and  $\nu_\beta$ , the mixing matrix can be written as

$$\begin{pmatrix} \nu_\alpha \\ \nu_\beta \end{pmatrix} = \begin{pmatrix} \cos \theta & \sin \theta \\ -\sin \theta & \cos \theta \end{pmatrix} \begin{pmatrix} \nu_i \\ \nu_j \end{pmatrix}. \quad (2.1.14)$$

Hence, following the Eq. 2.1.13, we obtain  $\nu_\alpha \rightarrow \nu_\beta$  transition probability ( $\alpha \neq \beta$ ) as

$$P_{\nu_\alpha \rightarrow \nu_\beta}(L, E) = \sin^2 2\theta \sin^2 \frac{\Delta m_{ij}^2 L}{4E}. \quad (2.1.15)$$

Using the unitarity property of the mixing matrix, the survival probability of  $\nu_\alpha$  ( $\nu_\alpha \rightarrow \nu_\alpha$ ) can be written as

$$P_{\nu_\alpha \rightarrow \nu_\alpha}(L, E) = 1 - \sin^2 2\theta \sin^2 \frac{\Delta m_{ij}^2 L}{4E}. \quad (2.1.16)$$

Expressing  $\Delta m_{ij}^2$  in the units of  $\text{eV}^2$ ,  $E$  in MeV or GeV, and  $L$  in m or km, the above expression of survival probability can be written as

$$P_{\nu_\alpha \rightarrow \nu_\alpha}(L, E) = 1 - \sin^2 2\theta \sin^2 \left( 1.27 \frac{\Delta m_{ij}^2 [\text{eV}^2] L [\text{m}]}{E [\text{MeV}]} \right), \quad (2.1.17)$$

or

$$P_{\nu_\alpha \rightarrow \nu_\alpha}(L, E) = 1 - \sin^2 2\theta \sin^2 \left( 1.27 \frac{\Delta m_{ij}^2 [\text{eV}^2] L [\text{km}]}{E [\text{GeV}]} \right). \quad (2.1.18)$$

The amplitude of the oscillation is governed by the mixing angle, whereas the phase depends on the mass-squared difference and  $L/E$  ratio. The phase of the oscillation can be written as  $\pi \frac{L}{L^{\text{osc}}}$  with  $L^{\text{osc}}$  as the oscillation length. Therefore, using the phase factors in Eqs. 2.1.16, 2.1.17, and 2.1.18, we can write the expression of  $L^{\text{osc}}$  for neutrino oscillation as

$$L^{\text{osc}} = \frac{4\pi E}{\Delta m_{ij}^2} \simeq 2.47 \text{ m} \frac{E [\text{MeV}]}{\Delta m_{ij}^2 [\text{eV}^2]} = 2.47 \text{ km} \frac{E [\text{GeV}]}{\Delta m_{ij}^2 [\text{eV}^2]}. \quad (2.1.19)$$

The oscillation length increases as we go to higher energies and smaller mass-squared differences. In order to realize the effect of oscillation governed by  $\Delta m_{ij}^2$ , the neutrino detector should be kept at a distance  $L \sim L^{\text{osc}}$  from the neutrino source. If  $\Delta m_{ij}^2 = 2.4 \times 10^{-3} \text{ eV}^2$ , then neutrino with  $E = 5 \text{ GeV}$  has the oscillation length of the order of 5000 km, whereas with  $E = 100 \text{ GeV}$ ,  $L^{\text{osc}} \sim 100000 \text{ km}$ .

For  $2\nu$  mixing, oscillation from one flavor to another flavor is maximum in vacuum when neutrino energy ( $E$ ) and baseline ( $L$ ) satisfy the following relation,

$$\frac{\Delta m_{ij}^2 L}{4E} = (2n + 1) \frac{\pi}{2} \quad \text{with } n = 0, 1, 2.. \quad (2.1.20)$$

Next, we discuss the oscillation of neutrino in  $3\nu$  framework.

### • Oscillation in Three Neutrino Framework

To explain the  $3\nu$  mixing, the parameters that we need are 3 mixing angles,  $\theta_{23}$ ,  $\theta_{13}$ , and  $\theta_{12}$ , one Dirac phase  $\delta_{\text{CP}}$  related to the CP violation, and two independent mass-squared differences<sup>2</sup>. Following the standard Particle Data Group convention [4], we parametrize the vacuum Pontecorvo-Maki-Nakagawa-Sakata (PMNS) matrix [144, 145, 153] in the following fashion,

$$U = R(\theta_{23}) U_{\delta_{\text{CP}}} R(\theta_{13}) U_{\delta_{\text{CP}}}^\dagger R(\theta_{12}) \quad \text{where } U_{\delta_{\text{CP}}} = \text{diag}(1, 1, e^{i\delta_{\text{CP}}}), \quad (2.1.21)$$

with  $R(\theta_{ij})$  as the orthogonal rotation matrix for the rotation in  $i$ - $j$  plane with  $\theta_{ij}$  angle. The three flavor neutrino mixing matrix takes the form as

$$U = \begin{pmatrix} c_{12}c_{13} & s_{12}c_{13} & s_{13}e^{-i\delta_{\text{CP}}} \\ -s_{12}c_{23} - c_{12}s_{23}s_{13}e^{i\delta_{\text{CP}}} & c_{12}c_{23} - s_{12}s_{23}s_{13}e^{i\delta_{\text{CP}}} & s_{23}c_{13} \\ s_{12}s_{23} - c_{12}c_{23}s_{13}e^{i\delta_{\text{CP}}} & -c_{12}s_{23} - s_{12}c_{23}s_{13}e^{i\delta_{\text{CP}}} & c_{23}c_{13} \end{pmatrix} \quad (2.1.22)$$

with  $c_{ij} = \cos \theta_{ij}$  and  $s_{ij} = \sin \theta_{ij}$ . For antineutrino, the mixing matrix is  $U^*$ .

---

<sup>2</sup>For three independent mass eigenstates, we have three mass-squared differences,  $\Delta m_{21}^2$ ,  $\Delta m_{31}^2$ , and  $\Delta m_{32}^2$ . However, any two mass-squared differences are independent and can be used to get the third one.

Now, the evolution equation for three active neutrino flavors can be written in the following way,

$$i \frac{d}{dt} \begin{pmatrix} \nu_e(t) \\ \nu_\mu(t) \\ \nu_\tau(t) \end{pmatrix} = U \begin{pmatrix} 0 & 0 & 0 \\ 0 & \Delta m_{21}^2/2E & 0 \\ 0 & 0 & \Delta m_{31}^2/2E \end{pmatrix} U^\dagger \begin{pmatrix} \nu_e \\ \nu_\mu \\ \nu_\tau \end{pmatrix}. \quad (2.1.23)$$

For the  $3\nu$  mixing, we get the survival probability of  $\nu_\alpha$  in vacuum using  $N = 3$  in Eq. 2.1.13 as

$$P_{\alpha\alpha} = 1 - 4 \operatorname{Re}(|U_{\alpha 1}|^2 |U_{\alpha 2}|^2) \sin^2 \frac{\Delta m_{21}^2 L}{4E} - 4 \operatorname{Re}(|U_{\alpha 1}|^2 |U_{\alpha 3}|^2) \sin^2 \frac{\Delta m_{31}^2 L}{4E} - 4 \operatorname{Re}(|U_{\alpha 2}|^2 |U_{\alpha 3}|^2) \sin^2 \frac{\Delta m_{32}^2 L}{4E}. \quad (2.1.24)$$

In the above equation, we use  $\bar{\nu}_e$  as flavor state and plug the elements of PMNS matrix for antineutrino to get  $\bar{\nu}_e \rightarrow \bar{\nu}_e$  transition probability as given bellow,

$$P_{\bar{\nu}_e \rightarrow \bar{\nu}_e} = 1 - \sin^2 2\theta_{12} \cos^4 \theta_{13} \sin^2 \frac{\Delta m_{21}^2 L}{4E} - \cos^2 \theta_{12} \sin^2 2\theta_{13} \sin^2 \frac{\Delta m_{31}^2 L}{4E} - \sin^2 \theta_{12} \sin^2 2\theta_{13} \sin^2 \frac{\Delta m_{32}^2 L}{4E}. \quad (2.1.25)$$

The  $\bar{\nu}_e \rightarrow \bar{\nu}_e$  oscillation channel has played an important role to extract the values of several oscillation parameters, such as  $\theta_{13}$ ,  $\Delta m_{31}^2$ ,  $\theta_{12}$ , and  $\Delta m_{21}^2$ , in reactor antineutrino oscillation experiments. Fig. 2.1 presents the survival probability of  $\bar{\nu}_e$  as a function of baseline  $L$  with energy

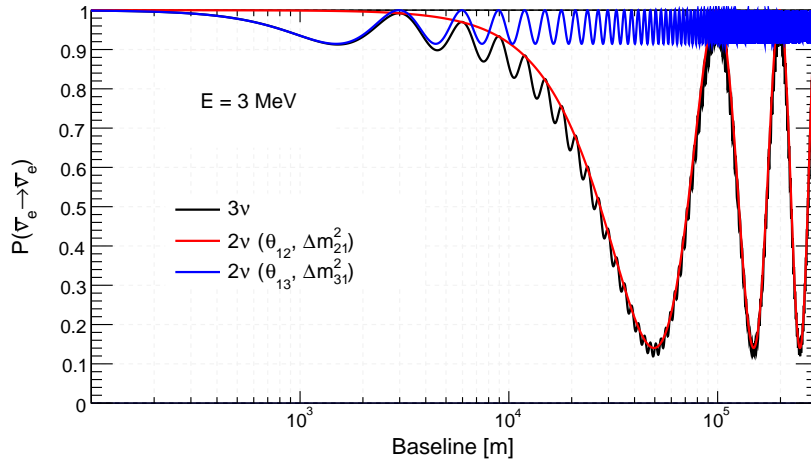


**Figure 2.1.** The survival probability of  $\bar{\nu}_e$  as a function of baseline  $L$  with neutrino energy 3 MeV. The black line presents the results in  $3\nu$  oscillation framework, whereas the red and blue lines are in the  $2\nu$  framework corresponding to mass-squared differences  $\Delta m_{21}^2 = 7.5 \times 10^{-5} \text{ eV}^2$  and  $\Delta m_{31}^2 = 2.5 \times 10^{-3} \text{ eV}^2$  respectively. Other oscillation parameters are  $\theta_{12} = 34^\circ$ ,  $\theta_{13} = 8.5^\circ$ .

$E = 3 \text{ MeV}$ . The black line presents the  $\bar{\nu}_e \rightarrow \bar{\nu}_e$  transition probability for  $3\nu$  mixing (Eq. 2.1.25).

We obtain red and blue lines for  $2\nu$  mixing using Eq. 2.1.16 replacing  $[\theta, \Delta m_{ij}^2]$  by  $[\theta_{12}, \Delta m_{21}^2]$  and  $[\theta_{13}, \Delta m_{31}^2]$  respectively. For Fig. 2.1, we use the following values of oscillation parameters:  $\Delta m_{21}^2 = 7.5 \times 10^{-5} \text{ eV}^2$ ,  $\Delta m_{31}^2 = 2.5 \times 10^{-3} \text{ eV}^2$ ,  $\theta_{12} = 34^\circ$ , and  $\theta_{13} = 8.5^\circ$ . One can note that the first minimum in blue ( $2\nu$  with  $\theta_{13}$  and  $\Delta m_{31}^2$ ) line, which appears at around 1.5 km, completely overlaps with black line ( $3\nu$ ) because the effect of oscillation governed by  $\theta_{12}$  and  $\Delta m_{21}^2$  is almost zero there. At  $L \sim 1.5 \text{ km}$  and  $E = 3 \text{ MeV}$ ,  $\sin^2(1.27 \frac{\Delta m_{21}^2 L}{E}) \sim 0.002$  which is negligible compared to  $\sin^2(1.27 \frac{\Delta m_{31}^2 L}{E})$  which is around 1 since  $\Delta m_{21}^2$  is  $\sim 30$  times smaller than  $\Delta m_{31}^2$ . The reactor antineutrino experiments Daya Bay and RENO discovered non-zero  $\theta_{13}$  using Eq. 2.1.16 with  $\theta \rightarrow \theta_{13}$  and  $\Delta m_{ij}^2 \rightarrow \Delta m_{31}^2$  [108, 109]. However, for the precision measurement, the small correction due to  $\theta_{12}$  and  $\Delta m_{21}^2$  is taken into account in their recent analyses [41, 154].

On the other hand, the impact of the oscillation due to  $\theta_{13}$  and  $\Delta m_{31}^2$  is small in the measurement of  $\theta_{12}$  and  $\Delta m_{21}^2$  at a baseline larger than 100 km since the phase of oscillation due to  $\Delta m_{31}^2$  gets averaged and the value of  $\theta_{13}$  is relatively small compared to  $\theta_{12}$ . The analysis of data of KamLAND experiment (baseline  $\sim 180 \text{ km}$ ) with  $2\nu$  mixing framework ( $\theta_{13} = 0$ ) provided the allowed range for  $\theta_{12}$  and  $\Delta m_{21}^2$  which are same as obtained from the solar neutrino fit however with a small disagreement<sup>3</sup> in the best-fit value of  $\theta_{12}$ . In Ref. [155–157], authors showed that the global fit of neutrino oscillation data with  $\theta_{13} \neq 0$ , this mismatch got reduced. Thus, it gave the hint of non-zero value of  $\theta_{13}$  which was measured later in reactor antineutrino experiments as discussed in Sec. 2.3.3.

## 2.2 Neutrino Oscillation in Matter

So far, we have discussed the neutrino oscillation in vacuum, and now, we illustrate the evolution of neutrino while they pass through matter. In 1978, Wolfenstein pointed out that the potential induced in the coherent forward elastic scattering of neutrinos with ambient matter fermions could modify the oscillation of propagating neutrinos through a medium [44]. Later, Mikheyev and Smirnov realized that the resonant amplification of neutrino oscillation may occur due to the presence of the matter induced potential, and they used this concept in the case of solar neutrino oscillation. The modification in the oscillation pattern due to matter potential is known as the “MSW”

<sup>3</sup>The fit of KamLAND data with  $\theta_{13} = 0$  favored slightly larger value for  $\theta_{12}$  than that from the solar data [12].

effect after the names of Mikheyev, Smirnov, and Wolfenstein for their pioneering contribution in this direction.

The normal matter contains electrons, protons, and neutrons, and all of the neutrino flavors ( $\nu_e$ ,  $\nu_\mu$ ,  $\nu_\tau$ ) can interact with these matter fermions through NC interaction mediated by  $Z^0$  boson (see right panel of Fig. 2.2 for Feynman diagram). The total matter potential created in the coherent forward elastic NC interactions of  $\nu_x$  ( $\nu_x \equiv \nu_e, \nu_\mu, \nu_\tau$ ) with all the matter fermions is given by

$$V_{NC} = -\frac{G_F N_n}{\sqrt{2}}, \quad (2.2.1)$$

where  $G_F$  is the Fermi coupling constant, and  $N_n$  is the neutron number density in the medium. For antineutrino,  $V_{NC}$  appears with same magnitude as neutrino but with + sign. Note that  $V_{NC}$  does not affect the neutrino oscillation as it is same for  $\nu_e$ ,  $\nu_\mu$ , and  $\nu_\tau$ .

An interesting point to note that the CC elastic scattering of  $\nu_e$  with electron mediated by  $W^\pm$  can take place in matter (see left panel of Fig. 2.2). Since there are no muons and tau leptons in normal matter, the CC elastic scattering of  $\nu_\mu$  and  $\nu_\tau$  is not possible to happen in matter. The potential induced in the coherent forward elastic CC interactions of  $\nu_e$  with ambient electrons in the medium is given by

$$V_{CC} = \sqrt{2} G_F N_e, \quad (2.2.2)$$

with  $N_e$  as the electron number density in the medium. For  $\bar{\nu}_e$ ,  $V_{CC} \rightarrow -V_{CC}$ . Putting the value of  $G_F$  in Eq. 2.2.2, and writing the electron density in terms of matter density ( $\rho$ ),  $V_{CC}$  can be written as

$$V_{CC} \simeq 7.6 \times Y_e \times \frac{\rho}{10^{14} \text{g/cm}^3} \text{ eV}, \quad (2.2.3)$$

where  $Y_e$  ( $\frac{N_e}{N_p + N_n}$ ) is the relative number density. For electrically neutral and isoscalar medium  $N_e = N_p$ <sup>4</sup> =  $N_n$ , and therefore,  $Y_e = 0.5$ . In the Earth core ( $\rho = 10 \text{ g/cm}^3$ ) and solar core ( $\rho = 100 \text{ g/cm}^3$ ), the values of  $V_{CC}$  are of the order of  $10^{-13} \text{ eV}$  and  $10^{-12} \text{ eV}$  respectively, whereas in case of a supernova ( $\rho \sim 10^{14} \text{ g/cm}^3$ ),  $V_{CC}$  is around few eV.

---

<sup>4</sup> $N_p$  denotes the proton number density in the medium.

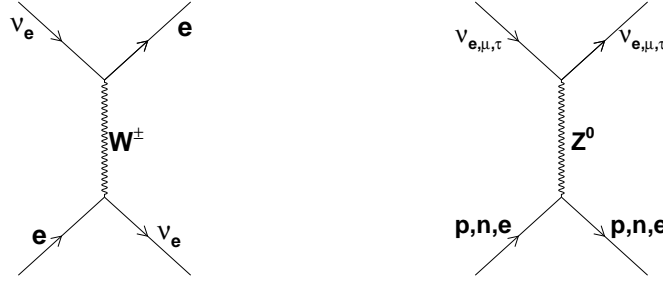


**Figure 2.2.** Feynman diagrams depicting neutrino scatterings inside the matter. Left panel shows CC interactions, whereas right panel describes NC processes.

In  $3\nu$  framework, the evolution equation of neutrino propagating through matter can be written as

$$i \frac{d}{dt} \begin{pmatrix} \nu_e(t) \\ \nu_\mu(t) \\ \nu_\tau(t) \end{pmatrix} = \left[ \frac{1}{2E} U \begin{pmatrix} 0 & 0 & 0 \\ 0 & \Delta m_{21}^2 & 0 \\ 0 & 0 & \Delta m_{31}^2 \end{pmatrix} U^\dagger + \begin{pmatrix} V_{CC} & 0 & 0 \\ 0 & 0 & 0 \\ 0 & 0 & 0 \end{pmatrix} \right] \begin{pmatrix} \nu_e \\ \nu_\mu \\ \nu_\tau \end{pmatrix}. \quad (2.2.4)$$

For antineutrino,  $U \rightarrow U^*$ ,  $V_{CC} \rightarrow -V_{CC}$ .

Now, we consider  $2\nu$  mixing to understand the neutrino oscillation in matter in a simpler way. As we mentioned earlier, we need one mixing angle  $\theta$  and one mass-squared difference  $\Delta m^2$  in case of  $2\nu$  mixing. In matter, the effective Hamiltonian of neutrino flavor state is

$$\begin{aligned} H_{\text{eff}} &= \frac{1}{2E} \begin{pmatrix} \cos \theta & \sin \theta \\ -\sin \theta & \cos \theta \end{pmatrix} \begin{pmatrix} 0 & 0 \\ 0 & \Delta m^2 \end{pmatrix} \begin{pmatrix} \cos \theta & -\sin \theta \\ \sin \theta & \cos \theta \end{pmatrix} + \begin{pmatrix} V_{CC} & 0 \\ 0 & 0 \end{pmatrix}, \\ &= \frac{1}{2E} \begin{pmatrix} \Delta m^2 \sin^2 \theta + 2EV_{CC} & \Delta m^2 \sin \theta \cos \theta \\ \Delta m^2 \sin \theta \cos \theta & \Delta m^2 \cos^2 \theta \end{pmatrix}. \end{aligned} \quad (2.2.5)$$

The mixing matrix of neutrino in matter can be estimated by diagonalizing the effective Hamiltonian ( $H_{\text{eff}}$ ) in the flavor state with the following orthogonal rotation matrix,

$$O = \begin{pmatrix} \cos \theta_m & -\sin \theta_m \\ \sin \theta_m & \cos \theta_m \end{pmatrix}, \quad (2.2.6)$$

such that

$$O^T H_{\text{eff}} O = \begin{pmatrix} m_{i,m}^2 & 0 \\ 0 & m_{j,m}^2 \end{pmatrix}, \quad (2.2.7)$$



where

$$\tan 2\theta_m = \frac{\sin 2\theta}{\cos 2\theta - \frac{2EV_{CC}}{\Delta m^2}}, \quad (2.2.8)$$

and

$$\Delta m_m^2 \equiv m_{i,m}^2 - m_{j,m}^2 = \sqrt{(\Delta m^2 \sin 2\theta)^2 + (\Delta m^2 \cos 2\theta - 2EV_{CC})^2}. \quad (2.2.9)$$

The parameters  $\theta_m$  and  $\Delta m_m^2$  are the mixing angle and the mass-squared difference in matter respectively. In contrast to the vacuum case, the mixing angle and mass-squared difference in matter are functions of neutrino energy and baseline. If  $V_{CC} > 0$  ( $< 0$ ) and  $\Delta m^2 > 0$  ( $< 0$ ), then as we increase the neutrino energy,  $\theta_m$  increases as compared to its value in vacuum, and  $m_{i,m}^2$  and  $m_{j,m}^2$  come closer to each other. For  $2EV_{CC} = \Delta m^2 \cos 2\theta$ ,  $\theta_m$  becomes  $45^\circ$  (see Eq. 2.2.8) which corresponds to the maximal mixing, and  $\Delta m_m^2$  (Eq. 2.2.9) becomes minimum. The energy at which the above condition is satisfied is called the resonance energy, and it is given by

$$E_{res} = \frac{\Delta m^2 \cos 2\theta}{2V_{CC}} = \frac{\Delta m^2 \cos 2\theta}{2\sqrt{2}G_F N_e}. \quad (2.2.10)$$

Replacing  $V_{CC}$  by its expression as given in Eq. 2.2.3, we can rewrite Eq. 2.2.10 as

$$E_{res} \simeq 6 \text{ GeV} \left[ \frac{|\Delta m^2|}{2.4 \times 10^{-3} \text{ eV}^2} \right] \cdot \left[ \frac{\cos 2\theta}{0.96} \right] \cdot \left[ \frac{5 \text{ g/cm}^3}{\rho} \right]. \quad (2.2.11)$$

For neutrinos propagating through a baseline<sup>5</sup> of constant matter density of about  $5 \text{ g/cm}^3$ , the resonance can occur at  $6 \text{ GeV}$  if mass-squared difference is around  $2.4 \times 10^{-3} \text{ eV}^2$  and  $\theta = 8.5^\circ$ . On the other hand, the mixing angle in matter (Eq. 2.2.8) can be written in terms of  $E_{res}$  in the following fashion,

$$\tan 2\theta_m = \frac{\tan 2\theta}{1 - \frac{E}{E_{res}}}. \quad (2.2.12)$$

For neutrino energy  $E > E_{res}$ , with increasing  $E$ ,  $\theta_m$  crosses  $45^\circ$  and approaches towards  $90^\circ$ , whereas  $\Delta m_m^2$  starts to increase sharply. Next, we discuss the results from solar, atmospheric, accelerator-based, and reactor neutrino experiments.

---

<sup>5</sup>The line-averaged constant matter density for baseline  $10700 \text{ km}$  through Earth is around  $5 \text{ g/cm}^3$  based on the Preliminary Reference Earth Model (PREM) [158] for the Earth matter density.

## 2.3 Experimental Results

Over the last two decades, several neutrino oscillation experiments have contributed to our knowledge on the neutrino oscillation parameters. Solar and atmospheric neutrino anomalies (discussed in Sec. 1.3) have been resolved independently as the solar and atmospheric neutrinos are sensitive to different  $L/E$  values. They are also different in many other aspects which will be clear in the following sections.

### 2.3.1 Solar Oscillation Parameters ( $\theta_{12}, \Delta m_{21}^2$ )

The solar neutrino oscillation parameters are measured in solar neutrino and reactor antineutrino based experiments. First, we discuss the solar neutrino experiments.

- **GALLEX:** GALLEX is a solar neutrino experiment which was operational during May 1991 to February 1997 at the Gran Sasso Underground Laboratory. It used 100 ton gallium chloride solution as the target material and counted neutrino induced nuclear reaction  $^{71}\text{Ga}(\nu_e, e)^{71}\text{Ge}$  by extracting  $^{71}\text{Ge}$  from the detector [113]. The threshold energy of neutrinos, which were detected in this experiment, was 233 keV. The observed neutrino interaction rate was  $[77.5 \pm 7.7]$  SNU ( $1\sigma$ ) obtained by combining the data collected over I-IV phases of running, though the expected rate was around 130 SNU using various solar models [113].
- **SAGE:** The Russian-American Gallium Experiment (SAGE) detected solar neutrinos using 50 ton liquid gallium metal detector located at a water equivalent depth of 4700 m under northern Caucasus mountain, Russia [159]. Like the GALLEX experiment, SAGE also counted the number of Ge produced through the nuclear reaction  $^{71}\text{Ga}(\nu_e, e)^{71}\text{Ge}$  in the detector. With the data collected during 1990 to 2007, the observed capture rate was  $65.4^{+3.1}_{-3.0}$  SNU [20]. This capture rate corresponds to only 50%-60% of the capture rate predicted by different Standard Solar Models. It is important to note that both the GALLEX and SAGE experiments measured the total solar neutrino events without having any information on their energy, direction, and timing.

- **Super-Kamiokande (SK):** The Super-Kamiokande experiment measures energy, direction, and timing information of solar neutrinos on an event-by-event basis. SK is a 50 kiloton (kt) water Cherenkov detector containing more than ten thousands of photomultiplier tubes (PMTs) located at a depth of 1 km in the Mozumi mine, Japan [160]. There are two parts of the detector. The inner detector (ID) contains 32 kt ultra pure water and is separated from the outer detector (OD) by optically isolated wall, the support structure for PMTs. Around 11146 inward-facing and 1185 outward-facing PMTs are used to view inner and outer detectors respectively. The PMT in Super-Kamiokande has the largest diameter of 50 cm in the world.

The detection of neutrinos in the Super-Kamiokande experiment is based on the observation of Cherenkov radiation produced by the final state charged particles. Any charged particle moving with velocity larger than light in the detector medium produces Cherenkov light. These photons deposit energies in the PMTs and form a ring-shaped image in the 2D projection. In case of multiple charge particles produced in the final state of a neutrino interaction, more than one rings are produced in the detector, and this type of event is called a multi-ring event. Using the charge and the timing information from each PMT signal, one can measure the energy and the direction of the final state particles and reconstruct the position of interaction vertex [161]. An important property of the Super-Kamiokande detector is that electrons and muons can be distinguished from each other by observing the pattern of the Cherenkov ring created by them. As electron and  $\pi^0 \rightarrow \gamma\gamma$  create the electromagnetic showers in the detector, the Cherenkov rings are diffuse and these types of events are called  $e$ -like events. On the other hand, muon and charged pion interactions in the detector do not produce showers and give rise to rings having clear and sharp edges which are called  $\mu$ -like or non-showering events.

The Super-Kamiokande experiment detects solar neutrinos by observing the recoil electrons from the elastic scattering of electron neutrinos in the detector. In the first 300 days of data, SK observed around  $4017 \pm 105(\text{stat.})^{+161}_{-116}(\text{syst.})$  solar neutrino events with recoil electron energy in the range of 6.5 MeV to 20 MeV [114]. The corresponding observed total  $\nu_e$  flux was  $2.42 \pm 0.06(\text{stat.})^{+0.10}_{-0.07}(\text{syst.}) \times 10^6 \text{ cm}^{-2}\text{s}^{-1}$  [114] which is approximately 36% of the flux predicted by the SSM. This observation confirmed the deficit in the solar neutrino events as

obtained in other solar neutrino experiments like Kamiokande, SAGE, and GALLEX. The Super-Kamiokande experiment has completed three data-taking periods, SK-I, -II, and -III, and now, the fourth phase of SK (SK-IV) is running since September of 2008. Combining all the four phases of data until March of 2016, the detected number of solar neutrino events in SK is around 46000 with an improved threshold recoil electron kinetic energy as 3.5 MeV [162]. Moreover, the Super-Kamiokande has reported an indication of the Earth matter effect in the solar neutrino events with  $3\sigma$  confidence level by measuring the day/night asymmetry as  $-3.6 \pm 1.6 (\text{stat.}) \pm 0.6 (\text{sys.})\%$  in SK-IV solar data, and the corresponding observed solar flux is  $[2.308 \pm 0.02 (\text{stat.})^{+0.039}_{-0.040} (\text{sys.})] \times 10^6 \text{ cm}^{-2}\text{s}^{-1}$  [163].

- Sudbury Neutrino Observatory (SNO):** The SNO experiment used one kiloton heavy-water Cherenkov detector located at 2 km underground in INCO's Creighton mine of Canada. The Cherenkov light produced by the charged particles inside the detector was observed through 9456 PMTs. The unique feature of SNO detector was its ability to distinguish CC, NC, and elastic-scattering events. The SNO detector observed solar neutrinos with a threshold energy of 1.4 MeV for NC and 2.2 MeV for CC events. This detector took data during May, 1999 to November, 2006. The data collected over a couple of years were able to prove that the neutrino flavors transform among each other, and the total NC events were consistent with the number of  $\nu_e$  predicted by the SSM [9]. This experiment also observed muons, which were produced in the interactions of high energy atmospheric neutrinos with the surrounding rocks [164]. The measured flux normalization of downward going atmospheric muon neutrinos was  $1.22 \pm 0.09$  times higher than what was obtained in the Bartol three-dimensional flux calculation [164, 165].
- Borexino:** More than 99% of the total solar neutrinos are in the low energy part ( $< 2 \text{ MeV}$ ) of the flux which includes the mono-energetic  ${}^7\text{Be}$  neutrinos and the continuous spectra due to  $pp$ ,  $pep$ , and CNO cycle. The real time detection of these neutrinos was first performed by the Borexino experiment in the underground laboratory at Gran Sasso, Italy [166–168]. The detection of low energy neutrino in the Borexino experiment is based on the elastic scattering of neutrino with electron in the organic liquid scintillator. Scintillation light produced by the recoil electron is detected by the PMTs to reconstruct the energy information in the Borexino. The direction information gets lost due to the isotropic nature of the emitted

light. The challenge in a low energy solar neutrino experiment is to achieve extremely high radiopurity in the detector so that the background becomes smaller in number than the signal events from  ${}^7\text{Be}$  neutrinos (0.5 counts/(day·ton)) [167]. The LMA-MSW, as discussed later in this section, is the solution of the solar neutrino anomaly, and it predicts that the vacuum dominated oscillation is supposed to happen for low energy solar neutrinos [169]. In this context, the detection of low energy neutrino is important to confirm in an independent way that the LMA-MSW is indeed the solution for the solar neutrino problem.

The important features of the observed solar neutrino spectrum, which helped to disentangle the solar neutrino problems were the following:

1. The observed  $\nu_e$  flux was smaller by almost half of the predicted solar flux.
2. No changes in the solar events over the time of a year were observed (no seasonal variations).
3. Almost no energy distortion in the observed solar neutrino events [170].

Various solutions could explain the reduction of solar neutrino flux which are listed below.

- The vacuum solution (VAC),  $\Delta m_{21}^2 \ll 10^{-9} \text{ eV}^2$ ,  $\theta_{12} \sim 45^\circ$ .
- Small Mixing Angle MSW solution (SMA-MSW),  $\Delta m_{21}^2 \ll 10^{-6} - 10^{-5} \text{ eV}^2$ ,  $\theta_{12} \sim 0.01^\circ$ .
- Low mass MSW solution (LOW-MSW)  $\Delta m_{21}^2 \ll 10^{-7} \text{ eV}^2$ ,  $\theta_{12} \sim 45^\circ$ .
- Large Mixing Angle MSW solution (LMA-MSW),  $\Delta m_{21}^2 \ll 10^{-5} - 10^{-4} \text{ eV}^2$ ,  $\theta_{12} \sim 45^\circ$ .

Marvelous data collected over the last two decades have ruled out the VAC, SMA-MSW, and LOW-MSW solutions, and the LMA-MSW solution has been confirmed.

- **KamLAND:** The Kamioka Liquid scintillator Anti-Neutrino Detector (KamLAND), a reactor based neutrino oscillation experiment, played an important role in measuring the solar neutrino parameters. The main component of the detector in the KamLAND experiment was 1 kt liquid scintillator (LS) filled in a nylon balloon. Purified mineral oil was used around the nylon balloon to shield LS from the natural radioactivity. A 3.2 kt water Cherenkov

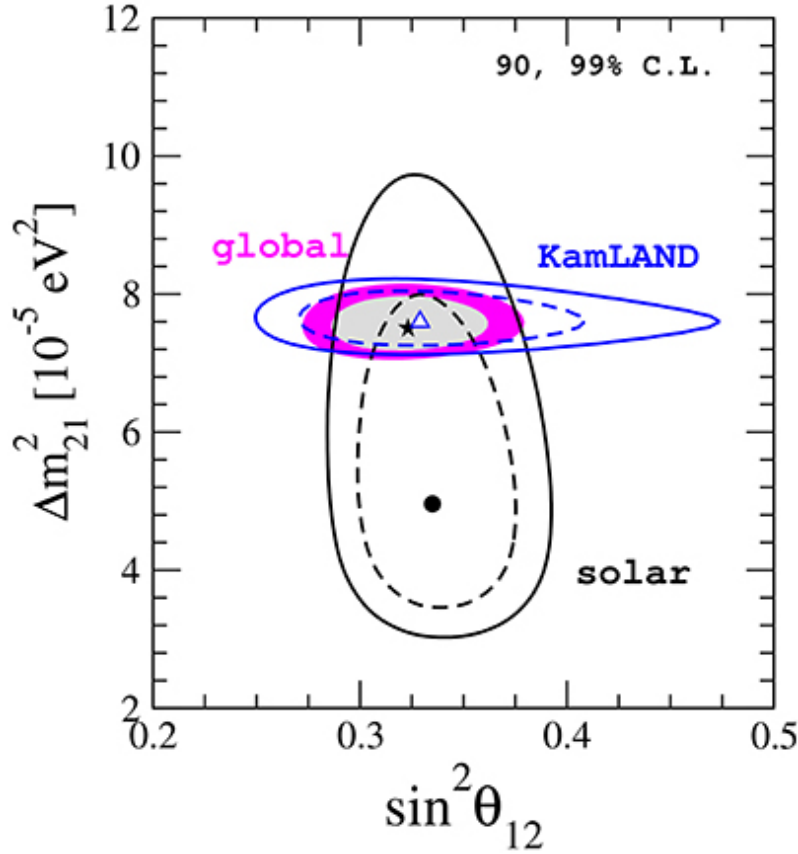


**Figure 2.3.** The allowed region in the plane of  $[\sin^2 \theta_{12}, \Delta m_{21}^2]$  obtained from the analysis of solar, KamLAND, and KamLAND + solar (global) data are shown with black lines, blue lines, and colored regions respectively.  $\theta_{13}$  is marginalized according to its latest measurement in reactor experiments. This figure is taken from Ref. [171].

detector at the outer part of the detector acted as the cosmic-ray veto. Anti-neutrino from 55 reactors in Japan were detected through inverse beta-decay process in the detector at an average distance of 180 km from the reactors. One of the main achievements of this experiment was the first evidence of  $\bar{\nu}_e$  disappearance. The direct confirmation of neutrino oscillation resulted in the precise measurement of the  $\Delta m_{21}^2$  [10, 11].

Fig. 2.3 shows the allowed region in the plane of  $[\sin^2 \theta_{12}, \Delta m_{21}^2]$  as obtained in Ref. [171] from the analysis of all the solar data (red lines), KamLAND data (blue lines), and KamLAND + solar data (green region). The best-fit values for the solar oscillation parameters and their  $1\sigma$  allowed ranges as obtained in the global fit [171] are

$$\sin^2 \theta_{12} = 0.321^{+0.018}_{-0.016}, \quad \Delta m_{21}^2 = [7.56 \pm 0.19] \times 10^{-5} \text{eV}^2.$$

### 2.3.2 Atmospheric Oscillation Parameters ( $\theta_{23}$ , $\Delta m_{32}^2$ )

Atmospheric as well as the accelerator-based long-baseline neutrino experiments have enormously contributed towards the estimation of  $\theta_{23}$  and  $\Delta m_{32}^2$ . The unique advantage of the atmospheric neutrino experiment is the possibility of exploring the neutrino oscillation over a wide range of baselines (100 km to 12,000 km) and neutrino energies (100 MeV to 100 GeV). On the other hand, a better understanding on the neutrino flux produced from the charged pion decay in accelerators and the use of near and far detectors have helped to reduce the cross-section uncertainties and systematic errors in the accelerator-based neutrino experiments. Therefore, both the atmospheric neutrino experiments and long-baseline experiments have played an important role to acquire the knowledge on  $\theta_{23}$  and  $\Delta m_{32}^2$ . Now, we briefly describe the experiments which contributed in measuring the values of  $\theta_{23}$  and  $\Delta m_{32}^2$ .

1. **Super-Kamiokande:** The Super-Kamiokande experiment is running for more than 20 years. It started data-taking in 1996, and since then, it has provided many crucial information to improve our understanding about neutrino oscillation parameters. The Super-Kamiokande atmospheric neutrino oscillation experiment has been able to observe the Earth matter effect and they have ruled out the vacuum oscillation at  $1.6\sigma$  confidence level [172] using  $\nu_e$  and  $\bar{\nu}_e$  event samples. The events in the range of multi-GeV energy are the golden data sample to probe the Earth matter effect and these events can be produced in the charged current quasi-elastic, single-pion, and deep-inelastic processes. To obtain the information on the oscillation parameters using the matter effect, one of the important requirements is the separation between neutrino and antineutrino events. In Ref. [172], the technique of separating the neutrino and antineutrino events in the SK detector has been discussed. In case of  $\bar{\nu}_e$ , it participates in the interaction  $\bar{\nu}_e n \rightarrow e^+ n \pi^-$ . Here, positron is accompanied by a  $\pi^-$  which often gets captured on a  $^{16}\text{O}$  nucleus, and we see the Cherenkov light due to only positron. But, the situation is different in case of  $\nu_e$  where an outgoing  $\pi^+$  in the reaction  $\nu_e n \rightarrow e^- n \pi^+$ , does not get captured by the  $^{16}\text{O}$  nucleus. The outgoing  $\pi^+$  finally gives rise to a delayed electron via its decay chain. In this manner  $\bar{\nu}_e$  events are extracted from the single-ring multi-GeV e-like data sample with a requirement that there are no delayed electrons in those event samples. This is the strategy that Super-Kamiokande has adopted to

distinguish the single-ring multi-GeV  $\bar{\nu}_e$ -like events from  $\nu_e$ -like events in SK. After applying this selection cut, 62.1% and 9.0% charged current electron neutrino and antineutrino events respectively get selected as  $\nu_e$ -like sample. These fractions in  $\bar{\nu}_e$ -like sample are 54.6% and 37.2%. The green line in Fig. 2.4 shows the parameter space in  $[\sin^2 \theta_{23}, \Delta m_{32}^2]$  plane allowed by the SK data of I, II, III, and IV phases of running [172].

2. **K2K:** The K2K (KEK to Kamioka) long-baseline neutrino oscillation experiment was operational during 1999 to 2004, and it used well-controlled and well-understood beam of muon neutrinos to confirm the oscillations previously observed by the Super-Kamiokande detector using atmospheric neutrinos [138]. The beam of muon-neutrinos was created from the 12 GeV proton synchrotron at the KEK facility with a peak energy around 1 GeV, and these neutrinos were detected in the Super-Kamiokande detector at a distance of 250 km from the KEK. The main achievement of the K2K was the confirmation of  $\nu_\mu$  disappearance with non-atmospheric neutrinos, which was quite helpful to establish the phenomenon of neutrino oscillation on a strong footing. It measured the values of atmospheric oscillation parameters as  $\sin^2 2\theta = 1$  and  $\Delta m^2 = 3.5 \times 10^{-3} \text{ eV}^2$  [173].

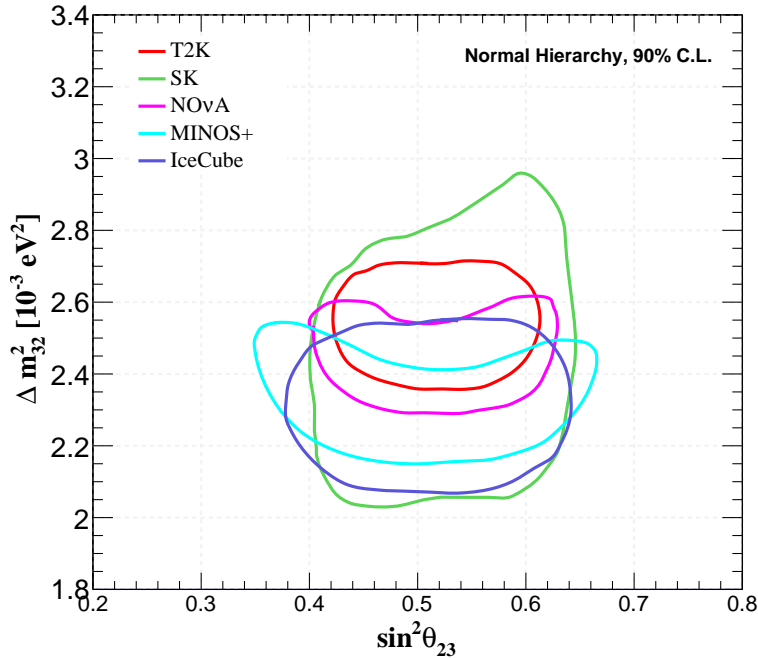


**Figure 2.4.** The parameter space at 90% C.L. in the plane of  $\sin^2 \theta_{23}$  vs.  $\Delta m_{32}^2$  obtained from the atmospheric experiments Super-Kamiokande (SK) [172], DeepCore/IceCube [174], accelerator-based experiments T2K [36], NOvA [38], and MINOS/MINOS+ [30].



3. **T2K:** The Tokai to Kamioka (T2K) experiment is a currently running long-baseline accelerator-based neutrino oscillation experiment [175]. One of the main goals of the T2K is to reveal whether CP is violated in lepton sector and it has already started to give hint of the maximal CP violation [36, 176]. T2K detects  $\nu_e$  and  $\nu_\mu$  in the beam produced at the J-PARC accelerator by hitting 30 GeV proton beam on graphite target. The produced charged pions and kaons are focused with three magnetic horn and are left to decay in a 96 m long pipe. The final yield is a narrow beam mainly composed of  $\nu_\mu$ . To measure the neutrino beam direction, flavor content, and flux spectrum, T2K uses two near detectors at a distance of 280 m from the target. One of these near detectors is located in the direction of beam (on-axis) and another is situated at an angle of  $2.5^\circ$  (off-axis) from the beam direction. As the far detector, T2K use the 50 kt Super-Kamiokande water Cherenkov detector located at an off-axis angle of  $2.5^\circ$  with a distance of 295 km from the J-PARC facility. The peak of the off-axis neutrino flux appears around 0.6 GeV. T2K was operated for about three years in neutrino mode, and currently it is taking data with the antineutrino beam. Details about the T2K detector can be found in [177]. The parameter space in the plane of  $\sin^2 \theta_{23}$  vs.  $\Delta m_{32}^2$  allowed by the recent data of T2K is shown in Fig. 2.4 with red line [36].
  
4. **MINOS:** The Main Injector Neutrino Oscillation Search (MINOS) experiment is another accelerator-based neutrino oscillation experiment which contributed significantly to the current knowledge of neutrino properties. This experiment detected the neutrinos and antineutrinos produced at the Fermi National Accelerator Laboratory by hitting a 120 GeV proton beam on a 95.4 cm long target. The produced charged particles, which were mainly  $\pi^\pm$  and  $K^\pm$ , were focused by the parabolic magnetic horn and were allowed to decay in a 675 m long decay pipe. During the decay process,  $\nu_\mu/\bar{\nu}_\mu$  are produced which were detected in the 0.98 kt near detector at 1 km away and 5.4 kt far detector at 735 km away from the target. MINOS used 2.54 cm thick steel plate and 1 cm thick plastic scintillator as tracking calorimeter detector with magnetic field of 1.3 tesla for the near and far detector. Details of detector design can be found in Ref. [178]. MINOS reported the disappearance of  $\nu_\mu$  and  $\bar{\nu}_\mu$  [29, 139, 179, 180] and constrained the parameter space in  $[\sin^2 \theta_{23}, \Delta m_{32}^2]$  plane as shown by the cyan line in Fig. 2.4 [30].

5. **NOvA:** NuMI Off-Axis  $\nu_e$  Appearance (NOvA) experiment is another currently running long-baseline neutrino oscillation experiment. It has the longest baseline of 810 km among all the on-going accelerator-based long-baseline neutrino experiments. NOvA has two functionally identical detectors, one is near detector, 0.3 kt, located at Fermilab, another is far detector, 14 kt, situated at Ash River, Minnesota. Both consist of liquid scintillators and wavelength shifting fibers connected to avalanche photodiodes [181]. Detectors of NOvA are placed at 14 mrad off-axis relative to the beam direction to have the narrow-band beam with a peak energy around 2 GeV. The parameter space in the plane of  $[\sin^2 \theta_{23}, \Delta m_{32}^2]$  allowed by the data of NOvA is shown in Fig. 2.4 by the pink line [38].
  
6. **OPERA:** The main goal of the OPERA experiment was to detect the  $\nu_\mu \rightarrow \nu_\tau$  transition. The detector of OPERA was made of massive lead plates as the target material and Emulsion Cloud Chamber (ECC) as the active element in alternate layers. OPERA observed for the first time  $\nu_\mu \rightarrow \nu_\tau$  transition directly by observing the tau leptons at the far detector in a  $\nu_\mu$  beam sent by CERN towards the far detector located at a distance of 730 km at the Gran Sasso Underground Laboratory of INFN [142]. The average energy of neutrino was 12 GeV in this experiment so that one can produce tau leptons at the far detector after  $\nu_\mu \rightarrow \nu_\tau$  transition.
  
7. **IceCube:** The main aim of the IceCube experiment is to observe very high energy atmospheric neutrinos as well as the astrophysical neutrinos coming from all the directions [96, 98, 99, 182]. The present detector of IceCube is an array of 5160 photomultiplier tubes (PMTs) buried over a volume of one cubic km in the South Pole glacial ice at a depth of 1.45 km. PMTs are supported by 86 strings, out of which 78 strings are arranged with a space of 125 m between each other. The central part of the IceCube is called DeepCore, where eight strings are closely aligned with a 40-70 m distance between them, which enables one to detect neutrino candidate with energy as low as 10 GeV. Therefore, the DeepCore data are sensitive to the atmospheric oscillation parameters [31]. The blue line in Fig. 2.4 presents the allowed range of atmospheric oscillation parameters using three years data of DeepCore [174].

The best-fit values of the atmospheric oscillation parameters as obtained from the global fit study in Ref. [14] are mentioned in Table 2.1.

### 2.3.3 Discovery of non-zero $\theta_{13}$

The smallest lepton mixing angle  $\theta_{13}$  is measured recently in reactor antineutrino experiments with far detector placed at around one kilometer from the sources by observing the disappearance of  $\bar{\nu}_e$  from the reactors. Fig. 2.1 shows the disappearance of 3 MeV  $\bar{\nu}_e$  as a function of baseline  $L$ . At around 1.5 km (this is the baseline of the furthest detector in the Daya Bay experiment), the phase of the oscillation  $1.27 \Delta m_{31}^2 L/E$  becomes  $\pi/2$  with  $\Delta m_{31}^2 = 2.5 \times 10^{-3} \text{ eV}^2$ , and we observe the maximum disappearance of  $\bar{\nu}_e$  corresponding to the oscillation governed by the mass-squared difference  $\Delta m_{31}^2$ . The amplitude of the oscillation at these location of maximum disappearance of  $\bar{\nu}_e$  would provide the measurement of  $\sin^2 2\theta_{13}$ . Next, we briefly describe the reactor experiments which have contributed significantly towards the measurement of the reactor mixing angle.

1. **Double Chooz:** Double Chooz experiment detected  $\bar{\nu}_e$  coming from two reactor cores of Chooz Nuclear Power Plant in France. Double Chooz used two identical detectors, one at an average distance of 1050 m (far detector) and another one at 400 m distance (near detector) from the reactor, both filled with 8 tons of Gd-loaded liquid scintillators as the neutrino target [183]. The inverse beta decay reaction of protons ( $\bar{\nu}_e + p \rightarrow e^+ + n$ ) in the detector volume was identified with the delayed coincidence of the signal from positron annihilation and from the neutron capture process in Gd or hydrogen nucleus. With rate plus spectral shape analysis of the data from far detector only, this experiment measured the non-zero value of  $\theta_{13}$  as  $\sin^2 2\theta_{13} = 0.109 \pm 0.030(\text{stat.}) \pm 0.025(\text{syst.})$  [110]. Using the data of far and near detectors collected over the period of 363 days and 258 days respectively, they obtained  $\sin^2 2\theta_{13} = 0.123 \pm 0.023$  (stat.+syst.) combining the data of neutron captured in Gd and hydrogen nucleus [184].
2. **Daya Bay:** The Daya Bay reactor antineutrino experiment has eight identical antineutrino detectors placed in three underground experimental halls at 470 m, 576 m (two near halls), and 1648 m (one far hall) distances from reactor cores in China [154]. Each detector consists of 20 tons of Gd-loaded liquid scintillator as the target material, 20 tons of liquid scintillator

at outer region as veto, and 37 tons of mineral oil as a shield from radioactivity. The method of detection of inverse beta decay process using photomultiplier tubes in this experiment is same as Double Chooz. With the rate only analysis of 55 days of data from 43000 ton-GW<sub>th</sub>-day livetime exposure, Daya Bay excluded the non-zero value with  $5\sigma$  C.L. and found  $\sin^2 2\theta_{13} = 0.092 \pm 0.013(\text{stat}) \pm 0.005(\text{syst.})$  [108]. The analysis of latest data collected over 1958 days in Daya Bay detector and containing total of about 4 million reactor  $\bar{\nu}_e$  events provided  $\sin^2 2\theta_{13} = 0.0856 \pm 0.0029$  [185]. It is worth to mention that the use of near and far detectors and huge statistics have helped to measure  $\theta_{13}$  with unprecedented accuracy in the Daya Bay experiment.

3. **RENO:** The RENO experiment detects  $\bar{\nu}_e$  from the Yonggwang Nuclear Plant in Korea [41, 186]. There are two identical detectors, near and far, which are situated at the distance of 294 m and 1383 m respectively from the reactor core. It uses 16 tons of Gd-loaded liquid scintillator as target material, 65 tons of mineral oil for radioactive shielding, and PMTs. With the 2200 live days of reactor  $\bar{\nu}_e$  data, RENO has observed 103212 (850666) at far and near detector and measured  $\sin^2 2\theta_{13} = 0.0896 \pm 0.0048(\text{stat.}) \pm 0.0047(\text{syst.})$  [187].

The best-fit value of  $\theta_{13}$  as obtained from the global fit study is mentioned in Table 2.1.

## 2.4 Current Status of Neutrino Oscillation Parameters

After the discovery of neutrino flavor oscillation in the Super-Kamiokande experiment, it has been confirmed in many other neutrino experiments which are described in the previous section. Moreover, the data from these experiments reveal that the three mixing angles ( $\theta_{23}$ ,  $\theta_{12}$ ,  $\theta_{13}$ ) and the two mass-squared differences ( $\Delta m_{21}^2$ ,  $\Delta m_{31}^2$ ) are non-zero, thereby establishing the three-flavor lepton mixing framework in the form of the Pontecorvo-Maki-Nakagawa-Sakata (PMNS) matrix [145, 153]. The best-fit values of these oscillation parameters and their  $1\sigma$  and  $3\sigma$  uncertainties are mentioned in Table 2.1 as obtained from the global fit of all the neutrino oscillation data available so far [14]. Other global fit studies [15, 16] also reveal the similar best-fit values and errors on these oscillation parameters. The value of  $\theta_{12}$  and  $\Delta m_{21}^2$  are precisely measured by the solar neutrino experiments [19–26] and reactor antineutrino experiments [27] through disappearance channel.

Parameter	Best fit $\pm 1\sigma$	$3\sigma$ range
$\sin^2 \theta_{12}$	$0.306^{+0.012}_{-0.012}$	$0.271 \rightarrow 0.345$
$\theta_{12}/^\circ$	$33.56^{+0.77}_{-0.75}$	$31.38 \rightarrow 35.99$
$\frac{\Delta m_{21}^2}{10^{-5} \text{eV}^2}$	$7.5^{+0.19}_{-0.17}$	$7.03 \rightarrow 8.09$
$\sin^2 \theta_{23}$ (NH)	$0.441^{+0.027}_{-0.021}$	$0.385 \rightarrow 0.635$
$\theta_{23}/^\circ$ (NH)	$41.6^{+1.5}_{-1.2}$	$38.4 \rightarrow 52.8$
$\sin^2 \theta_{23}$ (IH)	$0.587^{+0.020}_{-0.024}$	$0.393 \rightarrow 0.640$
$\theta_{23}/^\circ$ (IH)	$50.0^{+1.1}_{-1.4}$	$38.8 \rightarrow 53.1$
$\sin^2 \theta_{13}$ (NH)	$0.02166^{+0.00075}_{-0.00075}$	$0.01934 \rightarrow 0.02392$
$\theta_{13}/^\circ$ (NH)	$8.46^{+0.15}_{-0.15}$	$7.99 \rightarrow 8.90$
$\sin^2 \theta_{13}$ (IH)	$0.02179^{+0.00076}_{-0.00076}$	$0.01953 \rightarrow 0.02408$
$\theta_{13}/^\circ$ (IH)	$8.49^{+0.15}_{-0.15}$	$8.03 \rightarrow 8.93$
$\delta_{\text{CP}}$ (NH)	$261^{+51}_{-59}$	$0 \rightarrow 360$
$\delta_{\text{CP}}$ (IH)	$277^{+40}_{-46}$	$145 \rightarrow 391$
$\frac{\Delta m_{31}^2}{10^{-3} \text{eV}^2}$ (NH)	$2.524^{+0.039}_{-0.040}$	$2.407 \rightarrow 2.643$
$\frac{\Delta m_{32}^2}{10^{-3} \text{eV}^2}$ (IH)	$-2.514^{+0.038}_{-0.041}$	$-2.635 \rightarrow -2.399$

**Table 2.1.** The best-fit values of oscillation parameters and their  $3\sigma$  ranges as obtained in Ref. [14] from the global fit of world neutrino oscillation data. The results from other global fit studies [15, 16] are almost similar to these best-fit values and ranges.

The value of atmospheric mixing angle,  $\theta_{23}$ , and the magnitude of the atmospheric mass splitting,  $\Delta m_{31}^2$ , are obtained from the atmospheric neutrino experiments, Super-Kamiokande [28], IceCube DeepCore [31], and ANTARES [32], and accelerator-based neutrino experiments, MINOS [29, 30], T2K [33–36], and NO $\nu$ A [37, 38]. The smallest mixing angle  $\theta_{13}$  is also precisely measured with the help of modern reactor experiments like Daya Bay [39], Double Chooz [40], and RENO [41].

## 2.5 Remaining Unsolved Issues in Neutrino Oscillation

Despite the tremendous success that we have achieved in neutrino oscillation physics over the past two decades, there are still some important fundamental issues that need to be addressed in

currently running and upcoming neutrino oscillation experiments. Now, we briefly mention these issues.

- Mass Hierarchy of Neutrino:** The magnitude of the atmospheric neutrino mass splitting  $\Delta m_{31}^2$  has been measured with good accuracy, but, at present, we do not have the knowledge whether  $m_3 > m_1$  or  $m_3 < m_1$ . The present global data [14–16] of neutrino oscillation suggest two possibilities for the neutrino mass pattern:  $m_3 > m_2 > m_1$  which is known as normal hierarchy (NH) or normal ordering (NO) and  $m_2 > m_1 > m_3$  which is known as inverted hierarchy (IH) or inverted ordering (IO). The collected data of Super-Kamiokande atmospheric neutrino experiment over all the four phases (I–IV) with an exposure of 328 kt-year has preferred NH over IH at 93.0 % C.L. assuming the oscillation parameters at their best-fit values, and the preference becomes stronger when combined with the T2K data to constrain  $\theta_{13}$  [172].
- High Precision Measurement of the Atmospheric Mixing Angle:** Among the three mixing angles,  $\theta_{23}$  has the largest uncertainties at present. The global fits of the world neutrino data indicate towards two degenerate solutions for  $\theta_{23}$ : (i)  $< 45^\circ$ , known as lower octant (LO), and (ii)  $> 45^\circ$ , termed as higher octant (HO). Therefore, precision measurement of  $\theta_{23}$  and finding its correct octant (if  $\theta_{23} \neq 45^\circ$ ) are important goals of the current and the future neutrino oscillation experiments.
- Exploring the Leptonic CP-violation:** Determining the value of CP phase  $\delta_{\text{CP}}$  and exploring the possibility of CP violation in the neutral lepton sector (if  $\delta_{\text{CP}}$  differs from both 0 and  $\pi$ ) have emerged as the topmost priority in the field of neutrino oscillation physics. A possible observation of substantial amount of CP violation in neutrino oscillation may point towards the possibility that neutrinos are involved in generating observed matter-antimatter asymmetry in the Universe dynamically. There is a slight hint of CP violation (exclude  $\delta_{\text{CP}} = 0$  and  $\pi$ ) at 90% C.L. from the T2K data [36], and it also suggests that  $\delta_{\text{CP}}$  happens to be around  $3\pi/2$ .
- Tension between Solar and KamLAND Results:** A tiny but noticeable disagreement in the value of  $|\Delta m_{21}^2|$  is obtained from the fitting of solar neutrino data and of reactor antineutrino

data of KamLAND at  $2\sigma$  C.L. [14]. In future, we also need to resolve this tension with high precision solar neutrino data.

To pin down these unresolved issues with unprecedented accuracy, many high precision large scale neutrino facilities have been proposed, such as INO [42], PINGU [188, 189], ORCA [190], Hyper-Kamiokande [191, 192], DUNE [193], JUNO [194]. To gain further knowledge on the mass mixing parameters from the neutrino oscillation data, the matter effect [44–46] plays a very important role. The imprint of the solar matter effect helps us to establish that  $m_2$  is heavier than  $m_1$  using solar neutrino data [11, 12, 195]. While neutrinos traverse through huge matter density, they encounter the matter potential induced in coherent elastic scattering of  $\nu_e$  and  $\bar{\nu}_e$  with electrons in matter via exchange of the SM  $W^\pm$  boson. This matter induced potential can cause to have the MSW resonance [44–46] in the oscillation of neutrinos with NH, and for antineutrinos with IH. In near future, there is a chance to determine the neutrino mass ordering directly using the Earth matter effect in atmospheric neutrino experiments detecting neutrino and antineutrino separately [47, 49, 172, 188]. Next, we discuss briefly  $\nu_\mu \rightarrow \nu_\mu$  and  $\nu_e \rightarrow \nu_\mu$  oscillation channels which play an important role in atmospheric neutrino oscillation experiments.

## 2.6 Relevant Oscillation Channels in Atmospheric Experiments

In this section, we discuss  $\nu_\mu \rightarrow \nu_\mu$  and  $\nu_e \rightarrow \nu_\mu$  transition channels in the context of the atmospheric neutrino experiment. The exact formulae for these oscillation probabilities are difficult to derive analytically by diagonalizing the Hamiltonian in  $3\nu$  framework with a matter density profile. In Ref. [196], authors have obtained the analytical expressions for neutrino oscillation probabilities in matter of constant density by diagonalizing the effective Hamiltonian for neutrino flavor up to second order in both  $\alpha \equiv \Delta m_{21}^2 / \Delta m_{32}^2$  ( $\simeq 0.03$ ) and  $\sin \theta_{13}$  ( $\simeq 0.15$ ) putting  $\cos \theta_{13} = 1$ . Furthermore, in the ICAL detector at INO, neutrino energy ( $E$ ) in the range of 2 GeV to 10 GeV and with baselines ( $L$ ) in the range of 2000 km to 9000 km are suitable to extract the information on the oscillation parameters. For these choices of  $L$  and  $E$ , the oscillation due to solar mass-squared difference ( $\Delta m_{21}^2$ ) is not developed, and oscillations are mainly driven by the atmospheric mass splitting ( $\Delta m_{32}^2$ ). Therefore, to understand the transition probability of  $\nu_e \rightarrow \nu_\mu$  ( $P_{e\mu}$ ) and  $\nu_\mu \rightarrow \nu_\mu$  ( $P_{\mu\mu}$ ) in the context of the ICAL detector,  $\alpha = 0$  is a fair approximation. Putting  $\alpha = 0$  in

Eqs. 3.5 and 3.7 of Ref. [196], we get the following expressions for  $P_{e\mu}$  and  $P_{\mu\mu}$ ,

$$P_{e\mu} = 4 \underbrace{\sin^2 \theta_{13} \sin^2 \theta_{23} \frac{\sin^2 [(A-1)\Delta]}{(A-1)^2}}_{\equiv T_1}, \quad (2.6.1)$$

$$P_{\mu\mu} = 1 - \underbrace{\sin^2 2\theta_{23} \sin^2 \Delta}_{\equiv T_0} - 4 \underbrace{\sin^2 \theta_{13} \sin^2 \theta_{23} \frac{\sin^2 [(A-1)\Delta]}{(A-1)^2}}_{\equiv T_1} - \underbrace{\frac{2}{A-1} \sin^2 \theta_{13} \sin^2 2\theta_{23} \left( \sin \Delta \cos [A\Delta] \frac{\sin [(A-1)\Delta]}{A-1} - \frac{A}{2} \Delta \sin 2\Delta \right)}_{\equiv T_2}, \quad (2.6.2)$$

where

$$\Delta \equiv \frac{\Delta m_{31}^2 L}{4E}, \quad A \equiv \frac{2EV_{cc}}{\Delta m_{31}^2}. \quad (2.6.3)$$

Here, the only term in  $P_{e\mu}$ , which is denoted by  $T_1$ , also appears in the expression of  $P_{\mu\mu}$  but with the negative sign.  $T_1$  is basically the  $\theta_{13}$  driven  $\nu_e \rightarrow \nu_\mu$  or  $\nu_\mu \rightarrow \nu_e$  transition probability, and it contains the term  $A$  related to the matter induced potential  $V_{CC}$ . Note that in case of NH ( $\Delta m_{31}^2 > 0$ ),  $A$  is positive for neutrino and  $T_1$  can be enhanced, whereas for antineutrino,  $A$  is negative which does not allow such enhancement. On the other hand, for IH ( $\Delta m_{31}^2 < 0$ ), this enhancement can happen for antineutrino but not for neutrino. The term  $T_0$  in the expression of  $P_{\mu\mu}$  (Eq. 2.6.2) is equal to  $\nu_\mu \rightarrow \nu_\tau$  transition probability in 2-flavor framework in vacuum.

In Fig. 2.5, we show  $T_0$ ,  $T_1$ ,  $T_2$ , and  $P_{\mu\mu}$  by red, blue, green, and black lines respectively for a baseline of 5000 km through the Earth for neutrino (left panel) and antineutrino (right panel) with NH. The line-averaged constant matter density for the 5000 km baseline through the Earth is taken as 3.9 g/cm<sup>3</sup> based on the PREM profile [158] of the Earth matter density. The values of oscillation parameters are taken as  $\Delta m_{31}^2 = 2.5 \times 10^{-3}$  eV<sup>2</sup>,  $\theta_{23} = 45^\circ$ , and  $\theta_{13} = 8.5^\circ$ . The important features to note from Fig. 2.5 are as follows.

1. The red line ( $T_0$ ) in left panel is same as that in right panel since the oscillation probability for neutrino in  $2\nu$  framework in vacuum is equal to that for antineutrino. However,  $T_1$  and  $T_2$ , which contain matter term  $A$ , are different for neutrino and antineutrino since the signs of  $A$  are opposite for them as discussed earlier.



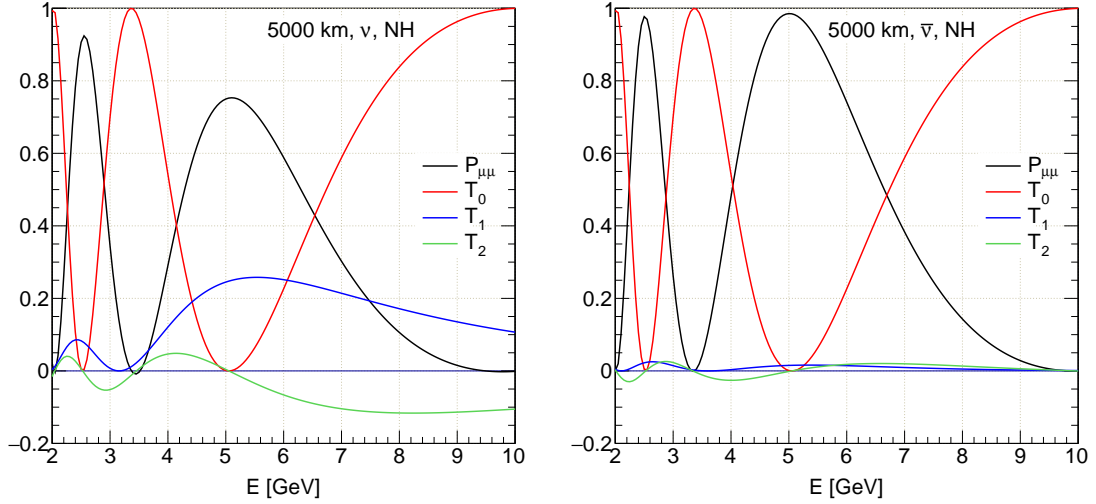


**Figure 2.5.** The variation of  $T_0$ ,  $T_1$ ,  $T_2$ , and  $P_{\mu\mu}$  (Eq. 2.6.2) with neutrino energy ( $E$ ) for a baseline of 5000 km through the Earth for neutrino (left panel) and antineutrino (right panel) with NH. The line-averaged constant matter density for the 5000 km baseline through the Earth is taken as  $3.9 \text{ g/cm}^3$  based on the PREM profile [158] of the Earth matter density. The values of oscillation parameters are taken as  $\Delta m_{31}^2 = 2.5 \times 10^{-3} \text{ eV}^2$ ,  $\theta_{23} = 45^\circ$ , and  $\theta_{13} = 8.5^\circ$ .

2. At  $E = 5 \text{ GeV}$  and  $L = 5000 \text{ km}$ ,  $\Delta \simeq \pi$ , and thus,  $T_0$  and  $T_2$  are zero as they are functions of  $\sin n\Delta$  with  $n = 1$  and  $2$  for both neutrino and antineutrino. Therefore,  $P_{\mu\mu}$  becomes  $1 - T_1$ , where  $T_1$  acquires a higher value for neutrino than antineutrino (see blue lines) with NH due to the matter effect as discussed before. Hence, at above mentioned  $L$  and  $E$  values, we get the smaller survival probability  $P_{\mu\mu}$  for neutrino as compared to that for antineutrino with NH.
3. At  $E = 10 \text{ GeV}$  and  $L = 5000 \text{ km}$ ,  $\Delta \simeq \pi/2$ ,  $T_1$  and  $T_2$  have the same magnitudes but the opposite signs, and thus, these two terms cancel each other resulting  $P_{\mu\mu} = T_0$ . For this reason, at above mentioned  $L$  and  $E$  values, we get the same oscillation probabilities for neutrino and antineutrino.

In an atmospheric neutrino experiment, the  $\nu_\mu$  ( $\phi_{\nu_\mu}^d$ ) flux reaching at the detector is contributed by the  $\nu_e$  ( $\phi_{\nu_e}^s$ ) and the  $\nu_\mu$  ( $\phi_{\nu_\mu}^s$ ) fluxes at the source through  $\nu_e \rightarrow \nu_\mu$  and  $\nu_\mu \rightarrow \nu_\mu$  channels respectively. Thus, we can write the neutrino flux at the detector as the following:

$$\phi_{\nu_\mu}^d = \phi_{\nu_\mu}^s \times P(\nu_\mu \rightarrow \nu_\mu) + \phi_{\nu_e}^s \times P(\nu_e \rightarrow \nu_\mu). \quad (2.6.4)$$

Therefore, if  $\phi_{\nu_\mu}^s = \phi_{\nu_e}^s$ , then the contribution from the term  $T_1$  would be cancelled completely in the atmospheric  $\nu_\mu$  events in a detector. But, in reality,  $\phi_{\nu_\mu}^s \simeq 2\phi_{\nu_e}^s$  in the range of neutrino energy 2 GeV to 10 GeV, thus  $\nu_\mu$  events in the ICAL detector will have the contribution from  $T_1$  and become sensitive to the octant information through  $\sin^2 \theta_{23}$  term in  $T_1$  (see Eq. 2.6.1). It is worthwhile to mention that matter effect in  $P_{\mu\mu}$  is contributed by both the terms  $T_1$  and  $T_2$  with  $\sin^2 \theta_{13}$  in argument. Therefore, the discovery of moderately large value of  $\theta_{13}$ , which is around  $8.5^\circ$ , opens up the possibility of determining the mass hierarchy using the Earth matter effect in neutrino and antineutrino events in the atmospheric neutrino experiment.

Huge possibilities of cutting edge research in the atmospheric neutrino experiments give a boost in building the magnetized ICAL detector at the facility of India-based Neutrino Observatory. In the next chapter, we discuss important components of the ICAL detector and its response towards muons and hadrons. Then, we estimate  $\mu^-$  and  $\mu^+$  events due to atmospheric neutrino and antineutrino for various choices of oscillation parameters.

# 3 The Magnetized ICAL detector

## Contents

---

<b>3.1 Components of the ICAL Detector . . . . .</b>	<b>48</b>
3.1.1 Glass Resistive Plate Chambers	49
3.1.2 The Magnetized Iron	51
<b>3.2 Detection Method in ICAL . . . . .</b>	<b>52</b>
3.2.1 The Detector Response for Muon	53
3.2.2 The Detector Response for Hadrons	55
<b>3.3 Expected Event Rates in the ICAL Detector . . . . .</b>	<b>57</b>
3.3.1 Unoscillated vs. Oscillated Event Rates	58
3.3.2 Event Rates for NH and IH	59
3.3.3 Event Rates for Various Choices of $\theta_{23}$	61
3.3.4 Event Rates as a function of $\Delta m_{32}^2$	63
<b>3.4 Summary and Concluding Remarks . . . . .</b>	<b>64</b>

---

The India-based Neutrino Observatory (INO) has planned to build an underground low background experimental facility at a depth of 1.5 km rock of the Bodi West Hills in the Theni district of India. One of the main experiments which will be housed in this underground laboratory of INO will use the 50 kiloton magnetized Iron CALorimeter (ICAL) detector to detect the atmospheric neutrinos and antineutrinos separately. The first ever detection of atmospheric neutrino happened in the deep underground laboratory at the Kolar Gold Fields (KGF) in India [89]. The experiment at the KGF was performed to look for the signal of proton decay and in that process, they detected atmospheric neutrinos and cosmic muons at various depths, from 300 meters to 2700 meters. The laboratory at the KGF was in operation until 1980. The remarkable success of the KGF

experiment in neutrino detection and the possibility of pursuing rich physics program with the help of atmospheric neutrinos have motivated us to construct the dedicated atmospheric neutrino detector called ICAL under the INO facility.

The primary physics goal of the ICAL detector is to unravel the mass hierarchy of neutrino using the Earth matter effect and to measure the neutrino mixing parameters precisely. It is worthwhile to mention that the matter effect [44–46] plays an important role to improve our knowledge on neutrino oscillation parameters. The matter induced potential for neutrino and antineutrino has the opposite signs, which causes the MSW resonance to occur for one of them depending on the neutrino mass hierarchy. Therefore, the separation of neutrino- and antineutrino-induced events in an experiment is crucial to determine the mass hierarchy of neutrino. The magnetic field inside the ICAL detector will be used to distinguish the charge of  $\mu^-$  and  $\mu^+$  on an event-by-event-basis. To accomplish the physics goal of ICAL, this detector is designed in such a way that it will have the excellent detection efficiency, energy resolution, and angular resolution for  $\nu_\mu/\bar{\nu}_\mu$  events having multi-GeV energy and traversing with baseline in the range of 2000 km to 12000 km through the Earth.

This chapter is organized as follows. In Sec. 3.1, we discuss the important elements of the ICAL detector. We describe in Sec. 3.2 the performance of the ICAL detector to reconstruct the four momenta of final state particles. In Sec. 3.3, we give the expected  $\mu^-$  and  $\mu^+$  event rates for various choices of oscillation parameters assuming 500 kt-yr exposure of the ICAL detector.

### 3.1 Components of the ICAL Detector

The ICAL detector will be composed of 50 kiloton (kt) magnetized iron plates as target and glass Resistive Plate Chambers (RPCs) as sensitive detector. The iron plates having a thickness of 5.6 cm and the glass RPC unit of dimension 2 m  $\times$  2 m will be assembled in alternate layers. Total 151 (150) horizontal layers of iron (RPCs) will be stacked, where the gap between two consecutive iron plates will be 4 cm. Fig. 3.1 presents a layout of the proposed ICAL detector. The plan is to have a modular structure for the detector with a dimension of 48 m (L)  $\times$  16 m (W)  $\times$  14.5 m (H), subdivided into 3 modules, each having a dimension of 16 m  $\times$  16 m  $\times$  14.5 m. The detailed speci-

figuration of the ICAL detector is given in Table 3.1. Next, we describe the RPC and the magnetized iron plates of the ICAL detector.

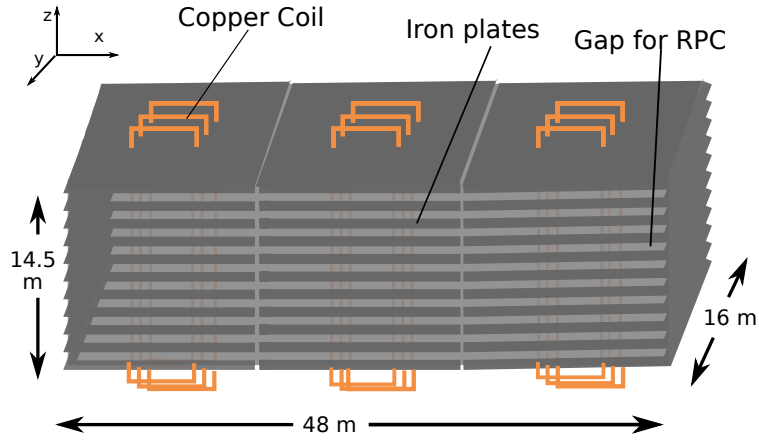


**Figure 3.1.** A pictorial representation of the proposed ICAL detector at the INO facility.

Number of modules	3
Dimension of each module	16 m $\times$ 16 m $\times$ 14.5 m
Total dimension	48 m $\times$ 16 m $\times$ 14.5 m
Number of layers	151
Thickness of iron plates	5.6 cm
Gap between two iron plates	4 cm
Magnetic field strength	1.5 T
RPC unit dimension	2 m $\times$ 2 m $\times$ 2.4 cm
Readout strip width	2.8 cm
Number of RPC units in X-direction	24
Number of RPC units in Y direction	8
Number of RPC units in Z-direction	150
Total RPC units	28800
Number of electronic channels	$3.9 \times 10^6$

**Table 3.1.** The specifications of the ICAL detector.

### 3.1.1 Glass Resistive Plate Chambers

In this section, we describe the construction of a glass RPC in the ICAL detector. Fig. 3.2 presents a pictorial demonstration of a glass RPC. The glass RPC consists of two parallel glass plates. Each of these plates has a thickness of 3 mm, and they are separated by a 2 mm gap in the ICAL detector.

This gap is maintained by the side spacers in four edges and the buttons in between plates fixed by glue. A gas mixture composed of mainly R134a ( $\sim 95.5\%$ ) is used to fill the glass gap and serves as the ionizing component. The outer layers of glass plates are coated by the conductive graphite and connected to a high voltage power supply. To operate the RPC in the avalanche mode, a uniform electric field of about 10 kV ( $\pm 5$  kV) is maintained across the gas gap. Moreover, a small amount of iso-butane (4.3 %) and SF<sub>6</sub> (0.2 %) are used to absorb the high energy photons and secondary electrons. This helps to have a stable operation for a long time period and to reduce the edging effect in the detector. The performance of glass RPC by varying the ratio of gas mixture composition in the context of ICAL detector at INO has been studied in Ref. [197].

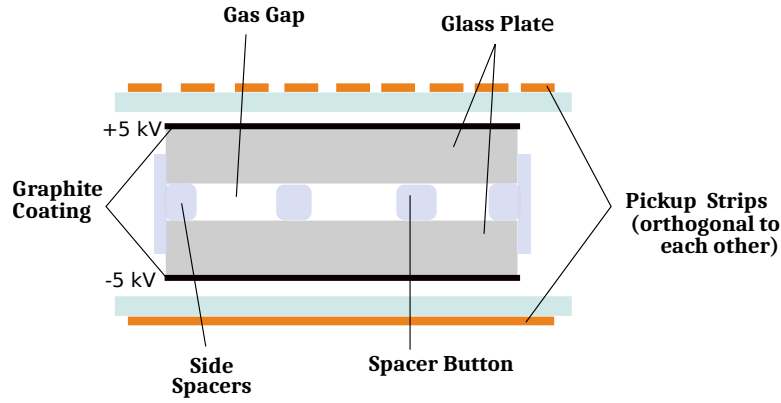


**Figure 3.2.** The layout of a glass Resistive Plate Chamber.

The charged particles, while passing through the RPC gas gap, ionize the gas molecules and generate the primary electrons. These electrons being accelerated by the local electric field in the gap initiate the multiplication process and produce secondary electrons. The operation in avalanche mode of the RPC and high resistive electrodes restrict the electron multiplication process in a small-scale region. Secondary electrons reduce the local electric field, and the recharging process induces a signal in both the electrodes. Two pickup panels, which consist of copper strips of width 2.8 cm at a 2 mm consecutive gap on honeycomb sheets, are kept close to electrodes. The pickup strips which are close to the region of multiplication receive the signal in both the pickup panels. The copper strips in these pickup panels are perpendicular in the  $X$ - $Y$  plane. Thus, the hit strips provide the  $X$  and  $Y$  positions of the charged particle in the RPC. In the ICAL detector, there will be 150 layers of RPC. The layer number corresponding to the hit RPC in the ICAL detector is used as the  $Z$  coordinate.

The average number of hit strips due to the ionization of gas molecules by muons in the RPC is around 1.5 [198]. The recovery time of RPC is around 2 ns, and with the offline correction technique, the time resolution of RPC can be improved to less than one ns [199]. Thus, the timing information from all the layers of hit RPC in the ICAL detector enables us to distinguish whether the charged particle is upward or downward going.

### 3.1.2 The Magnetized Iron

To accomplish the physics goal of the ICAL detector, 50 kt magnetized iron would serve as the target for neutrino interactions in the detector. Once built, this will be the World's largest magnet. The aim is to produce a uniform magnetic field of strength around 1.5 Tesla over the entire detector. Keeping in mind the mechanical constraints and the required power to produce the magnetic field, the iron plate units or tiles for ICAL are chosen as  $4\text{ m} \times 2\text{ m} \times 5.6\text{ cm}$  in dimension. Such tiles are assembled with a consecutive gap of 2 mm to construct  $16\text{ m} \times 16\text{ m} \times 5.6\text{ cm}$  iron layers. In each of the three modules, there will be total 151 layers of iron plates with 4 cm gap to accommodate the glass RPC between each of the two iron layers.

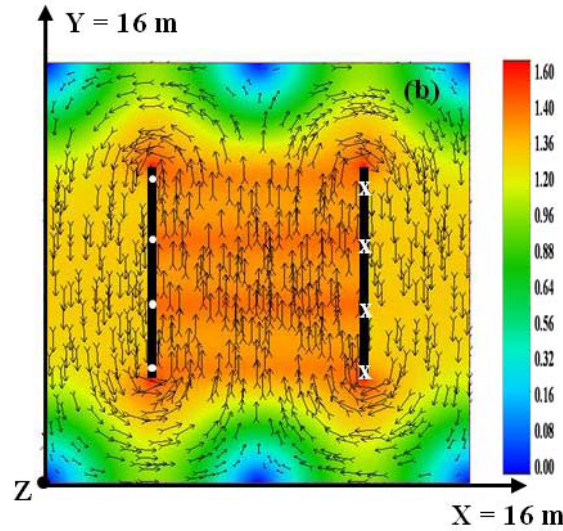


**Figure 3.3.** The magnetic field as obtained from a simulation study with one iron plate of dimension  $16\text{ m} \times 16\text{ m} \times 5.6\text{ cm}$ . This figure is taken from Ref. [200].

The copper coils to carry the magnetic field producing DC current are planned to be embedded in each ICAL module as shown in Fig. 3.1. The slots in iron plates through which the current carrying

coil passes can be discrete or continuous. The detailed simulation of magnetic field in Ref. [200] finds that the magnetic field is uniform over a larger region ( $\sim 75\%$ ) in case of continuous slots than a discrete configuration. They also estimated the magnetic field in single iron plate. Four coils each carrying 5 kA current and passing through two continuous slots were used. Fig. 3.3 shows the magnetic field strength and its direction averaged over a  $5\text{ cm} \times 5\text{ cm}$  pixel on iron plate. The white dots and cross points refer to the outward and inward directions of current. The magnetic field strength is almost uniform in the central region of iron plate, however it varies rapidly in the peripheral region. Therefore, the detector properties to reconstruct muon will be different in the central region from that in the peripheral region. For details on the magnetic field and its dependence on other aspects, see Ref. [200]. The detector response for muon and hadrons in the ICAL detector is discussed in the next section.

### 3.2 Detection Method in ICAL

The ICAL detector is a sampling calorimeter, comprised of RPCs and magnetized iron slabs stacked in alternate layers as discussed in previous sections. The detection of  $\nu_\mu$  ( $\bar{\nu}_\mu$ ) in the ICAL detector will be performed by observing the associated charged lepton  $\mu^-$  ( $\mu^+$ ) produced in the final state of charged current (CC) neutrino interaction. If the interaction is quasi-elastic, then the final state muon has almost the same energy as the initial neutrino, whereas if the interaction is CC deep inelastic, then some of the initial neutrino energy is carried away by the hadrons as created along with muon in the final state. For any charged particle passing through the detector, each RPC layer provides the position ( $X, Y, Z$ ) and time of hit in it. As muon is the minimum ionizing particle, thus the muon is supposed to give longest track in that event and the hadrons produce shower in detector. The magnetic field in the detector bends the charged particles depending on the direction of its motion. From the radius of curvature of muon and direction of bending, its momentum as well the charge are reconstructed. The total energy carried out by hadrons is also reconstructed from the total number of hits<sup>1</sup> in the shower. The detailed response of the detector to muon and hadrons are given in the following section.

---

<sup>1</sup>In ICAL, hit corresponds to the respective x or y information, z coordinate of the layer, and timing information.



### 3.2.1 The Detector Response for Muon

The geometry of the ICAL and propagation of particles through the detector are simulated in a package based on the GEANT4 [201] simulation toolkit. To estimate the detector properties, 10000 muons are passed through the ICAL detector with the vertex of interaction at the center of the second module ( $XYZ \equiv 8\text{ m} \times 8\text{ m} \times 10\text{ m}$ ). A simple track finder algorithm is used to find the longest track (muon-like track) in the event. Around 90% of the total number of muons with true momentum ( $P_{\text{in}}$ ) 2 GeV/c are reconstructed as the muon-like tracks, whereas for  $P_{\text{in}} = 5\text{ GeV/c}$ , around 95% muon like-tracks are reconstructed [202]. The muon-like tracks are fitted with a Kalman-filter based algorithm which extrapolates the initial vector ( $x$ ,  $y$ ,  $dx/dz$ ,  $dy/dz$ , charge-weighted inverse momentum  $q/p$ ) in the next layer incorporating the energy loss in iron and in other materials, local magnetic field, and multiple scattering. In each of the hit layer, the recorded and the extrapolated positions are compared, and after some iterations of doing so, the best fitted points are obtained in all the hit layers which reconstruct the final track. This best fitted track is used to estimate the vertex position, momentum, and charge of muon. The left panel of

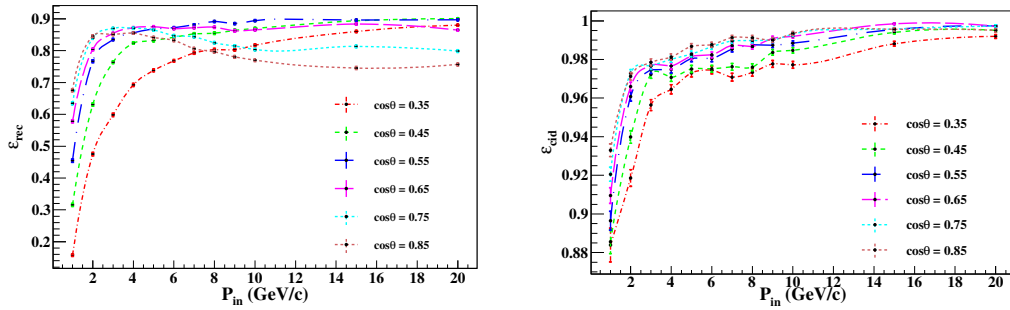


**Figure 3.4.** The variation of reconstruction (left panel) and charge identification (right panel) efficiencies with true muon energy  $P_{\text{in}}$  and true muon angle  $\cos \theta$ . These figures are taken from Ref. [202].

Fig. 3.4 shows the reconstruction efficiency of  $\mu^-$  as a function of true muon momentum. Different colored lines correspond to various true zenith angles of muon. It is noticed that the muon-like track is partially or fully contained depending on true momentum, location of interaction vertex, and zenith angle ( $\cos \theta_{\text{in}}$ ) of the muon. The efficiency to distinguish the upward and the downward going events is around 99.7% for  $P_{\text{in}} = 2\text{ GeV/c}$  and  $\cos \theta_{\text{in}} = 0.25$ . The right panel of Fig. 3.4 shows the charge identification (CID) efficiency as the function of true momentum and direction

of muon. One can see that the CID efficiency in the ICAL detector is more than 95% for  $P_{in}$  higher than 2 GeV/c [202].

The reconstructed energy and directions are fitted with the Gaussian distribution, and the RMS (standard deviation) value of fitted function quantifies the resolution of the reconstructed parameter. Fig. 3.5 shows the energy (left panel) and angular (right panel) resolutions for muon as a function of true energies and zenith angles at the ICAL detector. As far as the muon direction

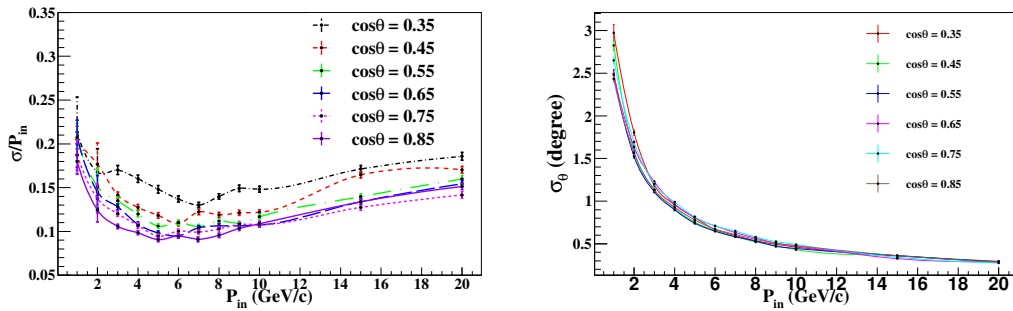


**Figure 3.5.** The muon energy and angular resolutions at the ICAL detector are shown in left and right panels respectively as a function of true muon energy  $P_{in}$  and true muon angle  $\cos\theta$ . These figures are taken from Ref. [202].

resolution ( $\sigma_\theta$ ) is concerned, it varies in the range of [0.5, 2] degree for true muon energy of 1 GeV to 20 GeV, and  $\sigma_\theta$  is almost independent of the true zenith angle of muon as can be seen in the right panel of Fig. 3.5. However, the energy resolution can vary with  $\cos\theta_{in}$  as shown in black ( $\cos\theta = 0.35$ ) and violet ( $\cos\theta = 0.85$ ) lines in left panel of Fig. 3.5. The relatively poor resolution in case of horizontal events is obtained due to the fact that a small number of layers get hit in these events which results in large uncertainties in the reconstructed momentum. Nevertheless, the momentum resolution of the ICAL detector is around 10-15% in case the vertex is in the central region of detector. A better energy resolution is obtained for the events with energy 4 GeV to 10 GeV where we expect the maximum sensitivity towards the issue of neutrino mass hierarchy.

In GEANT4 simulation, the events with energy 1-20 GeV and interaction vertex at the peripheral region of the detector are found to be reconstructed with 60-70% efficiency which is 20-30% less than that in the central region. The momentum resolution also gets worse and becomes around 15-24%. This deterioration of the detector response at peripheral region happens because most of the events are partially contained. and we have hits in very few layers. As a result, these events

get either discarded by the event selection criteria of total number of layers, or get fitted poorly with the Kalman filter. The first reason reduces the reconstruction efficiency, whereas the later one produces poor energy and direction resolutions. For more details on the detector response of ICAL for muon, see Refs. [202, 203].

### 3.2.2 The Detector Response for Hadrons

Around 4 GeV (8 GeV), the CC deep inelastic cross-section for neutrino (antineutrino) becomes larger as compared to two other CC processes which are quasi-elastic and resonance (see Fig. 4.4). We know that in deep inelastic scattering of neutrino, associate charged lepton gets produced along with many hadrons in the final state. As a result, we get a track like event for muon and a bunch of hits around the vertex due to hadrons. In case of neutral current events, final state consists of multiple hadrons with no track. Since the neutral current events are identical for all kinds of neutrino flavor, we do not consider these events in our analysis. However, for the study of mixing among active and sterile neutrinos, as sterile neutrino does not take part in the standard weak interaction, the deficit in total number of neutral current events can be an important smoking gun signal in search for sterile neutrinos. Therefore, the reconstruction of hadron energy is important in the study of standard oscillation as well as for the new physics searches.

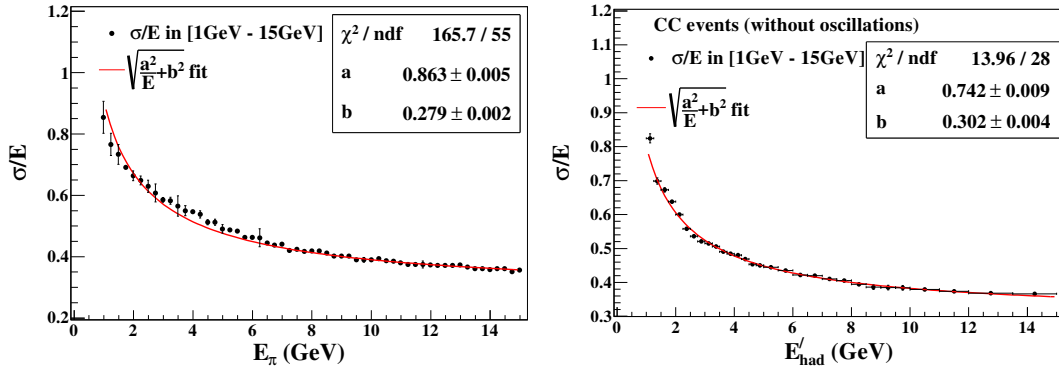


**Figure 3.6.** Left panel: The charged pion energy resolution at the ICAL detector. Right Panel: The hadron energy resolution obtained from the simulation with neutrino events that are generated using the NUANCE neutrino event generator. These figures are taken from Ref. [204].

In the final state of CC deep-inelastic scattering, various hadrons such as, pions, kaons, protons, and heavier excited particle states get produced. However, preliminary study finds that the hit

distributions for all of these different hadrons are similar in the ICAL detector. Since most of the hadrons are pions in the final state of neutrino interaction, the hit pattern for pions has been studied in the GEANT4 based simulation toolkit of ICAL [204]. On an average, 2 hits per GeV are found to be registered for pions in the detector. The distribution of total number of hits from a large number (10000) of pions with fixed energy is fitted with the Vavilov distribution function. The mean number of hit obtained from this fitting,  $\bar{n}(E)$ , follows the approximate relation  $\bar{n}(E) = n_0[1 - \exp(-E/E_0)]$  where  $n_0$  and  $E_0$  are constants. The parameters  $n_0$  and  $E_0$  are sensitive to the energy range of fit. For  $E \ll E_0$ ,  $\bar{n}(E) \approx n_0 E/E_0$ , and therefore the pion energy resolution can be written as [204]

$$\frac{\sigma}{E} \approx \frac{\Delta n(E)}{\bar{n}(E)}, \quad (3.2.1)$$

with  $\Delta n(E)$  is the square root of the variance of the Vavilov distribution. The left panel of Fig. 3.6 presents the variation of  $\sigma/E$  (pion energy resolution) with true pion energy  $E_\pi$ .

Neutrino events generated using the NUANCE [205] neutrino generator have been used in the study of the hadron energy reconstruction at the ICAL detector [204]. Here, the total true energy of hadrons in the final state of interaction is taken as the difference of incoming neutrino energy and outgoing muon energy ( $E'_{\text{had}} = E_\nu - E_\mu$ ), assuming that the nucleus is at rest and neglecting the nucleus binding energy. The hadron energy resolution at the ICAL detector is estimated in the same way as we evaluate the energy resolution of pions, and is presented in the right panel of Fig. 3.6. Comparing the left and right panels of Fig. 3.6, one can see that the energy resolutions obtained from the simulations with pion only (left panel) and that from the NUANCE-generated events (right panel) are almost similar.

In the experiment, number of hits due to hadrons are the only observables to reconstruct the hadron energy. Therefore, the hadron energy is calibrated from the number of hits registered in the detector due to hadrons. For a number of hits ( $N_{\text{hits}}$ ) in the detector (one point in the x-axis of Fig 3.7), the distribution of  $E'_{\text{had}}$  is fitted using the Vavilov distribution function. The mean of this distribution gives the hadron energy corresponding to a given number of hits ( $N_{\text{hits}}$ ) in the detector. Fig. 3.7 shows how the true hadron energy ( $E'_{\text{had}}$ ) varies with the number of hits produced in the detector. The error in the measurement of total hadron energy from the hits is the RMS of the

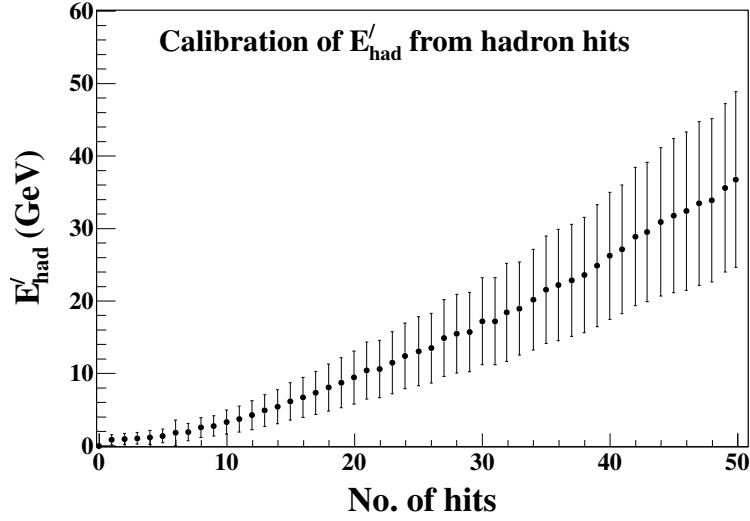


**Figure 3.7.** The relation between total number of hits registered in the ICAL detector due to hadrons and the total true energy of those hadrons ( $E'_{\text{had}} = E_\nu - E_\mu$ ). The black dots are mean, and the error bars denote  $\sigma$  of the Vavilov fits. This figure is taken from [204].

fit, and is presented by error bars in Fig. 3.7. Next, we present the total event rates in the ICAL detector for various choices oscillation parameters.

### 3.3 Expected Event Rates in the ICAL Detector

In this section, we estimate the event rates expected at the ICAL detector using 500 kt-yr exposure for various choices of oscillation parameters. The NUANCE neutrino event generator [205] is used to calculate the cross-section and to produce the unoscillated events at 50 kt ICAL detector. The neutrino events are folded with the energy and angular resolutions, and reconstruction and charge identification efficiencies obtained for the ICAL detector. Here, the results are produced using the atmospheric neutrino fluxes calculated for the Kamioka site [165]. The preliminary flux at the INO site has been calculated and it is observed that at low energy, fluxes at the INO site are smaller than that at the Kamioka site because of the strong horizontal component of geomagnetic fields of Earth at the INO site [206]. However, for energy  $E_\mu \gtrsim 4$  GeV, the energy spectrum of neutrino events as obtained at the ICAL detector with the fluxes for Kamioka and INO sites are similar (see Fig A.5 in Ref. [42]). We present the results in this section using the following values of oscillation parameters:  $\theta_{12} = 33.2^\circ$ ,  $\theta_{13} = 8.5^\circ$ ,  $\theta_{23} = 45^\circ$ ,  $\Delta m_{21}^2 = 7.5 \times 10^{-5} \text{ eV}^2$ ,  $\Delta m_{32}^2 = 2.36 \times 10^{-3} \text{ eV}^2$ , and  $\delta_{\text{CP}} = 0^\circ$ . We calculate the transition probabilities:  $\nu_e \rightarrow \nu_\mu$  ( $P_{e\mu}$ ),

$\nu_\mu \rightarrow \nu_e$  ( $P_{\mu e}$ ), and  $\nu_\mu$  ( $P_{\mu\mu}$ ) numerically using the PREM profile [158] for the Earth matter density. We use a reweighting algorithm<sup>2</sup> to get the oscillated neutrino events.

### 3.3.1 Unoscillated vs. Oscillated Event Rates

If there is no flavor oscillation, then the expected number of  $\mu^-$  and  $\mu^+$  events are 6672 and 2983 respectively at the ICAL detector with reconstructed muon energy ( $E_\mu$ ) in the range of [1, 21] GeV and reconstructed muon zenith angle ( $\cos \theta_\mu$ ) in the range of [-1, 1] using 500 kt-yr exposure. Once the oscillations of neutrino and antineutrino are taken into account using the reweighting algorithm, the expected  $\mu^-$  events become 4871 and  $\mu^+$  events turn out to be 2188. We obtain  $\mu^-$  ( $\mu^+$ ) events at ICAL from the survival of original  $\nu_\mu$  ( $\bar{\nu}_\mu$ ) flux and from the appearance of  $\nu_\mu$  ( $\bar{\nu}_\mu$ ) from  $\nu_e$  ( $\bar{\nu}_e$ ) flux. Table 3.2 shows the total number of  $\mu^-$  (left panel) and  $\mu^+$  (right panel) events

w/o oscillation	with oscillation	w/o oscillation	with oscillation
6672	4774 ( $\nu_\mu \rightarrow \nu_\mu$ )	2983	2177 ( $\bar{\nu}_\mu \rightarrow \bar{\nu}_\mu$ )
	97 ( $\nu_e \rightarrow \nu_\mu$ )		11 ( $\bar{\nu}_e \rightarrow \bar{\nu}_\mu$ )
	4871 (total $\mu^-$ )		2188 (total $\mu^+$ )

**Table 3.2.** Number of  $\mu^-$  (left panel) and  $\mu^+$  (right panel) events at ICAL with an exposure of 500 kt-yr. We sum over all the directions and reconstructed  $E_\mu$  in the range of 1 GeV to 21 GeV. In case of oscillation, we use  $\theta_{12} = 33.2^\circ$ ,  $\theta_{13} = 8.5^\circ$ ,  $\theta_{23} = 45^\circ$ ,  $\Delta m_{21}^2 = 7.5 \times 10^{-5} \text{ eV}^2$ , and  $\Delta m_{32}^2 = 2.36 \times 10^{-3} \text{ eV}^2$ .

as well as the individual contribution<sup>3</sup> coming from  $\nu_\mu \rightarrow \nu_\mu$  and  $\nu_e \rightarrow \nu_\mu$  oscillation channels. One can see that less than 2% of the total expected events in the ICAL detector are sourced from the  $\nu_e \rightarrow \nu_\mu$  channel. Nevertheless, the  $\nu_e \rightarrow \nu_\mu$  channel has an enormous impact in the study of the mass hierarchy using the atmospheric neutrino experiment as discussed in Sec. 2.6.

In Fig. 3.8, we show the distributions of  $\mu^-$  (left panel) and  $\mu^+$  (right panel) events as a function of reconstructed  $\cos \theta_\mu$  in a window of  $E_\mu \in [4, 6]$  GeV using 500 kt-yr exposure of the ICAL detector. We also present the statistical error of the number of events each  $\cos \theta_\mu$  bin. The red line displays the event spectrum taking the oscillation into account, whereas the black line depicts the

<sup>2</sup>We generate a uniform random number  $X$  in the range of 0 to 1. For a  $\nu_\mu$ -induced event with energy  $E$  and baseline  $L$ , if  $P_{\mu e}(E, L) \leq X \leq P_{\mu e}(E, L) + P_{\mu\mu}(E, L)$ , then the event is considered as the  $\nu_\mu$  event in the analysis. To include a  $\nu_\mu$ -induced event which appears from a  $\nu_e$  due to  $\nu_e \rightarrow \nu_\mu$  transition, first we generate events using  $\nu_e$  flux and  $\nu_\mu$  cross-sections. Then, for such an event with energy and baseline as  $E'$  and  $L'$  respectively, if  $X < P_{e\mu}(E', L')$ , then the event is taken as a  $\nu_\mu$  event in the analysis. For detailed discussion related to this issue, see Refs. [42, 47, 48].

<sup>3</sup>The separation between  $P_{e\mu}$  and  $P_{\mu\mu}$  channels is not possible in the atmospheric neutrino experiment. Nevertheless, to see the contribution from these two channels for understanding purpose, we present the events separately.

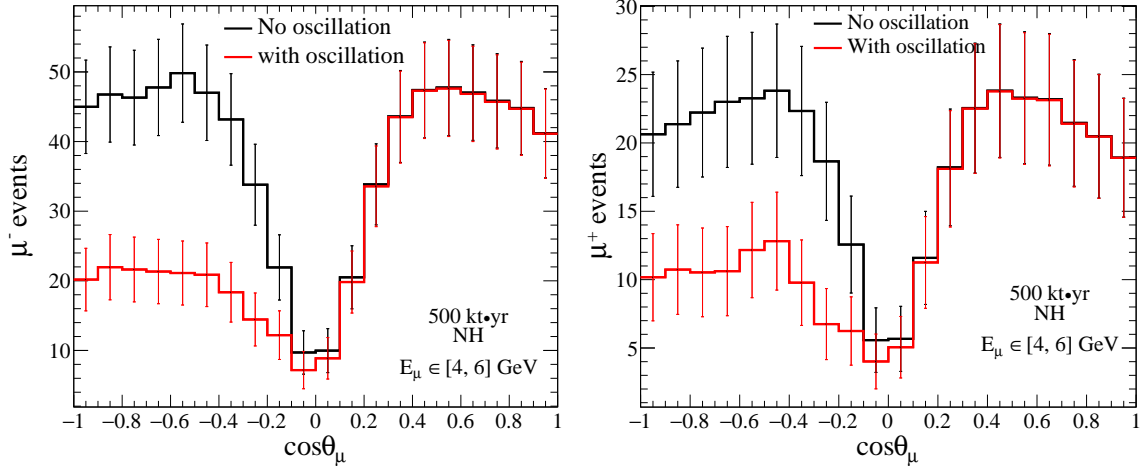


**Figure 3.8.** The event distributions for  $\mu^-$  (left panel) and  $\mu^+$  (right panel) as a function of reconstructed  $\cos \theta_\mu$  at ICAL with an exposure of 500 kt.yr. Here, the events are summed over the reconstructed  $E_\mu \in [4, 6]$  GeV. The black and red lines show events without and with oscillation respectively. In case of oscillation, we take  $\theta_{12} = 33.2^\circ$ ,  $\theta_{13} = 8.5^\circ$ ,  $\theta_{23} = 45^\circ$ ,  $\Delta m_{21}^2 = 7.5 \times 10^{-5} \text{ eV}^2$ ,  $\Delta m_{32}^2 = 2.36 \times 10^{-3} \text{ eV}^2$ , and  $\delta_{CP} = 0^\circ$ . Note that the y-axis ranges in left and right panels are different.

event spectrum for unoscillated case. One can see that red and black lines are well separated from each other for  $\cos \theta_\mu \in [-1, 0]$  (upward going events) in case of both  $\mu^-$  and  $\mu^+$ , whereas we do not see the oscillation for  $\cos \theta_\mu \in [0, 1]$  (downward going events).

### 3.3.2 Event Rates for NH and IH

One of the main goals of the ICAL detector is to answer the question that which neutrino mass eigenstate is the lightest one,  $m_1$  (valid for normal hierarchy, NH) or  $m_3$  (applicable inverted hierarchy, IH). To calculate the sensitivity of the ICAL detector to determine the mass hierarchy, we simulate the events with the true mass hierarchy (data), and fit the data with the events obtained with wrong mass hierarchy taking into account the systematic uncertainties and marginalizing over oscillation parameters. In doing so, if we take the magnitude of  $\Delta m_{31}^2$  same for NH and IH, and signs as +ve and -ve respectively, then the magnitude of  $\Delta m_{32}^2$  ( $\equiv \Delta m_{31}^2 - \Delta m_{21}^2$ ) for NH and IH becomes different. This results in different probabilities for IH and NH even when  $\theta_{13} = 0^4$ , and we get a spurious contribution to the statistical significance. To resolve this issue, while estimating

<sup>4</sup>With  $\theta_{13} = 0$ , the terms  $T_1$  and  $T_2$  in Eq. 2.6.2 are zero. Therefore, the probability expression in matter becomes same as that of in the vacuum, and there should not be any difference in oscillation probabilities with NH and IH with  $\theta_{13} = 0$ .

the sensitivity towards mass hierarchy, we use the effective mass splitting [207, 208]

$$\Delta m_{\text{eff}}^2 = \Delta m_{31}^2 - \Delta m_{21}^2 (\cos^2 \theta_{12} - \cos \delta_{\text{CP}} \sin \theta_{13} \sin 2\theta_{12} \tan \theta_{23}), \quad (3.3.1)$$

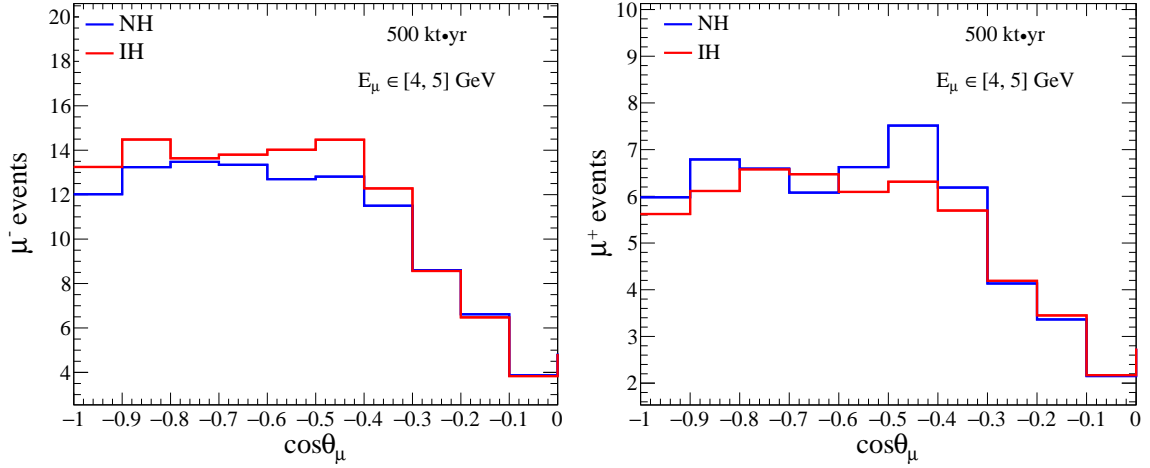
where  $\Delta m_{\text{eff}}^2$  has the same magnitude for NH and IH with +ve and -ve signs respectively.

Table 3.3 presents the total number of  $\mu^-$  (left table) and  $\mu^+$  (right table) events at the ICAL detector that are expected for NH and IH with 500 kt-yr exposure of the ICAL detector. These events are obtained for reconstructed  $E_\mu \in [1, 21]$  GeV and reconstructed  $\cos \theta_\mu \in [-1, 1]$ . For the understanding purpose, events coming from  $\nu_\mu \rightarrow \nu_\mu$  and  $\nu_e \rightarrow \nu_\mu$  oscillation channels are shown separately. The relative difference between events with IH and NH decreases when the

Channel	NH	IH
$\nu_\mu \rightarrow \nu_\mu$	4774	4899
$\nu_e \rightarrow \nu_\mu$	97	14
Total $\mu^-$	4871	4913

Channel	NH	IH
$\bar{\nu}_\mu \rightarrow \bar{\nu}_\mu$	2177	2119
$\bar{\nu}_e \rightarrow \bar{\nu}_\mu$	11	47
Total $\mu^+$	2188	2166

**Table 3.3.** Total number of  $\mu^-$  (left table) and  $\mu^+$  (right table) events expected at ICAL with NH (IH) is given in 2nd (3rd) column. We sum over all the directions and reconstructed  $E_\mu$  in the range of 1 GeV to 21 GeV and consider an exposure of 500 kt-yr. We take  $\theta_{12} = 33.2^\circ$ ,  $\theta_{13} = 8.5^\circ$ ,  $\theta_{23} = 45^\circ$ ,  $\Delta m_{21}^2 = 7.5 \times 10^{-5} \text{ eV}^2$ ,  $|\Delta m_{\text{eff}}^2| = 2.4 \times 10^{-3} \text{ eV}^2$ , and  $\delta_{\text{CP}} = 0^\circ$ .



**Figure 3.9.** The  $\mu^-$  (left panel) and  $\mu^+$  (right panel) event spectra as a function of reconstructed  $\cos \theta_\mu$  with mass hierarchy as NH (blue line) and IH (red line) using 500 kt-yr of ICAL exposure. Here, the reconstructed  $E_\mu$  is in the range of  $[4, 5]$  GeV. We use  $\theta_{12} = 33.2^\circ$ ,  $\theta_{13} = 8.5^\circ$ ,  $\theta_{23} = 45^\circ$ ,  $\Delta m_{21}^2 = 7.5 \times 10^{-5} \text{ eV}^2$ , and  $|\Delta m_{\text{eff}}^2| = 2.4 \times 10^{-3} \text{ eV}^2$ , and  $\delta_{\text{CP}} = 0^\circ$ . Note that the y-axis ranges in left and right panels are different.

contribution from appearance and disappearance channels are summed up, though the relative sep-



arations between IH and NH for individual channels are comparatively larger. We have explained the reason behind this in Sec. 2.6 using the probability expressions. One can see that the difference between the total event rates for IH and NH is not large. Nevertheless, the ICAL detector will be able to unravel the mass hierarchy using the spectral information of energy and zenith angle distributions of  $\mu^-$  and  $\mu^+$  events. In Fig. 3.9, we present the event spectra at the ICAL detector for NH (blue line) and IH (red line) with  $E_\mu \in [4, 5]$  GeV for 500 kt-yr exposure. The left and right panels are for the event distribution of  $\mu^-$  and  $\mu^+$  respectively. Using the reconstructed muon energy and muon direction ( $E_\mu, \cos \theta_\mu$ ), the ICAL detector will be able to determine the mass hierarchy with a  $2.7\sigma$  confidence level [47] using 500 kt-yr exposure. The sensitivity gets improved to more than  $3\sigma$  if the reconstructed hadron energy is included in the analysis [49].

### 3.3.3 Event Rates for Various Choices of $\theta_{23}$

The precision measurement of the atmospheric neutrino parameters is another goal of the ICAL detector. Table 3.4 presents the expected number of  $\mu^-$  (left) and  $\mu^+$  (right) events at the ICAL detector for three different values of  $\theta_{23}$ , viz.  $40^\circ$  (2nd column),  $45^\circ$  (3rd column), and  $50^\circ$  (4th column). These events are obtained with  $E_\mu \in [1, 21]$  GeV and  $\cos \theta_\mu \in [-1, 1]$  and using ICAL exposure of 500 kt-yr. Second and third rows of Table 3.4 present the events for disappearance and appearance channels respectively, and fourth row presents the total events.

Channel	$\theta_{23} = 40^\circ$	$\theta_{23} = 45^\circ$	$\theta_{23} = 50^\circ$	Channel	$\theta_{23} = 40^\circ$	$\theta_{23} = 45^\circ$	$\theta_{23} = 50^\circ$
$\nu_\mu \rightarrow \nu_\mu$	4881	4774	4763	$\bar{\nu}_\mu \rightarrow \bar{\nu}_\mu$	2202	2177	2198
$\nu_e \rightarrow \nu_\mu$	80	97	114	$\bar{\nu}_e \rightarrow \bar{\nu}_\mu$	10	11	12
Total $\mu^-$	4961	4871	4877	Total $\mu^+$	2212	2188	2210

**Table 3.4.** Total number of  $\mu^-$  (left panel) and  $\mu^+$  (right panel) events expected for different values of atmospheric mixing angle  $\theta_{23}$ . The numbers in 2nd, 3rd, and 4th columns are for  $\theta_{23} = 40^\circ$ ,  $45^\circ$ , and  $50^\circ$  respectively. We sum over all the directions and reconstructed muon energy ( $E_\mu$ ) in the range of 1 GeV to 21 GeV and consider ICAL exposure of 500 kt-yr. We use other oscillation parameters as  $\theta_{12} = 33.2^\circ$ ,  $\theta_{13} = 8.5^\circ$ ,  $\Delta m_{21}^2 = 7.5 \times 10^{-5} \text{ eV}^2$ ,  $\Delta m_{32}^2 = 2.36 \times 10^{-3} \text{ eV}^2$ , and  $\delta_{\text{CP}} = 0^\circ$ .

In Fig. 3.10, we present the event spectra of  $\mu^-$  (left panel) and  $\mu^+$  (right panel) events with different values of  $\theta_{23}$  expected at the 50 kt ICAL detector over 10 years of running. The blue, red, and green lines shows the event distributions for  $\theta_{23} = 40^\circ$ ,  $45^\circ$ , and  $50^\circ$  respectively with  $E_\mu$  in the range of  $[4, 5]$  GeV. The important features that we see in Fig. 3.10 are as follows.

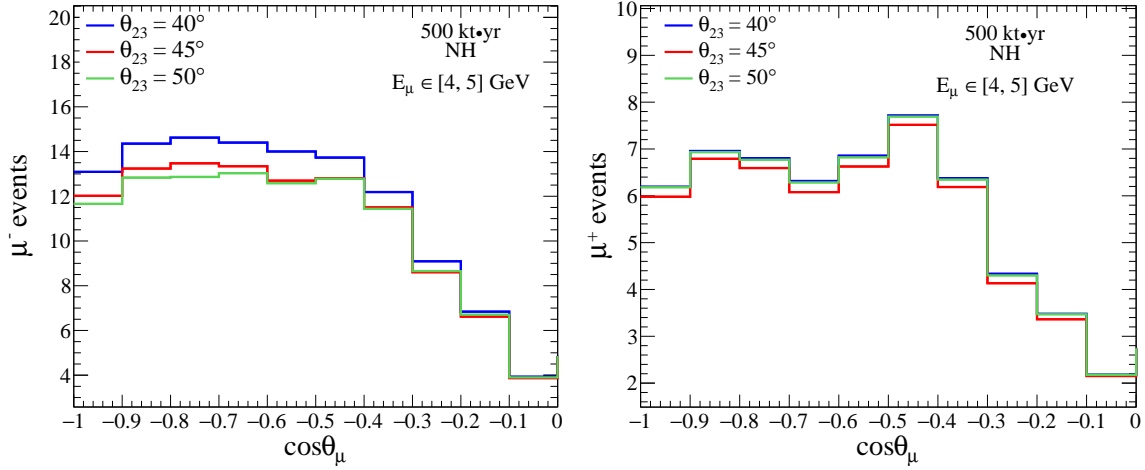


**Figure 3.10.** For different values of  $\theta_{23}$ , the expected  $\mu^-$  (left panel) and  $\mu^+$  (right panel) event spectra as a function of reconstructed  $\cos \theta_\mu$  at the ICAL detector with 500 kt-yr exposure. The blue, red, and green lines are for  $\theta_{23} = 40^\circ$ ,  $45^\circ$ , and  $50^\circ$  respectively. Here, the events are summed over reconstructed  $E_\mu \in [4, 5]$  GeV. Other oscillation parameters are taken as  $\theta_{12} = 33.2^\circ$ ,  $\theta_{13} = 8.5^\circ$ ,  $\theta_{23} = 45^\circ$ ,  $\Delta m_{21}^2 = 7.5 \times 10^{-5} \text{ eV}^2$ ,  $\Delta m_{32}^2 = 2.36 \times 10^{-3} \text{ eV}^2$ , and  $\delta_{\text{CP}} = 0^\circ$ . Note that the y-axis ranges in left and right panels are different.

1. The three lines (blue, red, and green lines) are different for both  $\mu^-$  and  $\mu^+$  since  $\theta_{23}$  appears in the amplitude of the probability expressions of appearance and disappearance channels (see Eqs. 2.6.1 and 2.6.2).
2. For  $\mu^+$  (right panel), the event spectrum for  $\theta_{23} = 40^\circ$  (blue line) and  $50^\circ$  (green line) overlap as antineutrino with NH does not feel the matter effect. In this case, antineutrino event is a function of  $\sin^2 2\theta_{23}$  which is blind to the octant information. Therefore,  $\mu^+$  events are insensitive to the  $\theta_{23}$  octant for NH. However,  $\mu^+$  events contribute to the  $\theta_{23}$  precision measurement.
3. For  $\mu^-$  (left panel), the green and blue lines are well separated indicating the contributions towards the octant resolution. We have seen that the term  $T_1$  in Eqs. 2.6.1 and 2.6.2 containing  $\sin^2 \theta_{23}$  has a significant contribution to  $\nu_\mu \rightarrow \nu_\mu$  and  $\nu_e \rightarrow \nu_\mu$  oscillation probabilities for neutrino with NH.

Using the spectral information on  $E_\mu$  and  $\cos \theta_\mu$  as the observables, the ICAL detector is expected to measure  $\sin^2 \theta_{23}$  with a relative  $1\sigma$  precision of 13.7% [48] with 500 kt-yr exposure. Including the information on reconstructed hadron energy along with the muon momenta, the sensitivity of ICAL detector is improved to 12% at  $1\sigma$  relative precision [49, 52].

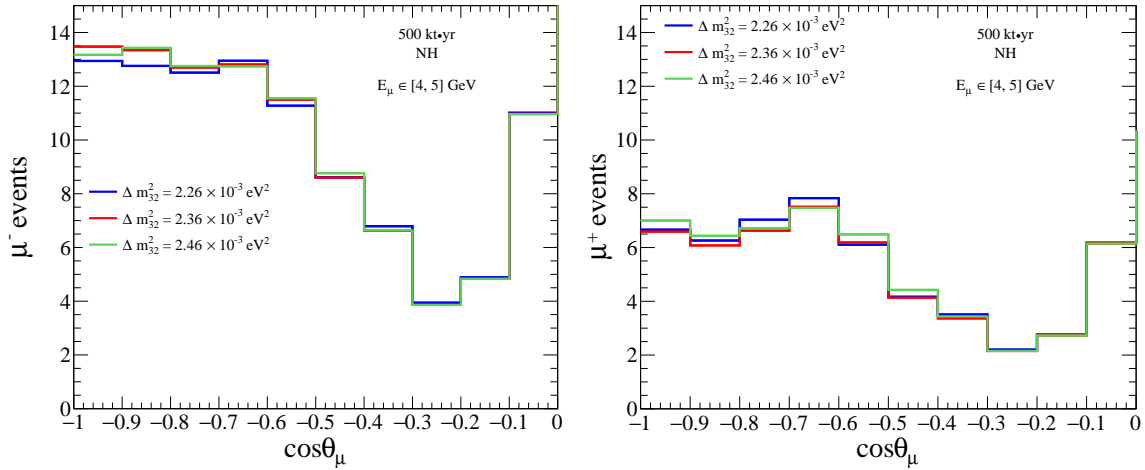


**Figure 3.11.** For different values of  $\Delta m_{32}^2$ , the expected  $\mu^-$  (left panel) and  $\mu^+$  (right panel) event spectra as a function of reconstructed  $\cos \theta_\mu$  at the ICAL detector with 500 kt-yr exposure. The blue, red, and green lines are for  $\Delta m_{32}^2 = 2.26 \times 10^{-3} \text{ eV}^2$ ,  $2.36 \times 10^{-3} \text{ eV}^2$ , and  $2.46 \times 10^{-3} \text{ eV}^2$  respectively. Here, the events are summed over reconstructed  $E_\mu \in [4, 5] \text{ GeV}$ . Other oscillation parameters are taken as  $\theta_{12} = 33.2^\circ$ ,  $\theta_{13} = 8.5^\circ$ ,  $\theta_{23} = 45^\circ$ ,  $\Delta m_{21}^2 = 7.5 \times 10^{-5} \text{ eV}^2$ , and  $\delta_{\text{CP}} = 0^\circ$ .

### 3.3.4 Event Rates as a function of $\Delta m_{32}^2$

In this section, we discuss the sensitivity of the ICAL detector to precisely measure the atmospheric mass splitting  $\Delta m_{32}^2$ . The total number of  $\mu^-$  events with  $\Delta m_{32}^2 = 2.26 \times 10^{-3} \text{ eV}^2$ ,  $2.36 \times 10^{-3} \text{ eV}^2$ , and  $2.46 \times 10^{-3} \text{ eV}^2$  are 4879, 4871, and 4880 respectively with  $E_\mu \in [1, 21] \text{ GeV}$  and  $\cos \theta_\mu \in [-1, 1]$  over an exposure of 500 kt-yr. The corresponding  $\mu^+$  events are 2212, 2188, and 2210. It is evident that the rate analysis will give very poor results on the  $\Delta m_{32}^2$  precision. Since  $\Delta m_{32}^2$  appears in the phase with neutrino energy and baseline, a large smearing in  $E_\mu$  and  $\cos \theta_\mu$  can wash out the information on  $\Delta m_{32}^2$ .

In Fig. 3.11, we present the distributions of  $\mu^-$  (left panel) and  $\mu^+$  (right panel) events as a function of  $\cos \theta_\mu$ . The blue, red, and green lines present the event spectra with  $\Delta m_{32}^2 = 2.26 \times 10^{-3} \text{ eV}^2$ ,  $2.36 \times 10^{-3} \text{ eV}^2$ , and  $2.46 \times 10^{-3} \text{ eV}^2$  respectively in the range of  $E_\mu \in [4, 5] \text{ GeV}$ . The reconstructed hadron information ( $E'_{\text{had}}$ ) has an important impact on the precision measurement of  $\Delta m_{32}^2$  in the ICAL detector. Due to the inclusion of the hadron energy information in the analysis, the expected accuracy with which ICAL will be able to measure  $\Delta m_{32}^2$  gets enhanced remarkably. The expected  $1\sigma$  accuracy on  $\Delta m_{32}^2$  with 500 kt-yr ICAL data is 4.2% with  $E_\mu$  and  $\cos \theta_\mu$ , whereas with  $E_\mu$ ,  $\cos \theta_\mu$ , and  $E'_{\text{had}}$  as observables, the expected  $1\sigma$  precision on  $\Delta m_{32}^2$  gets improved to 2.9% [48, 49, 52].

### 3.4 Summary and Concluding Remarks

The proposed 50 kt magnetized ICAL detector [43, 209] is designed to have 151 alternate layers of 5.6 cm thick iron plates (acting as target mass) and glass Resistive Plate Chambers (RPCs, acting as active detector elements). The plan is to have a modular structure for the detector with a dimension of 48 m (L)  $\times$  16 m (W)  $\times$  14.5 m (H), subdivided into 3 modules, each having a dimension of 16 m  $\times$  16 m  $\times$  14.5 m. The field strength of the magnetized iron plates will be around 1.5 T, with fields greater than 1 T over at least 85% of the detector volume [200]. Bending of charged particles in this magnetic field helps us to identify the charges of  $\mu^-$  and  $\mu^+$  which are produced in the charged current interactions of  $\nu_\mu$  and  $\bar{\nu}_\mu$  inside the detector. This magnetic field inside the detector is best suited to observe muons having energy in multi-GeV range, measure their charges, and reconstruct their momentum with high precision [202]. The capabilities of ICAL to measure three flavor oscillation parameters based on the information coming from muon energy ( $E_\mu$ ) and direction ( $\cos \theta_\mu$ ) have already been explored in Refs. [47, 48]. Recently it has been demonstrated that the ICAL detector has the ability to detect hadron showers and extract information about hadron energy from them [204, 210]. The energy of hadron ( $E'_{\text{had}} = E_\nu - E_\mu$ ) can be calibrated using number of hits in the detector due to hadron showers [204]. In Ref. [49], it has been shown that the inclusion of reconstructed hadron energy ( $E'_{\text{had}}$ ) as third observable with two other observables  $E_\mu$  and  $\cos \theta_\mu$  in the analysis on event-by-event basis, the sensitivities of the ICAL detector in measuring the neutrino oscillation parameters and revealing the mass hierarchy are enhanced. In the next chapter, we study the sensitivity of the ICAL detector to search for neutrinos produced in dark matter annihilation or/and decay.

# 4 Galactic Diffuse Dark matter

## Contents

---

<b>4.1 Introduction and Motivation . . . . .</b>	<b>65</b>
<b>4.2 Discussions on dark matter. . . . .</b>	<b>67</b>
4.2.1 Dark matter density profile	67
4.2.2 Annihilation of dark matter	69
4.2.3 Decay of dark matter	71
<b>4.3 Key features of ICAL detector. . . . .</b>	<b>72</b>
<b>4.4 Event spectrum and rates . . . . .</b>	<b>73</b>
<b>4.5 Simulation method. . . . .</b>	<b>76</b>
<b>4.6 Results . . . . .</b>	<b>77</b>
4.6.1 Constraints on annihilation of dark Matter	77
4.6.2 Constraints on decay of dark matter	80
4.6.3 Comparison with other experiments	83
4.6.4 The constraints on DM-induced neutrino flux	85
<b>4.7 Summary . . . . .</b>	<b>86</b>

---

## 4.1 Introduction and Motivation

Plethora of attempts are being made in the intensity, energy, and cosmic frontiers to build up knowledge about the Universe. Recent observations by Planck satellite [211] confirm that the baryonic and unknown non-baryonic matter (dark matter) contribute  $\sim 4.8\%$  and  $\sim 26\%$  of the total energy density of the Universe respectively. The first indication for the existence of dark matter

(DM) in the Universe was made by the Swiss astronomer Fritz Zwicky [212]. This observation was put on a solid footing by Vera Rubin and her collaborators [213]. The astrophysical [214,215] and cosmological observations [216,217] confirm the existence of dark matter from the length scales of a few kpc to a few Gpc.

All the astrophysical evidences of dark matter are through its gravitational interactions. The non-gravitational particle physics properties of DM particles are completely unknown. The relic abundance of cold dark matter (CDM) in the Universe is matched assuming a  $\sim 100$  GeV dark matter particle with electro-weak coupling strength. This class of particles is known as Weakly Interacting Massive Particle (WIMP) [218–220]. Supersymmetry, one of the most favored beyond-the-Standard Model theories, also predicts more than one dark matter candidates including the WIMP [221].

There are three types of detection methods for the search of DM: **(i) Direct detection:** DM particles are detected by observing recoiled nuclei from the scattering of DM particles in the laboratory. Experiments such as DAMA/LIBRA [222], LUX [223], CDMS [224], XENON [225], DarkSide [226], and PandaX [227] pursue this strategy. **(ii) Indirect detection:** It is possible that DM particles can decay and/or annihilate to any of the Standard Model (SM) particles like  $\nu\bar{\nu}$ ,  $t\bar{t}$ ,  $b\bar{b}$  etc. An excess (over standard astrophysical backgrounds) of these SM particles can be searched for to understand dark matter. The unstable SM particles decay to produce neutrinos and photons which can be searched for indirect detection. The prospects of dark matter searches through neutrino portal have been studied in the literature [228–242]. Fermi-LAT presents the analysis of its collected data of gamma rays having the energy in the range of 200 MeV to 500 GeV from Galactic halo in 5.8 years in Ref. [243]. Multiwavelength searches for dark matter have complementary reach [244]. Our focus in this work is on the indirect detection of dark matter via neutrinos and antineutrinos. **(iii) Collider searches:** The searches for supersymmetric DM candidates are carried out in LHC [245–247].

In this chapter, we study the indirect searches of dark matter using the 50 kt Magnetized Iron CALorimeter (MagICAL<sup>1</sup>) detector. We explore the sensitivity of the MagICAL detector to detect the neutrino and antineutrino events coming from the diffuse dark matter annihilation/decay in

---

<sup>1</sup>The “MagICAL” name is used here as the abbreviation of Magnetized Iron CALorimeter which is commonly known as ICAL detector. We prefer the name MagICAL to emphasize that magnetic field is present in the ICAL detector, which enables us to separate neutrino and anti-neutrino events.

the Milky Way galaxy. We present the expected constraint on the self-annihilation cross-section ( $\langle\sigma v\rangle$ ) and the decay lifetime ( $\tau$ ) of diffuse dark matter having mass in the range [2, 90] GeV and [4, 180] GeV respectively using an exposure of 500 kt·yr of the MagICAL detector.

We describe the dark matter density profile and the calculation of annihilation and decay rates of dark matter in Sec. 4.2. The key features of the MagICAL detector is presented in Sec. 4.3. Sec. 4.4 deals with the expected event distribution of atmospheric and DM induced neutrinos in the MagICAL detector. We present the simulation method in Sec. 4.5. The prospective limits on the self-annihilation cross-section and decay lifetime of dark matter are presented in Sec. 4.6. We compare our results with the existing bounds from other experiments. We also study the flux upper limit due to dark matter induced neutrinos in the MagICAL detector. We conclude in Sec. 4.7.

## 4.2 Discussions on dark matter

### 4.2.1 Dark matter density profile

The general parameterization of a spherically symmetric dark matter density profile is given by

$$\rho(r) = \frac{\rho_0}{[\delta + r/r_s]^\gamma \cdot [1 + (r/r_s)^\alpha]^{(\beta-\gamma)/\alpha}}. \quad (4.2.1)$$

The density,  $\rho(r)$ , is expressed in  $\text{GeV cm}^{-3}$  and  $r$  is the distance from the center of the galaxy in kpc. The parameter,  $r_s$ , is the scale radius in kpc. The shape of the outer profile is controlled by  $\alpha$  and  $\beta$ , whereas  $\gamma$  parametrizes the slope of the inner profile. The dark matter density at the Solar radius ( $R_{sc}$ ) is denoted by  $\rho_{sc}$ . We assume  $R_{sc} = 8.5$  kpc [248]. The normalization constant,  $\rho_0$ , and all the results are calculated using the values of parameters as given in Tab. 4.1.

Numerical simulations which involve only dark matter particles predict a cuspy profile [249–252]. Although these simulations reproduce the large-scale structure of the Universe, yet this prescription has challenges at scales below the size of a typical galaxy. It has been proposed that the addition of baryons can solve all of these small scale issues, although the results vary [253–261]. Present observations are not yet precise enough to distinguish between a cored and a cuspy profile [262].

To take this DM halo uncertainty into account, we generate all the results with two different DM profiles: Navarro Frenk White (NFW) profile [249], which represents cuspy halos, and the Burkert profile [263], which represents cored halos. The values of different parameters associated with these profiles are taken from Ref. [264]. In Fig. 4.1(a), we plot the NFW and Burkert dark matter density profiles with distance  $r$  from the center of the Milky Way galaxy by the black solid and green dashed lines respectively.

For conservativeness, we do not consider the effects of dark matter substructure. Depending on the value of the minimum halo mass and other astrophysical uncertainties, this can give a substantial contribution to the signal discussed here [265–270].

	$(\alpha, \beta, \gamma, \delta)$	$\rho_{sc}$ [GeV cm <sup>-3</sup> ]	$r_s$ [kpc]
NFW	(1, 3, 1, 0)	0.471	16.1
Burkert	(2, 3, 1, 1)	0.487	9.26

**Table 4.1.** The value of parameters associated with the NFW and Burkert profiles are listed here. They are same as in Ref. [264].

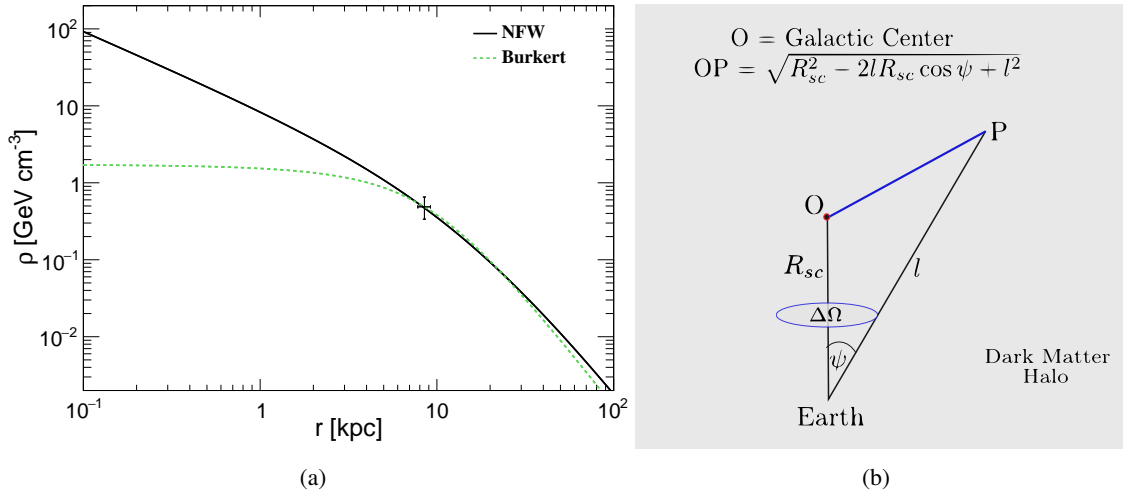


**Figure 4.1.** (a) Distribution of the dark matter density in the Milky Way galaxy for the NFW (black solid line) and Burkert profiles (green dashed line). The observational bounds on local dark matter density ( $\rho_{sc}$ ) and the solar radius ( $R_{sc}$ ) and their  $2\sigma$  uncertainties are indicated [214, 264]. (b) A schematic diagram of some part of the Milky Way dark matter halo. The Galactic center (GC) is denoted by O and  $R_{sc}$  is the distance between the Earth and the GC. The parameter  $l$  is the distance between point P and the Earth. The angle made at the Earth by points P and O and the corresponding solid angle are denoted by  $\psi$  and  $\Delta\Omega$  respectively.

In Fig. 4.1(b), a schematic diagram of a small portion of the Milky Way DM halo is shown with O as the Galactic center (GC). The dark matter density at point P with its distance  $l$  from the Earth



is a function of the length  $OP = \sqrt{R_{sc}^2 - 2lR_{sc} \cos \psi + l^2}$ . The angle made at the Earth by points P and O is  $\psi$  and the corresponding solid angle is  $\Delta\Omega$ .

### 4.2.2 Annihilation of dark matter

We consider the annihilation between a dark matter particle ( $\chi$ ) and its antiparticle ( $\bar{\chi}$ ) to produce a neutrino and an antineutrino in the final state with 100% branching ratio:

$$\chi + \bar{\chi} \rightarrow \nu + \bar{\nu}. \quad (4.2.2)$$

The neutrinos and antineutrinos of  $e$ ,  $\mu$ , and  $\tau$  flavors are assumed to be produced in 1:1:1 ratio at source. This ratio remains the same on arrival at the Earth surface after propagation through astrophysical distances (see Appendix A).

The number of  $\nu/\bar{\nu}$  from a direction  $\psi$  due to the annihilation of dark matter particles is proportional to the line of sight integration of the square of dark matter density:

$$\mathcal{J}^{ann}(\psi) = \frac{1}{R_{sc}\rho_{sc}^2} \int_0^{l_{max}} dl \rho^2 \left( \sqrt{R_{sc}^2 - 2lR_{sc} \cos \psi + l^2} \right). \quad (4.2.3)$$

The factor  $\frac{1}{R_{sc}\rho_{sc}^2}$  is included to make  $\mathcal{J}^{ann}(\psi)$  dimensionless. The upper limit  $l_{max}$  is the distance between the observer and the farthest point (denoted by P') in the Milky Way halo at the angle  $\psi$ . The radius of Milky Way galaxy is  $R_{MW}$  ( $= OP' = 100$  kpc), and thus

$$l_{max} = \sqrt{(R_{MW}^2 - R_{sc}^2 \sin^2 \psi)} + R_{sc} \cos \psi. \quad (4.2.4)$$

An increase of  $R_{MW}$  to 150 kpc enhances the value of  $\mathcal{J}^{ann}(\psi = 180^\circ)$  by 0.03%. The average value of  $\mathcal{J}^{ann}(\psi)$  over a solid angle  $2\pi \int_0^\psi \sin \psi' d\psi' = 2\pi(1 - \cos \psi)$  is

$$\mathcal{J}_{\Delta\Omega}^{ann}(\psi) = \frac{1}{2\pi(1 - \cos \psi)} \int_{\cos \psi}^1 2\pi d(\cos \psi') \mathcal{J}^{ann}(\psi'). \quad (4.2.5)$$

The variations of  $\mathcal{J}^{ann}(\psi)$  and  $\mathcal{J}_{\Delta\Omega}^{ann}(\psi)$  with angle  $\psi$  are shown by the black solid (green dashed) lines in left and right panels of Fig. 4.2 respectively using the NFW (Burkert) DM halo profile.

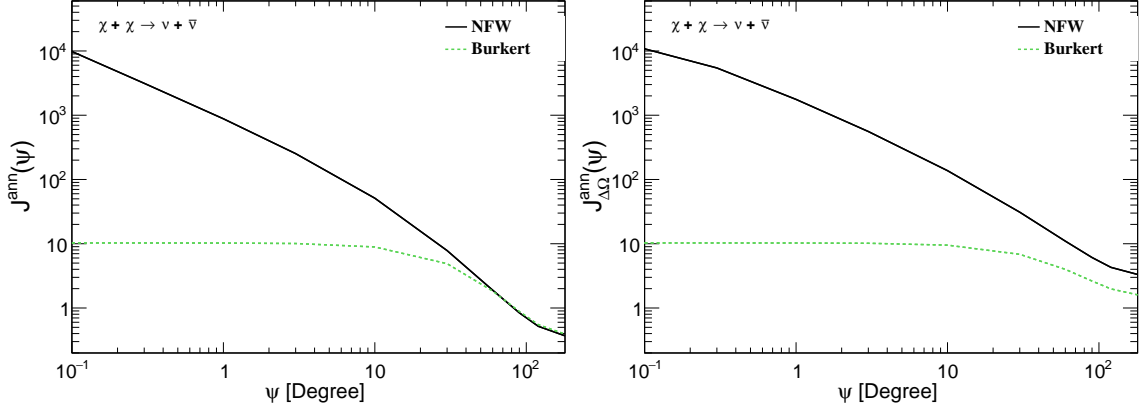


**Figure 4.2.** The value of  $\mathcal{J}^{ann}(\psi)$  (see Eq. 4.2.3) and its average ( $\mathcal{J}_{\Delta\Omega}^{ann}(\psi)$ ) over solid angle  $\Delta\Omega = 2\pi(1 - \cos\psi)$  (see Eq. 4.2.5) are shown in left and right panels. In both the panels, black solid and green dashed lines present the corresponding quantities for the NFW and Burkert profiles respectively. We use  $\mathcal{J}_{\Delta\Omega}^{ann}(\psi = 180^\circ)$  for the diffuse dark matter analysis, which has values 3.33 and 1.6 for the NFW and Burkert profiles respectively.

The value of  $\mathcal{J}_{\Delta\Omega}^{ann} = 3.33$  for the NFW profile and  $\mathcal{J}_{\Delta\Omega}^{ann} = 1.6$  for the Burkert profile with  $\Delta\Omega = 4\pi$ . The flux of each flavor of  $\nu/\bar{\nu}$  per unit energy range per unit solid angle (in units of  $\text{GeV}^{-1} \text{sr}^{-1} \text{cm}^{-2} \text{s}^{-1}$ ) produced in the final state of dark matter particle annihilation is given by

$$\frac{d^2\Phi_{\nu/\bar{\nu}}^{ann}}{dE d\Omega} = \frac{\langle\sigma_A v\rangle}{2} \mathcal{J}_{\Delta\Omega}^{ann} \frac{R_{sc}\rho_{sc}^2}{4\pi m_\chi^2} \frac{1}{3} \frac{dN^{ann}}{dE}, \quad (4.2.6)$$

where  $\langle\sigma_A v\rangle$  is the self-annihilation cross-section in units of  $\text{cm}^3 \text{s}^{-1}$ . The factor  $\frac{1}{2}$  is included as we assume that the dark matter particle is same as its own antiparticle. The factor  $\frac{1}{3}$  takes into account the flavor ratio of  $\nu/\bar{\nu}$  on the Earth's surface. The probability of  $\nu_e$ ,  $\nu_\mu$ , and  $\nu_\tau$  to be produced in the final state are the same. Therefore, the flux of  $\nu/\bar{\nu}$  with each lepton flavor is calculated as the total  $\nu/\bar{\nu}$  flux divided by the total number of lepton generations, which gives rise to the  $\frac{1}{3}$  factor in Eq. 4.2.6. The factor  $4\pi$  in the denominator is for the isotropic production of  $\nu\bar{\nu}$  in annihilation of dark matter. The parameter  $m_\chi$  is mass of the DM particles in units of GeV. The energy spectrum of  $\nu/\bar{\nu}$  is given by

$$\frac{dN^{ann}}{dE} = \delta(E_{\nu/\bar{\nu}} - m_\chi), \quad (4.2.7)$$

since dark matter particles in our galaxy are non-relativistic (local velocity  $\sim 10^{-3}c$ ).

### 4.2.3 Decay of dark matter

A dark matter particle is assumed to decay into  $\nu_e + \bar{\nu}_e$ ,  $\nu_\mu + \bar{\nu}_\mu$ , and  $\nu_\tau + \bar{\nu}_\tau$  with equal branching ratio:

$$\chi \rightarrow \nu + \bar{\nu}. \quad (4.2.8)$$

The  $\nu/\bar{\nu}$  flux from dark matter decay is proportional to the line of sight integral of the dark matter distribution,  $\mathcal{J}^{dec}(\psi)$ , with

$$\mathcal{J}^{dec}(\psi) = \frac{1}{R_{sc}\rho_{sc}} \int_0^{l_{max}} dl \rho \left( \sqrt{R_{sc}^2 - 2lR_{sc} \cos \psi + l^2} \right). \quad (4.2.9)$$

The quantity  $R_{sc}\rho_{sc}$  in the denominator makes  $\mathcal{J}^{dec}(\psi)$  dimensionless. All other symbols have same meaning as before. The quantity  $\mathcal{J}_{\Delta\Omega}^{dec}(\psi)$  represents the average value of  $\mathcal{J}^{dec}(\psi)$  over the solid angle  $\Delta\Omega = 2\pi(1 - \cos \psi)$ :

$$\mathcal{J}_{\Delta\Omega}^{dec}(\psi) = \frac{1}{2\pi(1 - \cos \psi)} \int_{\cos \psi}^1 2\pi d(\cos \psi') \mathcal{J}^{dec}(\psi'). \quad (4.2.10)$$

For the decaying dark matter,  $\mathcal{J}^{dec}(\psi)$  and  $\mathcal{J}_{\Delta\Omega}^{dec}(\psi)$  are shown in left and right panels of Fig. 4.3

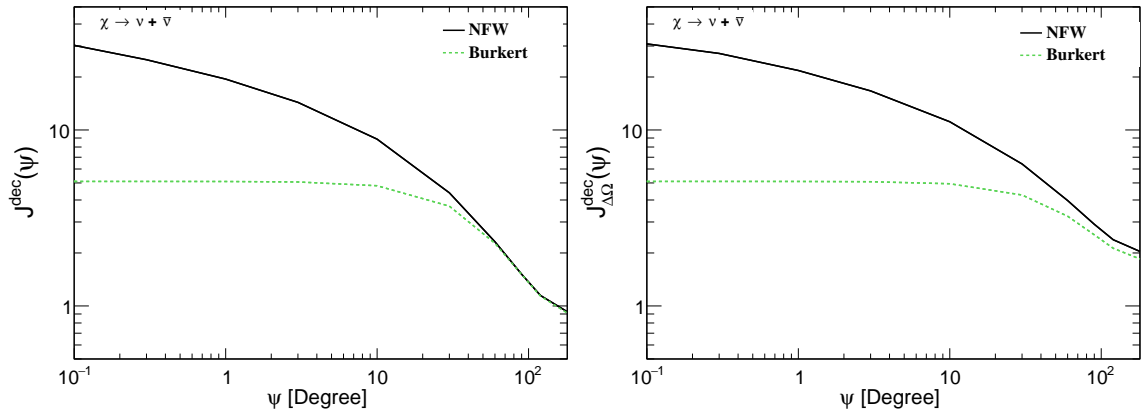


**Figure 4.3.** Line of sight integral for dark matter decay,  $\mathcal{J}^{dec}(\psi)$ , (see Eq. 4.2.9) vs.  $\psi$  and the average value of  $\mathcal{J}^{dec}(\psi)$  over solid angle  $\Delta\Omega$ , i.e.,  $\mathcal{J}_{\Delta\Omega}^{dec}(\psi)$  (see Eq. 4.2.10) for the decay process are shown in left and right panels respectively. In both the panels black solid and green dashed lines present the corresponding quantities for the NFW and the Burkert profiles respectively. We use the value of  $\mathcal{J}_{\Delta\Omega}^{dec}(\psi = 180^\circ)$  in our analysis, which are given by 2.04 and 1.85 for the NFW and Burkert profiles respectively.

respectively by the black solid (green dashed) lines using the NFW (Burkert) profile. We obtain

$\mathcal{J}_{\Delta\Omega}^{dec}(\psi = 180^\circ) = 2.04$  and  $1.85$  for the NFW and Burkert profile respectively. These agree with those presented in Ref. [271] up to uncertainties in the dark matter profile parameters.

The flux of neutrinos of each flavor per unit energy per unit solid angle in units of  $\text{GeV}^{-1}\text{sr}^{-1}\text{cm}^{-2}\text{s}^{-1}$  from the decay of dark matter particle is given by

$$\frac{d^2\Phi_{\nu/\bar{\nu}}^{dec}}{dE d\Omega} = \mathcal{J}_{\Delta\Omega}^{dec} \frac{R_{sc}\rho_{sc}}{4\pi m_\chi \tau} \frac{1}{3} \frac{dN^{dec}}{dE}, \quad (4.2.11)$$

where  $m_\chi$  is the mass of DM particle ( $\chi$ ) in GeV, and  $\tau$  is the decay lifetime of  $\chi$  in second. The factor  $\frac{1}{3}$  accounts for the averaging over total number of lepton flavors and  $4\pi$  implies isotropic decay. The mass of dark matter is shared by final  $\nu$  and  $\bar{\nu}$ , and thus, their energy spectrum can be written as

$$\frac{dN^{dec}}{dE} = \delta(E_{\nu/\bar{\nu}} - m_\chi/2). \quad (4.2.12)$$

### 4.3 Key features of ICAL detector

Energy resolution ( $\sigma_E$ ) (GeV)	$0.1 \times (E/\text{GeV})$
Angular resolution ( $\Delta\theta$ )	$10^\circ$
Detection efficiency ( $\mathcal{E}$ )	80%
CID efficiency ( $\mathcal{C}$ )	90%

**Table 4.2.** The detector characteristics used in the simulations. We use the same detector properties for  $\mu^-$  and  $\mu^+$  events.

In this phenomenological study, we explore the physics reach of MagICAL to see the signatures of Galactic diffuse dark matter through neutrino portal using the neutrino energy ( $E_\nu$ ) and zenith angle ( $\cos\theta_\nu$ ) as reconstructed variables. We consider reconstructed neutrino energy threshold to be 1 GeV for both  $\mu^-$  and  $\mu^+$  events. The energy resolution of the MagICAL detector is expected to be quite good, and we assume that the neutrino energy will be reconstructed with a Gaussian energy resolution of 10% of  $E/\text{GeV}$  (see Table 4.2). As far as the angular resolution is concerned, we use a constant angular resolution of  $10^\circ$ . For  $\mu^\pm$  events, the constant detection efficiency is 80%, and the constant charge identification (CID) efficiency is 90%. The detector properties that we use in our simulation agree quite well with the detector characteristics that have been considered in the existing phenomenological studies related to the MagICAL detector. For example see Refs.

[272–275]. We have checked that the representative choices of energy and angular resolutions of  $\nu_\mu$  and  $\bar{\nu}_\mu$  that we consider in this work can produce similar results for oscillation studies as obtained by the INO simulation code using muon momentum as variable. In this work, we assume that the 50 kt MagICAL detector will collect atmospheric neutrino data for 10 years giving rise to a total exposure of 500 kt-yr.

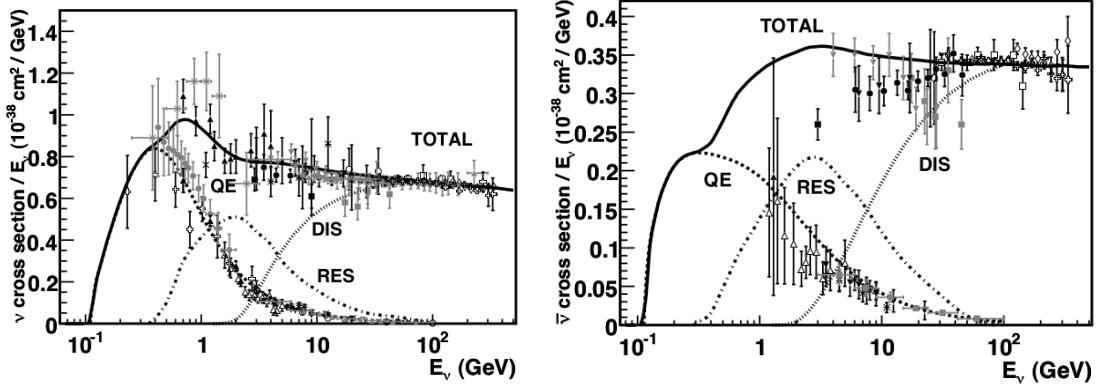


**Figure 4.4.** Total per nucleon charged current cross-section for neutrino (left panel) and antineutrino (right panel) as a function of neutrino energy. These cross-sections are for an isoscalar target. These plots are taken from Ref. [276]. Note that the y-axis ranges in left and right panels are different.

## 4.4 Event spectrum and rates

In this section, we present the expected event spectra and total event rates at the MagICAL detector. To estimate the number of expected  $\mu^-$  events<sup>2</sup> from atmospheric  $\nu_\mu$  and  $\bar{\nu}_\mu$ <sup>3</sup> in the  $i$ -th energy bin and  $j$ -th zenith bin at the MagICAL detector, we use the following expression [277],

$$\begin{aligned}
 N_{ij}^{atm}(\mu^-) = & 2\pi N_t \mathcal{T} \int_{E_{min}^i}^{E_{max}^i} dE' \int_{\cos \theta_{min}^j}^{\cos \theta_{max}^j} d(\cos \theta') \int_{-1}^1 d(\cos \theta) \int_0^\infty dE R(E, E') \\
 & R(\theta, \theta') \left[ \sigma_{\nu_\mu}^{CC}(E) \mathcal{E} C \left\{ \frac{d^2 \Phi_{\nu_\mu}}{d \cos \theta dE} P_{\mu\mu} + \frac{d^2 \Phi_{\nu_e}}{d \cos \theta dE} P_{e\mu} \right\} + \right. \\
 & \left. \bar{\sigma}_{\nu_\mu}^{CC}(E) \bar{\mathcal{E}} (1 - \bar{C}) \left\{ \frac{d^2 \bar{\Phi}_{\nu_\mu}}{d \cos \theta dE} \bar{P}_{\mu\mu} + \frac{d^2 \bar{\Phi}_{\nu_e}}{d \cos \theta dE} \bar{P}_{e\mu} \right\} \right]. \quad (4.4.1)
 \end{aligned}$$

In the above equation,  $\mathcal{T}$  is the total running time in second, and  $N_t$  is the total number of target nucleons in the detector. The quantities  $E$  ( $E'$ ) and  $\theta$  ( $\theta'$ ) are the true (reconstructed) neutrino

<sup>2</sup>The number of  $\mu^+$  events from atmospheric neutrinos can be estimated using Eq. 4.4.1 by considering appropriate flux, oscillation probability, cross-section, and detector properties.

<sup>3</sup>Atmospheric muon antineutrino flux gives rise to  $\mu^+$  events in the detector, which can be misidentified as  $\mu^-$  events.

energy and zenith angle respectively. For  $\mu^-$  ( $\mu^+$ ) events,  $\sigma_{\nu_\mu}^{CC}$  ( $\bar{\sigma}_{\nu_\mu}^{CC}$ ) is the total neutrino (antineutrino) per nucleon CC cross-section as shown in left (right) panel of Fig. 4.4. These cross-sections have been taken from Fig. 9 of Ref. [276]. We take the unoscillated atmospheric  $\nu_\mu$  and  $\nu_e$  fluxes estimated for the INO site in units of  $\text{m}^{-2}\text{s}^{-1}\text{GeV}^{-1} \text{sr}^{-1}$  from Ref. [88, 278]. The probability of a  $\nu_\mu$  ( $\nu_e$ ) to survive (appear) as  $\nu_\mu$  is denoted by  $P_{\mu\mu}$  ( $P_{e\mu}$ ). The parameters  $\mathcal{E}$  ( $\bar{\mathcal{E}}$ ) and  $C$  ( $\bar{C}$ ) are the detection and charge identification efficiencies respectively for  $\mu^-$  ( $\mu^+$ ) events. The quantities  $R(E, E')$  and  $R(\theta, \theta')$  are the Gaussian energy and angular resolution functions of the detector, which are expressed in the following way,

$$R(E, E') = \frac{1}{\sigma_E \sqrt{2\pi}} \exp\left\{-\frac{(E' - E)^2}{2\sigma_E^2}\right\}, \quad (4.4.2)$$

and

$$R(\theta, \theta') = \frac{1}{\sigma_\theta \sqrt{2\pi}} \exp\left\{-\frac{(\cos \theta' - \cos \theta)^2}{2\sigma_\theta^2}\right\}. \quad (4.4.3)$$

The parameters  $\sigma_E$  and  $\sigma_\theta$  ( $\sin \theta \Delta\theta$ ) denote the energy and angular resolutions as given in Table 4.2.

Observables	Range	Width	Total bins
$E_\nu$ (GeV)	1, 15	1	14
	15, 25	2	5
	25, 50	5	5
	50, 100	10	5
$\cos \theta_\nu$	-1, 1	0.5	4

**Table 4.3.** The binning scheme adopted for the reconstructed  $E_\nu$  and  $\cos \theta_\nu$  for each muon polarity. The last column depicts the total number of bins considered for each observable.

We can estimate the  $\mu^-$  events in the  $i$ -th energy bin and  $j$ -th angular bin from the dark matter induced neutrinos and antineutrinos by making suitable changes in Eq. 4.4.1 in the following fashion,

$$N_{ij}^{dm}(\mu^-) = 2\pi N_t \mathcal{T} \int_{E_{min}^i}^{E_{max}^i} dE' \int_{\cos \theta_{min}^j}^{\cos \theta_{max}^j} d(\cos \theta') \int_{-1}^1 d(\cos \theta) \int_0^\infty dE R(E, E') R(\theta, \theta') \frac{d^2 \Phi^{dm}}{d \cos \theta dE} \left[ \sigma_{\nu_\mu}^{CC}(E) \mathcal{E} C \left\{ P_{e\mu} + P_{\mu\mu} + P_{\tau\mu} \right\} + \bar{\sigma}_{\nu_\mu}^{CC}(E) \bar{\mathcal{E}} (1 - \bar{C}) \left\{ \bar{P}_{e\mu} + \bar{P}_{\mu\mu} + \bar{P}_{\tau\mu} \right\} \right]. \quad (4.4.4)$$

In case of dark matter annihilation and decay, we have fluxes of  $\nu_\tau$  and  $\bar{\nu}_\tau$  along with the fluxes of  $\nu_e$ ,  $\bar{\nu}_e$ ,  $\nu_\mu$ , and  $\bar{\nu}_\mu$ . The dark matter induced neutrino and antineutrino fluxes<sup>4</sup> for each flavor are estimated using Eqs. 4.2.6 and 4.2.11 for annihilation and decay processes respectively. In the above equation, the probability of  $\nu_\tau$  ( $\bar{\nu}_\tau$ ) to appear as  $\nu_\mu$  ( $\bar{\nu}_\mu$ ) at the detector is expressed by  $P_{\tau\mu}$  ( $\bar{P}_{\tau\mu}$ ). All the other symbols signify the same parameters as described in Eq. 4.4.1. In our analysis, we take  $\delta_{\text{CP}} = 0^\circ$  and therefore, we can write  $P_{\alpha\beta} = P_{\beta\alpha}$  and  $\bar{P}_{\alpha\beta} = \bar{P}_{\beta\alpha}$ . Due to these properties and unitary nature of the PMNS matrix  $U$  [144, 145, 153], the sums of oscillation probabilities for neutrino and antineutrino in above equation become 1. Therefore,  $\nu_\mu$  and  $\bar{\nu}_\mu$  event rates due to the dark matter annihilation/decay do not depend on the values of oscillation parameters.

In our simulation, the full three flavor neutrino oscillation probabilities are incorporated using the PREM profile for the Earth matter density [158]. The choices of central values of the oscillation parameters that are used in our simulation lie within the  $1\sigma$  range of these parameters as obtained from the recent global fit studies [14, 16, 279]. We produce all the results in this chapter using the following benchmark values of oscillation parameters:  $\sin^2 \theta_{23} = 0.5$ ,  $\sin^2 2\theta_{13} = 0.085$ ,  $\Delta m_{\text{eff}}^2 = \pm 2.4 \times 10^{-3} \text{ eV}^2$ ,  $\sin^2 2\theta_{12} = 0.84$ ,  $\Delta m_{21}^2 = 7.5 \times 10^{-5} \text{ eV}^2$ , and  $\delta_{\text{CP}} = 0^\circ$ . The (+) and (-) signs of  $\Delta m_{\text{eff}}^2$ <sup>5</sup> correspond to normal ordering (NO) and inverted ordering (IO) respectively. In fit, we keep the values of oscillation parameters and the choice of mass ordering fixed.

In this analysis, we binned the  $\nu$  and  $\bar{\nu}$  data separately using reconstructed observables  $E_\nu$  and  $\cos \theta_\nu$  as described in Table 4.3. There are total 29  $E_\nu$  bins in the range of  $E_\nu = [1, 100] \text{ GeV}$ . The bins of  $E_\nu$  are chosen uneven to ensure that they are consistent with the energy resolution of the detector at various energy ranges. The isotropic nature of the signal allows us to take coarser binning in  $\cos \theta_\nu$ , and we take four  $\cos \theta_\nu$  bins of equal size in the range  $[-1, 1]$ . We use comparatively finer bins for reconstructed  $E_\nu$  because the signal has a strong dependency on energy of neutrino. We adopt an optimized binning scheme so that we have at least 2 events in each bin. The total number of bins used in our analysis is  $29 \times 4 = 116$ . We show the signal and background event distribution plots as a function of reconstructed neutrino energy for various  $\cos \theta_\nu$  ranges in Sec. 4.6 (see Figs. 4.5 and 4.7).

<sup>4</sup>The amount of  $\nu_e$ ,  $\bar{\nu}_e$ ,  $\nu_\mu$ ,  $\bar{\nu}_\mu$ ,  $\nu_\tau$ , and  $\bar{\nu}_\tau$  fluxes from dark matter are same.

<sup>5</sup>The effective mass-squared difference,  $\Delta m_{\text{eff}}^2$ , is related to  $\Delta m_{31}^2$  and  $\Delta m_{21}^2$  through the expression [207, 208]:

$$\Delta m_{\text{eff}}^2 = \Delta m_{31}^2 - \Delta m_{21}^2 (\cos^2 \theta_{12} - \cos \delta_{\text{CP}} \sin \theta_{13} \sin 2\theta_{12} \tan \theta_{23}). \quad (4.4.5)$$

## 4.5 Simulation method

In our analysis, we consider the dark matter induced neutrinos as signal and treat atmospheric neutrinos as background. If  $N_{ij}^{atm}$  and  $N_{ij}^{dm}$  denote the number of  $\mu^-$  events produced from the interactions of atmospheric  $\nu_\mu$  and dark matter induced  $\nu_\mu$  respectively in the  $i$ -th energy and  $j$ -th angular bin (see Eqs. 4.4.1 and 4.4.4), then the Poissonian  $\chi^2$  [4] can be written as

$$\chi^2(\mu^-) = \min_{\zeta_{atm}, \zeta_{dm}} \sum_{i=1}^{N_{E_\nu}} \sum_{j=1}^{N_{\cos\theta_\nu}} 2 \left[ N_{ij}^{th}(\mu^-) - N_{ij}^{exp}(\mu^-) - N_{ij}^{exp}(\mu^-) \ln \frac{N_{ij}^{th}(\mu^-)}{N_{ij}^{exp}(\mu^-)} \right] + \zeta_{atm}^2 + \zeta_{dm}^2. \quad (4.5.1)$$

In the above equation,  $N_{ij}^{exp} = N_{ij}^{atm}$  and  $N_{ij}^{th} = N_{ij}^{atm} (1 + \pi_{atm} \zeta_{atm}) + N_{ij}^{dm} (1 + \pi_{dm} \zeta_{dm})$  neglecting higher order terms. Here,  $N_{E_\nu} = 29$  and  $N_{\cos\theta_\nu} = 4$  as mentioned in Table 4.3. The quantities  $\pi_{dm}$  and  $\pi_{atm}$  in Eq. 4.5.1 are the overall normalization errors on signal and background respectively. We take  $\pi_{dm} = \pi_{atm}^6 = 20\%$ . The systematic uncertainties in this analysis are incorporated using the pull method [281–283]. The parameters  $\zeta_{dm}$  and  $\zeta_{atm}$  are the pull variables due to the systematic uncertainties on signal and background respectively, which are calculated in this analysis using Eq. C.0.10 as given in Appendix C. In our analysis, we find that the values of  $\zeta_{dm}$  and  $\zeta_{atm}$  lie within the range -1 to 1. Following the same procedure,  $\chi^2(\mu^+)$  for  $\mu^+$  events is obtained. We calculate the total  $\chi^2$  by adding the individual contributions from  $\mu^-$  and  $\mu^+$  events in the following way<sup>7</sup>

$$\chi_{\text{total}}^2 = \chi^2(\mu^-) + \chi^2(\mu^+). \quad (4.5.2)$$

We notice that our results remain unchanged if we consider larger uncertainties on the atmospheric neutrino events. The reason behind this is that for any choice of  $m_\chi$  we have many bins in terms of the reconstructed observables  $E_\nu$  and  $\cos\theta_\nu$ , which are not affected by the dark matter induced neutrinos. Therefore these bins can constrain the uncertainties on the atmospheric neutrino flux. On the other hand, we notice that if we take the larger uncertainties on the dark matter induced neutrino events, say 30%, our final results get modified by 2 to 3%. It is worthwhile to mention

<sup>6</sup>A major part of this error stems from the uncertainty on atmospheric neutrino flux. For a detailed discussion on the uncertainties of the atmospheric neutrino flux, see Ref. [280].

<sup>7</sup>Here, we would like to mention that though we assume same amount of normalization uncertainties for  $\mu^-$  and  $\mu^+$  events, we get different values of  $\zeta_{dm}$  and  $\zeta_{atm}$  for  $\mu^-$  and  $\mu^+$  channels.



that the maximum uncertainty on the signal stems from the dark matter density profile. Therefore, we give our results assuming two different profiles for the dark matter density which are the NFW and the Burkert.

As we have discussed in Sec. 4.4, the dark matter induced signal does not depend on the oscillation parameters as long as we take the CP-violating phase  $\delta_{\text{CP}} = 0^\circ$ . The dependency on the oscillation parameters in the results comes only through the atmospheric neutrino background. We produce all the results assuming normal ordering both in data and theory. We have checked that the results hardly change if we consider inverted ordering. One of the main reasons behind this is that due to our choice of coarser reconstructed  $\cos \theta_\nu$  bins, the information coming from the MSW effect [44–46, 284] in the atmospheric neutrino events gets smeared out substantially. Another reason is that since the dark matter induced neutrino signal appears only in 2 to 3  $E_\nu$  bins (see in Figs. 4.5 and 4.7),  $\chi^2$  is hardly affected due to the change in atmospheric neutrino background in these bins when we switch from NO to IO.

## 4.6 Results

### 4.6.1 Constraints on annihilation of dark Matter

In this section, we present the constraints on self-annihilation cross-section of dark matter ( $\chi\chi \rightarrow \nu\bar{\nu}$ ) which can be obtained by 500 kt-yr of MagICAL exposure. The background consists of conventional atmospheric neutrinos, and the signal consists of neutrinos coming from dark matter annihilation. The simulated event spectra as a function of reconstructed neutrino energy in 500 kt-yr exposure of MagICAL detector are presented in Fig. 4.5. The quantity in the y-axis of Fig. 4.5 is the number of events per unit energy range multiplied by the mid value in each energy bin. In each panel, the black solid line represents the event distribution of conventional atmospheric  $\nu_\mu$ , denoted by ATM. If DM particles of mass 30 GeV, for example, self-annihilate to  $\nu\bar{\nu}$  pairs, then each of these  $\nu$  and  $\bar{\nu}$  will have 30 GeV of energy. The total neutrino event spectra in MagICAL detector in presence of DM annihilation are shown by the red dotted lines (ATM + DM) in Fig. 4.5. The value of self-annihilation cross-section of dark matter for these plots is taken to be  $3.5 \times 10^{-23} \text{ cm}^3 \text{ s}^{-1}$ .

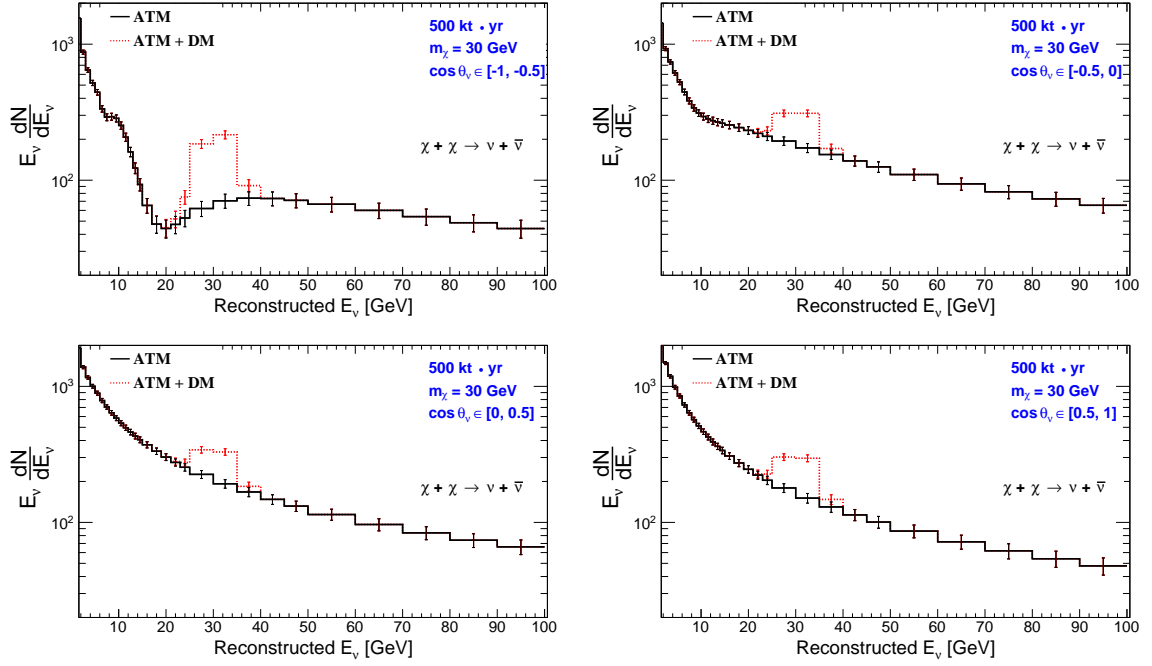


**Figure 4.5.** Event spectra of atmospheric  $\nu_\mu$  (denoted by ATM) are shown by the black solid lines. The predicted event distributions coming from atmospheric  $\nu_\mu$  and dark matter originated neutrino (ATM + DM) are shown in red dotted lines for different  $\cos\theta$  ranges using 500 kt·yr exposure of the MagICAL detector. The signal (DM) is coming from 30 GeV annihilating DM particles here. The mass ordering is taken as NO. The  $\chi\chi \rightarrow \nu\bar{\nu}$  cross-section is arbitrarily chosen to  $\langle\sigma v\rangle = 3.5 \times 10^{-23} \text{ cm}^3 \text{ s}^{-1}$  to have visual clarity.

An excess of  $\nu_\mu$  events due to dark matter annihilation appears over the ATM around reconstructed neutrino energy of 30 GeV. These events get distributed over nearby energy bins due to the finite energy resolution of the detector. The number of signal and atmospheric events in neutrino mode are 174 and 210 respectively in the energy range [25, 35] GeV and  $\cos\theta_\nu \in [-1, 1]$ . There are 4 panels: each represents the event distribution summed over different  $\cos\theta_\nu$  ranges. The figures in top panels portray the event spectra over  $\cos\theta_\nu \in [-1, -0.5]$  and  $[-0.5, 0.0]$  from left to right. These events are due to upward going neutrinos, which travel a long distance through the Earth matter before they reach the detector. Though in these panels, the signatures of neutrino flavor oscillation are seen in ATM spectra, but the imprints of the Earth matter effect are not visible due to the choice of our large  $\cos\theta_\nu$  bins. The energy distributions of downward going events are shown in bottom panels from left to right for  $\cos\theta_\nu \in [0.0, 0.5]$  and  $[0.5, 1.0]$  respectively. These neutrinos do not oscillate as they traverse a length smaller than the oscillation wavelength in multi-GeV range. The statistical error bars in these plots associated with different energy bins are equal to the square root of the number of events in the corresponding bins.

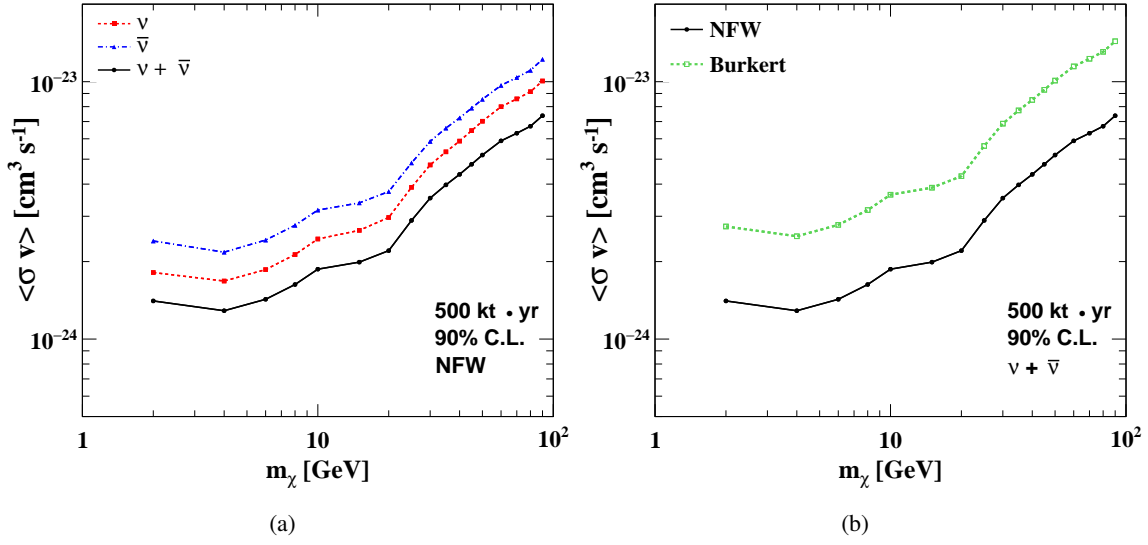


**Figure 4.6.** (a) The upper limit on self-annihilation cross-section of DM particle ( $\chi\chi \rightarrow \nu\bar{\nu}$ ) at 90% C.L. (1 d.o.f.) as a function of DM mass  $m_\chi$  using 500 kt·yr exposure of the MagICAL detector. The bound calculated with only  $\nu_\mu$  ( $\bar{\nu}_\mu$ )-induced events is shown with red dashed (blue dot-dashed) line as MagICAL can distinguish  $\nu_\mu$  from  $\bar{\nu}_\mu$ . The upper bound obtained by combining these two channels is also shown by the black solid line in the figure. We take the NFW as DM profile. (b) The upper bounds on the self-annihilation cross-section ( $\chi\chi \rightarrow \nu\bar{\nu}$ ) of dark matter are presented for the NFW (black solid) and Burkert (green dashed) profiles combining the information coming from  $\nu_\mu$  and  $\bar{\nu}_\mu$ . For both (a) and (b), the choice of mass ordering is NO.

The charge identification ability<sup>8</sup> of the MagICAL detector provides an opportunity to explore the same physics in neutrino and antineutrino channels separately. This is not possible in water Cherenkov, liquid scintillator, and liquid argon based detectors. The MagICAL detector will have separate data sets for  $\nu_\mu$  and  $\bar{\nu}_\mu$ . The total sensitivity is obtained by combining the  $\nu_\mu$  and  $\bar{\nu}_\mu$  data sets according to Eq. 4.5.2. We present results by using  $\nu_\mu$  and  $\bar{\nu}_\mu$  data separately, and then combining these two. The upper limits on self-annihilation cross-section ( $\langle\sigma v\rangle$ ) of DM particles for the process  $\chi\chi \rightarrow \nu\bar{\nu}$  at 90% C.L. (1 d.o.f.) that MagICAL will obtain with 10 years of data are represented in Fig. 4.6. The red dashed, blue dot-dashed, and the black solid lines in Fig. 4.6(a) represent the limits on  $\langle\sigma v\rangle$  from  $\nu_\mu$ ,  $\bar{\nu}_\mu$ , and the combination of  $\nu_\mu$  and  $\bar{\nu}_\mu$  data respectively using the NFW profile. Analysis with  $\nu_\mu$  gives tighter bound than  $\bar{\nu}_\mu$  because of the higher statistics of  $\nu_\mu$  over  $\bar{\nu}_\mu$ .

At higher energies, the atmospheric neutrino flux (background) decreases, and same happens to the signal coming from dark matter self annihilation because of its  $m_\chi^{-2}$  dependence (see Eq. 4.2.6).

<sup>8</sup>We have checked that  $\chi_\nu^2 + \chi_{\bar{\nu}}^2$  is better than  $\chi_{\nu+\bar{\nu}}^2$  by very little amount, which is around 2%. In our analysis, CID does not play an important role unlike in the case of mass ordering determination for the following reasons. First, the signal is independent of oscillation parameters and it appears only in two to three  $E_\nu$  bins. Secondly, the impact of the Earth matter effect in atmospheric  $\nu$  and  $\bar{\nu}$  events (background) gets reduced for our choices of large  $\cos\theta_\nu$  bins.

A competition between these two effects lowers the signal to background ratio for heavy dark matter particles. Thus, the bound on  $\langle\sigma v\rangle$  becomes weaker for heavy DM. We can have a rough estimate of how  $\langle\sigma v\rangle$  depends on  $m_\chi$  in the range say 4 to 8 GeV by mainly considering the energy dependence of flux and interaction cross-section in both signal and background. In this  $m_\chi$  range which also corresponds to neutrino energy range of 4 to 8 GeV, the atmospheric flux varies as  $\sim E_\nu^{-2.7}$ , whereas neutrinos flux from the annihilating DM goes as  $\langle\sigma v\rangle/m_\chi^2$ . For both signal and background, the neutrino-nucleon CC cross-section is approximately proportional to  $E_\nu$  or  $m_\chi$  in case of annihilation. Therefore, the neutrino signal from dark matter annihilation ( $S$ ) depends on  $m_\chi$  in the following way:  $S \propto \frac{\langle\sigma v\rangle}{m_\chi^2} \cdot m_\chi = \langle\sigma v\rangle/m_\chi$ . As far as background ( $B$ ) is concerned,  $B \propto m_\chi^{-2.7} \cdot m_\chi = m_\chi^{-1.7}$ . Hence, in case of annihilation,  $S/\sqrt{B} \propto \langle\sigma v\rangle \cdot m_\chi^{-0.15}$  or,  $\langle\sigma v\rangle \propto m_\chi^{0.15}$  if  $S/\sqrt{B}$  remains constant. From Fig. 4.6(a), we can see that at  $m_\chi = 4$  GeV, the limit on  $\langle\sigma v\rangle$  is  $1.2 \times 10^{-24} \text{ cm}^3 \text{ s}^{-1}$  in case of  $\nu + \bar{\nu}$  modes. Now, from our approximate expression as mentioned above, the limit on  $\langle\sigma v\rangle$  at  $m_\chi = 8$  GeV should be around  $1.2 \times 10^{-24} \times (8/4)^{0.15} \text{ cm}^3 \text{ s}^{-1} = 1.33 \times 10^{-24} \text{ cm}^3 \text{ s}^{-1}$ , which is indeed the case as can be seen from the black solid line in Fig. 4.6(a). If we want to do the same exercise for  $m_\chi < 4$  GeV, then the only change that we have to make is that the atmospheric neutrino flux varies as  $E_\nu^{-2}$  at those energies instead of  $E_\nu^{-2.7}$ . On the other hand, to explain the nature of the same curve for  $m_\chi$  above 8 GeV, we have to also take into account the effect of neutrino flavor oscillation and detector response which have nontrivial dependence on  $E_\nu$  whereas, the atmospheric neutrino flux still varies as  $E_\nu^{-2.7}$  in this energy range.

We compare the constraints with the NFW and the Burkert profiles by black solid and green dashed lines respectively in Fig. 4.6(b) combining the neutrino and antineutrino data. We obtain better sensitivity with the NFW profile than with the Burkert profile. The average value of  $\mathcal{J}$  factor over  $4\pi$  solid angle for the Burkert profile is smaller than that for the NFW profile. Thus, the signal strength with Burkert profile is smaller than that with the NFW profile. We have  $\mathcal{J}_{\Delta\Omega}^{ann} = 3.33$  and 1.60 for the NFW and Burkert profiles respectively with  $\Delta\Omega = 4\pi$ .

#### 4.6.2 Constraints on decay of dark matter

Assuming that dark matter particles have a mass of 30 GeV, and they decay to  $\nu\bar{\nu}$  pairs, then the energy that each  $\nu$  and  $\bar{\nu}$  carries is 15 GeV. These events give rise to an excess of  $\nu_\mu$  and  $\bar{\nu}_\mu$

events around reconstructed neutrino energy of 15 GeV on top of the atmospheric neutrino event distribution as shown in Fig. 4.7. The black solid lines represent the event distributions for the atmospheric neutrinos and the red dotted lines show event distributions for background along with the signal. The four panels in Fig. 4.7 correspond to different  $\cos \theta_\nu$  ranges as mentioned in the figure legends. Here, we assume the lifetime ( $\tau$ ) of dark matter to be  $4.7 \times 10^{24}$  s and we take 500 kt-yr exposure for the MagICAL detector. We can see from Fig. 4.7 that the events due to the decay of dark matter get distributed around 15 GeV due to the finite energy resolution of detector. In this case, the number of the signal and background events are 81 and 289 respectively in the reconstructed energy range [13, 17] GeV and  $\cos \theta_\nu \in [-1, 1]$ .

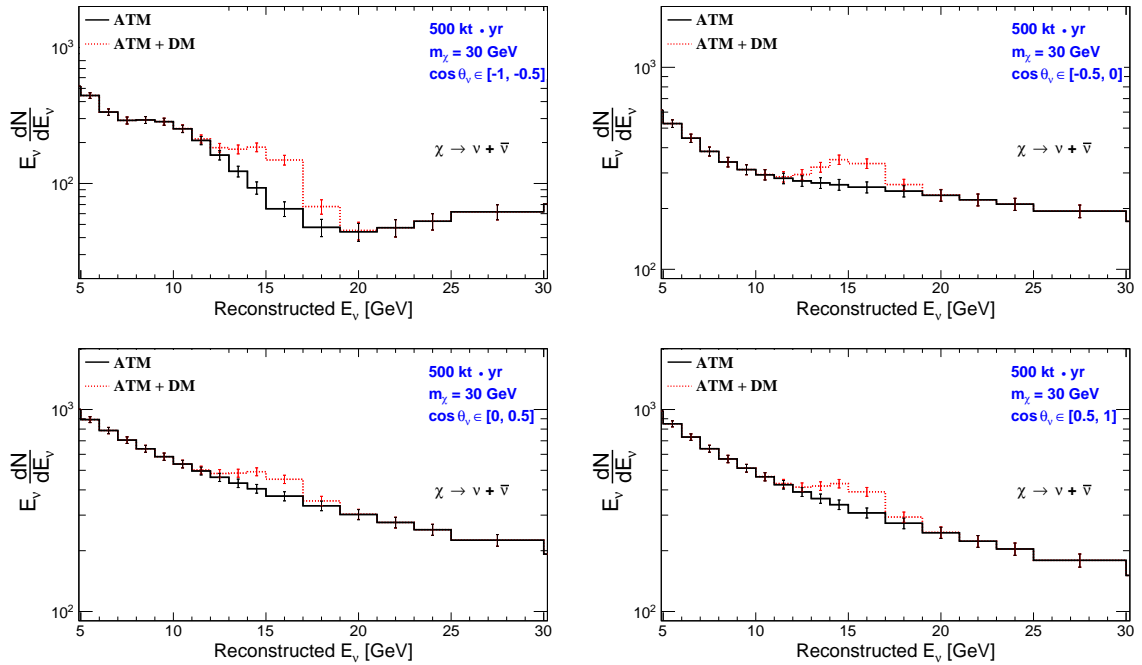


**Figure 4.7.** The event distribution of atmospheric  $\nu_\mu$  (denoted as ATM) and the predicted  $\nu_\mu$  event spectra in presence of decay of 30 GeV dark matter particles (denoted as ATM + DM) in different  $\cos \theta_\nu$  ranges using 500 kt-yr exposure of the MagICAL detector. Black solid (red dotted) line represents the ATM (ATM + DM). The mass ordering is taken as NO. The lifetime of dark matter is arbitrarily chosen ( $4.7 \times 10^{24}$  s) for sake of visual clarity.

The future sensitivity of the MagICAL detector to set a lower limit on the lifetime ( $\tau$ ) of dark matter as a function of  $m_\chi$  is shown in Fig. 4.8. We give the results at 90% C.L. (1 d.o.f.) assuming 500 kt-yr exposure of the proposed MagICAL detector. Here, we assume the dark matter density profile to be the NFW. The red dashed (blue dot-dashed) line in Fig. 4.8(a) represents the bound which we obtain using  $\nu_\mu$  ( $\bar{\nu}_\mu$ ) data set. The bound gets improved when we add the  $\nu_\mu$  and  $\bar{\nu}_\mu$  data

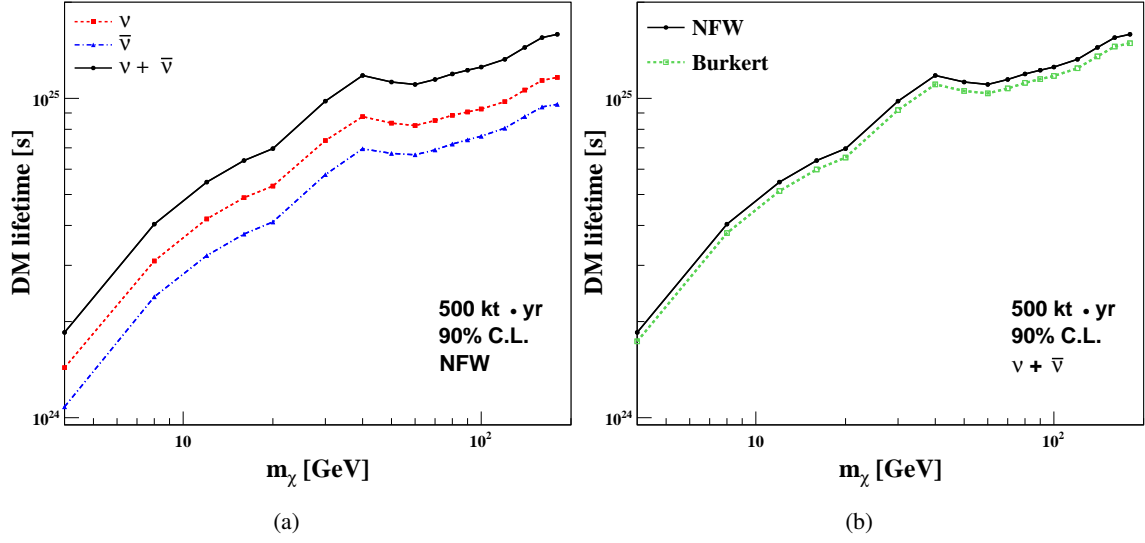


**Figure 4.8.** (a) The lower bound on the decay lifetime of dark matter ( $\chi \rightarrow \nu\bar{\nu}$ ) as a function of DM mass  $m_\chi$  at 90% C.L. (1 d.o.f.) obtained using only  $\nu_\mu$  and only  $\bar{\nu}_\mu$  data using 500 kt-yr exposure of MagICAL. The red dashed (blue dot-dashed) line shows the sensitivity coming from  $\nu_\mu$  ( $\bar{\nu}_\mu$ )-induced events. The black solid line represents the same combining  $\nu_\mu$  and  $\bar{\nu}_\mu$  events at  $\chi^2$  level. We take NO as mass ordering. (b) The constraints on the decay lifetime of dark matter ( $\chi \rightarrow \nu\bar{\nu}$ ) assuming the NFW (black solid line) and Burkert (green dashed line) profiles using 500 kt-yr of MagICAL exposure. Here the results are shown combining  $\nu$  and  $\bar{\nu}$  (see Sec. 4.5 for detail).

sets and the corresponding result is shown by the black solid line. Here, we see that the limits on the dark matter lifetime get improved when we consider higher  $m_\chi$ . It happens for the following reasons. The flux of neutrinos coming from the dark matter decay (signal) has a  $m_\chi^{-1}$  dependence (see Eq. 4.2.11) and the atmospheric neutrino flux (background) gets reduced substantially at higher energies. We find that in presence of these two competing effects, ultimately, the signal over background ratio gets improved for higher  $m_\chi$ , which allows us to place restrictive bounds on the lifetime of dark matter. In Fig. 4.8(a), we can explain how the limit on dark matter life time  $\tau$  depends on  $m_\chi$  in the range say  $8 \text{ GeV} \leq m_\chi \leq 16 \text{ GeV}$  by mainly taking into account the energy dependence of the flux and neutrino-nucleon CC cross-section in the same fashion which we adopt to explain the bound on  $\langle\sigma v\rangle$  in the previous section. The above range of  $m_\chi$  corresponds to the  $E_\nu$  range of 4 GeV to 8 GeV, since the neutrino energy from decaying DM is  $E_\nu = m_\chi/2$ . Here, the neutrino flux from decaying DM is proportional to  $\frac{1}{m_\chi \tau}$  (see Eq. 4.2.11). Thus, the neutrino signal ( $S$ ) from dark matter decay varies as  $S \propto \frac{1}{m_\chi \tau} \cdot m_\chi = 1/\tau$ , while the background varies with  $m_\chi$  in the same way as we see in case of annihilation which is  $B \propto m_\chi^{-1.7}$ . Hence, in case of decaying DM,  $S/\sqrt{B} \propto \frac{1}{\tau} \cdot m_\chi^{0.85}$  or,  $\tau \propto m_\chi^{0.85}$  for a fixed value of  $S/\sqrt{B}$ . From Fig 4.8(a), it can be seen that at  $m_\chi = 8 \text{ GeV}$ , the limit on  $\tau$  is  $4.0 \times 10^{24} \text{ s}$  combining  $\nu$  and  $\bar{\nu}$  modes. From

the simple  $m_\chi$  dependence of  $\tau$  that we discuss above, at 16 GeV, the limit on  $\tau$  should be around  $4.0 \times 10^{24} \times (16/8)^{0.85} \text{ s} = 7.21 \times 10^{24} \text{ s}$ , which is very close to the value as can be seen from the black solid line in Fig.4.8(a). To obtain the similar analytical understanding for  $m_\chi$  below 8 GeV, we need to make suitable changes in the energy dependence of atmospheric neutrino flux which we have already discussed in the previous section. Similarly, to see how  $\tau$  varies with  $m_\chi$  above 16 GeV, we have to also take into account the nontrivial energy dependence of neutrino flavor conversion and detector response along with flux and cross-section.

Due to the uncertainties in the dark matter density profiles, we present the bound on decay lifetime of dark matter with the profiles: NFW and Burkert by the black solid and green dashed line respectively in Fig.4.8(b). Ref. [53] considers only  $\mu^+\mu^-$  as final states for dark matter decay in the context of ICAL-INO, although their constraints are much weaker.

### 4.6.3 Comparison with other experiments

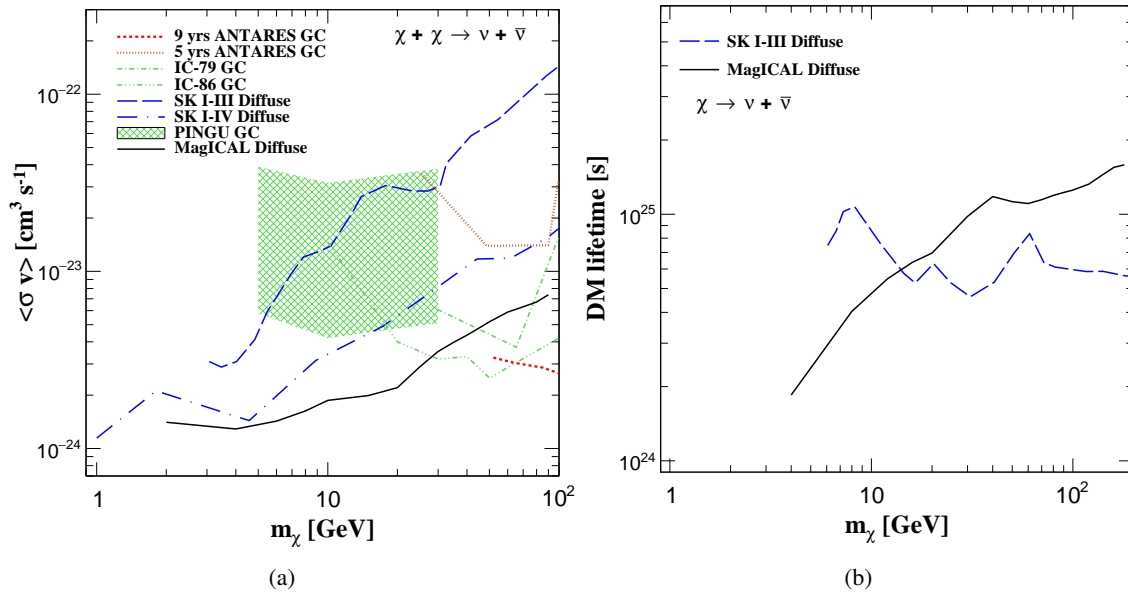


**Figure 4.9.** (a) Current bounds at 90% C.L. (1 d.o.f.) on self-annihilation cross-section which are obtained from the first three phases of Super-Kamiokande [231] (blue long-dashed line), the four phases of Super-Kamiokande [285] (blue long-dash-dotted line), IceCube [264, 286] (green dot-dashed and green triple-dot-dashed lines), and ANTARES [287, 288] (red dotted and red dashed lines) are shown. The future sensitivity of PINGU [188] with its 1 year of exposure is shown by green shaded region. We compare these limits with the bound obtained from 500 kt-yr MagICAL (black solid line) detector. For all the cases the NFW profile is used. (b) Blue long-dashed line shows the current bound on decay lifetime of DM from the first three phases of Super-Kamiokande [231] using the NFW profile. We compare this limit with the performance of 500 kt-yr MagICAL detector (black solid line) using the same NFW profile.

Various experiments present the bounds on the self-annihilation cross-section of  $\chi\chi \rightarrow \nu\bar{\nu}$  and the decay lifetime of  $\chi \rightarrow \nu\bar{\nu}$  processes. Fig. 4.9(a) shows a comparison of the current bounds on  $\langle\sigma v\rangle$  at 90% C.L. (1 d.o.f.) from the first three phases of the Super-Kamiokande [231] (blue long-dashed line), the four phases of the Super-Kamiokande [285] (blue long-dash-dotted line), IceCube [264, 286] (green dot-dashed and green triple-dot-dashed lines), ANTARES [287, 288] (red dotted and red dashed lines), PINGU [188] (green shade), and from the MagICAL detector (black solid line) for the process  $\chi\chi \rightarrow \nu\bar{\nu}$ . We do not show the weaker limits from Baikal NT200 [289]. In Fig. 4.9(b), we compare the limits on decay lifetime ( $\tau$ ) for the process  $\chi \rightarrow \nu\bar{\nu}$  from the first three phases of the Super-Kamiokande experiment [231] (blue long-dashed line) and the present work (black solid line).

Due to the lower energy threshold of MagICAL, the dark matter constraints can be estimated for  $m_\chi$  values which are as low as 2 GeV and 4 GeV in case of annihilating and decaying dark matter respectively. The good energy and direction resolutions of MagICAL detector help to strongly constrain the  $\langle\sigma v\rangle$  and  $\tau$  for  $m_\chi$  in multi-GeV range. The constraints on  $\langle\sigma v\rangle$  obtained using 319.7 live-days of data from IceCube operating in its 79 string configuration during 2010 and 2011 are stronger than MagICAL for dark matter masses heavier than  $\sim 50$  GeV (see green dot-dashed line in Fig. 4.9(a)) [234, 264, 290–299]. But, if we consider the limits on  $\langle\sigma v\rangle$  estimated using three years of the IceCube/DeepCore data [286], then their performance becomes better than the MagICAL detector for  $m_\chi \geq 30$  GeV (see green triple-dot-dashed line in Fig. 4.9(a)). Using the 9 years data of ANTARES, no excess was found over the expected neutrino events in the range of WIMP mass  $50 \text{ GeV} \leq m_\chi \leq 100 \text{ GeV}$ , and they presented the most stringent constraint on  $\langle\sigma v\rangle$  for  $m_\chi \geq 70 \text{ GeV}$  [288]. However, for dark matter masses  $\lesssim 100 \text{ GeV}$ , the potential constraints from MagICAL are comparable or slightly better than that from Super-Kamiokande [231, 285]. The limit on  $\langle\sigma v\rangle$  by 500 kt-yr exposure of MagICAL detector is better than that from 1 year exposure of PINGU [188]. The constraints on dark matter annihilation and decay that we show in Fig. 4.9 can only be obtained from neutrino telescopes, including liquid scintillator detectors [300, 301]. The dark matter masses that we consider are too low for efficient electroweak bremsstrahlung, and hence gamma-ray constraints on this channel are weak [302–310]. Since MagICAL can distinguish between  $\mu^+$  and  $\mu^-$ , it can also give constraints on exotic lepton number violating dark matter interactions. The potential dark matter constraints from Baikal-GVD, and



Hyper-Kamiokande will be stronger or comparable [311, 312]. The complementarity of INO-MagICAL with PINGU and Hyper-Kamiokande will certainly make dark matter physics richer.

#### 4.6.4 The constraints on DM-induced neutrino flux

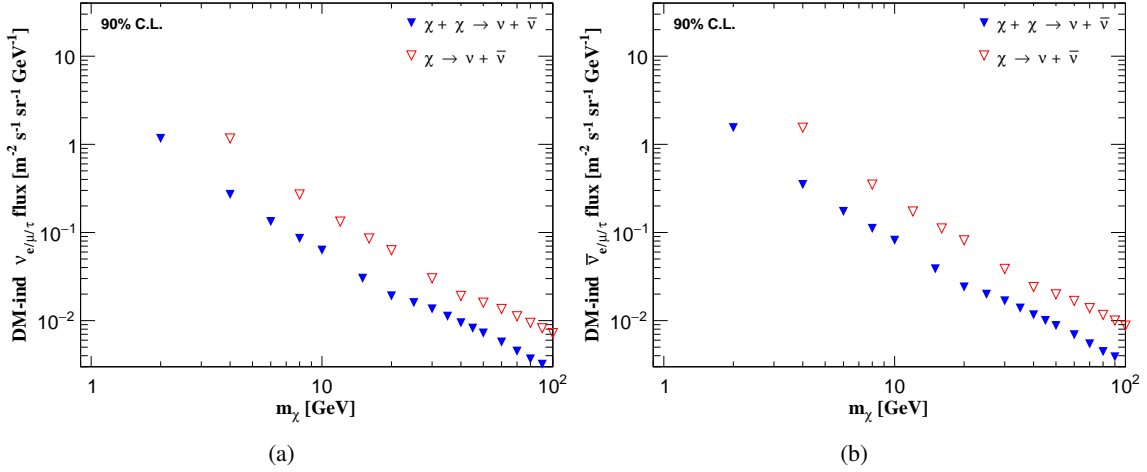


**Figure 4.10.** The limit on (a)  $\nu_{e/\mu/\tau}$  and (b)  $\bar{\nu}_{e/\mu/\tau}$  flux produced from the dark matter in Milky Way galaxy at 90% C.L. (1 d.o.f.) by 500 kt-yr MagICAL detector. The blue filled and red empty triangles are for the annihilation and decay of dark matter particles respectively.

We can use the constraints on  $\langle\sigma v\rangle$  (see Sec. 4.6.1) and  $\tau$  (see Sec. 4.6.2) in Eqs. 4.2.6 and 4.2.11 respectively to place the upper bound on the neutrino and antineutrino flux from dark matter. In Fig. 4.10(a), the blue filled triangles and red empty triangles depict the upper bounds on  $\nu_e/\nu_\mu/\nu_\tau$  flux at 90% C.L. (1 d.o.f.) using the constraints on  $\langle\sigma v\rangle$  (in case of annihilation) and  $\tau$  (in case of decay) respectively. Fig. 4.10(b) shows the same for  $\bar{\nu}_e/\bar{\nu}_\mu/\bar{\nu}_\tau$  flux. The mass ordering is taken as NO and the dark matter profile is assumed to be NFW. We can see from both the panels in Fig. 4.10 that the limits on neutrino (left panel) and antineutrino (right panel) flux from both annihilation and decay improve as we increase the value of  $m_\chi$ . We can understand this behavior in the following way. We know that the atmospheric neutrino event rates which serve as background for annihilation and decay decrease as we go to higher neutrino energy. This can be clearly seen from Fig. 4.5 and also Fig. 4.7. This is also true for atmospheric antineutrino events. Since, the atmospheric neutrino and antineutrino backgrounds get reduced when we go from lower to higher  $m_\chi$ , we need less dark matter induced neutrino and antineutrino flux for both annihilation and decay to obtain the same confidence level in  $\Delta\chi^2$  which is 2.71 at 90% C.L. (1 d.o.f.). Hence, we can place better constraints on the DM induced neutrino and antineutrino flux as we move from lower

to higher  $m_\chi$  values. Another feature that is emerging from both the panels in Fig. 4.10 that we have better constraints on the neutrino and antineutrino flux obtained from the annihilation of dark matter as compare to its decay for a fixed  $m_\chi$ . We can also explain this feature in the following way. For a fixed value of  $m_\chi$ , the available energy of neutrino and antineutrino,  $E_{\nu/\bar{\nu}}$ , is equal to  $m_\chi$  for annihilation and  $m_\chi/2$  for decay. Let us consider the case for  $m_\chi = 10$  GeV in both the panels. In this case, the available neutrino/antineutrino energy for annihilation (decay) is 10 GeV (5 GeV). Now, we already know that the background events induced by atmospheric neutrino and antineutrino flux are higher at 5 GeV (in case of decay) as compared to 10 GeV (in case of annihilation). Therefore, for a fixed choice of  $m_\chi$  value, we need higher neutrino and antineutrino flux from decaying DM as compare to annihilating DM to place the constraints at same confidence level.

## 4.7 Summary

We explore the prospects of detecting diffuse dark matter in the Milky Way galaxy at the proposed INO-MagICAL detector. The future sensitivity of 500 kt-yr MagICAL detector to constrain the dark matter self-annihilation cross-section ( $\langle\sigma v\rangle$ ) and decay lifetime ( $\tau$ ) for  $\chi\chi \rightarrow \nu\bar{\nu}$  and  $\chi \rightarrow \nu\bar{\nu}$  processes respectively are estimated. We find that MagICAL will be able to probe new parameter space for low mass dark matter.

Combining information from  $\nu$  and  $\bar{\nu}$  modes, the future limits on  $\langle\sigma v\rangle$  and  $\tau$  are  $\leq 1.87 \times 10^{-24}$   $\text{cm}^3 \text{ s}^{-1}$  and  $\geq 4.8 \times 10^{24}$  s respectively at 90% C.L. (1 d.o.f.) for  $m_\chi = 10$  GeV assuming the NFW profile. These limits will be novel and they will address many viable dark matter models. The limits for higher dark matter masses will also be competitive with other neutrino telescopes.

We have also shown the bounds on  $\langle\sigma v\rangle$  and  $\tau$  with  $\nu$  and  $\bar{\nu}$  data separately. This enables us to probe the same physics through the  $\nu$  and  $\bar{\nu}$  channels due to the charge identification capability of the MagICAL detector.

Although, we have studied the processes  $\chi\chi \rightarrow \nu\bar{\nu}$  and  $\chi \rightarrow \nu\bar{\nu}$ , other final states like  $\mu^+\mu^-$ ,  $\tau^+\tau^-$ ,  $b\bar{b}$  are also possible. The constraints on these channels obtained from the gamma-ray detectors are much stronger, and hence we do not consider them. Since the analysis is done for the diffuse

dark matter component of the Milky Way galaxy, the constraints on self-annihilation cross-section and decay lifetime are robust and conservative, and the constraints have mild dependence on the dark matter profile. Besides new and novel methods in dark matter indirect detection physics [313, 314], it is imperative that we fully utilize the capabilities of new and upcoming detectors. Our work explores the capabilities of INO-MagICAL to search for dark matter, and we encourage the community to look into this signature in more detail.

In the following chapter, we discuss about a lepton-violating Non-Standard Interaction (NSI) of neutrino which can happen in BSM scenarios. We consider the effect of such interactions in model-independent and effective framework, and estimate the sensitivity of the ICAL detector to explore such NSI. If NSI is present in the nature with even small coupling strength, it may impact the precision measurement of the oscillation parameters in an experiment. We have addressed this issue using the ICAL detector, and next chapter presents the results of this study.

# 5 Non-Standard Interactions

## Contents

---

<b>5.1 Introduction</b>	<b>88</b>
<b>5.2 Existing Limits on NSI Parameter <math>\varepsilon_{\mu\tau}</math></b>	<b>90</b>
<b>5.3 <math>\nu_\mu \rightarrow \nu_\mu</math> transition with non-zero <math>\varepsilon_{\mu\tau}</math></b>	<b>92</b>
<b>5.4 Expected Events at ICAL with non-zero <math>\varepsilon_{\mu\tau}</math></b>	<b>94</b>
5.4.1 Total Event Rates	94
5.4.2 Event Spectra	96
<b>5.5 Simulation Method</b>	<b>97</b>
5.5.1 Binning Scheme in $(E_\mu, \cos \theta_\mu, E'_{\text{had}})$ Plane	97
5.5.2 Numerical Analysis	98
<b>5.6 Results</b>	<b>100</b>
5.6.1 Expected Bounds on NSI parameter $\varepsilon_{\mu\tau}$	100
5.6.2 Advantage of having Charge Identification Capability	104
5.6.3 Impact of non-zero $\varepsilon_{\mu\tau}$ on Mass Hierarchy Determination	105
5.6.4 Precision Measurement of Atmospheric Parameters with non-zero $\varepsilon_{\mu\tau}$	106
<b>5.7 Summary and Concluding Remarks</b>	<b>108</b>

---

## 5.1 Introduction

In this chapter, we study the impact of neutral current (NC) non-standard interactions (NSI's) of neutrino which may arise when atmospheric neutrinos travel long distances inside the Earth. While NC NSI's affect neutrinos during their propagation, there are charged-current NSI's which may

modify the neutrino fluxes at the production stage and interaction cross-section at the detection level. In this work, we only focus on the NC NSI's, and do not consider NSI's at production and detection level. In most of the cases, NSI's come into the picture as a low-energy manifestation of high-energy theory involving new heavy states. For a detailed discussion on this topic, see the reviews [171, 315–317]. Therefore, at low energies, a neutral current NSI can be described by a four-fermion dimension-six operator [44],

$$\mathcal{L}_{\text{NC-NSI}} = -2 \sqrt{2} G_F \varepsilon_{\alpha\beta}^{Cf} (\bar{\nu}_\alpha \gamma^\rho P_L \nu_\beta) (\bar{f} \gamma_\rho P_C f), \quad (5.1.1)$$

where  $G_F$  is the Fermi coupling constant,  $\varepsilon_{\alpha\beta}^{Cf}$  is the dimensionless parameter which represents the strength of NSI relative to  $G_F$ , and  $\nu_\alpha$  and  $\nu_\beta$  are the neutrino fields of flavor  $\alpha$  and  $\beta$  respectively. Here,  $f$  denotes the matter fermions, electron ( $e$ ), up-quark ( $u$ ), and down-quark ( $d$ ). Here,  $P_L = (1 - \gamma_5)/2$ ,  $P_R = (1 + \gamma_5)/2$ , and the subscript  $C = L, R$  expresses the chirality of the  $ff$  current. Due to the hermiticity of the interaction, we have  $\varepsilon_{\alpha\beta}^{Cf} = (\varepsilon_{\beta\alpha}^{Cf})^*$ .

The NSI's of neutrino with matter fermions can give rise to the additional matter induced potentials apart from the standard MSW potential due to the  $W$ -mediated interactions in matter denoted by  $V_{CC}$  (see Eq. 2.2.2). The total relative strength of the matter induced potential generated by the NC NSI's of neutrinos with all the matter fermions ( $\nu_\alpha + f \rightarrow \nu_\beta + f$ ) can be written in the following fashion,

$$\varepsilon_{\alpha\beta} = \sum_{f=e,u,d} \frac{V_f}{V_{CC}} (\varepsilon_{\alpha\beta}^{Lf} + \varepsilon_{\alpha\beta}^{Rf}), \quad (5.1.2)$$

where  $V_f = \sqrt{2} G_F N_f$ ,  $f = e, u, d$ . The quantity  $N_f$  denotes the number density of matter fermion  $f$  in the medium. For antineutrino,  $V_f \rightarrow -V_f$ . In general, the total matter induced potential in presence of all the possible NC non-standard interactions of neutrino with matter fermions can be written as

$$H_{\text{mat}} = \sqrt{2} G_F N_e \begin{pmatrix} 1 + \varepsilon_{ee} & \varepsilon_{e\mu} & \varepsilon_{e\tau} \\ \varepsilon_{e\mu}^* & \varepsilon_{\mu\mu} & \varepsilon_{\mu\tau} \\ \varepsilon_{e\tau}^* & \varepsilon_{\mu\tau}^* & \varepsilon_{\tau\tau} \end{pmatrix}. \quad (5.1.3)$$

In the present study, we focus our investigation to flavor violating NSI parameter  $\varepsilon_{\mu\tau}$ , that is, we only allow  $\varepsilon_{\mu\tau}$  to be non-zero in our analysis, and assume all other NSI parameters to be zero. We also consider  $\varepsilon_{\mu\tau}$  to be real since its associated phase has very little impact on  $\nu_\mu \rightarrow \nu_\mu$  survival

channel. Since the atmospheric neutrino oscillation is mainly governed by  $\nu_\mu \rightarrow \nu_\tau$  transition, it is expected that NSI parameter  $\varepsilon_{\mu\tau}$  would have significant impact on this oscillation channel, which in turn can modify  $\nu_\mu \rightarrow \nu_\mu$  survival probability by a considerable amount. We can study this effect by observing the atmospheric neutrinos at the proposed 50 kt magnetized ICAL detector. If we will not see any significant deviation from the standard  $\mu^-$  and  $\mu^+$  event spectra at ICAL, we can use this fact to place tight constraints on NSI parameter  $\varepsilon_{\mu\tau}$ . This is the main theme of our present study.

This chapter is organized in the following fashion. In Sec. 5.2, we briefly review the existing bounds on NSI parameter  $\varepsilon_{\mu\tau}$  from various neutrino oscillation experiments. We discuss the possible modification in oscillation probabilities of neutrino and antineutrino due to non-zero  $\varepsilon_{\mu\tau}$  in Sec. 5.3. In Sec. 5.4, we present the expected total  $\mu^-$  and  $\mu^+$  events and their distributions as a function of reconstructed  $E_\mu$  and  $\cos\theta_\mu$  for the following three cases: (i)  $\varepsilon_{\mu\tau} = 0$  (SM), (ii)  $\varepsilon_{\mu\tau} = 0.05$ , and (iii)  $\varepsilon_{\mu\tau} = -0.05$  using 500 kt-yr exposure of the ICAL detector. In Sec. 5.5, we discuss the numerical procedure and various binning schemes that we use in our analysis. We present all the results of our study in Sec. 5.6 where we show the following: (a) The possible improvement in the sensitivity of the ICAL detector in constraining  $\varepsilon_{\mu\tau}$  due to the inclusion of events  $E_\mu$  range of 11 to 21 GeV in addition to the events that belong to the  $E_\mu$  range of 1 to 11 GeV. (b) How much the limit on  $\varepsilon_{\mu\tau}$  can be improved by considering the information on reconstructed hadron energy ( $E'_{\text{had}}$ ) as an additional observable along with reconstructed variables  $E_\mu$  and  $\cos\theta_\mu$  on an event-by-event basis. (c) We show the advantage of having charge identification capability in the ICAL detector in placing competitive constraint on  $\varepsilon_{\mu\tau}$ . (d) We also explore the possible impact of non-zero  $\varepsilon_{\mu\tau}$  in determining the mass hierarchy and in the precision measurement of atmospheric oscillation parameters. We provide a summary of this study in Sec. 5.7.

## 5.2 Existing Limits on NSI Parameter $\varepsilon_{\mu\tau}$

There are existing constraints on the NSI parameter  $\varepsilon_{\mu\tau}$  from various neutrino oscillation experiments. The Super-Kamiokande collaboration performed an analysis of the atmospheric neutrino data collected during its phase-I and -II run assuming only NSI's with  $d$ -quarks [318]. The fol-

lowing bounds at 90% C.L. are obtained:

$$|\varepsilon| = |\varepsilon_{\mu\tau}^d| < 0.011, \quad |\varepsilon'| = |\varepsilon_{\tau\tau}^d - \varepsilon_{\mu\mu}^d| < 0.049. \quad (5.2.1)$$

Since  $N_d = N_u = 3N_e$  for an electrically neutral and isoscalar Earth matter, the above constraints as obtained in Ref. [318] are actually on the NSI parameters  $\varepsilon_{\alpha\beta}/3$ . Therefore, the above constraints at 90% C.L. can be interpreted as

$$|\varepsilon_{\mu\tau}| < 0.033, \quad |\varepsilon_{\tau\tau} - \varepsilon_{\mu\mu}| < 0.147. \quad (5.2.2)$$

Recently, the authors in Ref. [319] considered the possibility of NSI's in  $\mu$ - $\tau$  sector in the one-year high-energy through-going muon data of IceCube. In their analysis, they included various systematic uncertainties on both the atmospheric neutrino flux and detector properties, which they incorporated via several nuisance parameters. They obtained the following limits

$$-6.0 \times 10^{-3} < \varepsilon_{\mu\tau} < 5.4 \times 10^{-3} \quad \text{at 90\% credible interval (C.I.).} \quad (5.2.3)$$

The IceCube-DeepCore collaboration also searched for NSI's involving  $\varepsilon_{\mu\tau}$  [320]. Using their three years of atmospheric muon neutrino disappearance data, they placed the following constraint at 90% confidence level

$$-6.7 \times 10^{-3} < \varepsilon_{\mu\tau} < 8.1 \times 10^{-3}. \quad (5.2.4)$$

A preliminary analysis to constrain the NSI parameters in context of the ICAL detector was performed in Ref. [57]. Using an exposure of 500 kt-yr and considering only muon momentum ( $E_\mu, \cos \theta_\mu$ ) as observable, the authors in Ref. [57] obtained the following bound

$$-0.015 (-0.027) < \varepsilon_{\mu\tau} < 0.015 (0.027) \quad \text{at 90 (3}\sigma\text{) C.L. with NH.} \quad (5.2.5)$$

In the present study, we estimate new constraints on  $\varepsilon_{\mu\tau}$  considering the reconstructed hadron energy ( $E'_{\text{had}}$ ) as an additional observable along with the reconstructed  $E_\mu$  and  $\cos \theta_\mu$  on an event-by-event basis at the ICAL detector.

### 5.3 $\nu_\mu \rightarrow \nu_\mu$ transition with non-zero $\varepsilon_{\mu\tau}$

This section is devoted to explore the effect of non-zero  $\varepsilon_{\mu\tau}$  in the oscillation of atmospheric neutrino and antineutrino propagating long distances through the Earth matter. For this, we numerically estimate the three-flavor oscillation probabilities including NSI parameter  $\varepsilon_{\mu\tau}$  and using the PREM profile [158] for the Earth matter density. The NSI parameter  $\varepsilon_{\mu\tau}$  modifies the evolution of neutrino in matter, which in the flavor basis takes the following form,

$$i \frac{d}{dt} \begin{pmatrix} \nu_e(t) \\ \nu_\mu(t) \\ \nu_\tau(t) \end{pmatrix} = \frac{1}{2E} \left[ U \begin{pmatrix} 0 & 0 & 0 \\ 0 & \Delta m_{21}^2 & 0 \\ 0 & 0 & \Delta m_{31}^2 \end{pmatrix} U^\dagger + 2\sqrt{2}G_F N_e E \begin{pmatrix} 1 & 0 & 0 \\ 0 & 0 & \varepsilon_{\mu\tau} \\ 0 & \varepsilon_{\mu\tau} & 0 \end{pmatrix} \right] \begin{pmatrix} \nu_e \\ \nu_\mu \\ \nu_\tau \end{pmatrix}, \quad (5.3.1)$$

where  $\varepsilon_{\mu\tau}$  is real in our analysis.

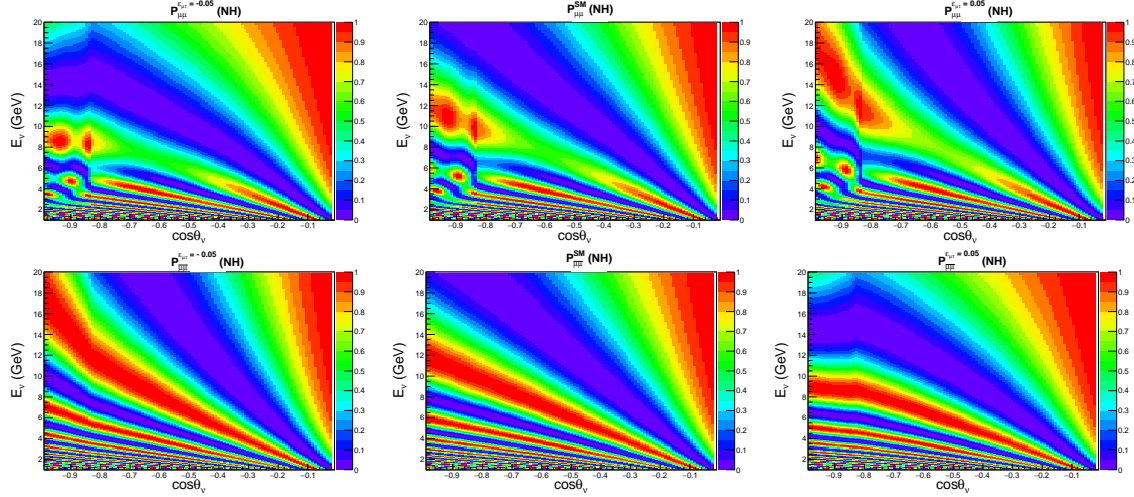


**Figure 5.1.** The oscillograms for  $\nu_\mu \rightarrow \nu_\mu$  ( $\bar{\nu}_\mu \rightarrow \bar{\nu}_\mu$ ) channel in  $E_\nu$ ,  $\cos\theta_\nu$  plane are shown in top (bottom) panels for three different scenarios: i)  $\varepsilon_{\mu\tau} = -0.05$  (left panel), ii)  $\varepsilon_{\mu\tau} = 0.0$  (the SM case, middle panel), and iii)  $\varepsilon_{\mu\tau} = 0.05$  (right panel). Here, in all the panels, we assume NH.

In upper panels of Fig. 5.1, we present the oscillograms for  $\nu_\mu$  survival channel in the plane of  $\cos\theta_\nu$  vs.  $E_\nu$  considering NH. Here, we draw the oscillograms for three different cases: i)  $\varepsilon_{\mu\tau} = -0.05$  (left panel), ii)  $\varepsilon_{\mu\tau} = 0.0$  (the SM case, middle panel), and iii)  $\varepsilon_{\mu\tau} = 0.05$  (right panel). The lower panel depicts the same but for  $\bar{\nu}_\mu \rightarrow \bar{\nu}_\mu$  oscillation channel. To prepare Fig. 5.1, we take the following benchmark values of vacuum oscillation parameters in three-flavor:  $\sin^2\theta_{23} = 0.5$ ,  $\sin^2 2\theta_{13} = 0.1$ ,  $\sin^2\theta_{12} = 0.3$ ,  $\Delta m_{21}^2 = 7.5 \times 10^{-5} \text{ eV}^2$ ,  $\Delta m_{\text{eff}}^2 = 2.4 \times 10^{-3} \text{ eV}^2$ , and  $\delta_{\text{CP}} = 0^\circ$ . To



estimate the value of  $\Delta m_{31}^2$  from  $\Delta m_{\text{eff}}^2$ , we use the Eq. 3.3.1, where  $\Delta m_{\text{eff}}^2$  has the same magnitude for NH and IH with +ve and -ve signs respectively. It is evident from Fig. 5.1 that in the presence of -ve and +ve non-zero values of  $\varepsilon_{\mu\tau}$ , both  $\nu_\mu$  and  $\bar{\nu}_\mu$  survival probabilities get modified at higher energies and longer baselines. To visualize these modifications in oscillation probabilities more

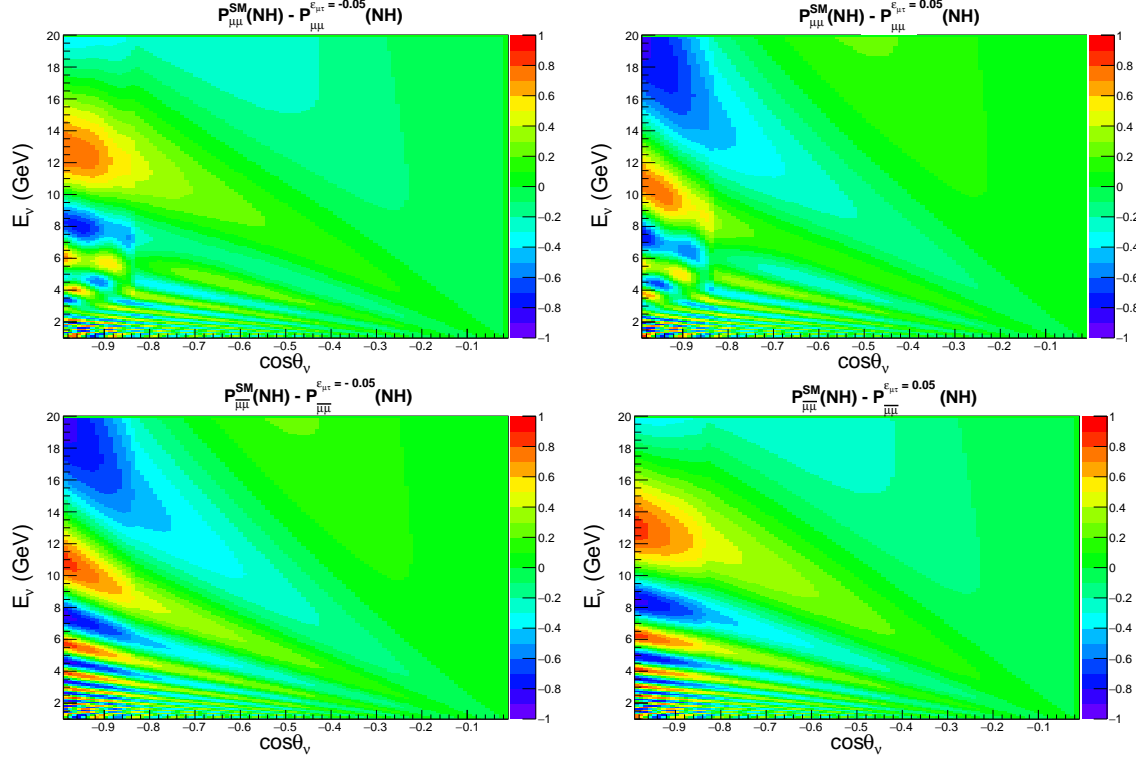


**Figure 5.2.** The upper left panel shows the difference in  $\nu_\mu \rightarrow \nu_\mu$  oscillation channel between the SM case ( $\varepsilon_{\mu\tau} = 0$ ) and  $\varepsilon_{\mu\tau} = -0.05$ . In the top right panel, the difference is due to the SM case and  $\varepsilon_{\mu\tau} = 0.05$ . The lower panels are for  $\bar{\nu}_\mu \rightarrow \bar{\nu}_\mu$  oscillation channel. Here, in all the panels, we assume NH.

clearly, we give Fig. 5.2 where we plot the difference in  $\nu_\mu \rightarrow \nu_\mu$  survival channel considering the cases  $\varepsilon_{\mu\tau} = 0$  (the SM case) and  $\varepsilon_{\mu\tau} = -0.05$  (see top left panel). In top right panel, we present the same for the cases  $\varepsilon_{\mu\tau} = 0$  (the SM case) and  $\varepsilon_{\mu\tau} = 0.05$ . The lower panels are for antineutrinos. In all the panels, we see a visible difference in  $\nu_\mu$  survival channel due to the presence of non-zero  $\varepsilon_{\mu\tau}$  as compared to the SM case ( $\varepsilon_{\mu\tau} = 0.0$ ) at higher baselines with  $\cos\theta_\nu$  in the range  $-1$  to  $-0.8$ . This range of  $\cos\theta_\nu$  corresponds to the baseline in the range  $\sim 12700$  km to  $10000$  km where neutrinos mostly travel through inner and outer part of the Earth's core<sup>1</sup> and have access to large Earth matter effect. Also, we see a trend that the impact of NSI's is large at higher energies where

<sup>1</sup>According to a simplified version of the PREM profile [158], the inner core has a radius of  $\sim 1220$  km with an average density of  $13 \text{ g/cm}^3$ . For outer core,  $R_{\text{min}} \approx 1220$  km and  $R_{\text{max}} \approx 3480$  km with an average density of  $11.3 \text{ g/cm}^3$ . Note that in our analysis, we consider the detailed version of the PREM.

the three-flavor oscillations are suppressed because the oscillation lengths ( $L^{\text{osc}} = \frac{4\pi E}{\Delta m_{ij}^2}$ ) are large at higher energies.

## 5.4 Expected Events at ICAL with non-zero $\varepsilon_{\mu\tau}$

The Monte Carlo based neutrino event generator NUANCE [205] is used to simulate the CC interactions of  $\nu_\mu$  and  $\bar{\nu}_\mu$  in the ICAL detector. To generate events in NUANCE, we give a simple geometry of the ICAL detector with 150 alternate layers of iron and glass plates in each module. We have three such modules to account for the 50 kt ICAL detector. As far as the neutrino flux is concerned in generating the neutrino events in the present study, we use the flux as predicted at Kamioka<sup>2</sup> [165]. To reduce the statistical fluctuation, we generate the unoscillated CC neutrino and antineutrino events considering a very high exposure of 1000 years and 50 kt ICAL. Then, we implement various oscillation probabilities using the reweighting algorithm as discussed in Sec. 3.3. Next, we fold the oscillated events with detector response for muon and hadron which are already described in Secs. 3.2.1 and 3.2.2 respectively. In the present study, we assume that the ICAL particle reconstruction algorithms can separate the hits due to the hadron shower from the hits originating from a muon track with 100% efficiency. It means that whenever a muon is reconstructed, we consider all the other hits to be part of the hadronic shower in order to calibrate the hadron energy. Finally, the reconstructed  $\mu^-$  and  $\mu^+$  events are scaled down to the exposure of 10 years for 50 kt ICAL. Now, we present the expected  $\mu^-$  and  $\mu^+$  events for 500 kt-yr exposure of the ICAL detector assuming the SM case ( $\varepsilon_{\mu\tau} = 0$ ) and  $\varepsilon_{\mu\tau} = \pm 0.05$ . To estimate these event rates, we use the values of oscillation parameters as considered in Sec. 5.3 to draw the oscillograms.

### 5.4.1 Total Event Rates

First, we address the following question: can we see the signature of non-zero  $\varepsilon_{\mu\tau}$  in the total number of  $\mu^-$  and  $\mu^+$  events which will be collected at the ICAL detector over 10 years of running? To have an answer of this question, we estimate the total number of events for the following three

---

<sup>2</sup>Preliminary calculation of the expected fluxes at the INO site has been performed in Ref. [88, 206]. The visible differences between the neutrino fluxes at the Kamioka and INO sites appear at lower energies. The main reason behind this is that the horizontal components of the geo-magnetic field are different at the Kamioka (30  $\mu$ T) and INO (40  $\mu$ T) locations. We plan to use these new fluxes estimated for the INO site (see Ref. [88]) in future studies.

cases: i)  $\varepsilon_{\mu\tau} = 0.05$ , ii)  $\varepsilon_{\mu\tau} = 0$  (the SM case), and iii)  $\varepsilon_{\mu\tau} = -0.05$ . We present these numbers in Table 5.1 with NH and using 500 kt-yr exposure of the ICAL detector integrating over entire ranges of  $E_\mu$ ,  $\cos \theta_\mu$ , and  $E'_{\text{had}}$  that we consider in our analysis. As far as the binning schemes are

$\varepsilon_{\mu\tau}$	low-energy (LE)		high-energy (HE)	
	$\mu^-$	$\mu^+$	$\mu^-$	$\mu^+$
0.05	4574 (total)	2029 (total)	4879 (total)	2192 (total)
	4473 ( $P_{\mu\mu}$ )	2016 ( $P_{\bar{\mu}\bar{\mu}}$ )	4778 ( $P_{\mu\mu}$ )	2179 ( $P_{\bar{\mu}\bar{\mu}}$ )
	100 ( $P_{e\mu}$ )	13 ( $P_{\bar{e}\bar{\mu}}$ )	101 ( $P_{e\mu}$ )	13 ( $P_{\bar{e}\bar{\mu}}$ )
SM	4562 (total)	2035 (total)	4870 (total)	2188 (total)
	4458 ( $P_{\mu\mu}$ )	2022 ( $P_{\bar{\mu}\bar{\mu}}$ )	4765 ( $P_{\mu\mu}$ )	2175 ( $P_{\bar{\mu}\bar{\mu}}$ )
	104 ( $P_{e\mu}$ )	13 ( $P_{\bar{e}\bar{\mu}}$ )	105 ( $P_{e\mu}$ )	13 ( $P_{\bar{e}\bar{\mu}}$ )
-0.05	4553 (total)	2037 (total)	4890 (total)	2191 (total)
	4444 ( $P_{\mu\mu}$ )	2024 ( $P_{\bar{\mu}\bar{\mu}}$ )	4780 ( $P_{\mu\mu}$ )	2178 ( $P_{\bar{\mu}\bar{\mu}}$ )
	109 ( $P_{e\mu}$ )	13 ( $P_{\bar{e}\bar{\mu}}$ )	110 ( $P_{e\mu}$ )	13 ( $P_{\bar{e}\bar{\mu}}$ )

**Table 5.1.** Expected number of  $\mu^-$  and  $\mu^+$  events for 500 kt-yr exposure of the ICAL detector considering low-energy (LE) and high-energy (HE) binning schemes. We present the event rates for the following three cases: i)  $\varepsilon_{\mu\tau} = 0.05$ , ii)  $\varepsilon_{\mu\tau} = 0$  (the SM case), and iii)  $\varepsilon_{\mu\tau} = -0.05$ . Apart from showing the total  $\mu^-$  event rates, we also give the estimates of individual event rates coming from  $\nu_\mu \rightarrow \nu_\mu$  ( $P_{\mu\mu}$ ) disappearance channel and  $\nu_e \rightarrow \nu_\mu$  ( $P_{e\mu}$ ) appearance channel. For  $\mu^+$  events also, we separately show the contributions from  $\bar{\nu}_\mu \rightarrow \bar{\nu}_\mu$  ( $P_{\bar{\mu}\bar{\mu}}$ ) disappearance channel and  $\bar{\nu}_e \rightarrow \bar{\nu}_\mu$  ( $P_{\bar{e}\bar{\mu}}$ ) appearance channel. Here, we consider NH and assume the benchmark values of the oscillation parameters as mentioned in Sec. 5.4.

concerned, we use the low-energy (LE) and high-energy (HE) binning schemes<sup>3</sup>, and for both these binning schemes, we take the entire range of  $\cos \theta_\mu$  spanning over -1 to 1. The energy ranges for reconstructed  $E_\mu$  and  $E'_{\text{had}}$  are different in LE and HE binning schemes. For LE binning scheme,  $E_\mu \in [1, 11]$  GeV and  $E'_{\text{had}} \in [0, 15]$  GeV. In case of HE binning scheme,  $E_\mu \in [1, 21]$  GeV, and  $E'_{\text{had}} \in [0, 25]$  GeV. When we increase the reconstructed muon energy from 11 GeV to 21 GeV and reconstructed hadron energy from 15 GeV to 25 GeV, the number of  $\mu^-$  and  $\mu^+$  events get increased by 300 and 150 respectively for 500 kt-yr exposure of the ICAL detector. Apart from showing the total  $\mu^-$  event rates in Table 5.1, we also present the estimates of individual events coming from  $\nu_\mu \rightarrow \nu_\mu$  ( $P_{\mu\mu}$ ) disappearance channel and  $\nu_e \rightarrow \nu_\mu$  ( $P_{e\mu}$ ) appearance channel. Also, for  $\mu^+$  events, we separately show the contributions originating from  $\bar{\nu}_\mu \rightarrow \bar{\nu}_\mu$  ( $P_{\bar{\mu}\bar{\mu}}$ ) disappearance and  $\bar{\nu}_e \rightarrow \bar{\nu}_\mu$  ( $P_{\bar{e}\bar{\mu}}$ ) appearance channels. Here, we see that only  $\sim 2\%$  of the total  $\mu^-$  events at the ICAL detector come via the appearance channel. Note that the differences in the total number of  $\mu^-$  and  $\mu^+$  events between the SM case ( $\varepsilon_{\mu\tau} = 0$ ) and non-zero  $\varepsilon_{\mu\tau}$  of  $\pm 0.05$  are not significant. But, later while presenting our final results, we see that the ICAL detector can place competitive

<sup>3</sup>For a detailed description of the two binning schemes that we consider in our analysis, see Sec. 5.5.1.

constraints on  $\varepsilon_{\mu\tau}$  by exploiting the useful information contained in the spectral distributions of  $\mu^-$  and  $\mu^+$  events as a function of reconstructed observables  $E_\mu$ ,  $\cos\theta_\mu$ , and  $E'_{\text{had}}$ . To establish this claim, now, we show how the expected  $\mu^-$  and  $\mu^+$  event spectra get modified in the presence of non-zero  $\varepsilon_{\mu\tau}$  in terms of reconstructed  $E_\mu$  and  $\cos\theta_\mu$  while integrating over entire range of  $E'_{\text{had}}$ .

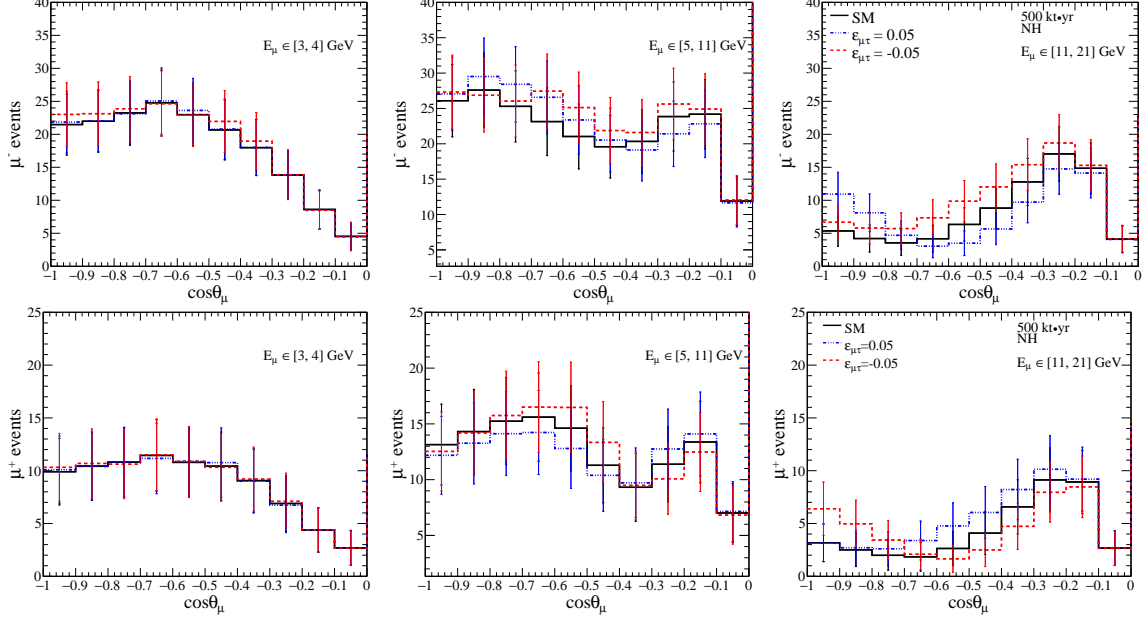


**Figure 5.3.** The distributions of  $\mu^-$  (upper panels) and  $\mu^+$  (lower panels) events for three different  $E_\mu$  ranges: [3, 4] GeV in left panel, [5, 11] GeV in middle panel, and [11, 21] GeV in right panel. In each panel, we consider three different cases: i)  $\varepsilon_{\mu\tau} = 0.05$  (blue line), ii)  $\varepsilon_{\mu\tau} = 0$  (the SM case, black line), and iii)  $\varepsilon_{\mu\tau} = -0.05$  (red line). Here, we sum over  $E'_{\text{had}}$  in its entire range of 0 to 25 GeV and show the results for 500 kt-yr exposure and assuming NH.

#### 5.4.2 Event Spectra

In Fig. 5.3, we show the distributions of  $\mu^-$  (upper panels) and  $\mu^+$  (lower panels) events as a function of reconstructed  $\cos\theta_\mu$  for three different ranges of  $E_\mu$  ranges. The ranges of  $E_\mu$  that we consider in left, middle, and right panels are [3, 4] GeV, [5, 11] GeV, and [11, 21] GeV respectively. Here, we integrate over  $E'_{\text{had}}$  in its entire range of 0 to 25 GeV. In each panel, we compare the event spectra for three different cases: i)  $\varepsilon_{\mu\tau} = 0.05$  (blue line), ii)  $\varepsilon_{\mu\tau} = 0$  (the SM case, black line), and iii)  $\varepsilon_{\mu\tau} = -0.05$  (red line). Before we discuss the impact of non-zero  $\varepsilon_{\mu\tau}$ , we would like to mention few general features that are emerging from various panels in Fig. 5.3. For both  $\mu^-$  (upper panels) and  $\mu^+$  (lower panels), the number of events get reduced as we go to higher energies. It happens because of  $\sim E_\nu^{-2.7}$  dependence of the atmospheric neutrino flux. Though the neutrino fluxes are higher along the horizontal direction ( $\cos\theta_\mu$  around 0) as compared to the other

directions (for detailed discussion, see Ref. [88]), but, due to the poor reconstruction efficiency of the ICAL detector along the horizontal direction [202], we see a suppression in  $\mu^-$  and  $\mu^+$  event rates around  $\cos \theta_\mu \in [-0.1, 0]$  irrespective of the choices of  $E_\mu$  ranges. Important to note that as we proceed towards higher  $E_\mu$ , the relative differences in  $\mu^-$  and  $\mu^+$  event rates between the SM case ( $\varepsilon_{\mu\tau} = 0$ ) and non-zero  $\varepsilon_{\mu\tau}$  ( $\pm 0.05$ ) get increased for a wide range of  $\cos \theta_\mu$ . We see similar features in Fig. 5.2 in Sec. 5.3, where we show the differences in  $\nu_\mu \rightarrow \nu_\mu$  oscillograms due to the SM case ( $\varepsilon_{\mu\tau} = 0$ ) and non-zero  $\varepsilon_{\mu\tau}$  ( $\pm 0.05$ ). We show the improvement in the sensitivity to constrain  $\varepsilon_{\mu\tau}$  due to high energy events in Sec. 5.6.1. Next, we discuss the numerical technique and analysis procedure which we adopt to obtain the final results.

## 5.5 Simulation Method

### 5.5.1 Binning Scheme in $(E_\mu, \cos \theta_\mu, E'_{\text{had}})$ Plane

In the present study, we produce all the results with low-energy (LE) and high-energy (HE) binning schemes. Table 5.2 shows the detailed information about the LE binning scheme for the three reconstructed observables  $E_\mu$ ,  $\cos \theta_\mu$ , and  $E'_{\text{had}}$ . Table 5.3 portrays the same for the HE binning scheme. In case of LE binning scheme, the range of  $E_\mu$  is  $[1, 11]$  GeV with total 10 bins each having a width of 1 GeV. In case of HE binning scheme, we extend the range of  $E_\mu$  up to 21 GeV by adding two additional bins in the range of 11 to 21 GeV, where each bin has a width of 5 GeV. As far as reconstructed  $E'_{\text{had}}$  is concerned, in case of LE (HE) binning scheme, the considered range is 0 to 15 GeV (0 to 25 GeV). We can see from Table 5.2 and Table 5.3 that the first three bins for  $E'_{\text{had}}$  are same for both the binning schemes, whereas the last bin extend from 4 to 15 GeV (4 to 25 GeV) for LE (HE) binning scheme. For both these binning schemes, we consider the entire range of  $\cos \theta_\mu$  from -1 to 1. For upward going events, that is  $\cos \theta_\mu \in [-1, 0]$ , we consider 10 uniform bins each having width of 0.1. For downward going events, that is  $\cos \theta_\mu \in [0, 1]$ , we consider 5 uniform bins each having width of 0.2. Important to note that the downward going events do not have enough path length to oscillate, but, these events play an important role to increase the overall statistics and to minimize the effect of normalization uncertainties in atmospheric neutrino fluxes.

Here, we would like to mention that we have not optimized these binning schemes to obtain the best sensitivities, but we ensure that there are sufficient statistics in most of the bins.

Observable	Range	Bin width	No. of bins	Total bins
$E_\mu$ (GeV)	[1, 11]	1	10	10
$\cos \theta_\mu$	[-1.0, 0.0]	0.1	10	15
	[0.0, 1.0]	0.2	5	
$E'_{\text{had}}$ (GeV)	[0, 2]	1	2	4
	[2, 4]	2	1	
	[4, 15]	11	1	

**Table 5.2.** The low-energy (LE) binning scheme considered for different reconstructed observables ( $E_\mu$ ,  $\cos \theta_\mu$ ,  $E'_{\text{had}}$ ) associated with each of the muon polarities. The total number of bins for each of these observables are given in 5th column.

Observable	Range	Bin width	No. of bins	Total bins
$E_\mu$ (GeV)	[1, 11]	1	10	12
	[11, 21]	5	2	
$\cos \theta_\mu$	[-1.0, 0.0]	0.1	10	15
	[0.0, 1.0]	0.2	5	
$E'_{\text{had}}$ (GeV)	[0, 2]	1	2	4
	[2, 4]	2	1	
	[4, 25]	21	1	

**Table 5.3.** The high-energy (HE) binning scheme considered for different reconstructed observables ( $E_\mu$ ,  $\cos \theta_\mu$ ,  $E'_{\text{had}}$ ) associated with each of the muon polarities. The total number of bins for each of these observables are given in 5th column.

## 5.5.2 Numerical Analysis

In our analysis, the  $\chi^2$  function gives us the median sensitivity of the experiment in the frequentist approach [321]. We use the following Poissonian  $\chi^2_-$  for  $\mu^-$  events in our statistical analysis considering  $E_\mu$ ,  $\cos \theta_\mu$ , and  $E'_{\text{had}}$  as observables (the so-called “3D” analysis as considered in [49]):

$$\chi^2_-(3\text{D}) = \min_{\zeta_l} \sum_{i=1}^{N_{E'_{\text{had}}}} \sum_{j=1}^{N_{E_\mu}} \sum_{k=1}^{N_{\cos \theta_\mu}} 2 \left[ N_{ijk}^{\text{theory}} - N_{ijk}^{\text{data}} - N_{ijk}^{\text{data}} \ln \left( \frac{N_{ijk}^{\text{theory}}}{N_{ijk}^{\text{data}}} \right) \right] + \sum_{l=1}^5 \zeta_l^2, \quad (5.5.1)$$

with

$$N_{ijk}^{\text{theory}} = N_{ijk}^0 \left( 1 + \sum_{l=1}^5 \pi_{ijk}^l \zeta_l \right). \quad (5.5.2)$$

In the above equations,  $N_{ijk}^{\text{data}}$  and  $N_{ijk}^{\text{theory}}$  denote the observed and expected number of  $\mu^-$  events in a given  $[E_\mu, \cos \theta_\mu, E'_{\text{had}}]$  bin. In case of LE (HE) binning scheme,  $N_{E_\mu} = 10$  (12),  $N_{\cos \theta_\mu} = 15$ , and  $N_{E'_{\text{had}}} = 4$ . In Eq. 5.5.2,  $N_{ijk}^0$  represents the number of expected events without systematic uncertainties. Following Ref. [47], we consider five systematic errors in our analysis: 20% flux normalization error, 10% error in cross-section, 5% tilt error, 5% zenith angle error, and 5% overall systematics. We incorporate these systematic uncertainties in our simulation using the well known “pull” method [281, 283, 322]. In Eq. 5.5.1 and Eq. 5.5.2, the quantities  $\zeta_l$  denote the “pulls” due to the systematic uncertainties, and the values of these pulls are calculated using Eq. C.0.11 as given in Appendix C.

When we produce results with only  $E_\mu$  and  $\cos \theta_\mu$  as observables and do not use the information on hadron energy  $E'_{\text{had}}$  (the so-called “2D” analysis as considered in Ref. [47]), the Poissonian  $\chi^2_-$  for  $\mu^-$  events takes the form

$$\chi^2_-(2D) = \min_{\zeta_l} \sum_{j=1}^{N_{E_\mu}} \sum_{k=1}^{N_{\cos \theta_\mu}} 2 \left[ N_{jk}^{\text{theory}} - N_{jk}^{\text{data}} - N_{jk}^{\text{data}} \ln \left( \frac{N_{jk}^{\text{theory}}}{N_{jk}^{\text{data}}} \right) \right] + \sum_{l=1}^5 \zeta_l^2, \quad (5.5.3)$$

with

$$N_{jk}^{\text{theory}} = N_{jk}^0 \left( 1 + \sum_{l=1}^5 \pi_{jk}^l \zeta_l \right). \quad (5.5.4)$$

In Eq. 5.5.3,  $N_{jk}^{\text{data}}$  and  $N_{jk}^{\text{theory}}$  indicate the observed and expected number of  $\mu^-$  events in a given  $[E_\mu, \cos \theta_\mu]$  bin. In Eq. 5.5.4,  $N_{jk}^0$  stands for the number of expected events without systematic errors. In case of LE (HE) binning scheme,  $N_{E_\mu} = 10$  (12) and  $N_{\cos \theta_\mu} = 15$ .

For both the “2D” and “3D” analyses, the  $\chi^2_+$  for  $\mu^+$  events is determined following the same technique described above. We add the individual contributions from  $\mu^-$  and  $\mu^+$  events to estimate the total  $\chi^2$  for both the “2D” and “3D” schemes:

$$\chi^2_{\text{ICAL}} = \chi^2_- + \chi^2_+. \quad (5.5.5)$$

In our analysis, we simulate the prospective data considering the following benchmark values of the oscillation parameters:  $\sin^2 \theta_{23} = 0.5$ ,  $\sin^2 2\theta_{13} = 0.1$ ,  $\sin^2 \theta_{12} = 0.3$ ,  $\Delta m_{21}^2 = 7.5 \times 10^{-5} \text{ eV}^2$ , and  $|\Delta m_{\text{eff}}^2| = 2.4 \times 10^{-3} \text{ eV}^2$ . To estimate the value of  $\Delta m_{31}^2$  from  $\Delta m_{\text{eff}}^2$ , we use the Eq. 3.3.1,

where  $\Delta m_{\text{eff}}^2$  has the same magnitude for NH and IH with +ve and -ve signs respectively. In the fit, we first minimize  $\chi_{\text{ICAL}}^2$  (see Eq. 5.5.5) with respect to the “pull” variables  $\zeta_i$ , and then marginalize over the oscillation parameters  $\sin^2 \theta_{23}$  in the range  $[0.36, 0.66]$ ,  $|\Delta m_{\text{eff}}^2|$  in the range  $[2.1, 2.6] \times 10^{-3}$  eV<sup>2</sup>, and over both the choices of mass hierarchy, NH and IH, while keeping  $\theta_{12}$ ,  $\Delta m_{21}^2$ ,  $\sin^2 2\theta_{13}$  fixed at their benchmark values. We consider  $\delta_{\text{CP}} = 0^\circ$  throughout our analysis.

## 5.6 Results

### 5.6.1 Expected Bounds on NSI parameter $\varepsilon_{\mu\tau}$

We quantify the statistical significance of the analysis to constrain the NSI parameter  $\varepsilon_{\mu\tau}$  in the following fashion

$$\Delta\chi_{\text{ICAL-NSI}}^2 = \chi_{\text{ICAL}}^2(\text{SM} + \varepsilon_{\mu\tau}) - \chi_{\text{ICAL}}^2(\text{SM}) . \quad (5.6.1)$$

Here,  $\chi_{\text{ICAL}}^2(\text{SM})$  and  $\chi_{\text{ICAL}}^2(\text{SM} + \varepsilon_{\mu\tau})$  are calculated by fitting the prospective data with zero (the SM case) and non-zero value of NSI parameter  $\varepsilon_{\mu\tau}$  respectively. In our analysis procedure, statistical fluctuations are suppressed, and therefore,  $\chi_{\text{ICAL}}^2(\text{SM}) \approx 0$ .

Let us first identify the regions in  $\cos \theta_\mu$  and  $E_\mu$  plane which give significant contributions towards  $\Delta\chi_{\text{ICAL-NSI}}^2$ . In Fig. 5.4, we show the distribution<sup>4</sup> of  $\Delta\chi_{\text{ICAL-NSI}}^2$  from  $\mu^-$  events in the reconstructed  $[\cos \theta_\mu - E_\mu]$  plane using 500 kt·yr exposure of the ICAL detector and assuming NH. In all the panels of Fig. 5.4, we consider  $\varepsilon_{\mu\tau} = 0.05$  in the fit and show the results for the following four different choices of binning schemes and observables: i) top left panel: [LE, 2D], ii) top right panel: [LE, 3D], iii) bottom left panel: [HE, 2D], iv) bottom right panel: [HE, 3D]. We show the distribution of  $\Delta\chi_{\text{ICAL-NSI}}^2$  from  $\mu^+$  events in the plane of reconstructed  $\cos \theta_\mu$  and  $E_\mu$  for these four different cases in Fig. 5.5 considering  $\varepsilon_{\mu\tau} = 0.05$  in the fit. In left panels of Figs. 5.4 and Fig. 5.5, we show the sensitivity in the plane of reconstructed  $\cos \theta_\mu$  and  $E_\mu$  for the “2D” analysis, where we do not use any information on hadrons. But, in right panels of these figures, we portray the sensitivity in the plane of reconstructed  $\cos \theta_\mu$  and  $E_\mu$  for the “3D” case, where the events

<sup>4</sup>In Fig. 5.4, we do not consider the constant contributions in  $\chi^2$  coming from the term which involves five pull parameters  $\zeta_i^2$  in Eq. 5.5.1 and Eq. 5.5.3. Also, we do not marginalize over the oscillation parameters in the fit to produce these figures. We adopt the same strategy for Fig. 5.5 as well. Note that we show our final results considering full pull contributions and marginalizing over the oscillation parameters in the fit as mentioned in previous section.



are further divided into four sub-bins depending on the reconstructed hadron energy for LE (see Table 5.2) and HE binning schemes (see Table 5.3).

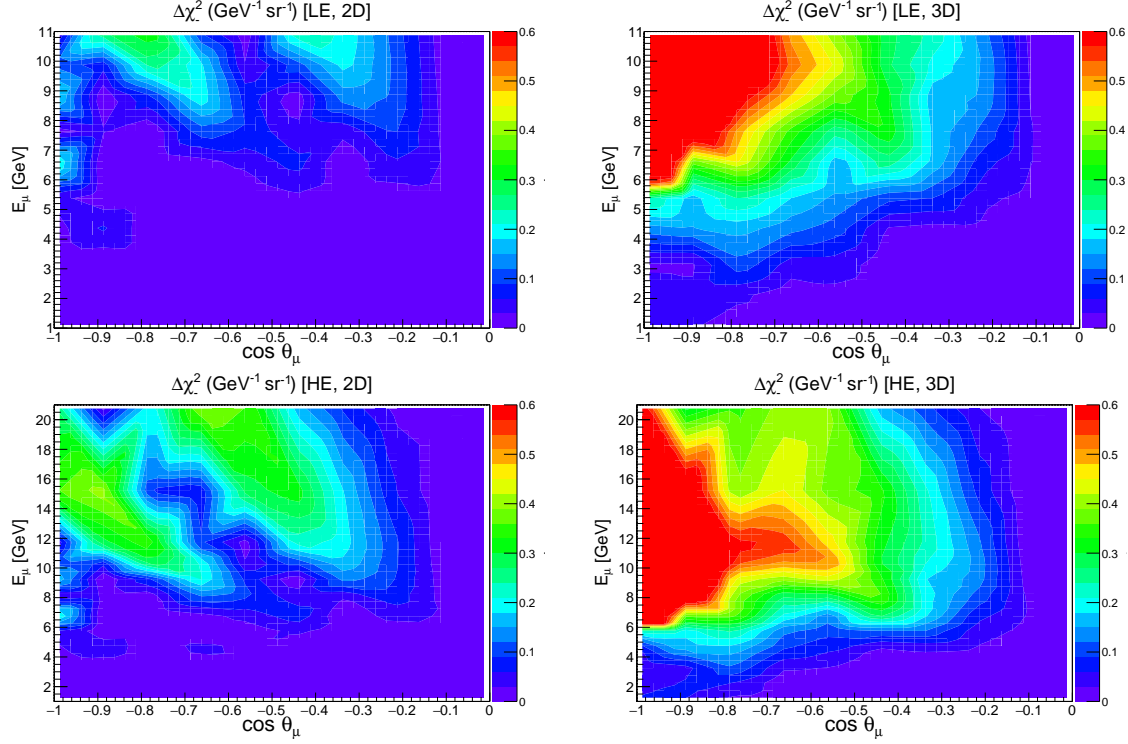


**Figure 5.4.** Distributions of  $\Delta\chi^2_{\text{ICAL-NSI}}$  (per unit area) from  $\mu^-$  events in reconstructed  $\cos\theta_\mu$  and  $E_\mu$  plane assuming non-zero  $\varepsilon_{\mu\tau}$  in the fit with a strength of 0.05. The top (bottom) panels are for the LE (HE) binning scheme. For a given binning scheme, left and right panels are obtained with  $[E_\mu, \cos\theta_\mu]$  and  $[E_\mu, \cos\theta_\mu, E'_{\text{had}}]$  respectively. In all the panels, we use 500 kt-yr exposure and assume NH in both data and theory.

The common features which are emerging from all the panels in Fig. 5.4 and Fig. 5.5 are that most of the sensitivity towards the NSI parameter  $\varepsilon_{\mu\tau}$  stems from higher energies and longer baselines where the matter effect term  $2\sqrt{2}G_F N_e E$  becomes sizeable. We observe similar trends in Fig. 5.2 where we plot the differences in  $\nu_\mu \rightarrow \nu_\mu$  oscillation probabilities for the cases  $\varepsilon_{\mu\tau} = 0$  and  $\varepsilon_{\mu\tau} = \pm 0.05$ . The event spectra as shown in Fig. 5.3 also confirm this fact. Fig. 5.4 and Fig. 5.5 clearly demonstrate while going from LE to HE binning scheme that the sensitivity towards the NSI parameter  $\varepsilon_{\mu\tau}$  get enhanced due to the increment in the range of  $E_\mu$  from 11 GeV to 21 GeV and for extending the fourth  $E'_{\text{had}}$  bin from 15 GeV to 25 GeV. We can also observe from these figures that with the addition of hadron energy information, the area in the  $E_\mu$ - $\cos\theta_\mu$  plane which contributes significantly to  $\Delta\chi^2_\pm$  increases, consequently enhancing the net  $\Delta\chi^2_\pm$  for both LE and HE binning schemes. Here, we would like to mention that the increase in  $\chi^2_\pm$  is not just due

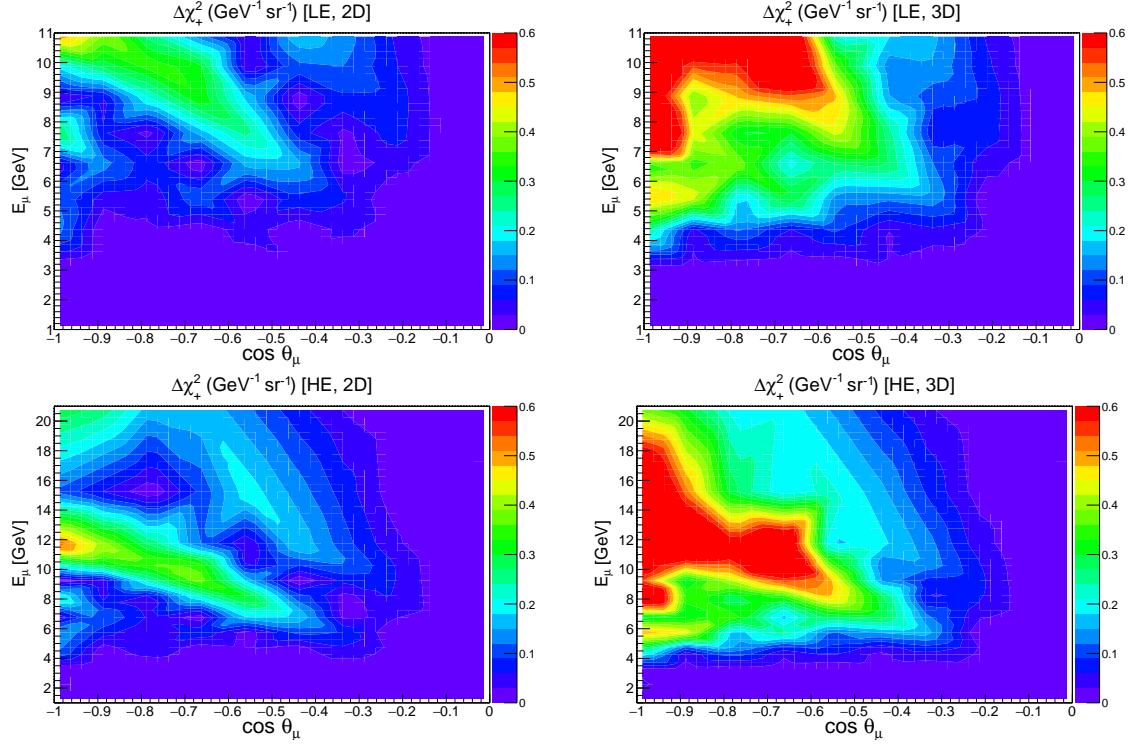


**Figure 5.5.** Distributions of  $\Delta\chi^2_{\text{ICAL-NSI}}$  (per unit area) from  $\mu^+$  events in reconstructed  $\cos\theta_\mu$  and  $E_\mu$  plane assuming non-zero  $\varepsilon_{\mu\tau}$  in the fit with a strength of 0.05. The top (bottom) panels are for the LE (HE) binning scheme. For a given binning scheme, left and right panels are obtained with  $[E_\mu, \cos\theta_\mu]$  and  $[E_\mu, \cos\theta_\mu, E'_{\text{had}}]$  respectively. In all the panels, we use 500 kt-yr exposure and assume NH in both data and theory.

to the information contained in  $E'_{\text{had}}$ , but also due to the valuable information coming from the correlation between  $E'_{\text{had}}$  and muon momentum ( $E_\mu, \cos\theta_\mu$ ).

In Fig. 5.6, we show the sensitivity of the ICAL detector to constrain  $\varepsilon_{\mu\tau}$  using an exposure of 500 kt-yr and assuming NH as the true mass hierarchy. We obtain these results after performing marginalization over  $\theta_{23}$ ,  $\Delta m_{\text{eff}}^2$ , and both the choices of mass hierarchy as discussed in Sec. 5.5.2. In the left (right) panel, the results are shown for the LE (HE) binning scheme. In each panel, the red solid line shows the sensitivity for the “3D” case where we consider  $E_\mu$ ,  $\cos\theta_\mu$ , and  $E'_{\text{had}}$  as observables. The black dashed line in each panel portrays the sensitivity for the “2D” case considering  $E_\mu$  and  $\cos\theta_\mu$  as observables. We see considerable improvement in the sensitivity for both the LE and HE binning schemes when we add  $E'_{\text{had}}$  along with  $E_\mu$  and  $\cos\theta_\mu$  as observables. We see significant gain in the sensitivity when we increase the  $E_\mu$  range from 11 GeV to 21 GeV and extend the fourth  $E'_{\text{had}}$  bin from 15 GeV to 25 GeV. It is evident from both the panels in Fig. 5.6

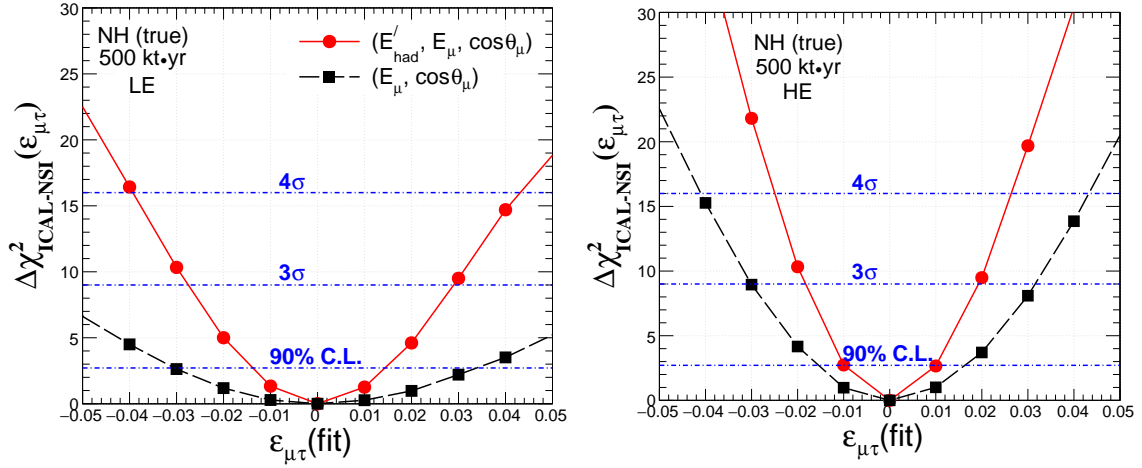


**Figure 5.6.** The sensitivity of the ICAL detector to set upper bounds on the NSI parameter  $\varepsilon_{\mu\tau}$  using 500 kt·yr exposure and assuming NH as true mass hierarchy. Left (right) panel is with LE (HE) binning scheme. In each panel, the red solid line shows the sensitivity for the "3D" where we consider  $E_\mu, \cos \theta_\mu$ , and  $E'_{\text{had}}$  as observables. The black dashed line in each panel portrays the sensitivity for the 2D case considering  $E_\mu$  and  $\cos \theta_\mu$  as observables. These results are obtained after performing marginalization over  $\theta_{23}$ ,  $\Delta m_{\text{eff}}^2$ , and both choices of mass hierarchy.

that for the [HE, 3D] case, we obtain the best sensitivity towards the NSI parameter  $\varepsilon_{\mu\tau}$ , whereas the [LE, 2D] mode gives the most conservative limits.

Observable	Binning scheme	Constraints at $3\sigma$ (90% C.L.)	
		NH (true)	IH (true)
$(E_\mu, \cos \theta_\mu)$	LE	$-0.06 < \varepsilon_{\mu\tau} < 0.07$ ( $-0.03 < \varepsilon_{\mu\tau} < 0.034$ )	$-0.062 < \varepsilon_{\mu\tau} < 0.07$ ( $-0.032 < \varepsilon_{\mu\tau} < 0.034$ )
	HE	$-0.03 < \varepsilon_{\mu\tau} < 0.031$ ( $-0.016 < \varepsilon_{\mu\tau} < 0.016$ )	$-0.032 < \varepsilon_{\mu\tau} < 0.032$ ( $-0.016 < \varepsilon_{\mu\tau} < 0.016$ )
$(E_\mu, \cos \theta_\mu, E'_{\text{had}})$	LE	$-0.028 < \varepsilon_{\mu\tau} < 0.03$ ( $-0.014 < \varepsilon_{\mu\tau} < 0.014$ )	$0.03 < \varepsilon_{\mu\tau} < 0.032$ ( $-0.015 < \varepsilon_{\mu\tau} < 0.016$ )
	HE	$-0.018 < \varepsilon_{\mu\tau} < 0.019$ ( $-0.01 < \varepsilon_{\mu\tau} < 0.01$ )	$-0.02 < \varepsilon_{\mu\tau} < 0.02$ ( $-0.01 < \varepsilon_{\mu\tau} < 0.01$ )

**Table 5.4.** The expected bound on  $\varepsilon_{\mu\tau}$  for four different choices of binning schemes and observables at  $3\sigma$  and 90% C.L. obtained using 500 kt·yr exposure of the ICAL detector. We give results for the both choices of true mass hierarchy. To obtain these constraints, we marginalize over  $\theta_{23}$ ,  $\Delta m_{\text{eff}}^2$ , and both the choices of mass hierarchy in the fit.

The  $3\sigma$  (90%) confidence level bounds on the flavor violating NSI parameter  $\varepsilon_{\mu\tau}$  obtained using 500 kt·yr exposure of the ICAL are listed in Table 5.4. The results are shown for true NH (3rd column) and true IH (4th column). For the [HE, 3D] case, we expect the best limit of  $-0.01 < \varepsilon_{\mu\tau} < 0.01$  at 90% C.L. using 500 kt·yr exposure of the ICAL detector and irrespective of the

choices of true mass hierarchy. For the [LE, 2D] mode, we obtain the most conservative limit of  $-0.03 < \varepsilon_{\mu\tau} < 0.034$  at 90% confidence level assuming NH as true choice.

### 5.6.2 Advantage of having Charge Identification Capability

As discussed in Sec. 3.1.2, the ICAL detector is expected to have a uniform magnetic field of strength around 1.5 Tesla over the entire detector. It will enable the ICAL detector to identify the  $\mu^-$  and  $\mu^+$  events separately by observing the bending of their tracks in the opposite directions in the presence of the magnetic field. We label this feature of ICAL as the charge identification (CID) capability. In Ref. [202], it has been demonstrated that the ICAL detector will have a very good CID efficiency over a wide range of reconstructed  $E_\mu$  and  $\cos\theta_\mu$ . In this work, we estimate for the first time the gain in the sensitivity that ICAL may have in constraining the NSI parameter  $\varepsilon_{\mu\tau}$  due to its CID capability. In each panel of Fig. 5.7, we show the expected sensitivity of ICAL in constraining  $\varepsilon_{\mu\tau}$  with (red solid line) and without (black dashed line) CID capability using 500 kt-yr exposure and assuming NH. While preparing these plots, we keep the oscillation parameters fixed in the fit and depict the result for the 2D:  $E_\mu, \cos\theta_\mu$  (3D:  $E_\mu, \cos\theta_\mu, E'_{\text{had}}$ ) mode in the left (right) panel assuming the HE binning scheme. It is apparent from Fig. 5.7 that the CID capability of ICAL in distinguishing  $\mu^-$  and  $\mu^+$  events plays an important role to make it sensitive to the NSI parameter  $\varepsilon_{\mu\tau}$  like the mass hierarchy measurements [42, 49]. In the following, we quote the 90%

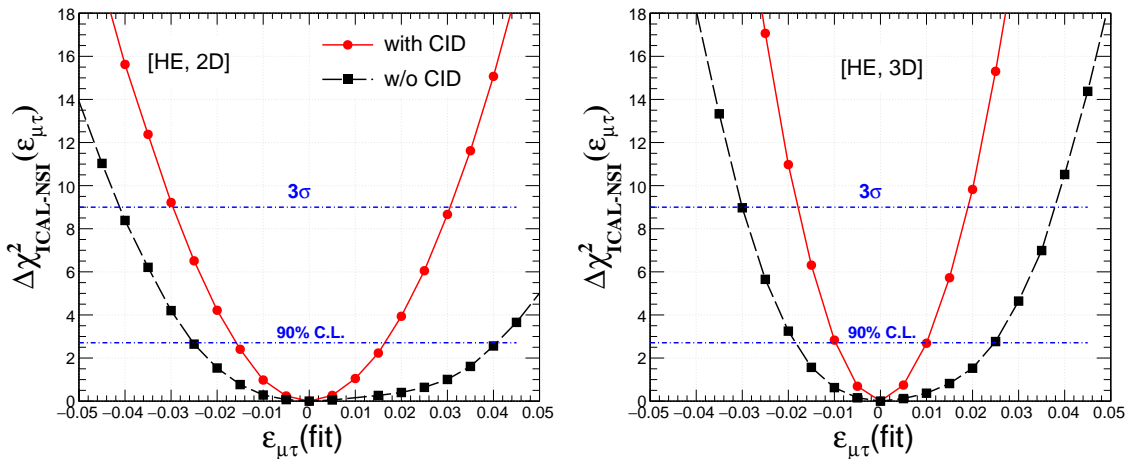


**Figure 5.7.** In each panel, the red solid (black dashed) line shows the expected sensitivity on  $\varepsilon_{\mu\tau}$  with (without) charge identification capability of ICAL. The left (right) panel is for the 2D:  $E_\mu, \cos\theta_\mu$  (3D:  $E_\mu, \cos\theta_\mu, E'_{\text{had}}$ ) mode assuming the HE binning scheme. We consider 500 kt-yr exposure and NH. Here, we keep all the oscillation parameters fixed in the fit (fixed parameter scenario).

confidence level limits on  $\varepsilon_{\mu\tau}$  that the ICAL detector can place with and without CID capabilities for [HE, 2D] and [HE, 3D] modes.

- [HE, 2D] mode (left panel of Fig. 5.7):

$$\begin{aligned} \text{with CID :} & \quad -0.015 < \varepsilon_{\mu\tau} < 0.017 & \text{at 90\% C.L. ,} \\ \text{without CID :} & \quad -0.025 < \varepsilon_{\mu\tau} < 0.04 & \text{at 90\% C.L.} \end{aligned} \quad (5.6.2)$$

- [HE, 3D] mode (right panel of Fig. 5.7):

$$\begin{aligned} \text{with CID :} & \quad -0.01 < \varepsilon_{\mu\tau} < 0.011 & \text{at 90\% C.L. ,} \\ \text{without CID :} & \quad -0.018 < \varepsilon_{\mu\tau} < 0.025 & \text{at 90\% C.L.} \end{aligned} \quad (5.6.3)$$

The limits on  $\varepsilon_{\mu\tau}$  mentioned in Eq. 5.6.2 and Eq. 5.6.3 clearly demonstrate the improvement that the ICAL detector can have in constraining the NSI parameter  $\varepsilon_{\mu\tau}$  due its CID capability.

### 5.6.3 Impact of non-zero $\varepsilon_{\mu\tau}$ on Mass Hierarchy Determination

This section is devoted to study how the flavor violating NSI parameter  $\varepsilon_{\mu\tau}$  affects the mass hierarchy measurement which is the prime goal of the ICAL detector. We quantify the performance ICAL to rule out the wrong hierarchy by adopting the following  $\chi^2$  expression:

$$\Delta\chi^2_{\text{ICAL-MH}} = \chi^2_{\text{ICAL}}(\text{false MH}) - \chi^2_{\text{ICAL}}(\text{true MH}) . \quad (5.6.4)$$

Here, we obtain  $\chi^2_{\text{ICAL}}(\text{true MH})$  and  $\chi^2_{\text{ICAL}}(\text{false MH})$  by performing the fit to the prospective data assuming true and false mass hierarchy respectively. Since the statistical fluctuations are suppressed in our analysis,  $\chi^2_{\text{ICAL}}(\text{true MH}) \approx 0$ . First, we estimate the sensitivity of the ICAL detector to determine the neutrino mass hierarchy by adopting the procedure as outlined in Ref. [49] for the standard case, which we denote as “ $\Delta\chi^2_{\text{ICAL-MH}}(\text{SM})$ ” in the third column of Table 5.5. Next, to estimate the mass hierarchy sensitivity in the presence of non-zero  $\varepsilon_{\mu\tau}$ , we adopt the following strategy. We generate the data with a given mass hierarchy assuming  $\varepsilon_{\mu\tau} = 0$ . Then, while fitting the prospective data with the opposite hierarchy, we introduce  $\varepsilon_{\mu\tau}$  in the fit and marginalize over it in the range of - 0.1 to 0.1 along with the oscillation parameters  $\theta_{23}$  and  $\Delta m^2_{\text{eff}}$  in their allowed

True MH	Analysis Mode	$\Delta\chi^2_{\text{ICAL-MH}}(\text{SM})$	$\Delta\chi^2_{\text{ICAL-MH}}(\text{SM} + \varepsilon_{\mu\tau})$	Reduction
LE binning scheme				
NH	$(E_\mu, \cos \theta_\mu)$	5.62	4.81	14.4%
	$(E_\mu, \cos \theta_\mu, E'_{\text{had}})$	8.66	7.49	13.5%
IH	$(E_\mu, \cos \theta_\mu)$	5.31	4.14	22.0%
	$(E_\mu, \cos \theta_\mu, E'_{\text{had}})$	8.48	6.88	18.9%
HE binning scheme				
NH	$(E_\mu, \cos \theta_\mu)$	5.96	5.37	9.9%
	$(E_\mu, \cos \theta_\mu, E'_{\text{had}})$	9.13	8.16	10.6%
IH	$(E_\mu, \cos \theta_\mu)$	5.66	4.95	12.5%
	$(E_\mu, \cos \theta_\mu, E'_{\text{had}})$	8.99	7.66	14.8%

**Table 5.5.** The mass hierarchy sensitivity of the ICAL detector using 500 kt·yr exposure. For the “SM” case (third column), we do not consider  $\varepsilon_{\mu\tau}$  in data and in fit. For the “SM +  $\varepsilon_{\mu\tau}$ ” case (fourth column), we introduce  $\varepsilon_{\mu\tau}$  in the fit and marginalize over it in the range of  $[-0.1, 0.1]$  along with oscillation parameters  $\theta_{23}$  and  $\Delta m_{\text{eff}}^2$ . Last column shows how much the mass hierarchy sensitivity deteriorates in presence of  $\varepsilon_{\mu\tau}$  as compared to the SM case. We present our results for various choices of binning schemes and observables assuming both true NH and true IH.

ranges as mentioned in Sec. 5.5. We label this result as “ $\Delta\chi^2_{\text{ICAL-MH}}(\text{SM} + \varepsilon_{\mu\tau})$ ” in the fourth column of Table 5.5. We show our results for various choices of binning schemes and observables assuming both true NH and true IH. We consider 500 kt·yr exposure of the ICAL detector. We can see from Table 5.5 that depending on the choice of true mass hierarchy and the analysis mode, the mass hierarchy sensitivity of ICAL gets reduced by 10 to 20% due to the presence of non-zero  $\varepsilon_{\mu\tau}$  in the fit.

#### 5.6.4 Precision Measurement of Atmospheric Parameters with non-zero $\varepsilon_{\mu\tau}$

Next, we turn our attention to the precise measurement of atmospheric oscillation parameters  $\sin^2 \theta_{23}$  and  $|\Delta m_{32}^2|$  using 500 kt·yr exposure of the ICAL detector. We quantify this performance indicator using the following expression:

$$\Delta\chi^2_{\text{ICAL-PM}}(\sin^2 \theta_{23}, |\Delta m_{32}^2|) = \chi^2_{\text{ICAL}}(\sin^2 \theta_{23}, |\Delta m_{32}^2|) - \chi_0^2, \quad (5.6.5)$$

where  $\chi_0^2$  is the minimum value of  $\chi^2_{\text{ICAL}}$  in the allowed parameter range. Since we suppress the statistical fluctuations, we have  $\chi_0^2 \approx 0$ . First, considering  $\sin^2 \theta_{23}(\text{true}) = 0.5$  and  $|\Delta m_{32}^2|(\text{true}) = 2.4 \times 10^{-3} \text{ eV}^2$ , we estimate the allowed regions in  $\sin^2 \theta_{23} - |\Delta m_{32}^2|$  (test) plane in the absence of  $\varepsilon_{\mu\tau}$  at 90% C.L. (2 d.o.f.). We show these results for the “SM” case using solid lines in Fig. 5.8 for

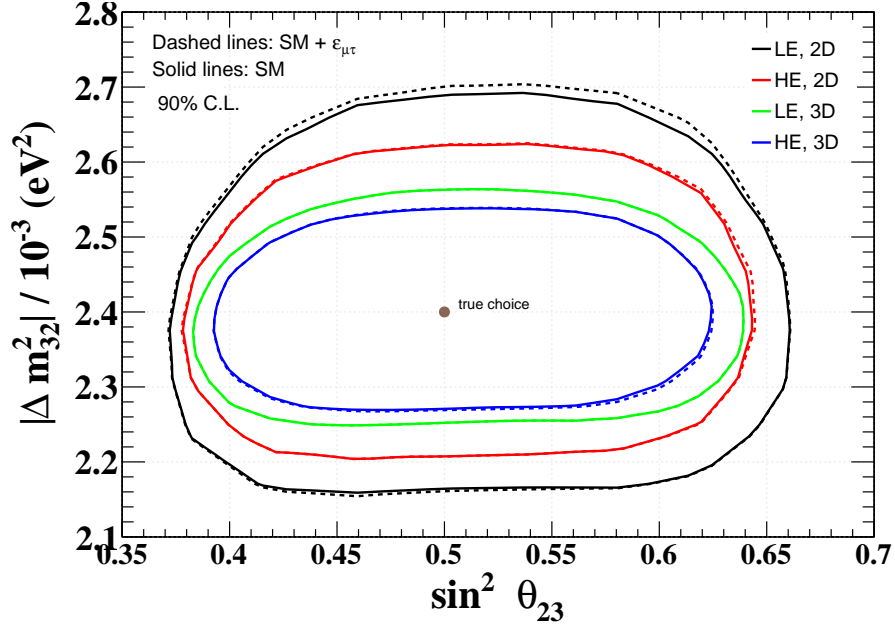


**Figure 5.8.** 90% C.L. (2 d.o.f.) allowed regions in  $\sin^2 \theta_{23}$  -  $|\Delta m_{32}^2|$  plane for 500 kt-yr exposure of the ICAL detector assuming NH. The brown dot represents the true choices of  $\sin^2 \theta_{23}$  and  $|\Delta m_{32}^2|$ . The solid lines show the results for the “SM” case, where we do not consider  $\varepsilon_{\mu\tau}$  in data and in fit. The dashed lines portray the results when we introduce  $\varepsilon_{\mu\tau}$  in the fit and marginalize over its  $\pm 10\%$  range. For other details, see text.

various analysis modes. For the [HE, 3D] case, we achieve the best precision for the atmospheric parameters, and for the [LE, 2D] case, we have the most conservative results.

Next, we study the impact of non-zero  $\varepsilon_{\mu\tau}$  in the precision measurement of atmospheric parameters in the following fashion. We again generate the prospective data considering the true values of  $\sin^2 \theta_{23}$  and  $|\Delta m_{32}^2|$  as mentioned above. Then, while estimating the allowed regions in  $\sin^2 \theta_{23}$  -  $|\Delta m_{32}^2|$  (test) plane, we introduce  $\varepsilon_{\mu\tau}$  in the fit and marginalize over it in the range of  $[-0.1, 0.1]$ . We present these results for the “SM +  $\varepsilon_{\mu\tau}$ ” case at 90% C.L. (2 d.o.f.) with the help of dashed lines in Fig. 5.8 for various analysis modes. We do not see any appreciable change in the contours when we introduce  $\varepsilon_{\mu\tau}$  in the fit and vary in its  $\pm 10\%$  range. It suggests that the precision measurement of atmospheric oscillation parameters at the ICAL detector is quite robust even if we marginalize over  $\varepsilon_{\mu\tau}$  in the fit. Similar results were obtained by the Super-Kamiokande Collaboration in Ref. [318], where they studied the impact of NSI’s in  $\nu_\mu$ - $\nu_\tau$  sector using their Phase I and Phase II atmospheric data.

## 5.7 Summary and Concluding Remarks

In this chapter, we explore the possibility of lepton flavor violating neutral current non-standard interactions (NSI's) of atmospheric neutrino and antineutrino while they travel long distances inside the Earth matter before reaching to the ICAL detector. During the propagation of these neutrinos, we allow an extra interaction vertex with  $\nu_\mu$  as the incoming particle and  $\nu_\tau$  as the outgoing one and vice versa. With such an interaction vertex, the neutral current non-standard interaction of neutrino with matter fermions gives rise to a new matter potential whose relative strength as compared to the standard matter potential ( $V_{CC}$ ) is denoted by  $\varepsilon_{\mu\tau}$ .

We show that the ICAL detector would be able to place tight constraints on the NSI parameter  $\varepsilon_{\mu\tau}$  considering reconstructed hadron energy and muon momentum as observables. We find that with  $E_\mu \in [1, 11]$  GeV and with  $[E_\mu, \cos \theta_\mu]$  as observables, the expected limit on  $\varepsilon_{\mu\tau}$  at 90% C.L. is  $-0.03 < \varepsilon_{\mu\tau} < 0.03$ . If we increase the muon energy range from 11 to 21 GeV ( $E_\mu \in [1, 21]$  GeV) and consider the reconstructed hadron energy ( $E'_{\text{had}}$ ) as an extra observable on top of the four momenta of muon ( $E_\mu, \cos \theta_\mu$ ), we find a significant improvement in the limit which is  $-0.01 < \varepsilon_{\mu\tau} < 0.01$  at 90% C.L. using 500 kt-yr exposure of the ICAL detector. We observe that the charge identification capability of the ICAL detector plays an important role to obtain these tight constraints on  $\varepsilon_{\mu\tau}$  as mentioned above.

Assuming 1 to 21 GeV reconstructed muon energy range and considering  $E_\mu$ ,  $\cos \theta_\mu$ , and  $E'_{\text{had}}$  as observables, we find that the mass hierarchy sensitivity at the ICAL detector deteriorates by  $\sim 10\%$  if we introduce the NSI parameter  $\varepsilon_{\mu\tau}$  in the fit and marginalize over it in the range of -0.1 to 0.1 along with other standard oscillation parameters. On the other hand, the precision measurement of atmospheric oscillation parameters at the ICAL detector is quite robust even if we marginalize over the NSI parameter  $\varepsilon_{\mu\tau}$  in fit in the range -0.1 to 0.1.



# 6 Long-Range Force

## Contents

---

<b>6.1 Introduction and Motivation . . . . .</b>	<b>109</b>
<b>6.2 Three-Flavor Neutrino Oscillation with Long-Range Forces. . . . .</b>	<b>111</b>
6.2.1 Modification of Oscillation Parameters	113
6.2.2 Comparison between Analytical and Numerical Results	118
<b>6.3 Neutrino Oscillograms in <math>(E_\nu, \cos \theta_\nu)</math> Plane . . . . .</b>	<b>120</b>
6.3.1 Oscillograms for $\nu_e \rightarrow \nu_\mu$ Appearance Channel	121
6.3.2 Oscillograms for $\nu_\mu \rightarrow \nu_\mu$ Disappearance Channel	122
<b>6.4 Event Spectrum in the ICAL Detector . . . . .</b>	<b>123</b>
<b>6.5 Simulation Procedure. . . . .</b>	<b>125</b>
6.5.1 Binning Scheme for Observables $(E_\mu, \cos \theta_\mu, E'_{\text{had}})$	125
6.5.2 Numerical Analysis	126
<b>6.6 Results . . . . .</b>	<b>126</b>
<b>6.7 Summary and Conclusions . . . . .</b>	<b>129</b>

---

## 6.1 Introduction and Motivation

One of the possible ways to extend the SM gauge group  $SU(3)_C \times SU(2)_L \times U(1)_Y$  with minimal matter content is by introducing anomaly free  $U(1)$  symmetries with the gauge quantum number (for vectorial representations) [323, 324]

$$Q = a_0(B - L) + a_1(L_e - L_\mu) + a_2(L_e - L_\tau) + a_3(L_\mu - L_\tau). \quad (6.1.1)$$

Here,  $B$  and  $L$  are baryon and lepton numbers respectively.  $L_i$  are lepton flavor numbers and  $a_i$  with  $i = 0, 1, 2, 3$  are arbitrary constants. Note that the SM remains invariant and renormalizable if we extend its gauge group in the above way [325]. There are three lepton flavor combinations: i)  $L_e - L_\mu$  ( $a_1 = 1, a_{0,2,3} = 0$ ), ii)  $L_e - L_\tau$  ( $a_2 = 1, a_{0,1,3} = 0$ ), and iii)  $L_\mu - L_\tau$  ( $a_3 = 1, a_{0,1,2} = 0$ ), which can be gauged in an anomaly free way with the particle content of the SM [326–329]. Over the last two decades, it has been confirmed that neutrinos do oscillate from one flavor to another, which requires that they should have non-degenerate masses and mix among each other [4]. To make it happen, the above mentioned U(1) gauge symmetries have to be broken in Nature [330, 331]. It is quite obvious that the resultant gauge boson should couple to matter very weakly to escape direct detection. On top of it, if the extra gauge boson associated with this abelian symmetry is very light, then it can give rise to long-range force having terrestrial range (greater than or equal to the Sun-Earth distance) [330, 332, 333]. Interestingly, this LRF depends on the leptonic content and the mass of an object. Therefore it violates the universality of free fall which can be tested in the classic lunar ranging [334, 335], and Eötvös type gravity experiments [336, 337]. Lee and Yang gave this idea long back in Ref. [338]. Later, Okun used their idea and gave a  $2\sigma$  bound on  $\alpha < 3.4 \times 10^{-49}$  ( $\alpha$  stands for the strength of long-range potential) for a range of the Sun-Earth distance or more [339, 340].

The coupling of the solar electron to  $L_e - L_{\mu/\tau}$  gauge boson leads to a flavor-dependent long-range potential for neutrinos [341–343], which can affect neutrino oscillations [330–333, 344, 345] in spite of such tight constraint on  $\alpha$  as mentioned above. Here,  $(L_e - L_{\mu/\tau})$ -charge of  $\nu_e$  is opposite to that of  $\nu_\mu$  or  $\nu_\tau$ , which results in new non-universal flavor-diagonal neutral current (FDNC) interactions of neutrinos. These new interactions along with the standard  $W$ -exchange interactions between ambient electrons and propagating  $\nu_e$  in matter can alter the effective values of oscillation parameters in non-trivial fashion [346]. For an example, the electrons inside the Sun can generate a flavor-dependent long-range potential  $V_{e\mu/e\tau}$  at the Earth surface which has the following form [330, 331],

$$V_{e\mu/e\tau}(R_{SE}) = \alpha_{e\mu/e\tau} \frac{N_e^\odot}{R_{SE}} \approx 1.3 \times 10^{-14} \text{ eV} \left( \frac{\alpha_{e\mu/e\tau}}{10^{-53}} \right), \quad (6.1.2)$$

where  $\alpha_{e\mu/e\tau} = \frac{g_{e\mu/e\tau}^2}{4\pi}$  is the “fine structure constant” of the new abelian symmetry and  $g_{e\mu/e\tau}$  is the corresponding gauge coupling. In above equation,  $N_e^\odot$  denotes the total number of electrons ( $\approx 10^{57}$ ) in the Sun [347] and  $R_{SE}$  is the Sun-Earth distance  $\approx 1.5 \times 10^{13} \text{ cm} = 7.6 \times 10^{26}$

$\text{GeV}^{-1}$ . The LRF potential  $V_{e\mu/e\tau}$  in Eq. 6.1.2 comes with a negative sign for antineutrinos and can be probed separately in ICAL along with the corresponding potential for neutrinos. The LRF potential due to the electrons inside the Earth with the Earth-radius range ( $R_E \sim 6400 \text{ km}$ ) is roughly one order of magnitude smaller as compared to the potential due to the Sun. Therefore, we safely neglect the contributions coming from the Earth [330, 331].

There are already tight constraints on the effective gauge coupling  $\alpha_{e\mu/e\tau}$  of  $L_e - L_{\mu/\tau}$  abelian symmetry using the data from various neutrino oscillation experiments. In Ref. [330], an upper bound of  $\alpha_{e\mu} < 5.5 \times 10^{-52}$  at 90% C.L. was obtained using the atmospheric neutrino data of the Super-Kamiokande experiment. The corresponding limit on  $\alpha_{e\tau}$  is  $< 6.4 \times 10^{-52}$  at 90% confidence level. A global fit of the solar neutrino and KamLAND data in the presence of LRF was performed in [331]. They gave an upper bound of  $\alpha_{e\mu} < 3.4 \times 10^{-53}$  at  $3\sigma$  C.L. assuming  $\theta_{13} = 0^\circ$ . Their limit on  $\alpha_{e\tau}$  is  $< 2.5 \times 10^{-53}$  at  $3\sigma$ . In Ref. [344], the authors performed a similar analysis to derive the limits on LRF mediated by vector and non-vector (scalar or tensor) neutral bosons assuming one mass scale dominance. A preliminary study to constrain the LRF parameters in the context of ICAL detector was carried out in Ref. [345]. Using an exposure of one Mton-yr and considering only the muon momentum as observable, an expected upper bound of  $\alpha_{e\mu/e\tau} \lesssim 1.65 \times 10^{-53}$  at  $3\sigma$  was obtained for ICAL.

In this chapter, we investigate in detail the possible impacts of non-universal flavor-diagonal neutral current long-range interactions in the oscillations of neutrinos and antineutrinos in the context of INO-ICAL experiment. These new interactions come into the picture due to flavor-dependent, vector-like, leptonic long-range force (LRF), like those mediated by the  $L_e - L_\mu$  or  $L_e - L_\tau$  gauge boson, which is very light and neutral.

In Sec. 6.2, we study in detail how the three-flavor oscillation picture gets modified in presence of long-range potential. We present compact analytical expressions for the effective oscillations parameters in presence of LRF. Next, we show the accuracy of our analytical probability expressions (for  $L_e - L_\tau$ ) by comparing them with the exact numerical results. In Appendix B, we perform the similar comparison for the  $L_e - L_\mu$  symmetry. In Sec. 6.3, we draw the neutrino oscillograms in  $(E_\nu, \cos \theta_\nu)$  plane for  $\nu_e \rightarrow \nu_\mu$  and  $\bar{\nu}_\mu \rightarrow \bar{\nu}_e$  oscillation channels in presence of  $L_e - L_{\mu,\tau}$  symmetry. In Sec. 6.4, we show the expected event spectra in ICAL with and without LRF. Sec. 6.5 deals with

the simulation procedure that we adopt in this work. Next, we derive the expected constraints on  $\alpha_{e\mu, e\tau}$  from ICAL in Sec. 6.6, and discuss few other interesting results. Finally, we summarize and draw our conclusions in Sec. 6.7.

## 6.2 Three-Flavor Neutrino Oscillation with Long-Range Forces

In this section, we discuss how the flavor-dependent long-range potential due to the electrons inside the sun modify the oscillation of terrestrial neutrinos. In presence of LRF, the effective Hamiltonian (in the flavor basis) for neutrino propagation inside the Earth is given by

$$H_f = U \begin{bmatrix} 0 & 0 & 0 \\ 0 & \frac{\Delta m_{21}^2}{2E} & 0 \\ 0 & 0 & \frac{\Delta m_{31}^2}{2E} \end{bmatrix} U^\dagger + \begin{bmatrix} V_{CC} & 0 & 0 \\ 0 & 0 & 0 \\ 0 & 0 & 0 \end{bmatrix} + \begin{bmatrix} \zeta & 0 & 0 \\ 0 & \xi & 0 \\ 0 & 0 & \eta \end{bmatrix}, \quad (6.2.1)$$

where  $U$  is the vacuum PMNS matrix [144, 145, 153],  $E$  denotes the energy of neutrino, and  $V_{CC}$  represents the Earth matter potential which can be expressed as

$$V_{CC} = \sqrt{2} G_F N_e \simeq 7.6 \times 10^{-14} \times Y_e \times \rho [\text{g/cm}^3] \text{ eV}. \quad (6.2.2)$$

In above,  $G_F$  is the Fermi coupling constant,  $N_e$  is the number density of electron inside the Earth,  $\rho$  stands for matter density, and  $Y_e (\frac{N_e}{N_p + N_n})$  is the relative electron number density. Here,  $N_p$  and  $N_n$  are the proton and neutron densities respectively. For an electrically neutral and isoscalar medium,  $N_e = N_p = N_n$  and therefore,  $Y_e = 0.5$ . In Eq. 6.2.1,  $\zeta$ ,  $\xi$ , and  $\eta$  appear due to the long-range potential. In case of  $L_e - L_\mu$  symmetry,  $\zeta = -\xi = V_{e\mu}$  with  $\eta = 0$ . On the other hand, if the underlying symmetry is  $L_e - L_\tau$ , then  $\zeta = -\eta = V_{e\tau}$  with  $\xi = 0$ . Here,  $V_{e\mu}$  ( $V_{e\tau}$ ) is the LRF potential due to the interactions mediated by neutral gauge boson corresponding to  $L_e - L_\mu$  ( $L_e - L_\tau$ ) symmetry. Since the strength of  $V_{e\mu/e\tau}$  (see Eq. 6.1.2) does not depend on the Earth matter density, hence its value remains same for all the baselines. In case of antineutrino, the sign of  $V_{CC}$ ,  $V_{e\mu}$ ,  $V_{e\tau}$ , and  $\delta_{CP}$  will be reversed.

It is evident from Eq. 6.2.1 that if the strength of  $V_{e\mu/e\tau}$  is comparable to  $\Delta m_{31}^2/2E$  and  $V_{CC}$ , then LRF would certainly affect the neutrino propagation. Now, let us consider some benchmark

choices of energies ( $E$ ) and baselines ( $L$ ) for which the above mentioned quantities are comparable in the context of ICAL detector. This detector is quite efficient to detect neutrinos and antineutrinos separately in multi-GeV energy range with baselines in the range of 2000 to 8000 km where we have substantial Earth matter effect. Therefore, in Table 6.1, we show the comparison for three choices of  $E$  and  $L$ : (2 GeV, 2000 km), (5 GeV, 5000 km), and (15 GeV, 8000 km). Using Eq. 6.2.2, we estimate the size of  $V_{CC}$  for these three baselines for which the line-averaged constant Earth matter densities ( $\rho$ ) based on the PREM [348] profile are 3.46 g/cm<sup>3</sup>, 3.9 g/cm<sup>3</sup>, and 4.26 g/cm<sup>3</sup> respectively. From Eq. 6.1.2, we obtain the values of  $V_{e\mu/e\tau}$  for two benchmark choices of  $\alpha_{e\mu/e\tau}$ :  $10^{-52}$  and  $3 \times 10^{-53}$  (see last column of Table 6.1). We compute the value of  $\Delta m_{31}^2/2E$  assuming the best fit value of  $\Delta m_{31}^2 = 2.524 \times 10^{-3} \text{ eV}^2$  [14]. Table 6.1 shows that the quantities  $\Delta m_{31}^2/2E$ ,  $V_{CC}$ , and  $V_{e\mu/e\tau}$  are of comparable strengths for our benchmark choices of  $E$ ,  $L$ , and  $\alpha_{e\mu/e\tau}$ . It suggests that they can interfere with each other to alter the oscillation probabilities significantly. Next, we study the modification of oscillation parameters in matter in presence of LRF potential.

$L$ (km) ( $\cos \theta_\nu$ )	$E$ (GeV)	$\frac{\Delta m_{31}^2}{2E}$ (eV)	$V_{CC}$ (eV)	$V_{e\mu/e\tau}$ (eV)	
				$\alpha_{e\mu/e\tau} = 10^{-52}$	$\alpha_{e\mu/e\tau} = 3 \times 10^{-53}$
2000 (-0.15)	2	$6.3 \times 10^{-13}$	$1.3 \times 10^{-13}$	$1.3 \times 10^{-13}$	$0.39 \times 10^{-13}$
5000 (-0.39)	5	$2.5 \times 10^{-13}$	$1.5 \times 10^{-13}$	$1.3 \times 10^{-13}$	$0.39 \times 10^{-13}$
8000 (-0.63)	15	$0.84 \times 10^{-13}$	$1.6 \times 10^{-13}$	$1.3 \times 10^{-13}$	$0.39 \times 10^{-13}$

**Table 6.1.** The values of  $\Delta m_{31}^2/2E$  (third column),  $V_{CC}$  (fourth column), and  $V_{e\mu/e\tau}$  (fifth column) for our benchmark choices of  $E$ ,  $L$ , and  $\alpha_{e\mu/e\tau}$ . We take  $\Delta m_{31}^2 = 2.524 \times 10^{-3} \text{ eV}^2$ . Based on the PREM profile, the line-averaged constant Earth matter densities for 2000 km, 5000 km, and 8000 km baselines are 3.46 g/cm<sup>3</sup>, 3.9 g/cm<sup>3</sup>, and 4.26 g/cm<sup>3</sup> respectively. The parameter  $\theta_\nu$  is the zenith angle for a given baseline.

### 6.2.1 Modification of Oscillation Parameters

The approximate analytical expressions for the effective mass-squared differences and mixing angles in presence of  $V_{CC}$  and  $V_{e\mu}$  (due to  $L_e - L_\mu$  symmetry) have been given in Ref. [333]. In this chapter, we derive the analytical expressions for  $L_e - L_\tau$  symmetry. Assuming  $\delta_{CP} = 0^\circ$ , the effective Hamiltonian can be written as

$$H_f = R_{23}(\theta_{23}) R_{13}(\theta_{13}) R_{12}(\theta_{12}) H_0 R_{12}^T(\theta_{12}) R_{13}^T(\theta_{13}) R_{23}^T(\theta_{23}) + V, \quad (6.2.3)$$

where for the PMNS matrix ( $U$ ), we follow the CKM parameterization [4]. In the above equation,  $H_0 = \text{Diag}(0, \Delta_{21}, \Delta_{31})$  with  $\Delta_{21} \equiv \Delta m_{21}^2/2E$  and  $\Delta_{31} \equiv \Delta m_{31}^2/2E$ . For  $L_e - L_\tau$  symmetry,  $V = \text{Diag}(V_{CC} + V_{e\tau}, 0, -V_{e\tau})$ . Considering maximal mixing for  $\theta_{23}$  ( $= 45^\circ$ ), we rewrite  $H_f$  in the following way

$$H_f = \Delta_{31} \begin{pmatrix} b_{11} & b_{12} & b_{13} \\ b_{12} & b_{22} & b_{23} \\ b_{13} & b_{23} & b_{33} \end{pmatrix}, \quad (6.2.4)$$

where

$$b_{11} = A + W + \sin^2 \theta_{13} + \alpha \sin^2 \theta_{12} \cos^2 \theta_{13}, \quad (6.2.5)$$

$$b_{12} = \frac{1}{\sqrt{2}} \left[ \cos \theta_{13} (\alpha \cos \theta_{12} \sin \theta_{12} + \sin \theta_{13} - \alpha \sin^2 \theta_{12} \sin \theta_{13}) \right], \quad (6.2.6)$$

$$b_{13} = \frac{1}{\sqrt{2}} \left[ \cos \theta_{13} (-\alpha \cos \theta_{12} \sin \theta_{12} + \sin \theta_{13} - \alpha \sin^2 \theta_{12} \sin \theta_{13}) \right], \quad (6.2.7)$$

$$b_{22} = \frac{1}{2} \left[ \cos^2 \theta_{13} + \alpha \cos^2 \theta_{12} - \alpha \sin 2\theta_{12} \sin \theta_{13} + \alpha \sin^2 \theta_{12} \sin^2 \theta_{13} \right], \quad (6.2.8)$$

$$b_{23} = \frac{1}{2} \left[ \cos^2 \theta_{13} - \alpha \cos^2 \theta_{12} + \alpha \sin^2 \theta_{12} \sin^2 \theta_{13} \right], \quad (6.2.9)$$

$$b_{33} = \frac{1}{2} \left[ \cos^2 \theta_{13} + \alpha \cos^2 \theta_{12} + \alpha \sin 2\theta_{12} \sin \theta_{13} + \alpha \sin^2 \theta_{12} \sin^2 \theta_{13} - 2W \right]. \quad (6.2.10)$$

In the above equations, the terms  $A$ ,  $W$ , and  $\alpha$  are defined as

$$A \equiv \frac{V_{CC}}{\Delta_{31}} = \frac{2EV_{CC}}{\Delta m_{31}^2}, \quad W \equiv \frac{V_{e\tau}}{\Delta_{31}} = \frac{2EV_{e\tau}}{\Delta m_{31}^2}, \quad \text{and } \alpha \equiv \frac{\Delta m_{21}^2}{\Delta m_{31}^2}. \quad (6.2.11)$$

The following unitary matrix  $\tilde{U}$  can almost diagonalize the effective Hamiltonian ( $H_f$ ):

$$\tilde{U} \equiv R_{23}(\theta_{23}^m) R_{13}(\theta_{13}^m) R_{12}(\theta_{12}^m), \quad (6.2.12)$$

such that

$$\tilde{U}^T H_f \tilde{U} \simeq \text{Diag}(m_{1,m}^2/2E, m_{2,m}^2/2E, m_{3,m}^2/2E). \quad (6.2.13)$$

In the above equation, we neglect the off-diagonal terms which are small. Diagonalizing the (2, 3) block of  $H_f$ , we get the following expression for  $\theta_{23}^m$

$$\tan 2\theta_{23}^m = \frac{\cos^2 \theta_{13} - \alpha \cos^2 \theta_{12} + \alpha \sin^2 \theta_{12} \sin^2 \theta_{13}}{-W + \alpha \sin 2\theta_{12} \sin \theta_{13}}. \quad (6.2.14)$$

We can obtain the expressions for  $\theta_{13}^m$  and  $\theta_{12}^m$  by diagonalizing the (1,3) and (1,2) blocks subsequently. These effective mixing angles can be written in following way

$$\tan 2\theta_{13}^m = \frac{\sin 2\theta_{13}(1 - \alpha \sin^2 \theta_{12})(\cos \theta_{23}^m + \sin \theta_{23}^m) - \alpha \sin 2\theta_{12} \cos \theta_{13}(\cos \theta_{23}^m - \sin \theta_{23}^m)}{\sqrt{2}(\lambda_3 - A - W - \sin^2 \theta_{13} - \alpha \sin^2 \theta_{12} \cos^2 \theta_{13})} \quad (6.2.15)$$

and

$$\tan 2\theta_{12}^m = \frac{\cos \theta_{13}^m [\sin 2\theta_{13}(1 - \alpha \sin^2 \theta_{12})(\cos \theta_{23}^m - \sin \theta_{23}^m) + \alpha \sin 2\theta_{12} \cos \theta_{13}(\cos \theta_{23}^m + \sin \theta_{23}^m)]}{\sqrt{2}(\lambda_2 - \lambda_1)}. \quad (6.2.16)$$

In the above expressions,  $\lambda_3$ ,  $\lambda_2$ , and  $\lambda_1$  take the following forms

$$\lambda_3 = \frac{1}{2} \left[ \cos^2 \theta_{13} + \alpha \cos^2 \theta_{12} + \alpha \sin^2 \theta_{12} \sin^2 \theta_{13} - W + \frac{(\alpha \sin 2\theta_{12} \sin \theta_{13} - W)}{\cos 2\theta_{23}^m} \right], \quad (6.2.17)$$

$$\lambda_2 = \frac{1}{2} \left[ \cos^2 \theta_{13} + \alpha \cos^2 \theta_{12} + \alpha \sin^2 \theta_{12} \sin^2 \theta_{13} - W - \frac{(\alpha \sin 2\theta_{12} \sin \theta_{13} - W)}{\cos 2\theta_{23}^m} \right], \quad (6.2.18)$$

and

$$\lambda_1 = \frac{1}{2} \left[ (\lambda_3 + A + W + \sin^2 \theta_{13} + \alpha \sin^2 \theta_{12} \cos^2 \theta_{13}) - \frac{(\lambda_3 - A - W - \sin^2 \theta_{13} - \alpha \sin^2 \theta_{12} \cos^2 \theta_{13})}{\cos 2\theta_{13}^m} \right]. \quad (6.2.19)$$

The eigenvalues  $m_{i,m}^2/2E$  ( $i = 1, 2, 3$ ) can be written in following fashion

$$\frac{m_{3,m}^2}{2E} = \frac{\Delta_{31}}{2} \left[ \lambda_3 + A + W + \sin^2 \theta_{13} + \alpha \sin^2 \theta_{12} \cos^2 \theta_{13} + \frac{\lambda_3 - A - W - \sin^2 \theta_{13} - \alpha \sin^2 \theta_{12} \cos^2 \theta_{13}}{\cos 2\theta_{13}^m} \right], \quad (6.2.20)$$

$$\frac{m_{2,m}^2}{2E} = \frac{\Delta_{31}}{2} \left[ \lambda_1 + \lambda_2 - \frac{\lambda_1 - \lambda_2}{\cos 2\theta_{12}^m} \right], \quad (6.2.21)$$

and

$$\frac{m_{1,m}^2}{2E} = \frac{\Delta_{31}}{2} \left[ \lambda_1 + \lambda_2 + \frac{\lambda_1 - \lambda_2}{\cos 2\theta_{12}^m} \right]. \quad (6.2.22)$$

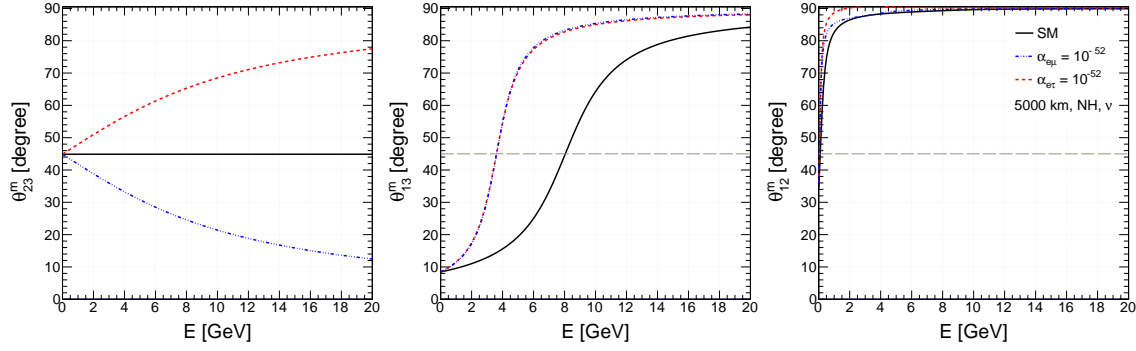


**Figure 6.1.** The variations in the effective mixing angles with the neutrino energy  $E$  in the presence of  $V_{CC}$  and  $V_{e\mu/e\tau}$ . The left, middle, and right panels show the effective value of  $\theta_{23}^m$ ,  $\theta_{13}^m$ , and  $\theta_{12}^m$  respectively for  $L = 5000$  km and NH. In each panel, the black solid line is for the SM case, whereas the blue dash-dotted and red dashed lines are for  $\alpha_{e\mu} = 10^{-52}$  and  $\alpha_{e\tau} = 10^{-52}$  respectively.

To estimate the effective values of oscillation parameters in presence of  $V_{CC}$  and  $V_{e\mu/e\tau}$ , we take the following benchmark values of vacuum oscillation parameters:  $\sin^2 \theta_{23} = 0.5$ ,  $\sin^2 2\theta_{13} = 0.0847$ ,  $\sin^2 \theta_{12} = 0.306$ ,  $\Delta m_{21}^2 = 7.5 \times 10^{-5} \text{ eV}^2$ ,  $\Delta m_{31}^2 = 2.524 \times 10^{-3} \text{ eV}^2$ . In Fig. 6.1, we plot the effective values of  $\theta_{23}^m$  (left panel),  $\theta_{13}^m$  (middle panel), and  $\theta_{12}^m$  (right panel) as functions of the neutrino energy  $E$ . These plots are for neutrino with  $L = 5000$  km and NH. In each panel, we draw the curves for the following three cases<sup>1</sup>: i)  $\alpha_{e\mu} = \alpha_{e\tau} = 0$  (the SM case), ii)  $\alpha_{e\mu} = 10^{-52}$ ,  $\alpha_{e\tau} = 0$  iii)  $\alpha_{e\mu} = 0$ ,  $\alpha_{e\tau} = 10^{-52}$ . We repeat the same exercise for the effective mass-squared differences<sup>2</sup> in Fig. 6.2. From the extreme right panel of Fig. 6.1, we can see that  $\theta_{12}^m$  approaches to  $90^\circ$  very rapidly as we increase  $E$ . This behavior is true for the SM case and as well as for non-zero  $\alpha_{e\mu/e\tau}$ , but it is not true for  $\theta_{23}^m$  and  $\theta_{13}^m$ . The long-range potential  $V_{e\mu/e\tau}$  modifies  $\theta_{23}^m$  significantly as can be seen from the extreme left panel of Fig. 6.1. As we approach to higher energies,  $\theta_{23}^m$  deviates from the maximal mixing and its value decreases (increases) very sharply for non-zero  $\alpha_{e\mu}$  ( $\alpha_{e\tau}$ ). This opposite behavior in the variation of  $\theta_{23}^m$  for finite  $\alpha_{e\mu}$  and  $\alpha_{e\tau}$  affect the oscillation probabilities in different manner, which we discuss in next subsection. Note that  $\theta_{23}^m$  is independent of  $V_{CC}$  (see Eq. 6.2.14). Therefore, its value remains same for all the baselines and same is true for the SM case as well as for non-zero  $\alpha_{e\mu/e\tau}$ . In case of  $\theta_{13}^m$  (see middle panel of Fig. 6.1), the impact of  $V_{e\mu}$  and  $V_{e\tau}$  are same and its variation is quite different as compared to  $\theta_{23}^m$ . Assuming NH, as we go to higher energies,  $\theta_{13}^m$  quickly reaches to maximal mixing (resonance point) for both the symmetries as compared to the SM case. Finally, it approaches toward  $90^\circ$  as

<sup>1</sup>In case of non-zero  $\alpha_{e\tau}$ , we use Eq. 6.2.14, Eq. 6.2.15, and Eq. 6.2.16. For non-zero  $\alpha_{e\mu}$ , we take the help of Eq. 3.16, Eq. 3.17, and Eq. 3.18 as given in Ref. [333].

<sup>2</sup>For non-zero  $\alpha_{e\tau}$ , we obtain the effective values of  $\Delta m_{31,m}^2$  and  $\Delta m_{21,m}^2$  using Eq. 6.2.20, Eq. 6.2.21, and Eq. 6.2.22. For finite  $\alpha_{e\mu}$ , we derive the same using Eq. 3.22, Eq. 3.23, and Eq. 3.24 as given in Ref. [333].



we further increase the energy. For  $\alpha_{e\mu/e\tau} = 10^{-52}$ , the resonance occurs around 3.5 GeV for 5000 km baseline. An analytical expression for the resonance energy can be obtained from Eq. 6.2.15 assuming  $\theta_{13}^m = 45^\circ$ . In one mass scale dominance approximation ( $\Delta m_{21}^2 = 0$ , *i.e.*  $\alpha = 0$ ), the expression for the resonance energy  $E_{\text{res}}$  can be obtained from the following:

$$\lambda_3 = A + W + \sin^2 \theta_{13}. \quad (6.2.23)$$

Assuming  $\alpha = 0$  in Eqs. 6.2.17 and 6.2.14, we get a simplified expression of  $\lambda_3$  which appears as

$$\lambda_3 = \frac{1}{2} [\cos^2 \theta_{13} - W + \sqrt{W_{e\tau}^2 + \cos^4 \theta_{13}}] \simeq \frac{1}{2} [2 \cos^2 \theta_{13} - W], \quad (6.2.24)$$

since at  $E_{\text{res}}$ , the term  $W^2$  is small compared to  $\cos^4 \theta_{13}$ , and we can safely neglect it. Comparing Eq. 6.2.24 and Eq. 6.2.23, we obtain a simple and compact expression for  $E_{\text{res}}$ :

$$E_{\text{res}} = \frac{\Delta m_{31}^2 \cos 2\theta_{13}}{2V_{CC} + 3V_{e\tau}}. \quad (6.2.25)$$

Note that in the absence of LRF, the above equation boils down to the well-known expression for  $E_{\text{res}}$  in the SM case. Also, we notice that the expression for resonance energy is same for both  $L_e - L_\tau$  and  $L_e - L_\mu$  symmetries (see Eq. 3.27 in Ref. [333]). It is evident from Eq. 6.2.25 that for a fixed baseline, in the presence of  $V_{e\mu/e\tau}$ , the resonance takes place at lower energy as compared to the SM case (see middle panel of Fig. 6.1). We observe from both the panels of Fig. 6.2 that in presence of LRF, the variations in  $\Delta m_{31,m}^2$  and  $\Delta m_{21,m}^2$  with energy are different as compared to the SM case. Interesting to note that both  $V_{e\mu}$  and  $V_{e\tau}$  modify the values of effective mass-squared differences in same fashion. In case of  $\Delta m_{21,m}^2$  (see right panel of Fig. 6.2), it increases with energy and can be comparable to the vacuum value of  $\Delta m_{31}^2$  at around  $E = 10$  GeV for both the SM and SM + LRF scenarios. For  $\Delta m_{31,m}^2$  (see left panel of Fig. 6.2), the change with energy is very mild in the SM case, but in presence of LRF,  $\Delta m_{31,m}^2$  gets increased substantially as we approach to higher energies. In case of antineutrino, the effective values of oscillation parameters can be obtained in the similar fashion by just replacing  $A \rightarrow -A$  and  $W \rightarrow -W$  in Eqs. 6.2.14 to 6.2.22. Next, we compare the neutrino and antineutrino oscillation probabilities obtained from our analytical expressions with those calculated numerically.

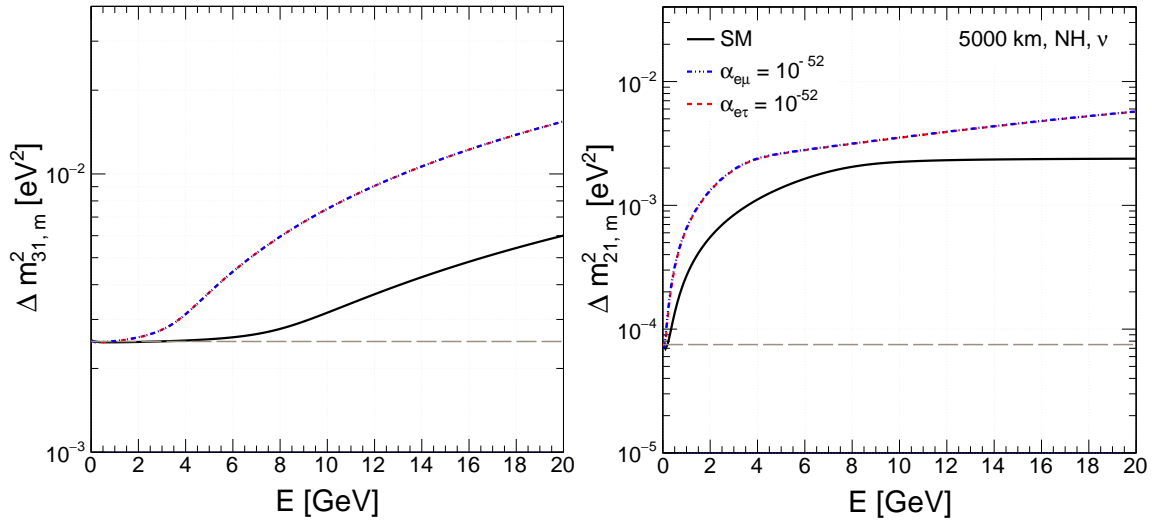


**Figure 6.2.** The variations in the  $\Delta m_{31,m}^2$  ( $\equiv m_{3,m}^2 - m_{1,m}^2$ , left panel) and  $\Delta m_{21,m}^2$  ( $\equiv m_{2,m}^2 - m_{1,m}^2$ , right panel) with the neutrino energy  $E$  in presence of  $V_{CC}$  and  $V_{e\mu/\tau}$  for  $L=5000$  km and NH. We give plots for three different cases: i)  $\alpha_{e\mu} = \alpha_{e\tau} = 0$  (the SM case, black solid line), ii)  $\alpha_{e\mu} = 10^{-52}$ ,  $\alpha_{e\tau} = 0$  (blue dash-dotted line), and iii)  $\alpha_{e\mu} = 0$ ,  $\alpha_{e\tau} = 10^{-52}$  (red dashed line).

### 6.2.2 Comparison between Analytical and Numerical Results

We obtain the analytical probability expressions in the presence of  $V_{CC}$  and  $V_{e\mu/\tau}$  by replacing the well known vacuum values of the elements of  $U_{PMNS}$  and the mass-squared differences  $\Delta m_{ij}^2$  with their effective values as discussed in the previous section. In Fig. 6.3, we show our approximate  $\nu_e \rightarrow \nu_\mu$  ( $\bar{\nu}_e \rightarrow \bar{\nu}_\mu$ ) oscillation probabilities in the top left (right) panel as a function of  $E$  against the exact numerical results considering  $L = 5000$  km<sup>3</sup> and NH. We repeat the same for  $\nu_\mu \rightarrow \nu_\mu$  ( $\bar{\nu}_\mu \rightarrow \bar{\nu}_\mu$ ) survival channels in bottom left (right) panel. We perform these comparisons among analytical (solid curves) and numerical (dashed curves) cases for both the SM and SM + LRF scenarios assuming our benchmark choice of  $\alpha_{e\tau} = 10^{-52}$ . For  $L_e - L_\mu$  symmetry, we perform the similar comparison in Fig. B.1 (see Appendix B). For the SM case ( $\alpha_{e\tau} = 0$ ), our approximate results match exactly with numerically obtained probabilities. In the presence of  $L_e - L_\tau$  symmetry, we see that our analytical expressions work quite well and can produce almost accurate  $L/E$  oscillation patterns.

We can see from the top left panel of Fig. 6.3 that for non-zero  $\alpha_{e\tau}$ , the location of the first oscillation maximum shifts toward lower energy (from 5.8 GeV to 3.5 GeV) and also its amplitude gets

<sup>3</sup>For both analytical and numerical calculations, we take the line-averaged constant Earth matter density based on the PREM profile [348].

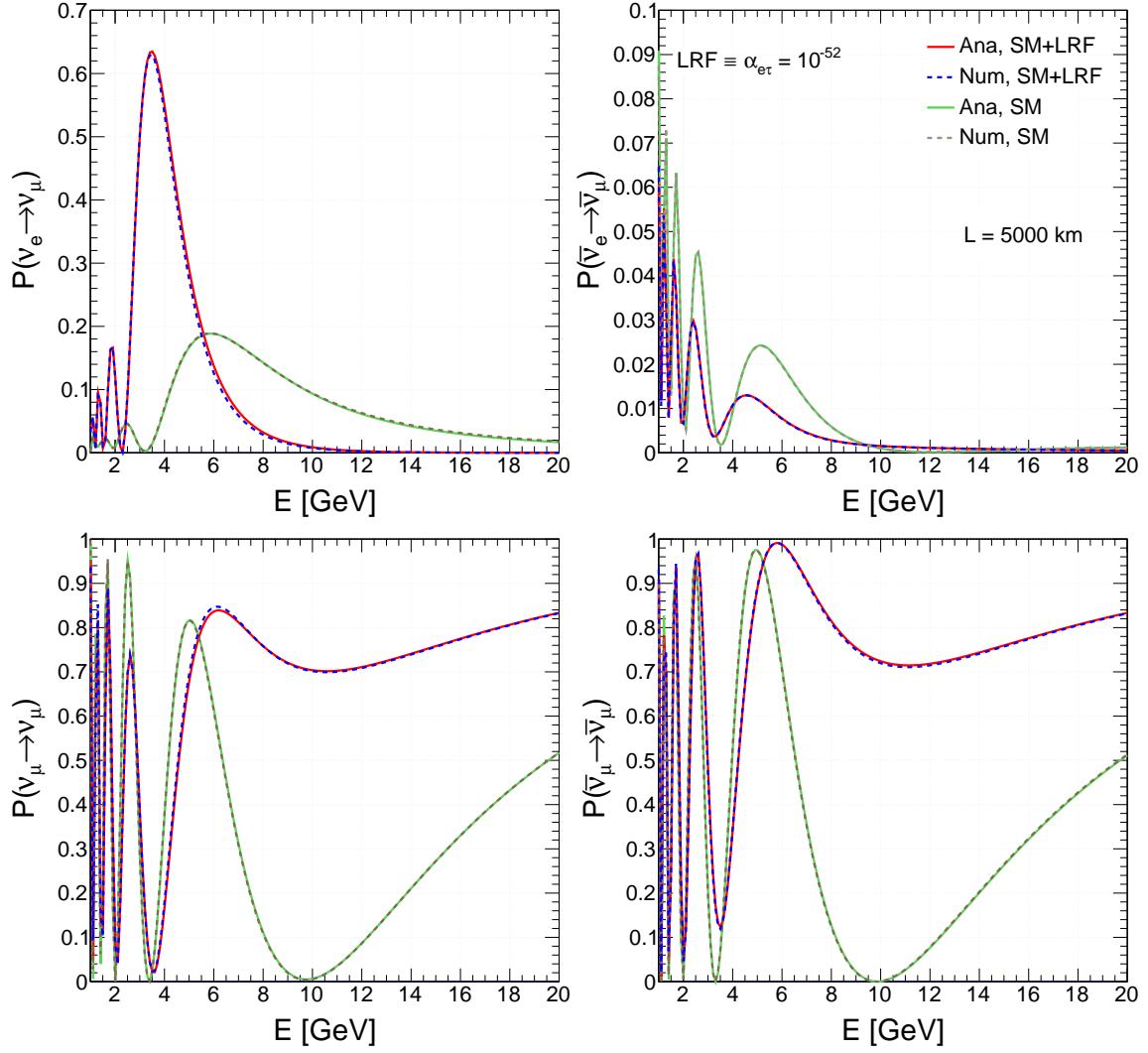


**Figure 6.3.**  $\nu_e \rightarrow \nu_\mu$  ( $\bar{\nu}_e \rightarrow \bar{\nu}_\mu$ ) transition probability for 5000 km in upper left (right) panel assuming NH. In bottom left (right) panel, we show  $\nu_\mu \rightarrow \nu_\mu$  ( $\bar{\nu}_\mu \rightarrow \bar{\nu}_\mu$ ) survival probability. In all the panels, we compare our analytical expressions (solid curves) to the exact numerical results (dashed curves) for the SM and SM + LRF cases. For LRF, we consider  $\alpha_{e\tau} = 10^{-52}$ . Note that the y-axis ranges are different in the upper left and right panels.

enhanced (from 0.18 to 0.64) for  $\nu_e \rightarrow \nu_\mu$  transition probability assuming NH. To understand this feature, we can use the following simple expression<sup>4</sup> for  $P(\nu_e \rightarrow \nu_\mu)$  considering  $\theta_{12}^m = 90^\circ$  (see right panel of Fig. 6.1):

$$P_{e\mu} = \sin^2 \theta_{23}^m \sin^2 2\theta_{13}^m \sin^2 \frac{\Delta m_{32,m}^2 L}{4E}. \quad (6.2.26)$$

As can be seen from the previous section,  $\theta_{23}^m$  does not “run” for the SM case, but for non-zero  $\alpha_{e\tau}$ , it approaches toward  $90^\circ$  as we increase  $E$ . As far as  $\theta_{13}^m$  is concerned, it quickly reaches to the resonance point at a lower energy for non-zero  $\alpha_{e\tau}$  as compared to  $\alpha_{e\tau} = 0$  case. Also,  $\Delta m_{32,m}^2$

<sup>4</sup>We obtain this formula using the general expression as given in Eq. 3.30 in Ref. [333].

$(\Delta m_{31,m}^2 - \Delta m_{21,m}^2)$  decreases with energy as  $\Delta m_{21,m}^2$  increases substantially in comparison to  $\Delta m_{31,m}^2$  till  $E \sim 4$  GeV for 5000 km baseline. The modifications of mixing parameters in different fashion are responsible to shift the location of first oscillation maximum toward lower energy and also to enhance its amplitude.

In case of  $\nu_\mu \rightarrow \nu_\mu$  survival probability ( $P_{\mu\mu}$ ), we can use the following simple expression assuming  $\theta_{12}^m = 90^\circ$ :

$$P_{\mu\mu} = 1 - \sin^2 2\theta_{23}^m \left[ \cos^2 \theta_{13}^m \sin^2 \frac{\Delta m_{31,m}^2 L}{4E} + \frac{1}{4} \tan^2 \theta_{23}^m \sin^2 2\theta_{13}^m \sin^2 \frac{\Delta m_{32,m}^2 L}{4E} + \sin^2 \theta_{13}^m \sin^2 \frac{\Delta m_{21,m}^2 L}{4E} \right]. \quad (6.2.27)$$

In the above expression, the term  $\sin^2 2\theta_{23}^m$  plays an important role. Now, we see from left panel of Fig. 6.1 that as we go to higher energies,  $\theta_{23}^m$  deviates from the maximal mixing very sharply in presence of LRF. For this reason, the value of  $\sin^2 2\theta_{23}^m$  gets reduced substantially, which ultimately enhances the survival probability for non-zero  $\alpha_{e\tau}$  as can be seen from the bottom left panel of Fig. 6.3. In the energy range of 6 to 20 GeV, we see a substantial enhancement in  $P_{\mu\mu}$  with non-zero  $\alpha_{e\tau}$  as compared to the SM case. The same is true for non-zero  $\alpha_{e\mu}$  as can be seen from Fig. B.1 in Appendix B. We see a similar increase in case of  $\bar{\nu}_\mu \rightarrow \bar{\nu}_\mu$  survival channel with NH (see bottom right panel of Fig. 6.3). We observe this behavior for other baselines as well in Figs. 6.6 and 6.8, which we discuss later.

### 6.3 Neutrino Oscillograms in $(E_\nu, \cos \theta_\nu)$ Plane

The atmospheric neutrino experiments deal with a wide range of baselines and energies. Therefore, it is quite important to see how the long-range forces under discussion affect the neutrino oscillation probabilities for all possible choices of baseline ( $\cos \theta_\nu$ ) and energy ( $E_\nu$ ) which are relevant for the ICAL detector. We perform this study by drawing the neutrino oscillograms in  $(E_\nu, \cos \theta_\nu)$  plane using the full three-flavor probability expressions with the varying Earth matter densities as given in the PREM profile [348]. Although in atmospheric neutrino experiments, it is not possible to measure the oscillation probabilities for  $\nu_e \rightarrow \nu_\mu$  and  $\nu_\mu \rightarrow \nu_\mu$  channels separately,

but to explain their features from our analytical expressions, here we present the oscillograms for appearance and disappearance probabilities separately.

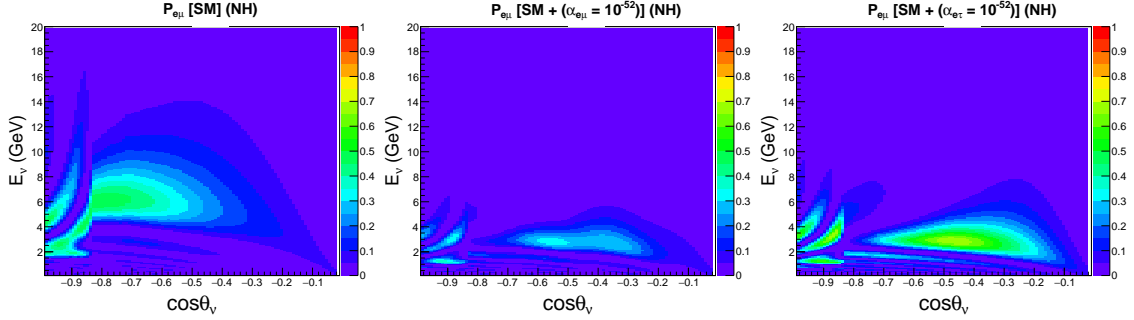


**Figure 6.4.** The oscillograms for  $\nu_e \rightarrow \nu_\mu$  channel in  $E_\nu, \cos \theta_\nu$  plane for three different scenarios: i)  $\alpha_{e\mu} = \alpha_{e\tau} = 0$  (the SM case, left panel), ii)  $\alpha_{e\mu} = 10^{-52}$ ,  $\alpha_{e\tau} = 0$  (middle panel), and iii)  $\alpha_{e\mu} = 0$ ,  $\alpha_{e\tau} = 10^{-52}$  (right panel). Here, in all the panels, we assume NH.

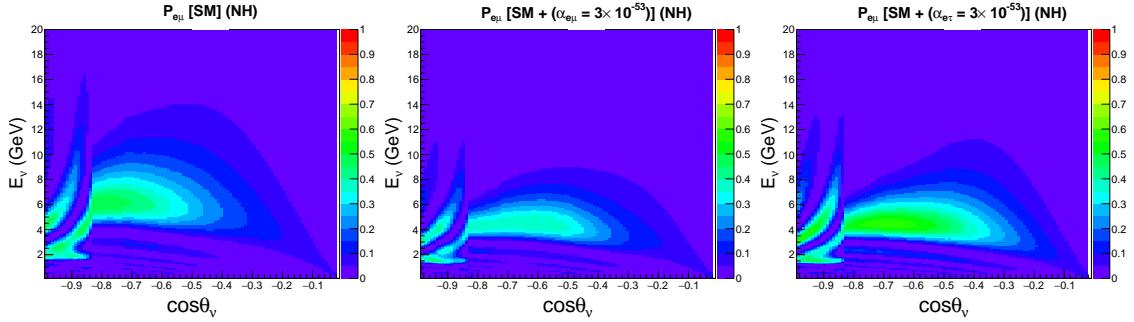


**Figure 6.5.** The oscillograms for  $\nu_e \rightarrow \nu_\mu$  channel in  $E_\nu, \cos \theta_\nu$  plane for three different scenarios: i)  $\alpha_{e\mu} = \alpha_{e\tau} = 0$  (the SM case, left panel), ii)  $\alpha_{e\mu} = 3 \times 10^{-53}$ ,  $\alpha_{e\tau} = 0$  (middle panel), and iii)  $\alpha_{e\mu} = 0$ ,  $\alpha_{e\tau} = 3 \times 10^{-53}$  (right panel). Here, in all the panels, we assume NH.

### 6.3.1 Oscillograms for $\nu_e \rightarrow \nu_\mu$ Appearance Channel

Fig. 6.4 shows the oscillograms for  $\nu_e$  to  $\nu_\mu$  appearance channel in  $E_\nu$  and  $\cos \theta_\nu$  plane assuming NH. We present the oscillograms for three different cases: i) extreme left panel is for the SM case ( $\alpha_{e\mu} = \alpha_{e\tau} = 0$ ), ii) middle panel is for the SM + LRF ( $\alpha_{e\mu} = 10^{-52}$ ), and iii) extreme right panel deals with the SM + LRF ( $\alpha_{e\tau} = 10^{-52}$ ). For the SM case,  $\nu_e$  to  $\nu_\mu$  transition probability attains the maximum value around the resonance region which occurs in the range of  $E \in 4$  to  $8$  GeV and  $\cos \theta_\nu \in -0.8$  to  $-0.4$ . The resonance condition in presence of LRF (see Eq. 6.2.25) suggests that  $\theta_{13}^m$  can reach  $45^\circ$  at smaller energies and baselines as compared to the SM case. This feature gets reflected in the middle and right panels of Fig. 6.4 for non-zero  $\alpha_{e\mu}$  and  $\alpha_{e\tau}$  respectively. Fig. 6.4 also depicts that the value of  $P_{e\mu}$  decreases (increases) as compared to the SM case for non-zero

$\alpha_{e\mu}$  ( $\alpha_{e\tau}$ ). We can explain this behavior from the variation of  $\theta_{23}^m$  (see left panel of Fig. 6.1). In presence of  $L_e - L_\mu$  ( $L_e - L_\tau$ ) symmetry, the term  $\sin^2 \theta_{23}^m$  in Eq. 6.2.26 gets reduced (enhanced) as compared to the SM case, which subsequently decreases (increases) the value of  $P_{e\mu}$ . In Fig. 6.5, we draw the same plots for appearance channel but with smaller value of  $\alpha_{e\mu/e\tau}$  which is  $3 \times 10^{-53}$ .

### 6.3.2 Oscillograms for $\nu_\mu \rightarrow \nu_\mu$ Disappearance Channel

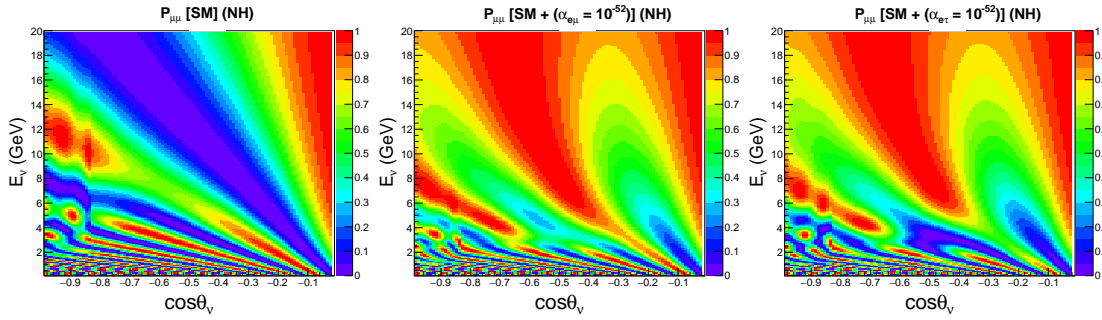


**Figure 6.6.** The oscillograms for  $\nu_\mu \rightarrow \nu_\mu$  channel in  $E_\nu$ ,  $\cos \theta_\nu$  plane for three different scenarios: i)  $\alpha_{e\mu} = \alpha_{e\tau} = 0$  (the SM case, left panel), ii)  $\alpha_{e\mu} = 10^{-52}$ ,  $\alpha_{e\tau} = 0$  (middle panel), and iii)  $\alpha_{e\mu} = 0$ ,  $\alpha_{e\tau} = 10^{-52}$  (right panel). Here, in all the panels, we assume NH.

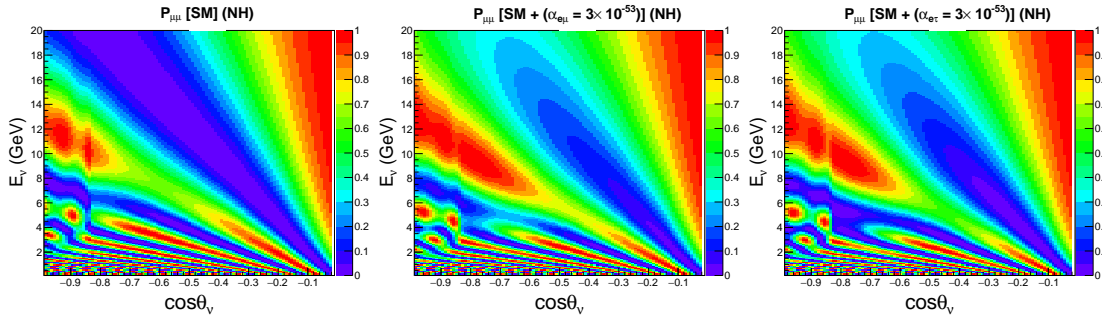


**Figure 6.7.** The oscillograms for  $\nu_\mu \rightarrow \nu_\mu$  channel in  $E_\nu$ ,  $\cos \theta_\nu$  plane for three different scenarios: i)  $\alpha_{e\mu} = \alpha_{e\tau} = 0$  (the SM case, left panel), ii)  $\alpha_{e\mu} = 3 \times 10^{-53}$ ,  $\alpha_{e\tau} = 0$  (middle panel), and iii)  $\alpha_{e\mu} = 0$ ,  $\alpha_{e\tau} = 3 \times 10^{-53}$  (right panel). Here, in all the panels, we assume NH.

In Fig. 6.6, we present the oscillograms for  $\nu_\mu$  survival channel in the plane of  $\cos \theta_\nu$  vs.  $E_\nu$  considering NH. Here, we draw the oscillograms for the same three cases as considered in Fig. 6.4. First, we notice that for  $E_\nu$  in the range of 6 to 20 GeV and  $\cos \theta_\nu$  in the range of -1 to -0.2, survival probability  $P_{\mu\mu}$  gets enhanced significantly for both non-zero  $\alpha_{e\mu}$  (middle panel) and  $\alpha_{e\tau}$  (right panel) as compared to the SM case (see left panel). The reason is the following. As we move to higher energies,  $\theta_{23}^m$  deviates from maximal mixing for both non-zero  $\alpha_{e\mu}$  and  $\alpha_{e\tau}$ . As a result, the term  $\sin^2 2\theta_{23}^m$  in Eq. 6.2.27 gets reduced and causes an enhancement in  $P_{\mu\mu}$ . In Fig. 6.6, we see some differences in the oscillogram patterns in the energy range of 2 to 5 GeV for  $L_e - L_\mu$

(middle panel) and  $L_e - L_\tau$  (right panel) symmetries. Let us try to understand the reason behind this. We have already seen that  $\theta_{23}^m$  “runs” in the opposite directions from  $45^\circ$  for  $L_e - L_\mu$  and  $L_e - L_\tau$  symmetries. Due to this, the only term  $\frac{1}{4} \tan^2 \theta_{23}^m \sin^2 2\theta_{13}^m$  in Eq. 6.2.27 gives different contributions for finite  $\alpha_{e\mu}$  and  $\alpha_{e\tau}$ . Around the resonance region ( $E \sim 2$  to  $5$  GeV),  $\theta_{13}^m$  attains the maximal value, and the strength of above mentioned term becomes quite significant which causes the differences in  $P_{\mu\mu}$  for these two U(1) symmetries under consideration. We see the effect of this feature in the top left panel of Fig. 6.8, which we discuss later. In Fig. 6.7, we repeated this study with smaller value of  $\alpha_{e\mu/e\tau}$  which is  $3 \times 10^{-53}$ .

## 6.4 Event Spectrum in the ICAL Detector

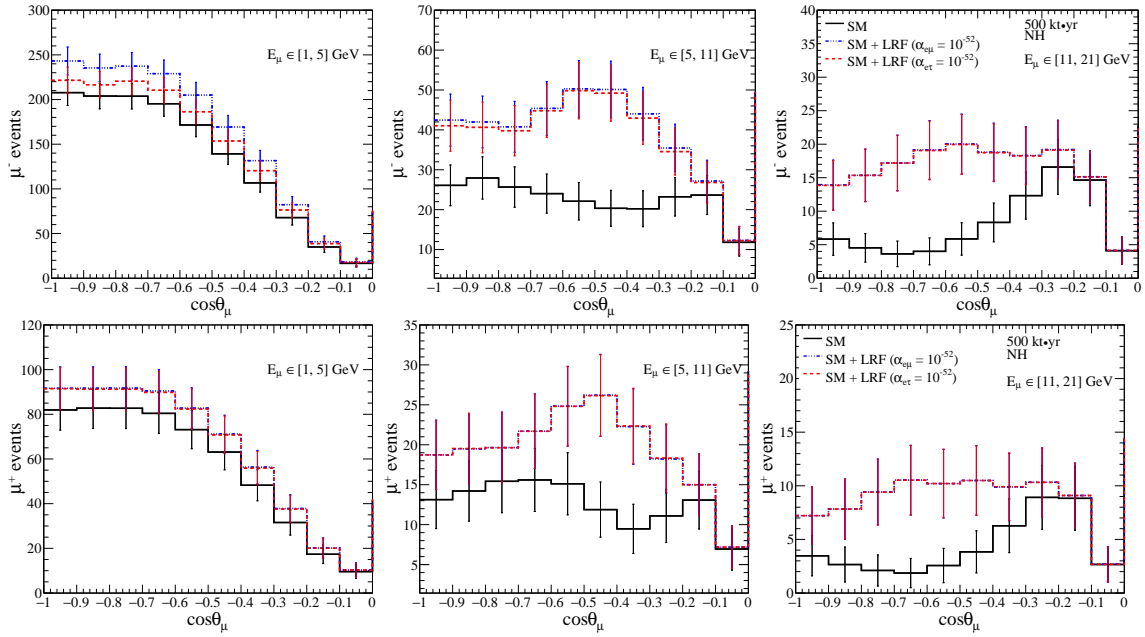


**Figure 6.8.** The distributions of  $\mu^-$  (upper panels) and  $\mu^+$  (lower panels) events for three different  $E_\mu$  bins: 1 to 5 GeV in left panel, 5 to 11 GeV in middle panel, and 11 to 21 GeV in right panel. In each panel, we consider three different cases: i)  $\alpha_{e\mu} = \alpha_{e\tau} = 0$  (the SM case, black solid line), ii)  $\alpha_{e\mu} = 10^{-52}$ ,  $\alpha_{e\tau} = 0$  (blue dash-dotted line), and iii)  $\alpha_{e\mu} = 0$ ,  $\alpha_{e\tau} = 10^{-52}$  (red dashed line). Here, we sum over  $E'_{\text{had}}$  in its entire range of 0 to 25 GeV and show the results for 500 kt-yr exposure and assuming NH.

In this section, we present the expected event spectra and total event rates in ICAL with and without long-range forces. Using the event generator NUANCE [205] and atmospheric neutrino fluxes at Kamioka<sup>5</sup> [165], we obtain the unoscillated event spectra for neutrino and antineutrino. After incorporating the detector response for muons and hadrons as described in Ref. [49] and

<sup>5</sup>Preliminary calculation of the expected fluxes at the INO site have been performed in Ref. [206]. We plan to use these fluxes in future analysis once they are finalized. The horizontal components of the geo-magnetic field are different

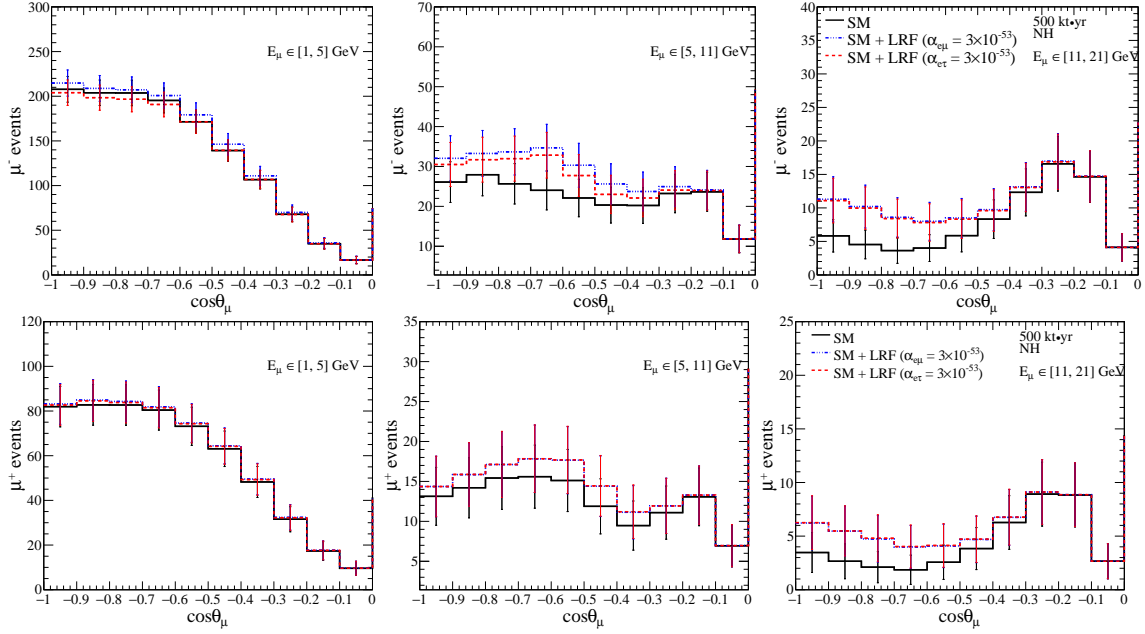


**Figure 6.9.** The distributions of  $\mu^-$  (upper panels) and  $\mu^+$  (lower panels) events for three different  $E_\mu$  bins: 1 to 5 GeV in left panel, 5 to 11 GeV in middle panel, and 11 to 21 GeV in right panel. In each panel, we consider three different cases: i)  $\alpha_{e\mu} = \alpha_{e\tau} = 0$  (the SM case, black solid line), ii)  $\alpha_{e\mu} = 3 \times 10^{-53}$ ,  $\alpha_{e\tau} = 0$  (blue dash-dotted line), and iii)  $\alpha_{e\mu} = 0$ ,  $\alpha_{e\tau} = 3 \times 10^{-53}$  (red dashed line). Here, we sum over  $E'_{\text{had}}$  in its entire range of 0 to 25 GeV and show the results for 500 kt-yr exposure and assuming NH.

for the benchmark values of the oscillation parameters as mentioned in Sec. 6.2.1 ( $\sin^2 \theta_{23} = 0.5$ ,  $\sin^2 2\theta_{13} = 0.0847$ , and NH), we obtain around 4870 (2187)  $\mu^-$  ( $\mu^+$ ) events for the SM case using a 500 kt-yr exposure. To obtain these event rates, we consider  $E_\mu$  in the range 1 to 21 GeV,  $\cos \theta_\mu$  in its entire range of -1 to 1, and  $E'_{\text{had}}$  in the range 0 to 25 GeV. In presence of  $L_e - L_\mu$  symmetry with  $\alpha_{e\mu} = 10^{-52}$ , the number of  $\mu^-$  ( $\mu^+$ ) events becomes 5365 (2373). For  $L_e - L_\tau$  symmetry with  $\alpha_{e\tau} = 10^{-52}$ , we get 5225  $\mu^-$  and 2369  $\mu^+$  events. In Fig. 6.8, we show the distribution of only upward going  $\mu^-$  (top panels) and  $\mu^+$  (bottom panels) events as a function of reconstructed  $\cos \theta_\mu$  in the range -1 to 0. Here, we integrate over the entire range of hadron energy ( $E'_{\text{had}} \in 0$  to 25 GeV), and display the event spectra considering three different  $E_\mu$  bins having the ranges 1 to 5 GeV (left panels), 5 to 11 GeV (middle panels), and 11 to 21 GeV (right panels). In each panel, we compare the event distribution for three different scenarios: i)  $\alpha_{e\mu} = \alpha_{e\tau} = 0$  (the SM case, black solid lines), ii)  $\alpha_{e\mu} = 10^{-52}$ ,  $\alpha_{e\tau} = 0$  (blue dash-dotted lines), and iii)  $\alpha_{e\mu} = 0$ ,  $\alpha_{e\tau} = 10^{-52}$  (red dashed lines). We observe a few interesting features in Fig. 6.8, which we discuss now.

---

at the INO (40  $\mu\text{T}$ ) and Kamioka (30  $\mu\text{T}$ ). Due to this reason, we observe a difference in atmospheric fluxes at these sites.



In all the panels of Fig. 6.8, we see an enhancement in the event rates for  $\cos \theta_\mu \in [-1, -0.2]$  in the presence of long-range forces as compared to the SM case. This mainly happens due to substantial increase in  $P_{\mu\mu}$  with finite  $\alpha_{e\mu}$  or  $\alpha_{e\tau}$  as compared to the SM case. We have already seen this feature in Fig. 6.6. Also, we see similar event distributions for both the symmetries in all the panels, except in the top left panel ( $E_\mu \in 1$  to 5 GeV), where we see some differences in the event spectra for  $L_e - L_\mu$  and  $L_e - L_\tau$  symmetries. We have already explained the reason behind this with the help of oscillogram patterns (see middle and right panels in Fig. 6.6) in Sec. 6.3.2. In Fig. 6.9, we observe similar effects in event distribution for  $\mu^-$  and  $\mu^+$  with the SM + LRF ( $\alpha_{e\mu/e\tau} = 3 \times 10^{-53}$ ) scenario. Next, we discuss the binning scheme for three observables ( $E_\mu$ ,  $\cos \theta_\mu$ , and  $E'_{\text{had}}$ ), and briefly describe the numerical technique and analysis procedure which we adopt to estimate the physics reach of ICAL.

## 6.5 Simulation Procedure

### 6.5.1 Binning Scheme for Observables ( $E_\mu$ , $\cos \theta_\mu$ , $E'_{\text{had}}$ )

Observable	Range	Bin width	No. of bins	Total bins
$E_\mu$ (GeV)	[1, 11]	1	10	12
	[11, 21]	5	2	
$\cos \theta_\mu$	[-1.0, 0.0]	0.1	10	15
	[0.0, 1.0]	0.2	5	
$E'_{\text{had}}$ (GeV)	[0, 2]	1	2	4
	[2, 4]	2	1	
	[4, 25]	21	1	

**Table 6.2.** The binning scheme considered for the reconstructed observables  $E_\mu$ ,  $\cos \theta_\mu$ , and  $E'_{\text{had}}$  for each muon polarity. In last column, we give the total number of bins taken for each observable.

Table 6.2 shows the binning scheme that we adopt in our simulation for three observables  $E_\mu$  ( $\in 1$  to 21 GeV),  $\cos \theta_\mu$  ( $\in -1$  to 1), and  $E'_{\text{had}}$  ( $\in 0$  to 25 GeV). In these ranges, we have total 12 bins for  $E_\mu$ , 15 bins for  $\cos \theta_\mu$ , and 4 bins for  $E'_{\text{had}}$ , resulting into a total of ( $12 \times 15 \times 4 =$ ) 720 bins per polarity. We consider the same binning scheme for  $\mu^-$  and  $\mu^+$  events. As we go to higher energies, the atmospheric neutrino flux decreases resulting in lower statistics. Therefore, we take wider bins for  $E_\mu$  and  $E'_{\text{had}}$  at higher energies. We do not perform any optimization study for binning, however we make sure that we have sufficient statistics in most of the bins without diluting the sensitivity

much. In our study, the upward going events ( $\cos \theta_\mu$  in the range 0 to -1) play an important role, where  $V_{CC}$ ,  $V_{e\mu/e\tau}$ , and  $\Delta m_{31}^2/2E$  become comparable and can interfere with each other (see discussion in Sec. 6.2). Therefore, we take 10 bins of equal width for upward going events which is compatible with the angular resolutions of muon achievable in ICAL. The downward going events do not undergo oscillations. But, they certainly enhance the overall statistics and help us to reduce the impact of normalization uncertainties in the atmospheric neutrino fluxes. Therefore, we include the downward going events in our simulation considering five  $\cos \theta_\mu$  bins of equal width in the range of 0 to 1.

### 6.5.2 Numerical Analysis

For this analysis, we follow the same technique for the simulation and numerical analysis as used for the study of Non-Standard Interactions (Chapter 5) and as discussed in Sec. 5.5.2. In the fit, we first minimize  $\chi_{\text{ICAL}}^2$  (Eq. 5.5.5) with respect to the pull variables  $\zeta_l$ , and then marginalize over the oscillation parameters  $\sin^2 \theta_{23}$  in the range 0.38 to 0.63 and  $\Delta m_{31}^2$  in the range 0.0024 eV<sup>2</sup> to 0.0026 eV<sup>2</sup>. While deriving the constraints on  $\alpha_{e\mu/e\tau}$ , we also marginalize  $\chi_{\text{ICAL}}^2$  over both NH and IH. We do not marginalize over  $\Delta m_{21}^2$ ,  $\sin^2 \theta_{12}$ , and  $\sin^2 2\theta_{13}$  since these parameters are already measured with high precision, and the existing uncertainties on these parameters do not alter our results. We consider  $\delta_{\text{CP}} = 0^\circ$  throughout our analysis.

## 6.6 Results

We quantify the statistical significance of the analysis to constrain the LRF parameters in the following way

$$\Delta\chi_{\text{ICAL-LRF}}^2 = \chi_{\text{ICAL}}^2(\text{SM} + \alpha_{e\mu/e\tau}) - \chi_{\text{ICAL}}^2(\text{SM}) . \quad (6.6.1)$$

Here,  $\chi_{\text{ICAL}}^2(\text{SM})$  and  $\chi_{\text{ICAL}}^2(\text{SM} + \alpha_{e\mu/e\tau})$  are calculated by fitting the “observed” data in the absence and presence of LRF parameters respectively. In our analysis, statistical fluctuations are suppressed, and therefore,  $\chi_{\text{ICAL}}^2(\text{SM}) \approx 0$ . Before we present the constraints on  $\alpha_{e\mu/e\tau}$ , we identify the regions in  $E_\mu$  and  $\cos \theta_\mu$  plane which give significant contributions toward  $\Delta\chi_{\text{ICAL-LRF}}^2$ .

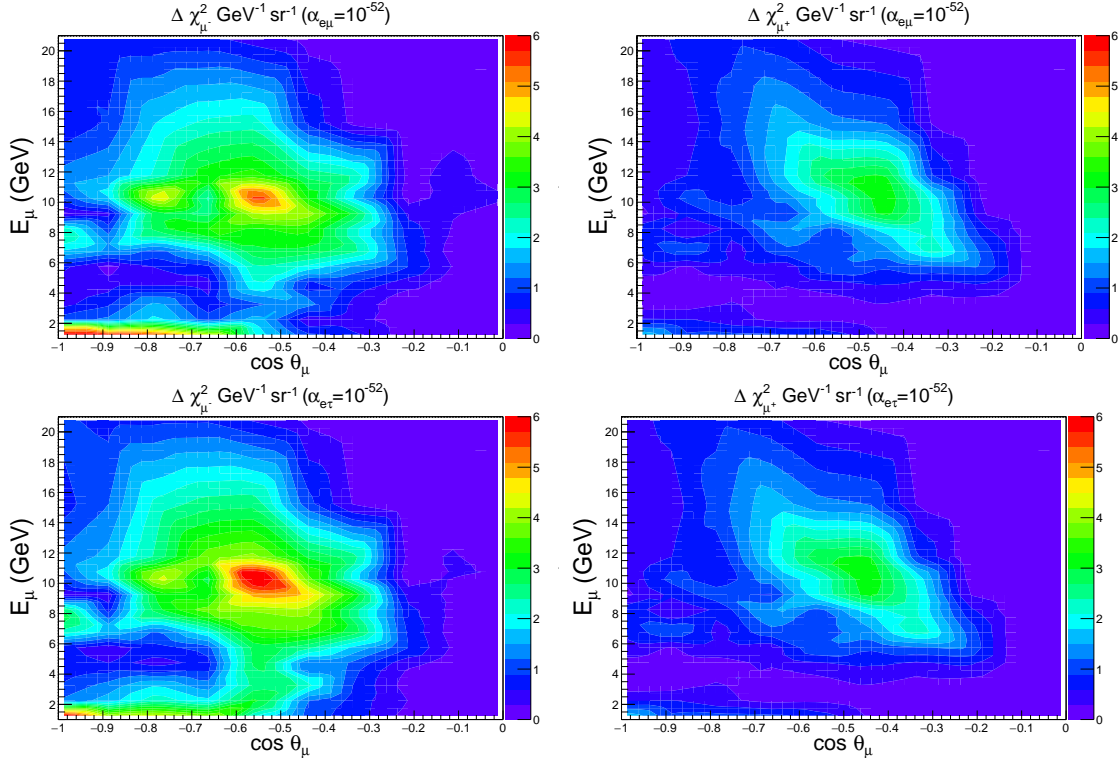


**Figure 6.10.** Distributions of  $\Delta\chi^2_{\text{ICAL-LRF}}$  (per unit area) in  $E_\mu$  and  $\cos\theta_\mu$  plane. The left (right) panels are for  $\mu^-$  ( $\mu^+$ ) events. In upper (lower) panels, we assume non-zero  $\alpha_{e\mu}$  ( $\alpha_{e\tau}$ ) in the fit with a strength of  $10^{-52}$ . In all the panels, we use 500 kt-yr exposure and assume NH in both data and theory.

In Fig. 6.10, we show the distribution<sup>6</sup> of  $\Delta\chi^2_{\mu^-}$  (left panels) and  $\Delta\chi^2_{\mu^+}$  (right panels) in the reconstructed  $E_\mu$  and  $\cos\theta_\mu$  plane, where the events are further divided into four sub-bins depending on the reconstructed hadron energy (see Table 6.2). In the upper (lower) panels of Fig. 6.10, we take non-zero  $\alpha_{e\mu}$  ( $\alpha_{e\tau}$ ) in the fit with a strength of  $10^{-52}$ . We clearly see from the left panels that for  $\mu^-$  events, most of the contributions ( $\sim 70\%$ ) stem from the range 6 to 15 GeV for  $E_\mu$  and for  $\cos\theta_\mu$ , the effective range is -0.8 to -0.4. We see similar trend for both the symmetries (see upper and lower panels) and for  $\mu^+$  events (see right panels) as well.

Fig. 6.11 shows the upper bound on  $\alpha_{e\mu}$  and  $\alpha_{e\tau}$  (one at-a-time) using 500 kt-yr exposure of ICAL if there is no signal of long-range forces in the data. We set new upper limit on  $\alpha_{e\mu}$  or  $\alpha_{e\tau}$  by generating the data with no long-range forces and fitting it with some non-zero value of  $\alpha_{e\mu/e\tau}$  by means of  $\chi^2$  technique as outlined in previous section. The corresponding  $\Delta\chi^2_{\text{ICAL-LRF}}$  obtained after marginalizing over  $\sin^2\theta_{23}$ ,  $\Delta m^2_{31}$ , hierarchy, and systematics parameters in the fit, is plotted

<sup>6</sup>In Fig. 6.10, we do not consider the constant contributions in  $\chi^2$  coming from the term which involves five pull parameters  $\zeta_i^2$  in Eq. 5.5.1. Also, we do not marginalize over the oscillation parameters in the fit to produce these figures. But, we show our final results considering full pull contributions and marginalizing over the oscillation parameters in the fit as mentioned in previous section.

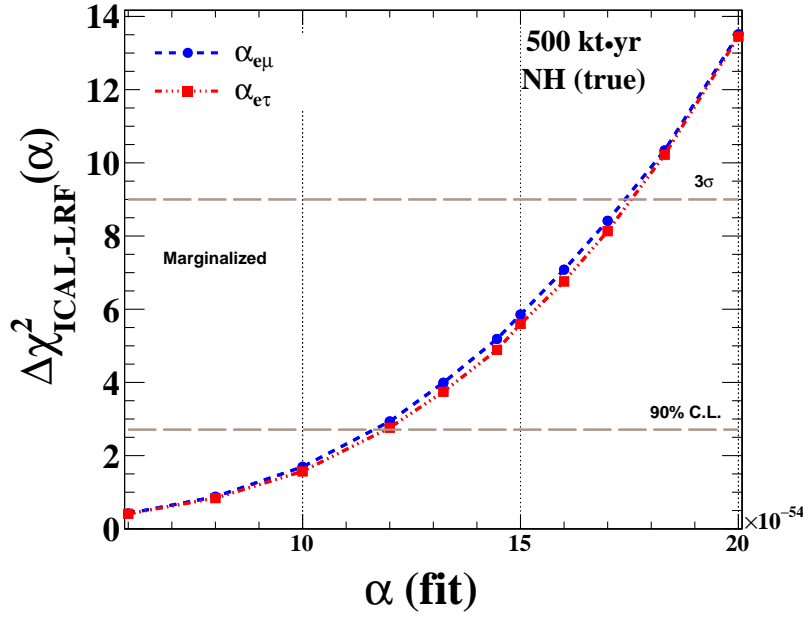


**Figure 6.11.** Sensitivity of ICAL to set upper limits on  $\alpha_{e\mu}$  (blue dashed line) and  $\alpha_{e\tau}$  (red dash-dotted line) using 500 kt·yr exposure and assuming NH as true choice.

in Fig. 6.11 as a function of  $\alpha_{e\mu/e\tau}$  (test). It gives a measure of the sensitivity reach of ICAL to the effective gauge coupling of LRF. For both the symmetries, we assume NH as true hierarchy. We obtain similar constraints for both the symmetries (one at-a-time) since  $\alpha_{e\mu}$  and  $\alpha_{e\tau}$  affect both  $P_{\mu\mu}$  and  $P_{e\mu}$  oscillation channels in almost similar fashion over a wide range of energies and baselines (see Figs. 6.4 and 6.6). The expected upper limit on  $\alpha_{e\mu/e\tau}$  from ICAL is  $< 1.2 \times 10^{-53}$  ( $1.75 \times 10^{-53}$ ) at 90% ( $3\sigma$ ) C.L. with 500 kt·yr exposure and NH as true hierarchy. This future limit on  $\alpha_{e\mu}$  from ICAL at 90% C.L. is  $\sim 46$  times better than the existing limit from the Super-Kamiokande experiment [330]. For  $\alpha_{e\tau}$ , the limit is 53 times better at 90% confidence level. We obtain similar constraints assuming IH as true hierarchy. We see a marginal improvement in the upper limits if we keep all the oscillation parameters fixed in the fit. In this fixed parameter case, the new bound becomes  $\alpha_{e\mu} < 1.63 \times 10^{-53}$  at  $3\sigma$  confidence level. We study few interesting issues in this fixed parameter scenario which we discuss now.

- **Advantage of Spectral Information:** In ICAL, we can bin the atmospheric neutrino/antineutrino events in the observables  $E_\mu$ ,  $\cos \theta_\mu$ , and  $E'_{\text{had}}$ . It helps us immensely to achieve hierarchy measurement at around  $3\sigma$  C.L. with 500 kt·yr exposure [49]. We find that the ability of using the spectral information in ICAL also plays an important role to place tight constraint on LRF parameters. For an example, if we rely only on the total  $\mu^-$  and  $\mu^+$  event rates,

the expected limit from ICAL becomes  $\alpha_{e\mu} < 2.2 \times 10^{-52}$  at  $3\sigma$  confidence level. This limit is almost 13 times weaker as compared to what we can obtain using the full spectral information.

- **Usefulness of Hadron Energy Information:** In our analysis, we use the hadron energy information ( $E'_{\text{had}}$ ) along with the muon momentum ( $E_\mu, \cos \theta_\mu$ ). We observe that with a value of  $\alpha_{e\mu} = 1.63 \times 10^{-53}$  in the fit,  $\Delta\chi^2_{\text{ICAL-LRF}}$  increases from 5.2 to 9 when we use  $E_\mu$ ,  $\cos \theta_\mu$ , and  $E'_{\text{had}}$  as our observables instead of only  $E_\mu$  and  $\cos \theta_\mu$ . It corresponds to about 73% improvement in the sensitivity.
- **The Role of Charge Identification Capability:** We also find that the charge identification capability of ICAL in distinguishing  $\mu^-$  and  $\mu^+$  events does not play an important role to constrain the LRF parameters unlike the mass hierarchy measurements. Since the long-range forces affect the  $\mu^-$  and  $\mu^+$  event rates in almost similar fashion as compared to the SM case (see Fig 6.8), it is not crucial to separate these events in our analysis in constraining the LRF parameters.

Before we summarize and draw our conclusions in the next section, we make few comments on how the presence of LRF parameters may affect the mass hierarchy measurement in ICAL. To perform this study, we generate the data with a given hierarchy and assuming  $\alpha_{e\mu} = \alpha_{e\tau} = 0$ . Then, while fitting the “observed” event spectrum with the opposite hierarchy, we introduce  $\alpha_{e\mu}$  or  $\alpha_{e\tau}$  (one at-a-time) in the fit and marginalize over it in the range of  $10^{-55}$  to  $10^{-52}$  along with other oscillation parameters. During this analysis, we find that the mass hierarchy sensitivity of ICAL gets reduced very marginally by around 5%.

## 6.7 Summary and Conclusions

The main goal of the proposed ICAL experiment at INO is to measure the neutrino mass hierarchy by observing the atmospheric neutrinos and antineutrinos separately and making use of the Earth matter effects on their oscillations. Apart from this, ICAL detector can play an important role to unravel various new physics scenarios beyond the SM (see Refs. [53–60]). In this chapter, we have studied in detail the capabilities of ICAL to constrain the flavor-dependent long-range lep-

tonic forces mediated by the extremely light and neutral bosons associated with gauged  $L_e - L_\mu$  or  $L_e - L_\tau$  symmetries. It constitutes a minimal extension of the SM preserving its renormalizability and may alter the expected event spectrum in ICAL. As an example, the electrons inside the sun can generate a flavor-dependent long-range potential  $V_{e\mu/e\tau}$  at the Earth surface, which may affect the effective values of oscillation parameters in presence of the Earth matter. Important point to note here is that for atmospheric neutrinos,  $\Delta m^2/2E \sim 2.5 \times 10^{-13}$  eV (assuming  $\Delta m^2 \sim 2.5 \times 10^{-3}$  eV<sup>2</sup> and  $E = 5$  GeV), which is comparable to  $V_{e\mu/e\tau}$  even for  $\alpha_{e\mu/e\tau} \sim 10^{-52}$ , and can influence the atmospheric neutrino experiments significantly. Also, for a wide range of baselines accessible in atmospheric neutrino experiments, the Earth matter potentials ( $V_{CC}$ ) are around  $10^{-13}$  eV (see Table 6.1), suggesting that  $V_{CC}$  can interfere with  $V_{e\mu/e\tau}$  and  $\Delta m_{31}^2/2E$ , and can modify the oscillation probability substantially. In this chapter, we have explored these interesting possibilities in the context of the ICAL detector.

After deriving approximate analytical expressions for the effective neutrino oscillation parameters in presence of  $V_{CC}$  and  $V_{e\mu/e\tau}$ , we compare the oscillation probabilities obtained using our analytical expressions with those calculated numerically. Then, we have studied the impact of long-range forces by drawing the neutrino oscillograms in  $E_\nu$  and  $\cos \theta_\nu$  plane using the full three-flavor probability expressions with the varying Earth matter densities based on the PREM profile [348]. We have also presented the expected event spectra and total event rates in ICAL with and without long-range forces. As non-zero  $\alpha_{e\mu}$  and  $\alpha_{e\tau}$  can change the standard  $3\nu$  oscillation picture of ICAL significantly, we can expect to place strong limits on these parameters if ICAL do not observe a signal of LRF in oscillations. The ICAL detector is sensitive to  $\alpha_{e\mu/e\tau} \geq 1.2 \times 10^{-53}$  ( $1.75 \times 10^{-53}$ ) at least at 90% ( $3\sigma$ ) confidence level with an exposure of 500 kt-yr. The expected bounds from the ICAL detector obtained from our analysis is comparable to the existing limits on  $\alpha_{e\mu/e\tau}$  using solar and KamLAND data in Ref. [331]. The future limit from ICAL at 90% C.L. on  $\alpha_{e\mu}$  ( $\alpha_{e\tau}$ ) is  $\sim 46$  (53) times better than the existing limit from the Super-Kamiokande experiment. One can see that we get almost similar bound on LRF as obtain in Ref. [345], but using only half of the exposure. We understand that this enormous improvement in the result happens mainly due to inclusion of reconstructed hadron energy information in our analysis. Here, we would like to mention that if the range of LRF is equal or larger than our distance from the Galactic Center, then the collective long-range potential due to all the electrons inside the Galaxy needs to be taken into

account [331]. In such cases, ICAL can be sensitive to even lower values of  $\alpha_{e\mu/e\tau}$ . We hope that our present work can be an important addition to the series of interesting physics studies which can be performed using the proposed ICAL detector at the India-based Neutrino Observatory.

# 7

## Summary and Future Scope

We have witnessed lots of surprises while dealing with neutrinos and we are pretty sure that neutrinos will continue to astonish us in future as well. The discovery of neutrino oscillation was indeed a surprise to us which reveals that neutrinos are not massless, and the basic Standard Model of particle physics needs to be extended to explain the neutrino mass and mixing. The standard three-flavor oscillation picture of neutrinos has been established quite firmly with the help of path-breaking experiments involving solar, atmospheric, reactor, and accelerator neutrinos. After the discovery of the smallest lepton mixing angle  $\theta_{13}$  in 2012 with the help of modern reactor experiments, the neutrino community has been able to identify the fundamental unknowns that need to be resolved in near future with the help of upcoming oscillation experiments. By performing a detailed R&D and publishing several high quality research papers over the last few years, the India-based Neutrino Observatory (INO) Collaboration has convinced the community that the planned 50 kt magnetized ICAL detector has immense potential to address some of these major unknowns using atmospheric neutrinos. In this thesis, we have made a sincere effort to demonstrate that this experimental facility can also offer an exceptional window to probe various new physics scenarios beyond the Standard Model. We hope that the research work performed in this thesis will certainly enhance the physics reach of the proposed ICAL detector at the INO facility and will serve as an important guidespot to study various beyond the Standard Model scenarios once the detector starts taking data. Now, we summarize the key findings of the research work that we have presented in this thesis and discuss the future scope.



## 7.1 Summary

The discovery of neutrino oscillation demands that neutrinos should have non-zero mass and they should mix with each other. Undoubtedly, this is the first exclusive evidence of the physics beyond the Standard Model. The neutrino oscillation experiments can also be sensitive to various other new physics searches which can be complementary to the searches for the new physics which are being performed at the LHC. In the present thesis, we asked a very important question whether the atmospheric neutrino oscillation data which will be collected by the proposed 50 kt magnetized ICAL detector under the INO facility would be able to reveal the signatures of various interesting new physics scenarios apart from its capability to address some fundamental unknowns in neutrino oscillation physics. With this aim, we performed the indirect searches of Galactic diffuse dark matter through its annihilation and/or decay via neutrinos in Chapter 4. In Chapter 5, we studied the possibility of non-standard neutrino interactions and its impact on the standard three-flavor oscillation parameters when neutrinos traverse long distances inside the Earth matter. Towards the end, in Chapter 6, we unravel the presence of new flavor-dependent long-range leptonic forces which may have significant impact on atmospheric neutrino oscillations. We believe that these interesting new physics studies in context of the upcoming 50 kt magnetized ICAL detector under the INO facility have certainly strengthen its physics reach.

We started the first chapter by briefly describing the essential neutrino properties in the basic Standard Model. Then, we discussed various natural and artificial sources of neutrinos which have contributed immensely to improve our understanding about the neutrinos over past few decades. After that, we briefly described the famous experiment performed by Cowan and Reines who detected neutrinos for the first time using reactors. Then, we introduced the famous solar and atmospheric neutrino anomalies which puzzled the neutrino scientists for few decades. Finally, we concluded this chapter providing the solution of these anomalies with the help of neutrino oscillations.

In Chapter 2, we discussed the theory of neutrino oscillation in a general framework considering the mixing of  $N$  number of neutrinos. This discussion was quite helpful to obtain the expression for oscillation probabilities in case of two-flavor and three-flavor frameworks. Next, we had a discussion on the oscillation of neutrino and antineutrino during their propagation through matter

in a two-flavor framework, and described briefly the so-called “MSW” effect which governs the “running” of various oscillation parameters inside the matter. Then, we gave a summary of the interesting results obtained from a few pioneering neutrino oscillation experiments which contributed significantly to establish the current three-flavor picture of neutrino oscillation. Towards the end of this chapter, we made a list of the remaining unsolved issues in neutrino oscillation physics, and discussed the relevant oscillation channels which are important for any atmospheric neutrino experiment to address these fundamental unknowns.

In Chapter 3, the important components of the ICAL detector and the method of reconstruction of observables that we adopt for this detector are illustrated. We calculated the expected event rates at ICAL using 500 kt-yr exposure with oscillation and without oscillation. Then, assuming oscillation, we gave the event rates for both normal and inverted mass orderings of neutrino. We also estimated the  $\mu^-$  and  $\mu^+$  assuming three possible values of  $\theta_{23}$  and  $\Delta m_{32}^2$  within their  $3\sigma$  allowed ranges.

Chapter 4 deals with the study that we performed on the indirect searches of the Galactic diffuse dark matter using the 50 kt magnetized ICAL detector. The cosmological observations have confirmed that around 26% of the total energy budget of the Universe goes to the non-luminous and non-baryonic dark matter. In our analysis, we assumed that the dark matter annihilates and/or decays isotropically via a pair of light neutrino and antineutrino which take part in the weak interaction. For the dark matter density, we considered the NFW and Burkert profiles to estimate our final results with cuspy and cored halos respectively. We took 10% energy resolution ( $\Delta E/E$ ) and a flat  $10^\circ$  angular resolution ( $\Delta\theta$ ) while calculating the events at the ICAL detector. As far as the detection and the charge identification efficiencies were concerned, we considered them as 80% and 90% respectively. Neutrinos from the annihilating dark matter would appear as an excess in the observed atmospheric neutrino event spectra at the ICAL detector with the reconstructed neutrino energy around dark matter mass. In case of decay, the reconstructed neutrino energy would be around the half of dark matter mass. We assumed that the dark matter is distributed isotropically over the  $4\pi$  solid angle. Thus, the neutrinos coming to the detector from all possible directions were equally important in our study. We presented the sensitivity of ICAL assuming 500 kt-yr exposure to set limits on the velocity-averaged self-annihilation cross-section ( $\langle\sigma v\rangle$ ) and decay lifetime ( $\tau$ ) of dark matter having mass in the range of  $2\text{ GeV} \leq m_\chi \leq 90\text{ GeV}$

and  $4 \text{ GeV} \leq m_\chi \leq 180 \text{ GeV}$  respectively, assuming no excess over the conventional atmospheric neutrino and antineutrino fluxes at the INO site. We showed that the ICAL detector would be able to set competitive constraints of  $\langle \sigma v \rangle \leq 1.87 \times 10^{-24} \text{ cm}^3 \text{ s}^{-1}$  for  $\chi\chi \rightarrow \nu\bar{\nu}$  process and  $\tau \geq 4.8 \times 10^{24} \text{ s}$  for  $\chi \rightarrow \nu\bar{\nu}$  channel at 90% C.L. (1 d.o.f) for  $m_\chi = 10 \text{ GeV}$  assuming the NFW as dark matter density profile.

In Chapter 5, we explored the possibility of lepton flavor violating neutral current non-standard interactions (NSI's) of atmospheric neutrino and antineutrino while they travel long distances inside the Earth matter before reaching to the ICAL detector. During the propagation of these neutrinos, we allowed an extra interaction vertex with  $\nu_\mu$  as the incoming particle and  $\nu_\tau$  as the outgoing one and vice versa. With such an interaction vertex, the neutral current non-standard interaction of neutrino with matter fermions gave rise to a new matter potential whose relative strength as compared to the standard matter potential ( $V_{CC}$ ) is denoted by  $\varepsilon_{\mu\tau}$ . We showed that the ICAL detector would be able to place tight constraints on the NSI parameter  $\varepsilon_{\mu\tau}$  considering reconstructed hadron energy and muon momentum as observables. We found that with  $E_\mu \in [1, 11] \text{ GeV}$  and with  $[E_\mu, \cos \theta_\mu]$  as observables, the expected limit on  $\varepsilon_{\mu\tau}$  at 90% C.L. is  $-0.03 < \varepsilon_{\mu\tau} < 0.03$ . If we increase the muon energy range from 11 to 21 GeV ( $E_\mu \in [1, 21] \text{ GeV}$ ) and consider the reconstructed hadron energy as an extra observable on top of the four momenta of muon ( $E_\mu, \cos \theta_\mu, E'_{\text{had}}$  as observables), we find a significant improvement in the limit which is  $-0.01 < \varepsilon_{\mu\tau} < 0.01$  at 90% C.L. using 500 kt-yr exposure of the ICAL detector. We found that the charge identification ability of the ICAL detector plays an important role to obtain these tight constraints on  $\varepsilon_{\mu\tau}$  which are mentioned above. Assuming 1 to 21 GeV reconstructed muon energy range and considering  $E_\mu, \cos \theta_\mu$ , and  $E'_{\text{had}}$  as observables, we found that the mass hierarchy sensitivity at the ICAL detector with NH as the true choice deteriorates by  $\sim 10\%$  if we introduce the NSI parameter  $\varepsilon_{\mu\tau}$  in the fit and marginalize over it in the range of -0.1 to 0.1 along with other standard oscillation parameters. On the other hand, the precision measurement of atmospheric oscillation parameters at the ICAL detector was found to be quite robust even if we marginalize over the NSI parameter  $\varepsilon_{\mu\tau}$  in the fit in its range  $-0.1$  to  $0.1$ .

In Chapter 6, we studied the impact of the flavor-dependent long-range leptonic forces mediated by the ultra-light and neutral bosons associated with gauged  $L_e - L_\mu$  or  $L_e - L_\tau$  symmetry, which constitutes a minimal extension of the Standard Model. In presence of these new anomaly-free abelian

symmetries, the Standard Model remains invariant and renormalizable, and can lead to interesting phenomenological consequences. For an example, the electrons inside the Sun can generate a flavor-dependent long-range potential at the Earth surface, which can enhance  $\nu_\mu$  and  $\bar{\nu}_\mu$  survival probabilities over a wide range of energies and baselines in atmospheric neutrino experiments. In this chapter, we explored in detail the possible influence of these long-range flavor-diagonal neutral current interactions due to  $L_e - L_\mu$  and  $L_e - L_\tau$  symmetries (one at-a-time) in the context of proposed 50 kt magnetized ICAL detector at INO. Combining the information on muon momentum and hadron energy on an event-by-event basis, ICAL would be sensitive to long-range forces at 90% ( $3\sigma$ ) C.L. with 500 kt-yr exposure if the effective gauge coupling  $\alpha_{e\mu/e\tau} > 1.2 \times 10^{-53}$  ( $1.75 \times 10^{-53}$ ).

## 7.2 Future Scope

The studies described in this thesis can be extended in the following two directions. There are ample scope to improve our knowledge about the detector response of ICAL. We can also explore several interesting beyond the Standard Model scenarios using the expected atmospheric data from ICAL.

While we perform the studies with reconstructed muon momenta and hadron energy as observables, we consider only CC event where we have a muon track and possibly a hadron shower in the final state. It may not be always possible to have a clear distinction between the muon track and hadron shower in all events. In our study, we assume that the hits generated due to a muon track and hadron shower can be separated with 100% efficiency using the ICAL particle reconstruction algorithm. To be more precise, whenever we reconstruct a muon track, we consider all the other hits to be a part of the hadron shower to perform the hadron energy calibration. It means that the neutrino event reconstruction efficiency is the same as the muon reconstruction efficiency. We need to address these issues related to the detector simulation in future, which in turn can affect the sensitivity results presented in this thesis. Also, in our analysis, we have not included any background hits which can arise due to neutral current events, charged current  $\nu_e$  events, cosmic muons, and noise due to electronics. Needless to mention that the systematic uncertainties due to these effects need to be taken into account in future as our knowledge about ICAL will be refined.

As far as the physics studies are concerned, there is enough room to address several interesting issues which we have not considered in this thesis. For an instance, we perform the indirect searches of Galactic diffuse dark matter, but at the same time, the study of dark matter at the Galactic Center would be quite interesting since the directional information of neutrino reaching at the detector can improve the signal over background ratio significantly. While addressing the issue of neutral current non-standard interaction of neutrino, we consider only flavor changing NSI parameter  $\varepsilon_{\mu\tau}$ . One can also study the impact of other NSI parameters such as  $\varepsilon_{e\mu}$ ,  $\varepsilon_{e\tau}$ ,  $\varepsilon_{ee}$ ,  $\varepsilon_{\mu\mu}$ , and  $\varepsilon_{\tau\tau}$  considering one NSI parameter non-zero at-a-time. In the study of long-range forces, we have considered the flavor symmetries  $L_e - L_\mu$  and  $L_e - L_\tau$ . In future, we would like to see how  $L_\mu - L_\tau$  flavor symmetry can alter the expected atmospheric neutrino and antineutrino event rates at ICAL.

# **Appendices**

# A Oscillation of Neutrinos

## Travelling Astronomical Distances

From Eq. 2.1.10, we can write the oscillation probability of neutrino from one flavor ( $\alpha$ ) to another flavor ( $\beta$ ) in vacuum as

$$P_{\nu_\alpha \rightarrow \nu_\beta}(L) = \sum_{i=j=1}^N |U_{\alpha i}|^2 |U_{\beta j}|^2 + 2 \sum_{i>j=1}^N \text{Re} \left( U_{\alpha i}^* U_{\beta i} U_{\alpha j} U_{\beta j}^* \right) \cos \frac{\Delta m_{ij}^2 L}{2E} + 2 \sum_{i>j=1}^N \text{Im} \left( U_{\alpha i}^* U_{\beta i} U_{\alpha j} U_{\beta j}^* \right) \sin \frac{\Delta m_{ij}^2 L}{2E}, \quad (\text{A.0.1})$$

where  $U$  is the PMNS matrix [144, 145, 153].  $E$  and  $L$  denote the neutrino energy and baseline respectively. While performing the indirect searches of Galactic diffuse dark matter in the context of ICAL, we are interested in the multi-GeV neutrinos coming from the annihilation/decay of dark matter particles. Also, these neutrinos traverse astronomical distances before they reach at the detector. Therefore, we can safely assume that the oscillation length associated with these neutrinos with mass-splittings as suggested by solar, atmospheric, or LSND data is much smaller than the astronomical distances that they travel ( $L^{\text{osc}} \ll L$ ). Therefore, 2nd and 3rd terms in Eq. A.0.1 get averaged out to zero due to very rapid oscillations, and give rise to the following expression

$$P_{\alpha\beta} = \sum_{k=1}^3 |U_{\alpha k}|^2 |U_{\beta k}|^2. \quad (\text{A.0.2})$$

We assume that the annihilation/decay of dark matter particles produce  $\nu_e$ ,  $\nu_\mu$ , and  $\nu_\tau$  in the ratio of 1:1:1 at the source. During their propagation through the astronomical distance from source to

detector, neutrinos go through vacuum. Now, imposing the unitary property of  $U$  in Eq. [A.0.2](#), one can easily see that the ratio of neutrino flavors at the Earth surface remains 1:1:1, and this is true irrespective of the values of oscillation parameters.



# B Oscillations with $L_e - L_\mu$

## Symmetry

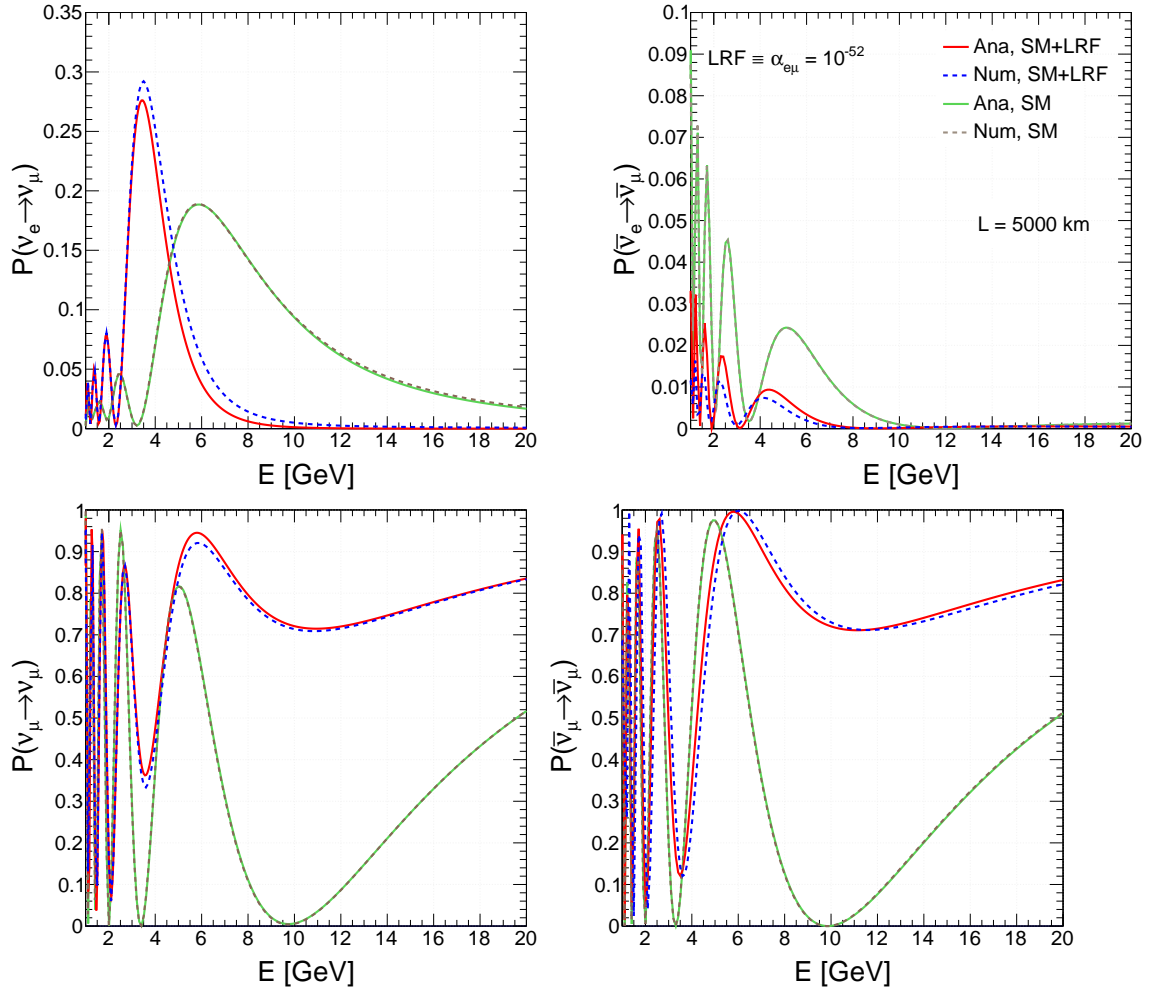


Fig. B.1 shows approximate  $\nu_e \rightarrow \nu_\mu$  ( $\bar{\nu}_e \rightarrow \bar{\nu}_\mu$ ) oscillation probabilities in the top left (right) panel as a function of  $E$  against the exact numerical results considering  $L = 5000$  km and NH. We repeat the same for  $\nu_\mu \rightarrow \nu_\mu$  ( $\bar{\nu}_\mu \rightarrow \bar{\nu}_\mu$ ) survival channels in bottom left (right) panel. We perform these comparisons among analytical (solid curves) and numerical (dashed curves) cases for both the SM and SM + LRF scenarios considering our benchmark choice of  $\alpha_{e\mu} = 10^{-52}$ . For the SM case ( $\alpha_{e\mu} = 0$ ), the approximate results match very nicely with numerically obtained probabilities. Analytical expressions also work quite well in the presence of  $L_e - L_\mu$  symmetry, and can produce almost accurate  $L/E$  oscillation patterns.

# C Treatment of Systematic Uncertainties

In all the studies that we have done in this thesis, the uncertainties on various parameters such as cross-section, fluxes, and so on are included using the well-known “pull” method [281–283]. In pull method, the systematic uncertainties are parameterized with a set of variables ( $\xi_l$ ) which are called pulls. The basic idea is to express the simulated events ( $N_{ijk}^{\text{theory}}$ ) in terms of theoretical prediction, pull parameters, and systematic uncertainties in the following way,

$$N_{ijk}^{\text{theory}} = N_{ijk}^0 \left( 1 + \sum_{l=1}^N \pi_{ijk}^l \xi_l \right), \quad (\text{C.0.1})$$

where  $N_{ijk}^0$  is the event number with theoretical prediction but without systematic uncertainties, and  $\pi_{ijk}^l$  is the error of  $l$ -th systematic variable.

On the other hand,  $\chi^2$  function is written in terms of the Poissonian  $\chi^2$  to take into account the deviation of simulated events from experimental events ( $N_{ijk}^{\text{data}}$ ) and the penalties<sup>1</sup> to take care the error in systematic uncertainties and theoretical inputs from their standard values. The  $\chi^2$  function is minimized over the pull parameters  $\xi_l$ ,

$$\chi^2 = \min_{\xi_l} \sum_{i=1}^{N_{E'_{\text{had}}}} \sum_{j=1}^{N_{E_{\mu}}} \sum_{k=1}^{N_{\cos \theta_{\mu}}} \left[ 2(N_{ijk}^{\text{theory}} - N_{ijk}^{\text{data}}) - 2N_{ijk}^{\text{data}} \ln \left( \frac{N_{ijk}^{\text{theory}}}{N_{ijk}^{\text{data}}} \right) \right] + \sum_{l=1}^5 \xi_l^2. \quad (\text{C.0.2})$$

---

<sup>1</sup>If the sources of uncertainties are independent, then the pull variables are uncorrelated, and the penalty term can be written as  $\sum_{l=1}^5 \xi_l^2$ .

For minimum value of  $\chi^2$ , we know that

$$\frac{\partial \chi^2}{\partial \xi_p} = 0. \quad (\text{C.0.3})$$

After partial derivative of Eq. C.0.2 with respect to  $\xi_p$ , we get

$$\frac{\partial \chi^2}{\partial \xi_p} = \sum_{i=1}^{N_{\text{had}}'} \sum_{j=1}^{N_{E\mu}} \sum_{k=1}^{N_{\cos\theta_\mu}} 2 \frac{\partial N_{ijk}^{\text{theory}}}{\partial \xi_p} - 2 \frac{N_{ijk}^{\text{data}}}{N_{ijk}^{\text{theory}}} \frac{dN_{ijk}^{\text{theory}}}{\partial \xi_p} + 2 \sum_{l=1}^5 \xi_l \frac{d\xi_l}{d\xi_p}. \quad (\text{C.0.4})$$

Using Eq. C.0.1, the following two terms of Eq. C.0.4 can be written as

$$\frac{dN_{ijk}^{\text{theory}}}{d\xi_p} = \frac{d}{d\xi_p} \left[ N_{ijk}^0 \left( 1 + \sum_{l=1}^5 \pi_{ijk}^l \xi_l \right) \right] = N_{ijk}^0 \sum_{l=1}^5 \pi_{ijk}^l \delta_{lp} = N_{ijk}^0 \pi_{ijk}^p, \quad (\text{C.0.5})$$

and

$$\frac{N_{ijk}^{\text{data}}}{N_{ijk}^{\text{theory}}} = \frac{N_{ijk}^{\text{data}}}{N_{ijk}^0} \left( 1 + \sum_{l=1}^5 \pi_{ijk}^l \xi_l \right)^{-1}. \quad (\text{C.0.6})$$

For uncorrelated pull parameters, we have

$$\frac{d\xi_l}{d\xi_p} = \delta_{lp}, \text{ which is } 1 \text{ for } l = p; \text{ else } 0. \quad (\text{C.0.7})$$

Now, replacing the quantities in Eq. C.0.3 from Eq. C.0.4, Eq. C.0.5, and Eq. C.0.6, we can write

$$\begin{aligned} & \sum_{i=1}^{N_{\text{had}}'} \sum_{j=1}^{N_{E\mu}} \sum_{k=1}^{N_{\cos\theta_\mu}} N_{ijk}^0 \pi_{ijk}^p - \frac{N_{ijk}^{\text{data}}}{N_{ijk}^0} \left( 1 + \sum_{l=1}^5 \pi_{ijk}^l \xi_l \right)^{-1} N_{ijk}^0 \pi_{ijk}^p + \xi_p = 0. \\ \Rightarrow & \sum_{i=1}^{N_{\text{had}}'} \sum_{j=1}^{N_{E\mu}} \sum_{k=1}^{N_{\cos\theta_\mu}} N_{ijk}^0 \pi_{ijk}^p - N_{ijk}^{\text{data}} \pi_{ijk}^p \left( 1 + \sum_{l=1}^5 \pi_{ijk}^l \xi_l \right)^{-1} + \xi_p = 0. \end{aligned} \quad (\text{C.0.8})$$

With the term  $\left( 1 + \sum_{l=1}^5 \pi_{ijk}^l \xi_l \right)^{-1}$  expanded and keeping the terms up to the first order, Eq. C.0.8 can be written as

$$\sum_{i=1}^{N_{\text{had}}'} \sum_{j=1}^{N_{E\mu}} \sum_{k=1}^{N_{\cos\theta_\mu}} N_{ijk}^0 \pi_{ijk}^p - N_{ijk}^{\text{data}} \pi_{ijk}^p \left( 1 - \sum_{l=1}^5 \pi_{ijk}^l \xi_l \right) + \xi_p = 0,$$

$$\Rightarrow \sum_{i=1}^{N_{\text{had}}'} \sum_{j=1}^{N_{E\mu}} \sum_{k=1}^{N_{\cos\theta\mu}} N_{ijk}^{\text{data}} \pi_{ijk}^p \sum_{l=1}^5 \pi_{ijk}^l \xi_l + \xi_p = \sum_{i=1}^{N_{\text{had}}'} \sum_{j=1}^{N_{E\mu}} \sum_{k=1}^{N_{\cos\theta\mu}} (N_{ijk}^{\text{data}} - N_{ijk}^0) \pi_{ijk}^p. \quad (\text{C.0.9})$$

If we have two systematic variables, the following equation can be used to calculate the value of pull parameters,

$$\begin{bmatrix} 1 + \sum_{i,j,k} N_{ijk}^{\text{data}} (\pi_{ijk}^1)^2 & \sum_{i,j,k} N_{ijk}^{\text{data}} \pi_{ijk}^1 \pi_{ijk}^2 \\ \sum_{i,j,k} N_{ijk}^{\text{data}} \pi_{ijk}^2 \pi_{ijk}^1 & 1 + \sum_{i,j,k} N_{ijk}^{\text{data}} (\pi_{ijk}^2)^2 \end{bmatrix} \begin{bmatrix} \xi_1 \\ \xi_2 \end{bmatrix} = \sum_{i,j,k} (N_{ijk}^{\text{data}} - N_{ijk}^0) \begin{bmatrix} \pi_{ijk}^1 \\ \pi_{ijk}^2 \end{bmatrix}. \quad (\text{C.0.10})$$

We have used Eq. C.0.10 to calculate pulls in the analysis described in Chapter 4.

For 5 pull parameters, we have

$$A B = C, \quad (\text{C.0.11})$$

with

$$A = \begin{pmatrix} 1 + \sum N_{ijk}^{\text{data}} (\pi_{ijk}^1)^2 & \sum N_{ijk}^{\text{data}} \pi_{ijk}^1 \pi_{ijk}^2 & \sum N_{ijk}^{\text{data}} \pi_{ijk}^1 \pi_{ijk}^3 & \sum N_{ijk}^{\text{data}} \pi_{ijk}^1 \pi_{ijk}^4 & \sum N_{ijk}^{\text{data}} \pi_{ijk}^1 \pi_{ijk}^5 \\ \sum N_{ijk}^{\text{data}} \pi_{ijk}^2 \pi_{ijk}^1 & 1 + \sum N_{ijk}^{\text{data}} (\pi_{ijk}^2)^2 & \sum N_{ijk}^{\text{data}} \pi_{ijk}^2 \pi_{ijk}^3 & \sum N_{ijk}^{\text{data}} \pi_{ijk}^2 \pi_{ijk}^4 & \sum N_{ijk}^{\text{data}} \pi_{ijk}^2 \pi_{ijk}^5 \\ \sum N_{ijk}^{\text{data}} \pi_{ijk}^3 \pi_{ijk}^1 & \sum N_{ijk}^{\text{data}} \pi_{ijk}^3 \pi_{ijk}^2 & 1 + \sum N_{ijk}^{\text{data}} (\pi_{ijk}^3)^2 & \sum N_{ijk}^{\text{data}} \pi_{ijk}^3 \pi_{ijk}^4 & \sum N_{ijk}^{\text{data}} \pi_{ijk}^3 \pi_{ijk}^5 \\ \sum N_{ijk}^{\text{data}} \pi_{ijk}^4 \pi_{ijk}^1 & \sum N_{ijk}^{\text{data}} \pi_{ijk}^4 \pi_{ijk}^2 & \sum N_{ijk}^{\text{data}} \pi_{ijk}^4 \pi_{ijk}^3 & \sum N_{ijk}^{\text{data}} (\pi_{ijk}^4)^2 & \sum N_{ijk}^{\text{data}} \pi_{ijk}^4 \pi_{ijk}^5 \\ \sum N_{ijk}^{\text{data}} \pi_{ijk}^5 \pi_{ijk}^1 & \sum N_{ijk}^{\text{data}} \pi_{ijk}^5 \pi_{ijk}^2 & \sum N_{ijk}^{\text{data}} \pi_{ijk}^5 \pi_{ijk}^3 & \sum N_{ijk}^{\text{data}} \pi_{ijk}^5 \pi_{ijk}^4 & 1 + \sum N_{ijk}^{\text{data}} (\pi_{ijk}^5)^2 \end{pmatrix}, \quad (\text{C.0.12})$$

$$B = \begin{bmatrix} \xi_1 \\ \xi_2 \\ \xi_3 \\ \xi_4 \\ \xi_5 \end{bmatrix}, \quad C = \sum_{i,j,k} (N_{ijk}^{\text{data}} - N_{ijk}^0) \begin{bmatrix} \pi_{ijk}^1 \\ \pi_{ijk}^2 \\ \pi_{ijk}^3 \\ \pi_{ijk}^4 \\ \pi_{ijk}^5 \end{bmatrix}. \quad (\text{C.0.13})$$

The value of pull variables  $\{\xi_l\}$  can be calculated with the inverse of matrix  $A$  multiplied with matrix  $C$ . This is the way we have calculated the pull parameters in the studies as described in Chapter 5 and Chapter 6.

# Bibliography

- [1] R. Mohapatra, S. Antusch, K. Babu, G. Barenboim, M.-C. Chen, et al., *Theory of neutrinos: A White paper*, *Rept.Prog.Phys.* **70** (2007) 1757–1867, [[hep-ph/0510213](#)].
- [2] A. Strumia and F. Vissani, *Neutrino masses and mixings and...*, [hep-ph/0606054](#).
- [3] M. Gonzalez-Garcia and M. Maltoni, *Phenomenology with Massive Neutrinos*, *Phys.Rept.* **460** (2008) 1–129, [[arXiv:0704.1800](#)].
- [4] **Particle Data Group** Collaboration, C. Patrignani et al., *Review of Particle Physics*, *Chin. Phys.* **C40** (2016), no. 10 100001.
- [5] **Super-Kamiokande** Collaboration, Y. Fukuda et al., *Evidence for oscillation of atmospheric neutrinos*, *Phys. Rev. Lett.* **81** (1998) 1562–1567, [[hep-ex/9807003](#)].
- [6] T. J. Haines et al., *Calculation of Atmospheric Neutrino Induced Backgrounds in a Nucleon Decay Search*, *Phys. Rev. Lett.* **57** (1986) 1986–1989.
- [7] **kamiokande-II** Collaboration, k. S. Hirata et al., *Experimental Study of the Atmospheric Neutrino Flux*, *Phys. Lett.* **B205** (1988) 416. [,447(1988)].
- [8] **Super-Kamiokande** Collaboration, Y. Fukuda et al., *Study of the atmospheric neutrino flux in the multi-GeV energy range*, *Phys. Lett.* **B436** (1998) 33–41, [[hep-ex/9805006](#)].
- [9] **SNO** Collaboration, Q. Ahmad et al., *Direct evidence for neutrino flavor transformation from neutral current interactions in the Sudbury Neutrino Observatory*, *Phys.Rev.Lett.* **89** (2002) 011301, [[nucl-ex/0204008](#)].

- [10] **KamLAND** Collaboration, K. Eguchi et al., *First results from KamLAND: Evidence for reactor anti-neutrino disappearance*, *Phys. Rev. Lett.* **90** (2003) 021802, [[hep-ex/0212021](#)].
- [11] **KamLAND** Collaboration, T. Araki et al., *Measurement of neutrino oscillation with KamLAND: Evidence of spectral distortion*, *Phys.Rev.Lett.* **94** (2005) 081801, [[hep-ex/0406035](#)].
- [12] **KamLAND** Collaboration, S. Abe et al., *Precision Measurement of Neutrino Oscillation Parameters with KamLAND*, *Phys.Rev.Lett.* **100** (2008) 221803, [[arXiv:0801.4589](#)].
- [13] **KamLAND** Collaboration, A. Gando et al., *Reactor On-Off Antineutrino Measurement with KamLAND*, *Phys. Rev.* **D88** (2013), no. 3 033001, [[arXiv:1303.4667](#)].
- [14] I. Esteban, M. C. Gonzalez-Garcia, M. Maltoni, I. Martinez-Soler, and T. Schwetz, *Updated fit to three neutrino mixing: exploring the accelerator-reactor complementarity*, *JHEP* **01** (2017) 087, [[arXiv:1611.01514](#)].
- [15] P. F. de Salas, D. V. Forero, C. A. Ternes, M. Tortola, and J. W. F. Valle, *Status of neutrino oscillations 2017*, [arXiv:1708.01186](#).
- [16] F. Capozzi, E. Di Valentino, E. Lisi, A. Marrone, A. Melchiorri, and A. Palazzo, *Global constraints on absolute neutrino masses and their ordering*, [arXiv:1703.04471](#).
- [17] G. H. Collin, C. A. Argüelles, J. M. Conrad, and M. H. Shaevitz, *First Constraints on the Complete Neutrino Mixing Matrix with a Sterile Neutrino*, *Phys. Rev. Lett.* **117** (2016), no. 22 221801, [[arXiv:1607.00011](#)].
- [18] S. Gariazzo, C. Giunti, M. Laveder, and Y. F. Li, *Updated Global 3+1 Analysis of Short-BaseLine Neutrino Oscillations*, *JHEP* **06** (2017) 135, [[arXiv:1703.00860](#)].
- [19] B. Cleveland, T. Daily, J. Davis, Raymond, J. R. Distel, K. Lande, et al., *Measurement of the solar electron neutrino flux with the Homestake chlorine detector*, *Astrophys.J.* **496** (1998) 505–526.

- [20] **SAGE** Collaboration, J. N. Abdurashitov et al., *Measurement of the solar neutrino capture rate with gallium metal. III: Results for the 2002–2007 data-taking period*, *Phys. Rev.* **C80** (2009) 015807, [[arXiv:0901.2200](#)].
- [21] F. Kaether, W. Hampel, G. Heusser, J. Kiko, and T. Kirsten, *Reanalysis of the GALLEX solar neutrino flux and source experiments*, *Phys. Lett.* **B685** (2010) 47–54, [[arXiv:1001.2731](#)].
- [22] **Super-Kamiokande** Collaboration, J. Hosaka et al., *Solar neutrino measurements in super-Kamiokande-I*, *Phys.Rev.* **D73** (2006) 112001, [[hep-ex/0508053](#)].
- [23] **Super-Kamiokande** Collaboration, J. P. Cravens et al., *Solar neutrino measurements in Super-Kamiokande-II*, *Phys. Rev.* **D78** (2008) 032002, [[arXiv:0803.4312](#)].
- [24] **Super-Kamiokande** Collaboration, K. Abe et al., *Solar neutrino results in Super-Kamiokande-III*, *Phys. Rev.* **D83** (2011) 052010, [[arXiv:1010.0118](#)].
- [25] **SNO** Collaboration, B. Aharmim et al., *Combined Analysis of all Three Phases of Solar Neutrino Data from the Sudbury Neutrino Observatory*, *Phys. Rev.* **C88** (2013) 025501, [[arXiv:1109.0763](#)].
- [26] **Borexino** Collaboration, G. Bellini et al., *Measurement of the solar  $8B$  neutrino rate with a liquid scintillator target and 3 MeV energy threshold in the Borexino detector*, *Phys. Rev.* **D82** (2010) 033006, [[arXiv:0808.2868](#)].
- [27] **KamLAND** Collaboration, A. Gando et al., *Constraints on  $\theta_{13}$  from A Three-Flavor Oscillation Analysis of Reactor Antineutrinos at KamLAND*, *Phys. Rev.* **D83** (2011) 052002, [[arXiv:1009.4771](#)].
- [28] **Super-Kamiokande** Collaboration, R. Wendell et al., *Atmospheric neutrino oscillation analysis with sub-leading effects in Super-Kamiokande I, II, and III*, *Phys.Rev.* **D81** (2010) 092004, [[arXiv:1002.3471](#)].
- [29] **MINOS** Collaboration, P. Adamson et al., *Measurement of Neutrino and Antineutrino Oscillations Using Beam and Atmospheric Data in MINOS*, *Phys.Rev.Lett.* **110** (2013), no. 25 251801, [[arXiv:1304.6335](#)].



- [30] **MINOS** Collaboration, P. Adamson et al., *Electron neutrino and antineutrino appearance in the full MINOS data sample*, *Phys.Rev.Lett.* **110** (2013) 171801, [[arXiv:1301.4581](#)].
- [31] **IceCube** Collaboration, M. G. Aartsen et al., *Determining neutrino oscillation parameters from atmospheric muon neutrino disappearance with three years of IceCube DeepCore data*, *Phys. Rev.* **D91** (2015), no. 7 072004, [[arXiv:1410.7227](#)].
- [32] **ANTARES** Collaboration, S. Adrian-Martinez et al., *Measurement of Atmospheric Neutrino Oscillations with the ANTARES Neutrino Telescope*, *Phys. Lett.* **B714** (2012) 224–230, [[arXiv:1206.0645](#)].
- [33] **T2K** Collaboration, K. Abe et al., *Precise Measurement of the Neutrino Mixing Parameter  $\theta_{23}$  from Muon Neutrino Disappearance in an Off-Axis Beam*, *Phys.Rev.Lett.* **112** (2014) 181801, [[arXiv:1403.1532](#)].
- [34] **T2K** Collaboration, K. Abe et al., *Observation of Electron Neutrino Appearance in a Muon Neutrino Beam*, *Phys.Rev.Lett.* **112** (2014) 061802, [[arXiv:1311.4750](#)].
- [35] **T2K** Collaboration, K. Abe et al., *Updated T2K measurements of muon neutrino and antineutrino disappearance using  $1.5 \times 10^{21}$  protons on target*, *Phys. Rev.* **D96** (2017), no. 1 011102, [[arXiv:1704.06409](#)].
- [36] **T2K** Collaboration, K. Abe et al., *Combined Analysis of Neutrino and Antineutrino Oscillations at T2K*, *Phys. Rev. Lett.* **118** (2017), no. 15 151801, [[arXiv:1701.00432](#)].
- [37] **NOvA** Collaboration, P. Adamson et al., *Measurement of the neutrino mixing angle  $\theta_{23}$  in NOvA*, *Phys. Rev. Lett.* **118** (2017), no. 15 151802, [[arXiv:1701.05891](#)].
- [38] **NOvA** Collaboration, P. Adamson et al., *Constraints on Oscillation Parameters from  $\nu_e$  Appearance and  $\nu_\mu$  Disappearance in NOvA*, *Phys. Rev. Lett.* **118** (2017), no. 23 231801, [[arXiv:1703.03328](#)].
- [39] **Daya Bay** Collaboration, F. An et al., *Spectral measurement of electron antineutrino oscillation amplitude and frequency at Daya Bay*, *Phys.Rev.Lett.* **112** (2014) 061801, [[arXiv:1310.6732](#)].

- [40] **Double Chooz** Collaboration, Y. Abe et al., *Improved measurements of the neutrino mixing angle  $\theta_{13}$  with the Double Chooz detector*, *JHEP* **1410** (2014) 086, [[arXiv:1406.7763](#)].
- [41] **RENO** Collaboration, J. H. Choi et al., *Observation of Energy and Baseline Dependent Reactor Antineutrino Disappearance in the RENO Experiment*, *Phys. Rev. Lett.* **116** (2016), no. 21 211801, [[arXiv:1511.05849](#)].
- [42] **ICAL** Collaboration, S. Ahmed et al., *Physics Potential of the ICAL detector at the India-based Neutrino Observatory (INO)*, *Pramana* **88** (2017), no. 5 79, [[arXiv:1505.07380](#)].
- [43] India-based Neutrino Observatory (INO), <http://www.ino.tifr.res.in/ino/>.
- [44] L. Wolfenstein, *Neutrino Oscillations in Matter*, *Phys.Rev.* **D17** (1978) 2369–2374.
- [45] S. Mikheev and A. Y. Smirnov, *Resonance Amplification of Oscillations in Matter and Spectroscopy of Solar Neutrinos*, *Sov.J.Nucl.Phys.* **42** (1985) 913–917.
- [46] S. Mikheev and A. Y. Smirnov, *Resonant amplification of neutrino oscillations in matter and solar neutrino spectroscopy*, *Nuovo Cim.* **C9** (1986) 17–26.
- [47] A. Ghosh, T. Thakore, and S. Choubey, *Determining the Neutrino Mass Hierarchy with INO, T2K, NOvA and Reactor Experiments*, *JHEP* **1304** (2013) 009, [[arXiv:1212.1305](#)].
- [48] T. Thakore, A. Ghosh, S. Choubey, and A. Dighe, *The Reach of INO for Atmospheric Neutrino Oscillation Parameters*, *JHEP* **05** (2013) 058, [[arXiv:1303.2534](#)].
- [49] M. M. Devi, T. Thakore, S. K. Agarwalla, and A. Dighe, *Enhancing sensitivity to neutrino parameters at INO combining muon and hadron information*, *JHEP* **1410** (2014) 189, [[arXiv:1406.3689](#)].
- [50] A. Ajmi, A. Dev, M. Nizam, N. Nayak, and S. Uma Sankar, *Improving the hierarchy sensitivity of ICAL using neural network*, *J. Phys. Conf. Ser.* **888** (2017), no. 1 012151, [[arXiv:1510.02350](#)].
- [51] D. Kaur, M. Naimuddin, and S. Kumar, *The sensitivity of the ICAL detector at India-based Neutrino Observatory to neutrino oscillation parameters*, *Eur. Phys. J.* **C75** (2015), no. 4 156, [[arXiv:1409.2231](#)].

- [52] L. S. Mohan and D. Indumathi, *Pinning down neutrino oscillation parameters in the 2–3 sector with a magnetised atmospheric neutrino detector: a new study*, *Eur. Phys. J.* **C77** (2017), no. 1 54, [[arXiv:1605.04185](#)].
- [53] N. Dash, V. M. Datar, and G. Majumder, *Sensitivity for detection of decay of dark matter particle using ICAL at INO*, *Pramana* **86** (2016), no. 4 927–937, [[arXiv:1410.5182](#)].
- [54] N. Dash, V. M. Datar, and G. Majumder, *Sensitivity of the INO-ICAL detector to magnetic monopoles*, *Astropart. Phys.* **70** (2015) 33–38, [[arXiv:1406.3938](#)].
- [55] A. Chatterjee, R. Gandhi, and J. Singh, *Probing Lorentz and CPT Violation in a Magnetized Iron Detector using Atmospheric Neutrinos*, *JHEP* **06** (2014) 045, [[arXiv:1402.6265](#)].
- [56] A. Chatterjee, P. Mehta, D. Choudhury, and R. Gandhi, *Testing nonstandard neutrino matter interactions in atmospheric neutrino propagation*, *Phys. Rev.* **D93** (2016), no. 9 093017, [[arXiv:1409.8472](#)].
- [57] S. Choubey, A. Ghosh, T. Ohlsson, and D. Tiwari, *Neutrino Physics with Non-Standard Interactions at INO*, *JHEP* **12** (2015) 126, [[arXiv:1507.02211](#)].
- [58] S. P. Behera, A. Ghosh, S. Choubey, V. M. Datar, D. K. Mishra, and A. K. Mohanty, *Search for the sterile neutrino mixing with the ICAL detector at INO*, *Eur. Phys. J.* **C77** (2017), no. 5 307, [[arXiv:1605.08607](#)].
- [59] S. Choubey, S. Goswami, C. Gupta, S. M. Lakshmi, and T. Thakore, *Sensitivity to neutrino decay with atmospheric neutrinos at INO*, [arXiv:1709.10376](#).
- [60] S. Choubey, A. Ghosh, and D. Tiwari, *Prospects of Indirect Searches for Dark Matter at INO*, [arXiv:1711.02546](#).
- [61] A. Khatun, R. Laha, and S. K. Agarwalla, *Indirect searches of Galactic diffuse dark matter in INO-MagICAL detector*, *JHEP* **06** (2017) 057, [[arXiv:1703.10221](#)].
- [62] A. Khatun, T. Thakore, and S. K. Agarwalla, *Can INO be Sensitive to Flavor-Dependent Long-Range Forces?*, *JHEP* **04** (2018) 023, [[arXiv:1801.00949](#)].

- [63] A. Khatun, S. S. Chatterjee, T. Thakore, and S. K. Agarwalla, *Constraining Non-Standard Interactions of Neutrino Using ICAL Detector at INO*, *Springer Proc. Phys.* **203** (2018) 289–292.
- [64] T. Thakore, M. M. Devi, S. K. Agarwalla, and A. Dighe, *Active-sterile neutrino oscillations at INO-ICAL over a wide mass-squared range*, *JHEP* **08** (2018) 022, [[arXiv:1804.09613](https://arxiv.org/abs/1804.09613)].
- [65] W. Pauli, *On the Earlier and more recent history of the neutrino*, *Camb. Monogr. Part. Phys. Nucl. Phys. Cosmol.* **14** (2000) 1–22.
- [66] E. Fermi, *An attempt of a theory of beta radiation. I.*, *Z. Phys.* **88** (1934) 161–177.
- [67] E. Fermi, *Trends to a Theory of beta Radiation. (In Italian)*, *Nuovo Cim.* **11** (1934) 1–19. [,535(1934)].
- [68] B. Pontecorvo, *Nuclear capture of mesons and the meson decay*, *Phys. Rev.* **72** (1947) 246.
- [69] G. Puppi, *On Mesons in Cosmic Radiation. (In Italian)*, *Nuovo Cim.* **5** (1948) 587–588. [,590(1948)].
- [70] O. Klein, *Mesons and nucleons*, *Nature* **161** (1948) 897–899.
- [71] C.-N. Yang and J. Tiomno, *Reflection Properties of Spin 1/2 Fields and a Universal Fermi Type Interaction*, *Phys. Rev.* **79** (1950) 495–498.
- [72] T. D. Lee and C.-N. Yang, *Question of Parity Conservation in Weak Interactions*, *Phys. Rev.* **104** (1956) 254–258.
- [73] C. S. Wu, E. Ambler, R. W. Hayward, D. D. Hoppes, and R. P. Hudson, *Experimental Test of Parity Conservation in Beta Decay*, *Phys. Rev.* **105** (1957) 1413–1414.
- [74] M. Goldhaber, L. Grodzins, and A. W. Sunyar, *Helicity of Neutrinos*, *Phys. Rev.* **109** (1958) 1015–1017.
- [75] T. D. Lee and C.-N. Yang, *Parity Nonconservation and a Two Component Theory of the Neutrino*, *Phys. Rev.* **105** (1957) 1671–1675. [,245(1957)].

- [76] E. C. G. Sudarshan and R. E. Marshak, *Chirality invariance and the universal V-A theory of weak interactions*, in *A gift of prophecy: Essays in celebration of the life of Robert Eugene Marshak*, pp. 18–42, 1990. [,516(1990)].
- [77] E. C. G. Sudarshan and R. E. Marshak, *Origin of the Universal V-A theory*, *AIP Conf. Proc.* **300** (1994) 110–124. [,0001(1984)].
- [78] R. E. Marshak, S. Okubo, and G. Sudarshan, *V-A theory and the decay of the hyperon*, *Phys. Rev.* **113** (1959) 944–954.
- [79] S. L. Glashow, *Partial Symmetries of Weak Interactions*, *Nucl. Phys.* **22** (1961) 579–588.
- [80] S. Weinberg, *A Model of Leptons*, *Phys. Rev. Lett.* **19** (1967) 1264–1266.
- [81] M. Gell-Mann, *A Schematic Model of Baryons and Mesons*, *Phys. Lett.* **8** (1964) 214–215.
- [82] H. Fritzsch, M. Gell-Mann, and H. Leutwyler, *Advantages of the Color Octet Gluon Picture*, *Phys. Lett.* **47B** (1973) 365–368.
- [83] **Gargamelle Neutrino** Collaboration, F. J. Hasert et al., *Observation of Neutrino Like Interactions Without Muon Or Electron in the Gargamelle Neutrino Experiment*, *Phys. Lett.* **B46** (1973) 138–140. [,5.15(1973)].
- [84] **UA1** Collaboration, G. Arnison et al., *Experimental Observation of Isolated Large Transverse Energy Electrons with Associated Missing Energy at  $s^{1/2} = 540\text{-GeV}$* , *Phys. Lett.* **B122** (1983) 103–116. [,611(1983)].
- [85] **UA2** Collaboration, M. Banner et al., *Observation of Single Isolated Electrons of High Transverse Momentum in Events with Missing Transverse Energy at the CERN anti-p p Collider*, *Phys. Lett.* **B122** (1983) 476–485. [,7.45(1983)].
- [86] **CMS** Collaboration, S. Chatrchyan et al., *Observation of a new boson at a mass of 125 GeV with the CMS experiment at the LHC*, *Phys. Lett.* **B716** (2012) 30–61, [[arXiv:1207.7235](#)].
- [87] **ATLAS** Collaboration, G. Aad et al., *Observation of a new particle in the search for the Standard Model Higgs boson with the ATLAS detector at the LHC*, *Phys. Lett.* **B716** (2012) 1–29, [[arXiv:1207.7214](#)].

- [88] M. Honda, M. S. Athar, T. Kajita, K. Kasahara, and S. Midorikawa, *Atmospheric neutrino flux calculation using the NRLMSISE-00 atmospheric model*, *Phys. Rev.* **D92** (2015), no. 2 023004, [[arXiv:1502.03916](#)].
- [89] M. R. Krishnaswamy, M. G. K. Menon, F. R. S. Narasimham, V. S. Narasimham, K. Hinotani, N. Ito, S. Miyake, J. L. Osborne, A. J. Parsons, and A. W. Wolfendale, *The kolar gold fields neutrino experiment. 2. atmospheric muons at a depth of 7000hg cm to-the-minus-second(kolar)*, *Proc. Roy. Soc. Lond.* **A323** (1971) 511–522.
- [90] F. Reines, M. F. Crouch, T. L. Jenkins, W. R. Kropp, H. S. Gurr, G. R. Smith, J. P. F. Sellschop, and B. Meyer, *Evidence for high-energy cosmic ray neutrino interactions*, *Phys. Rev. Lett.* **15** (1965) 429–433.
- [91] R. Davis, Jr., D. S. Harmer, and K. C. Hoffman, *Search for neutrinos from the sun*, *Phys. Rev. Lett.* **20** (1968) 1205–1209.
- [92] **Kamiokande-II** Collaboration, K. S. Hirata et al., *Observation of B-8 Solar Neutrinos in the Kamiokande-II Detector*, *Phys. Rev. Lett.* **63** (1989) 16.
- [93] T. Araki et al., *Experimental investigation of geologically produced antineutrinos with KamLAND*, *Nature* **436** (2005) 499–503.
- [94] **Borexino** Collaboration, M. Agostini et al., *Spectroscopy of geoneutrinos from 2056 days of Borexino data*, *Phys. Rev.* **D92** (2015), no. 3 031101, [[arXiv:1506.04610](#)].
- [95] **KamLAND** Collaboration, A. Gando et al., *Partial radiogenic heat model for Earth revealed by geoneutrino measurements*, *Nature Geo.* **4** (2011) 647–651.
- [96] **IceCube** Collaboration, M. G. Aartsen et al., *Observation of High-Energy Astrophysical Neutrinos in Three Years of IceCube Data*, *Phys. Rev. Lett.* **113** (2014) 101101, [[arXiv:1405.5303](#)].
- [97] **IceCube** Collaboration, M. G. Aartsen et al., *The IceCube Neutrino Observatory - Contributions to ICRC 2017 Part II: Properties of the Atmospheric and Astrophysical Neutrino Flux*, [arXiv:1710.01191](#).

- [98] **Liverpool Telescope, MAGIC, H.E.S.S., AGILE, Kiso, VLA/17B-403, INTEGRAL, Kapteyn, Subaru, HAWC, Fermi-LAT, ASAS-SN, VERITAS, Kanata, IceCube, Swift NuSTAR Collaboration**, M. G. Aartsen et al., *Multimessenger observations of a flaring blazar coincident with high-energy neutrino IceCube-170922A*, *Science* **361** (2018), no. 6398 eaat1378, [[arXiv:1807.08816](#)].
- [99] **IceCube Collaboration**, M. G. Aartsen et al., *Neutrino emission from the direction of the blazar TXS 0506+056 prior to the IceCube-170922A alert*, *Science* **361** (2018), no. 6398 147–151, [[arXiv:1807.08794](#)].
- [100] **Kamiokande-II Collaboration**, K. Hirata et al., *Observation of a Neutrino Burst from the Supernova SN 1987a*, *Phys. Rev. Lett.* **58** (1987) 1490–1493. [,727(1987)].
- [101] R. M. Bionta et al., *Observation of a Neutrino Burst in Coincidence with Supernova SN 1987a in the Large Magellanic Cloud*, *Phys. Rev. Lett.* **58** (1987) 1494.
- [102] E. N. Alekseev, L. N. Alekseeva, I. V. Krivosheina, and V. I. Volchenko, *Detection of the Neutrino Signal From SN1987A in the LMC Using the Inr Baksan Underground Scintillation Telescope*, *Phys. Lett.* **B205** (1988) 209–214.
- [103] F. Vissani, *Comparative analysis of SN1987A antineutrino fluence*, *J. Phys.* **G42** (2015) 013001, [[arXiv:1409.4710](#)].
- [104] W. D. Arnett and J. L. Rosner, *Neutrino mass limits from sn1987a*, *Phys. Rev. Lett.* **58** (May, 1987) 1906–1909.
- [105] W. D. Arnett and J. L. Rosner, *Neutrino Mass Limits From Sn1987a*, *Phys. Rev. Lett.* **58** (1987) 1906.
- [106] S. H. Kahana, *Supernova mechanisms: Before and after sn1987a*, *International Astronomical Union Colloquium* **108** (1988) 354–360.
- [107] K. Sato and H. Suzuki, *Analysis of neutrino burst from the supernova 1987a in the large magellanic cloud*, *Phys. Rev. Lett.* **58** (Jun, 1987) 2722–2725.
- [108] **Daya Bay Collaboration**, F. An et al., *Observation of electron-antineutrino disappearance at Daya Bay*, *Phys.Rev.Lett.* **108** (2012) 171803, [[arXiv:1203.1669](#)].

- [109] **RENO** Collaboration, J. Ahn et al., *Observation of Reactor Electron Antineutrino Disappearance in the RENO Experiment*, *Phys.Rev.Lett.* **108** (2012) 191802, [[arXiv:1204.0626](#)].
- [110] **Double Chooz** Collaboration, Y. Abe et al., *Reactor electron antineutrino disappearance in the Double Chooz experiment*, *Phys. Rev.* **D86** (2012) 052008, [[arXiv:1207.6632](#)].
- [111] C. L. Cowan, F. Reines, F. B. Harrison, H. W. Kruse, and A. D. McGuire, *Detection of the free neutrino: A Confirmation*, *Science* **124** (1956) 103–104.
- [112] J. N. Bahcall and M. H. Pinsonneault, *Solar models with helium and heavy element diffusion*, *Rev. Mod. Phys.* **67** (1995) 781–808, [[hep-ph/9505425](#)].
- [113] **GALLEX** Collaboration, W. Hampel et al., *GALLEX solar neutrino observations: Results for GALLEX IV*, *Phys. Lett.* **B447** (1999) 127–133.
- [114] **Super-Kamiokande** Collaboration, Y. Fukuda et al., *Measurements of the solar neutrino flux from Super-Kamiokande’s first 300 days*, *Phys. Rev. Lett.* **81** (1998) 1158–1162, [[hep-ex/9805021](#)]. [Erratum: *Phys. Rev. Lett.* 81,4279(1998)].
- [115] **SNO** Collaboration, J. Boger et al., *The Sudbury neutrino observatory*, *Nucl. Instrum. Meth.* **A449** (2000) 172–207, [[nucl-ex/9910016](#)].
- [116] D. Casper et al., *Measurement of atmospheric neutrino composition with IMB-3*, *Phys. Rev. Lett.* **66** (1991) 2561–2564.
- [117] W. W. M. Allison et al., *Measurement of the atmospheric neutrino flavor composition in Soudan-2*, *Phys. Lett.* **B391** (1997) 491–500, [[hep-ex/9611007](#)].
- [118] **Frejus** Collaboration, K. Daum et al., *Determination of the atmospheric neutrino spectra with the Frejus detector*, *Z. Phys.* **C66** (1995) 417–428.
- [119] **NUSEX** Collaboration, M. Aglietta et al., *Experimental study of atmospheric neutrino flux in the NUSEX experiment*, *Europhys. Lett.* **8** (1989) 611–614.
- [120] **Super-Kamiokande** Collaboration, T. Kajita, E. Kearns, and M. Shiozawa, *Establishing atmospheric neutrino oscillations with Super-Kamiokande*, *Nucl. Phys.* **B908** (2016) 14–29.



- [121] **Super-Kamiokande** Collaboration, Y. Fukuda et al., *Measurement of a small atmospheric muon-neutrino / electron-neutrino ratio*, *Phys. Lett.* **B433** (1998) 9–18, [[hep-ex/9803006](#)].
- [122] J. Kameda, *Detailed studies of neutrino oscillations with atmospheric neutrinos of wide energy range from 100 MeV to 1000 GeV in Super-Kamiokande*. PhD thesis, Tokyo U., 2002.
- [123] S. M. Bilenky, *Neutrino oscillations: brief history and present status*, in *Proceedings, 22nd International Baldin Seminar on High Energy Physics Problems, Relativistic Nuclear Physics and Quantum Chromodynamics, (ISHEPP 2014): Dubna, Russia, September 15-20, 2014*, 2014. [arXiv:1408.2864](#).
- [124] D. P. Roy, *Neutrino mass and oscillation: An Introductory review*, *Pramana* **54** (2000) 3–20, [[hep-ph/9903506](#)].
- [125] J. N. Bahcall, N. Cabibbo, and A. Yahil, *Are neutrinos stable particles?*, *Phys. Rev. Lett.* **28** (Jan, 1972) 316–318.
- [126] J. Schechter and J. W. F. Valle, *Neutrino decay and spontaneous violation of lepton number*, *Phys. Rev. D* **25** (Feb, 1982) 774–783.
- [127] A. Acker and S. Pakvasa, *Solar neutrino decay*, *Phys. Lett.* **B320** (1994) 320–322, [[hep-ph/9310207](#)].
- [128] P. Lipari and M. Lusignoli, *On exotic solutions of the atmospheric neutrino problem*, *Phys. Rev.* **D60** (1999) 013003, [[hep-ph/9901350](#)].
- [129] R. A. Gomes, A. L. G. Gomes, and O. L. G. Peres, *Constraints on neutrino decay lifetime using long-baseline charged and neutral current data*, *Phys. Lett.* **B740** (2015) 345–352, [[arXiv:1407.5640](#)].
- [130] J. R. Ellis, J. S. Hagelin, D. V. Nanopoulos, and M. Srednicki, *Search for Violations of Quantum Mechanics*, *Nucl. Phys.* **B241** (1984) 381. [,580(1983)].

- [131] C.-H. Chang, W.-S. Dai, X.-Q. Li, Y. Liu, F.-C. Ma, and Z.-j. Tao, *Possible effects of quantum mechanics violation induced by certain quantum gravity on neutrino oscillations*, *Phys. Rev.* **D60** (1999) 033006, [[hep-ph/9809371](#)].
- [132] E. Lisi, A. Marrone, and D. Montanino, *Probing possible decoherence effects in atmospheric neutrino oscillations*, *Phys. Rev. Lett.* **85** (2000) 1166–1169, [[hep-ph/0002053](#)].
- [133] S. R. Coleman and S. L. Glashow, *High-energy tests of Lorentz invariance*, *Phys. Rev.* **D59** (1999) 116008, [[hep-ph/9812418](#)].
- [134] A. G. Cohen and S. L. Glashow, *A Lorentz-Violating Origin of Neutrino Mass?*, [hep-ph/0605036](#).
- [135] **Super-Kamiokande** Collaboration, S. Fukuda et al., *Tau neutrinos favored over sterile neutrinos in atmospheric muon-neutrino oscillations*, *Phys. Rev. Lett.* **85** (2000) 3999–4003, [[hep-ex/0009001](#)].
- [136] K. Ishihara, *Study of  $\nu_\mu \rightarrow \nu_\tau$  and  $\nu_\mu \rightarrow \nu_{\text{sterile}}$  Neutrino Oscillations with the Atmospheric Neutrino Data in Super-Kamiokande*. PhD thesis, Tokyo U., ICRR, 1999.
- [137] S. Nakayama, *Limits on  $\nu_\mu \leftrightarrow \nu_{\text{sterile}}$  oscillations by the  $\pi^0/\mu$  measurement in the water Cherenkov detectors*. PhD thesis, Tokyo U., 2003.
- [138] **K2K** Collaboration, E. Aliu et al., *Evidence for muon neutrino oscillation in an accelerator-based experiment*, *Phys. Rev. Lett.* **94** (2005) 081802, [[hep-ex/0411038](#)].
- [139] **MINOS** Collaboration, D. G. Michael et al., *Observation of muon neutrino disappearance with the MINOS detectors and the NuMI neutrino beam*, *Phys. Rev. Lett.* **97** (2006) 191801, [[hep-ex/0607088](#)].
- [140] **T2K** Collaboration, K. Abe et al., *First Muon-Neutrino Disappearance Study with an Off-Axis Beam*, *Phys. Rev.* **D85** (2012) 031103, [[arXiv:1201.1386](#)].
- [141] **T2K** Collaboration, K. Abe et al., *Measurement of Muon Antineutrino Oscillations with an Accelerator-Produced Off-Axis Beam*, *Phys. Rev. Lett.* **116** (2016), no. 18 181801, [[arXiv:1512.02495](#)].

- [142] **OPERA** Collaboration, N. Agafonova et al., *Observation of a first  $\nu_\tau$  candidate in the OPERA experiment in the CNGS beam*, *Phys. Lett.* **B691** (2010) 138–145, [[arXiv:1006.1623](#)].
- [143] B. Pontecorvo, *Mesonium and anti-mesonium*, *Sov. Phys. JETP* **6** (1957) 429. [*Zh. Eksp. Teor. Fiz.*33,549(1957)].
- [144] B. Pontecorvo, *Inverse beta processes and nonconservation of lepton charge*, *Sov. Phys. JETP* **7** (1958) 172–173. [*Zh. Eksp. Teor. Fiz.*34,247(1957)].
- [145] Z. Maki, M. Nakagawa, and S. Sakata, *Remarks on the unified model of elementary particles*, *Prog. Theor. Phys.* **28** (1962) 870–880.
- [146] G. Danby, J. M. Gaillard, K. A. Goulianos, L. M. Lederman, N. B. Mistry, M. Schwartz, and J. Steinberger, *Observation of High-Energy Neutrino Reactions and the Existence of Two Kinds of Neutrinos*, *Phys. Rev. Lett.* **9** (1962) 36–44.
- [147] S. Eliezer and A. R. Swift, *Experimental Consequences of electron Neutrino-Muon-neutrino Mixing in Neutrino Beams*, *Nucl. Phys.* **B105** (1976) 45–51.
- [148] H. Fritzsch and P. Minkowski, *Vector-Like Weak Currents, Massive Neutrinos, and Neutrino Beam Oscillations*, *Phys. Lett.* **62B** (1976) 72–76.
- [149] S. M. Bilenky and B. Pontecorvo, *The Quark-Lepton Analogy and the Muonic Charge*, *Yad. Fiz.* **24** (1976) 603–608. [*Sov. J. Nucl. Phys.*24,316(1976)].
- [150] S. M. Bilenky and B. Pontecorvo, *Again on Neutrino Oscillations*, *Lett. Nuovo Cim.* **17** (1976) 569.
- [151] S. M. Bilenky and B. Pontecorvo, *Lepton Mixing and Neutrino Oscillations*, *Phys. Rept.* **41** (1978) 225–261.
- [152] **Planck** Collaboration, P. Ade et al., *Planck 2013 results. XVI. Cosmological parameters*, *Astron.Astrophys.* **571** (2014) A16, [[arXiv:1303.5076](#)].
- [153] B. Pontecorvo, *Neutrino Experiments and the Problem of Conservation of Leptonic Charge*, *Sov. Phys. JETP* **26** (1968) 984–988. [*Zh. Eksp. Teor. Fiz.*53,1717(1967)].

- [154] **Daya Bay** Collaboration, F. An et al., *A new measurement of antineutrino oscillation with the full detector configuration at Daya Bay*, [arXiv:1505.03456](#).
- [155] A. B. Balantekin and D. Yilmaz, *Contrasting solar and reactor neutrinos with a non-zero value of  $\theta_{13}$* , *J. Phys.* **G35** (2008) 075007, [[arXiv:0804.3345](#)].
- [156] G. L. Fogli, E. Lisi, A. Marrone, A. Palazzo, and A. M. Rotunno, *Hints of  $\theta_{13} > 0$  from global neutrino data analysis*, *Phys. Rev. Lett.* **101** (2008) 141801, [[arXiv:0806.2649](#)].
- [157] S. Goswami and A. Yu. Smirnov, *Solar neutrinos and 1-3 leptonic mixing*, *Phys. Rev.* **D72** (2005) 053011, [[hep-ph/0411359](#)].
- [158] A. Dziewonski and D. Anderson, *Preliminary reference earth model*, *Phys. Earth Planet. Interiors* **25** (1981) 297–356.
- [159] **SAGE** Collaboration, J. N. Abdurashitov et al., *Measurement of the solar neutrino capture rate with gallium metal*, *Phys. Rev.* **C60** (1999) 055801, [[astro-ph/9907113](#)].
- [160] **Super-Kamiokande** Collaboration, Y. Fukuda et al., *The Super-Kamiokande detector*, *Nucl. Instrum. Meth.* **A501** (2003) 418–462.
- [161] **Super-Kamiokande** Collaboration, M. Shiozawa, *Reconstruction algorithms in the Super-Kamiokande large water Cherenkov detector*, *Nucl. Instrum. Meth.* **A433** (1999) 240–246.
- [162] **Super-Kamiokande** Collaboration, T. Yano, *Solar Neutrino Results from Super-Kamiokande*, *PoS ICRC2017* (2018) 1066.
- [163] **Super-Kamiokande** Collaboration, K. Abe et al., *Solar Neutrino Measurements in Super-Kamiokande-IV*, *Phys. Rev.* **D94** (2016), no. 5 052010, [[arXiv:1606.07538](#)].
- [164] **SNO** Collaboration, B. Aharmim et al., *Measurement of the Cosmic Ray and Neutrino-Induced Muon Flux at the Sudbury Neutrino Observatory*, *Phys. Rev.* **D80** (2009) 012001, [[arXiv:0902.2776](#)].
- [165] M. Honda, T. Kajita, K. Kasahara, and S. Midorikawa, *Improvement of low energy atmospheric neutrino flux calculation using the JAM nuclear interaction model*, *Phys. Rev.* **D83** (2011) 123001, [[arXiv:1102.2688](#)].

- [166] **Borexino** Collaboration, G. Bellini et al., *First evidence of pep solar neutrinos by direct detection in Borexino*, *Phys. Rev. Lett.* **108** (2012) 051302, [[arXiv:1110.3230](#)].
- [167] **Borexino** Collaboration, C. Arpesella et al., *Direct Measurement of the Be-7 Solar Neutrino Flux with 192 Days of Borexino Data*, *Phys.Rev.Lett.* **101** (2008) 091302, [[arXiv:0805.3843](#)].
- [168] **Borexino** Collaboration, G. Bellini et al., *Final results of Borexino Phase-I on low energy solar neutrino spectroscopy*, *Phys. Rev.* **D89** (2014), no. 11 112007, [[arXiv:1308.0443](#)].
- [169] J. N. Bahcall and C. Pena-Garay, *Solar models and solar neutrino oscillations*, *New J. Phys.* **6** (2004) 63, [[hep-ph/0404061](#)].
- [170] **Super-Kamiokande** Collaboration, S. Fukuda et al., *Solar B-8 and hep neutrino measurements from 1258 days of Super-Kamiokande data*, *Phys. Rev. Lett.* **86** (2001) 5651–5655, [[hep-ex/0103032](#)].
- [171] Y. Farzan and M. Tortola, *Neutrino oscillations and Non-Standard Interactions*, *Front.in Phys.* **6** (2018) 10, [[arXiv:1710.09360](#)].
- [172] **Super-Kamiokande** Collaboration, K. Abe et al., *Atmospheric neutrino oscillation analysis with external constraints in Super-Kamiokande I-IV*, *Phys. Rev.* **D97** (2018), no. 7 072001, [[arXiv:1710.09126](#)].
- [173] **K2K** Collaboration, M. Ahn et al., *Measurement of Neutrino Oscillation by the K2K Experiment*, *Phys.Rev.* **D74** (2006) 072003, [[hep-ex/0606032](#)].
- [174] **IceCube** Collaboration, M. G. Aartsen et al., *Measurement of Atmospheric Neutrino Oscillations at  $6\text{--}56\text{ GeV}$  with IceCube DeepCore*, *Phys. Rev. Lett.* **120** (2018), no. 7 071801, [[arXiv:1707.07081](#)].
- [175] **T2K** Collaboration, K. Abe et al., *The T2K Experiment*, *Nucl.Instrum.Meth.* **A659** (2011) 106–135, [[arXiv:1106.1238](#)].
- [176] **T2K** Collaboration, K. Abe et al., *Measurements of neutrino oscillation in appearance and disappearance channels by the T2K experiment with  $6.6 \times 10^{20}$  protons on target*, *Phys.Rev.* **D91** (2015) 072010, [[arXiv:1502.01550](#)].

- [177] **T2K** Collaboration, K. Abe et al., *Neutrino oscillation physics potential of the T2K experiment*, *PTEP* **2015** (2015), no. 4 043C01, [[arXiv:1409.7469](#)].
- [178] **MINOS** Collaboration, I. Ambats et al., *The MINOS Detectors Technical Design Report*, .
- [179] **MINOS** Collaboration, P. Adamson et al., *Measurement of Neutrino Oscillations with the MINOS Detectors in the NuMI Beam*, *Phys.Rev.Lett.* **101** (2008) 131802, [[arXiv:0806.2237](#)].
- [180] **MINOS** Collaboration, P. Adamson et al., *Improved search for muon-neutrino to electron-neutrino oscillations in MINOS*, *Phys.Rev.Lett.* **107** (2011) 181802, [[arXiv:1108.0015](#)].
- [181] **NOvA** Collaboration, D. Ayres et al., *NOvA: Proposal to build a 30 kiloton off-axis detector to study  $\nu(\mu) \rightarrow \nu(e)$  oscillations in the NuMI beamline*, [hep-ex/0503053](#).
- [182] **IceCube** Collaboration, M. G. Aartsen et al., *Evidence for High-Energy Extraterrestrial Neutrinos at the IceCube Detector*, *Science* **342** (2013) 1242856, [[arXiv:1311.5238](#)].
- [183] **Double Chooz** Collaboration, T. Abrahão et al., *Novel event classification based on spectral analysis of scintillation waveforms in Double Chooz*, [arXiv:1710.04315](#).
- [184] **Double Chooz** Collaboration, A. Mereaglia, *Multi detector results from the Double Chooz experiment*, in *Proceedings, 52nd Rencontres de Moriond on Electroweak Interactions and Unified Theories: La Thuile, Italy, March 18-25, 2017*, pp. 359–366, 2017.
- [185] **Daya Bay** Collaboration, D. Adey et al., *Measurement of electron antineutrino oscillation with 1958 days of operation at Daya Bay*, [arXiv:1809.02261](#).
- [186] **RENO** Collaboration, E. Kwon, *Precise measurement of reactor antineutrino spectrum flux and spectrum at RENO*, *J. Phys. Conf. Ser.* **888** (2017), no. 1 012137.
- [187] **RENO** Collaboration, G. Bak et al., *Measurement of Reactor Antineutrino Oscillation Amplitude and Frequency at RENO*, *Phys. Rev. Lett.* **121** (2018), no. 20 201801, [[arXiv:1806.00248](#)].

- [188] **IceCube PINGU** Collaboration, M. G. Aartsen et al., *Letter of Intent: The Precision IceCube Next Generation Upgrade (PINGU)*, [arXiv:1401.2046](#).
- [189] **IceCube PINGU** Collaboration, K. Clark, *PINGU and the Neutrino Mass Hierarchy*, *Nucl. Part. Phys. Proc.* **273-275** (2016) 1870–1875.
- [190] **KM3Net** Collaboration, S. Adrian-Martinez et al., *Letter of intent for KM3NeT 2.0*, *J. Phys.* **G43** (2016), no. 8 084001, [[arXiv:1601.07459](#)].
- [191] **Hyper-Kamiokande Proto-Collaboration** Collaboration, K. Abe et al., *Physics potential of a long-baseline neutrino oscillation experiment using a J-PARC neutrino beam and Hyper-Kamiokande*, *PTEP* **2015** (2015) 053C02, [[arXiv:1502.05199](#)].
- [192] **Hyper-Kamiokande Proto** Collaboration, M. Yokoyama, *The Hyper-Kamiokande Experiment*, in *Proceedings, Prospects in Neutrino Physics (NuPhys2016): London, UK, December 12-14, 2016*, 2017. [arXiv:1705.00306](#).
- [193] **DUNE** Collaboration, R. J. Wilson, *DEEP UNDERGROUND NEUTRINO EXPERIMENT*, in *Proceedings, 17th Lomonosov Conference on Elementary Particle Physics: Moscow, Russia, August 20-26, 2015*, pp. 19–26, 2017.
- [194] **JUNO** Collaboration, G. Ranucci, *Status and prospects of the JUNO experiment*, *J. Phys. Conf. Ser.* **888** (2017), no. 1 012022.
- [195] M. Maltoni and A. Yu. Smirnov, *Solar neutrinos and neutrino physics*, *Eur. Phys. J.* **A52** (2016), no. 4 87, [[arXiv:1507.05287](#)].
- [196] E. K. Akhmedov, R. Johansson, M. Lindner, T. Ohlsson, and T. Schwetz, *Series expansions for three flavor neutrino oscillation probabilities in matter*, *JHEP* **04** (2004) 078, [[hep-ph/0402175](#)].
- [197] A. Gaur, A. Kumar, and M. Naimuddin, *Timing and charge measurement of single gap resistive plate chamber detectors for INO-ÅICAL experiment*, *Nucl. Instrum. Meth.* **A877** (2018) 246–251, [[arXiv:1709.08946](#)].
- [198] S. Pethuraj, V. M. Datar, G. Majumder, N. K. Mondal, K. C. Ravindran, and B. Satyanarayana, *Measurement of Cosmic Muon angular distribution and vertical*

- integrated flux by 2m×2m RPC stack at IICHEP-Madurai, JCAP* **1709** (2017), no. 09 021, [[arXiv:1706.00901](#)].
- [199] A. D. Bhatt, G. Majumder, N. K. Mondal, N. Pathaleswar, and B. Satyanarayana, *Improvement of time resolution in large area single gap Resistive Plate Chambers, Nucl. Instrum. Meth.* **A844** (2017) 53–61.
- [200] S. P. Behera, M. S. Bhatia, V. M. Datar, and A. K. Mohanty, *Simulation Studies for Electromagnetic Design of INO ICAL Magnet and its Response to Muons*, [arXiv:1406.3965](#).
- [201] **GEANT4** Collaboration, S. Agostinelli et al., *GEANT4: A Simulation toolkit, Nucl. Instrum. Meth.* **A506** (2003) 250–303.
- [202] A. Chatterjee, K. Meghna, K. Rawat, T. Thakore, V. Bhatnagar, et al., *A Simulations Study of the Muon Response of the Iron Calorimeter Detector at the India-based Neutrino Observatory, JINST* **9** (2014) P07001, [[arXiv:1405.7243](#)].
- [203] R. Kanishka, K. K. Meghna, V. Bhatnagar, D. Indumathi, and N. Sinha, *Simulations Study of Muon Response in the Peripheral Regions of the Iron Calorimeter Detector at the India-based Neutrino Observatory, JINST* **10** (2015), no. 03 P03011, [[arXiv:1503.03369](#)].
- [204] M. M. Devi, A. Ghosh, D. Kaur, L. S. Mohan, S. Choubey, et al., *Hadron energy response of the Iron Calorimeter detector at the India-based Neutrino Observatory, JINST* **8** (2013) P11003, [[arXiv:1304.5115](#)].
- [205] D. Casper, *The Nuance neutrino physics simulation, and the future, Nucl.Phys.Proc.Suppl.* **112** (2002) 161–170, [[hep-ph/0208030](#)].
- [206] M. Sajjad Athar, M. Honda, T. Kajita, K. Kasahara, and S. Midorikawa, *Atmospheric neutrino flux at INO, South Pole and Pyh asalmi, Phys.Lett.* **B718** (2013) 1375–1380, [[arXiv:1210.5154](#)].
- [207] H. Nunokawa, S. J. Parke, and R. Zukanovich Funchal, *Another possible way to determine the neutrino mass hierarchy, Phys.Rev.* **D72** (2005) 013009, [[hep-ph/0503283](#)].



- [208] A. de Gouvea, J. Jenkins, and B. Kayser, *Neutrino mass hierarchy, vacuum oscillations, and vanishing  $|U(e3)|$* , *Phys. Rev.* **D71** (2005) 113009, [[hep-ph/0503079](#)].
- [209] **ICAL** Collaboration, S. Ahmed et al., *Physics Potential of the ICAL detector at the India-based Neutrino Observatory (INO)*, [arXiv:1505.07380](#).
- [210] L. S. Mohan, A. Ghosh, M. M. Devi, D. Kaur, S. Choubey, A. Dighe, D. Indumathi, M. V. N. Murthy, and M. Naimuddin, *Simulation studies of hadron energy resolution as a function of iron plate thickness at INO-ICAL*, *JINST* **9** (2014), no. 09 T09003, [[arXiv:1401.2779](#)].
- [211] **Planck** Collaboration, P. A. R. Ade et al., *Planck 2015 results. XIII. Cosmological parameters*, *Astron. Astrophys.* **594** (2016) A13, [[arXiv:1502.01589](#)].
- [212] F. Zwicky, *Die Rotverschiebung von extragalaktischen Nebeln*, *Helv. Phys. Acta* **6** (1933) 110–127.
- [213] V. C. Rubin and W. K. Ford, Jr., *Rotation of the Andromeda Nebula from a Spectroscopic Survey of Emission Regions*, *Astrophys. J.* **159** (1970) 379–403.
- [214] L. E. Strigari, *Galactic Searches for Dark Matter*, *Phys. Rept.* **531** (2013) 1–88, [[arXiv:1211.7090](#)].
- [215] D. Clowe, M. Bradac, A. H. Gonzalez, M. Markevitch, S. W. Randall, C. Jones, and D. Zaritsky, *A direct empirical proof of the existence of dark matter*, *Astrophys. J.* **648** (2006) L109–L113, [[astro-ph/0608407](#)].
- [216] **WMAP Science Team** Collaboration, E. Komatsu et al., *Results from the Wilkinson Microwave Anisotropy Probe*, *PTEP* **2014** (2014) 06B102, [[arXiv:1404.5415](#)].
- [217] G. Steigman, *Neutrinos And Big Bang Nucleosynthesis*, *Adv. High Energy Phys.* **2012** (2012) 268321, [[arXiv:1208.0032](#)].
- [218] G. Jungman, M. Kamionkowski, and K. Griest, *Supersymmetric dark matter*, *Phys. Rept.* **267** (1996) 195–373, [[hep-ph/9506380](#)].
- [219] G. Bertone, D. Hooper, and J. Silk, *Particle dark matter: Evidence, candidates and constraints*, *Phys. Rept.* **405** (2005) 279–390, [[hep-ph/0404175](#)].

- [220] L. Bergström, *Nonbaryonic dark matter: Observational evidence and detection methods*, *Rept. Prog. Phys.* **63** (2000) 793, [[hep-ph/0002126](#)].
- [221] J. Ellis and K. A. Olive, *Supersymmetric Dark Matter Candidates*, [arXiv:1001.3651](#).
- [222] **DAMA, LIBRA** Collaboration, R. Bernabei et al., *New results from DAMA/LIBRA*, *Eur. Phys. J.* **C67** (2010) 39–49, [[arXiv:1002.1028](#)].
- [223] **LUX** Collaboration, D. S. Akerib et al., *Improved Limits on Scattering of Weakly Interacting Massive Particles from Reanalysis of 2013 LUX Data*, *Phys. Rev. Lett.* **116** (2016), no. 16 161301, [[arXiv:1512.03506](#)].
- [224] **SuperCDMS** Collaboration, R. Agnese et al., *New Results from the Search for Low-Mass Weakly Interacting Massive Particles with the CDMS Low Ionization Threshold Experiment*, *Phys. Rev. Lett.* **116** (2016), no. 7 071301, [[arXiv:1509.02448](#)].
- [225] **XENON100** Collaboration, E. Aprile et al., *Dark Matter Results from 225 Live Days of XENON100 Data*, *Phys. Rev. Lett.* **109** (2012) 181301, [[arXiv:1207.5988](#)].
- [226] **DarkSide** Collaboration, P. Agnes et al., *Results from the first use of low radioactivity argon in a dark matter search*, *Phys. Rev.* **D93** (2016), no. 8 081101, [[arXiv:1510.00702](#)].
- [227] **PandaX** Collaboration, X. Xiao et al., *Low-mass dark matter search results from full exposure of the PandaX-I experiment*, *Phys. Rev.* **D92** (2015), no. 5 052004, [[arXiv:1505.00771](#)].
- [228] M. Lindner, A. Merle, and V. Niro, *Enhancing Dark Matter Annihilation into Neutrinos*, *Phys. Rev.* **D82** (2010) 123529, [[arXiv:1005.3116](#)].
- [229] S. K. Agarwalla, M. Blennow, E. Fernandez Martinez, and O. Mena, *Neutrino Probes of the Nature of Light Dark Matter*, *JCAP* **1109** (2011) 004, [[arXiv:1105.4077](#)].
- [230] Y. Farzan, *Flavoring Monochromatic Neutrino Flux from Dark Matter Annihilation*, *JHEP* **02** (2012) 091, [[arXiv:1111.1063](#)].
- [231] P. Mijakowski, *Direct and Indirect Search for Dark Matter*. PhD thesis, Warsaw, Inst. Nucl. Studies, 2011.

- [232] M. Blennow, M. Carrigan, and E. Fernandez Martinez, *Probing the Dark Matter mass and nature with neutrinos*, *JCAP* **1306** (2013) 038, [[arXiv:1303.4530](#)].
- [233] M. Gustafsson, T. Hambye, and T. Scarna, *Effective Theory of Dark Matter Decay into Monochromatic Photons and its Implications: Constraints from Associated Cosmic-Ray Emission*, *Phys. Lett.* **B724** (2013) 288–295, [[arXiv:1303.4423](#)].
- [234] C. El Aisati, M. Gustafsson, T. Hambye, and T. Scarna, *Dark Matter Decay to a Photon and a Neutrino: the Double Monochromatic Smoking Gun Scenario*, *Phys. Rev.* **D93** (2016), no. 4 043535, [[arXiv:1510.05008](#)].
- [235] L. A. Anchordoqui, V. Barger, H. Goldberg, X. Huang, D. Marfatia, L. H. M. da Silva, and T. J. Weiler, *IceCube neutrinos, decaying dark matter, and the Hubble constant*, *Phys. Rev.* **D92** (2015), no. 6 061301, [[arXiv:1506.08788](#)].
- [236] C. Arina, S. Kulkarni, and J. Silk, *Monochromatic neutrino lines from sneutrino dark matter*, *Phys. Rev.* **D92** (2015), no. 8 083519, [[arXiv:1506.08202](#)].
- [237] V. Gonzalez Macias and J. Wudka, *Effective theories for Dark Matter interactions and the neutrino portal paradigm*, *JHEP* **07** (2015) 161, [[arXiv:1506.03825](#)].
- [238] V. Gonzalez-Mac˜anas, J. I. Illana, and J. Wudka, *A realistic model for Dark Matter interactions in the neutrino portal paradigm*, *JHEP* **05** (2016) 171, [[arXiv:1601.05051](#)].
- [239] J. D. Zornoza, *Indirect search for dark matter with neutrino telescopes*, [arXiv:1601.05691](#).
- [240] C. Garcia-Cely and J. Heeck, *Neutrino Lines from Majoron Dark Matter*, [arXiv:1701.07209](#).
- [241] J. F. Beacom, N. F. Bell, and G. D. Mack, *General Upper Bound on the Dark Matter Total Annihilation Cross Section*, *Phys. Rev. Lett.* **99** (2007) 231301, [[astro-ph/0608090](#)].
- [242] H. Yuksel, S. Horiuchi, J. F. Beacom, and S. Ando, *Neutrino Constraints on the Dark Matter Total Annihilation Cross Section*, *Phys. Rev.* **D76** (2007) 123506, [[arXiv:0707.0196](#)].

- [243] **Fermi-LAT** Collaboration, M. Ackermann et al., *Updated search for spectral lines from Galactic dark matter interactions with pass 8 data from the Fermi Large Area Telescope*, *Phys. Rev.* **D91** (2015), no. 12 122002, [[arXiv:1506.00013](#)].
- [244] R. Laha, K. C. Y. Ng, B. Dasgupta, and S. Horiuchi, *Galactic center radio constraints on gamma-ray lines from dark matter annihilation*, *Phys. Rev.* **D87** (2013), no. 4 043516, [[arXiv:1208.5488](#)].
- [245] **CMS** Collaboration, V. Khachatryan et al., *Search for dark matter and unparticles produced in association with a Z boson in proton-proton collisions at  $\sqrt{s} = 8$  TeV*, *Phys. Rev.* **D93** (2016), no. 5 052011, [[arXiv:1511.09375](#)].
- [246] **CMS** Collaboration, S. Chatrchyan et al., *Search for Dark Matter and Large Extra Dimensions in  $pp$  Collisions Yielding a Photon and Missing Transverse Energy*, *Phys. Rev. Lett.* **108** (2012) 261803, [[arXiv:1204.0821](#)].
- [247] **ATLAS** Collaboration, G. Aad et al., *Search for dark matter candidates and large extra dimensions in events with a photon and missing transverse momentum in  $pp$  collision data at  $\sqrt{s} = 7$  TeV with the ATLAS detector*, *Phys. Rev. Lett.* **110** (2013), no. 1 011802, [[arXiv:1209.4625](#)].
- [248] R. de Grijs and G. Bono, *Clustering of Local Group distances: publication bias or correlated measurements? IV. The Galactic Center*, *ArXiv e-prints* (Oct., 2016) [[arXiv:1610.02457](#)].
- [249] J. F. Navarro, C. S. Frenk, and S. D. M. White, *The Structure of cold dark matter halos*, *Astrophys. J.* **462** (1996) 563–575, [[astro-ph/9508025](#)].
- [250] J. Diemand, M. Kuhlen, and P. Madau, *Dark matter substructure and gamma-ray annihilation in the Milky Way halo*, *Astrophys. J.* **657** (2007) 262–270, [[astro-ph/0611370](#)].
- [251] J. Stadel, D. Potter, B. Moore, J. Diemand, P. Madau, M. Zemp, M. Kuhlen, and V. Quilis, *Quantifying the heart of darkness with GHALO - a multi-billion particle simulation of our galactic halo*, *Mon. Not. Roy. Astron. Soc.* **398** (2009) L21–L25, [[arXiv:0808.2981](#)].

- [252] J. F. Navarro, A. Ludlow, V. Springel, J. Wang, M. Vogelsberger, S. D. M. White, A. Jenkins, C. S. Frenk, and A. Helmi, *The Diversity and Similarity of Cold Dark Matter Halos*, *Mon. Not. Roy. Astron. Soc.* **402** (2010) 21, [[arXiv:0810.1522](#)].
- [253] G. Stinson, C. Brook, A. V. Maccio, J. Wadsley, T. R. Quinn, and H. M. P. Couchman, *Making Galaxies in a Cosmological Context: The Need for Early Stellar Feedback*, *Mon. Not. Roy. Astron. Soc.* **428** (2013) 129, [[arXiv:1208.0002](#)].
- [254] A. Di Cintio, C. B. Brook, A. V. Maccio, G. S. Stinson, A. Knebe, A. A. Dutton, and J. Wadsley, *The dependence of dark matter profiles on the stellar-to-halo mass ratio: a prediction for cusps versus cores*, *Mon. Not. Roy. Astron. Soc.* **437** (2014), no. 1 415–423, [[arXiv:1306.0898](#)].
- [255] E. Tollet et al., *NIHAO ? IV: core creation and destruction in dark matter density profiles across cosmic time*, *Mon. Not. Roy. Astron. Soc.* **456** (2016), no. 4 3542–3552, [[arXiv:1507.03590](#)].
- [256] T. K. Chan, D. KereÅa, J. OÃsorbe, P. F. Hopkins, A. L. Muratov, C. A. Faucher-GiguÃlre, and E. Quataert, *The impact of baryonic physics on the structure of dark matter haloes: the view from the FIRE cosmological simulations*, *Mon. Not. Roy. Astron. Soc.* **454** (2015), no. 3 2981–3001, [[arXiv:1507.02282](#)].
- [257] F. Marinacci, R. Pakmor, and V. Springel, *The formation of disc galaxies in high resolution moving-mesh cosmological simulations*, *Mon. Not. Roy. Astron. Soc.* **437** (2014), no. 2 1750–1775, [[arXiv:1305.5360](#)].
- [258] **AGORA** Collaboration, J.-h. Kim et al., *The AGORA High-Resolution Galaxy Simulations Comparison Project*, *Astrophys. J. Suppl.* **210** (2013) 14, [[arXiv:1308.2669](#)].
- [259] J. Schaye et al., *The EAGLE project: Simulating the evolution and assembly of galaxies and their environments*, *Mon. Not. Roy. Astron. Soc.* **446** (2015) 521–554, [[arXiv:1407.7040](#)].
- [260] M. Schaller, C. S. Frenk, R. G. Bower, T. Theuns, A. Jenkins, J. Schaye, R. A. Crain, M. Furlong, C. D. Vecchia, and I. G. McCarthy, *Baryon effects on the internal structure of*

- ?CDM haloes in the EAGLE simulations*, *Mon. Not. Roy. Astron. Soc.* **451** (2015), no. 2 1247–1267, [[arXiv:1409.8617](#)].
- [261] T. Sawala et al., *The APOSTLE simulations: solutions to the Local Group’s cosmic puzzles*, *Mon. Not. Roy. Astron. Soc.* **457** (2016), no. 2 1931–1943, [[arXiv:1511.01098](#)].
- [262] D. G. Cerdeno, M. Fornasa, A. M. Green, and M. Peiro, *How to calculate dark matter direct detection exclusion limits that are consistent with gamma rays from annihilation in the Milky Way halo*, [arXiv:1605.05185](#).
- [263] A. Burkert and J. Silk, *On the structure and nature of dark matter halos*, in *Dark matter in Astrophysics and Particle Physics* (H. V. Klapdor-Kleingrothaus and L. Baudis, eds.), p. 375, 1999. [astro-ph/9904159](#).
- [264] **IceCube** Collaboration, M. G. Aartsen et al., *Search for Dark Matter Annihilation in the Galactic Center with IceCube-79*, *Eur. Phys. J.* **C75** (2015), no. 10 492, [[arXiv:1505.07259](#)].
- [265] S. Ando, *Can dark matter annihilation dominate the extragalactic gamma-ray background?*, *Phys. Rev. Lett.* **94** (2005) 171303, [[astro-ph/0503006](#)].
- [266] K. C. Y. Ng, R. Laha, S. Campbell, S. Horiuchi, B. Dasgupta, K. Murase, and J. F. Beacom, *Resolving small-scale dark matter structures using multisource indirect detection*, *Phys. Rev.* **D89** (2014), no. 8 083001, [[arXiv:1310.1915](#)].
- [267] S. Campbell, *Gamma-ray probes of dark matter substructure*, *AIP Conf. Proc.* **1604** (2014) 11–21.
- [268] C. A. Correa, J. S. B. Wyithe, J. Schaye, and A. R. Duffy, *The accretion history of dark matter haloes ? III. A physical model for the concentration?mass relation*, *Mon. Not. Roy. Astron. Soc.* **452** (2015), no. 2 1217–1232, [[arXiv:1502.00391](#)].
- [269] R. Bartels and S. Ando, *Boosting the annihilation boost: Tidal effects on dark matter subhalos and consistent luminosity modeling*, *Phys. Rev.* **D92** (2015), no. 12 123508, [[arXiv:1507.08656](#)].

- [270] A. Moline, M. A. Sanchez-Conde, S. Palomares-Ruiz, and F. Prada, *Characterization of subhalo structural properties and implications for dark matter annihilation signals*, [arXiv:1603.04057](#).
- [271] S. Palomares-Ruiz, *Model-Independent Bound on the Dark Matter Lifetime*, *Phys. Lett. B* **665** (2008) 50–53, [[arXiv:0712.1937](#)].
- [272] S. T. Petcov and T. Schwetz, *Determining the neutrino mass hierarchy with atmospheric neutrinos*, *Nucl. Phys. B* **740** (2006) 1–22, [[hep-ph/0511277](#)].
- [273] M. Blennow and T. Schwetz, *Identifying the Neutrino mass Ordering with INO and NOvA*, *JHEP* **08** (2012) 058, [[arXiv:1203.3388](#)]. [Erratum: JHEP11,098(2012)].
- [274] M. Ghosh, P. Ghoshal, S. Goswami, and S. K. Raut, *Can atmospheric neutrino experiments provide the first hint of leptonic CP violation?*, *Phys. Rev. D* **89** (2014), no. 1 011301, [[arXiv:1306.2500](#)].
- [275] M. Ghosh, P. Ghoshal, S. Goswami, and S. K. Raut, *Evidence for leptonic CP phase from NOvA, T2K and ICAL: A chronological progression*, *Nucl. Phys. B* **884** (2014) 274–304, [[arXiv:1401.7243](#)].
- [276] J. A. Formaggio and G. P. Zeller, *From eV to EeV: Neutrino Cross Sections Across Energy Scales*, *Rev. Mod. Phys.* **84** (2012) 1307, [[arXiv:1305.7513](#)].
- [277] R. Gandhi, P. Ghoshal, S. Goswami, P. Mehta, S. U. Sankar, and S. Shalgar, *Mass Hierarchy Determination via future Atmospheric Neutrino Detectors*, *Phys. Rev. D* **76** (2007) 073012, [[arXiv:0707.1723](#)].
- [278] Atmospheric  $\nu$  fluxes for the INO site are in <http://www.icrr.u-tokyo.ac.jp/~mhonda/>.
- [279] D. V. Forero, M. Tortola, and J. W. F. Valle, *Neutrino oscillations refitted*, *Phys. Rev. D* **90** (2014), no. 9 093006, [[arXiv:1405.7540](#)].
- [280] M. Honda, T. Kajita, K. Kasahara, S. Midorikawa, and T. Sanuki, *Calculation of atmospheric neutrino flux using the interaction model calibrated with atmospheric muon data*, *Phys. Rev. D* **75** (2007) 043006, [[astro-ph/0611418](#)].

- [281] P. Huber, M. Lindner, and W. Winter, *Superbeams versus neutrino factories*, *Nucl.Phys.* **B645** (2002) 3–48, [[hep-ph/0204352](#)].
- [282] G. L. Fogli, E. Lisi, A. Marrone, D. Montanino, A. Palazzo, and A. M. Rotunno, *Solar neutrino oscillation parameters after first KamLAND results*, *Phys. Rev.* **D67** (2003) 073002, [[hep-ph/0212127](#)].
- [283] M. Gonzalez-Garcia and M. Maltoni, *Atmospheric neutrino oscillations and new physics*, *Phys.Rev.* **D70** (2004) 033010, [[hep-ph/0404085](#)].
- [284] L. Wolfenstein, *Neutrino Oscillations and Stellar Collapse*, *Phys. Rev.* **D20** (1979) 2634–2635.
- [285] **Super-Kamiokande** Collaboration, P. Mijakowski, *Indirect searches for dark matter particles at Super-Kamiokande*, *J. Phys. Conf. Ser.* **718** (2016), no. 4 042040.
- [286] **IceCube** Collaboration, M. G. Aartsen et al., *Search for Neutrinos from Dark Matter Self-Annihilations in the center of the Milky Way with 3 years of IceCube/DeepCore*, [arXiv:1705.08103](#).
- [287] **ANTARES** Collaboration, S. Adrian-Martinez et al., *Search of Dark Matter Annihilation in the Galactic Centre using the ANTARES Neutrino Telescope*, *JCAP* **1510** (2015), no. 10 068, [[arXiv:1505.04866](#)].
- [288] A. Albert et al., *Results from the search for dark matter in the Milky Way with 9 years of data of the ANTARES neutrino telescope*, [arXiv:1612.04595](#).
- [289] A. D. Avrorin et al., *Dark matter constraints from an observation of dSphs and the LMC with the Baikal NT200*, [arXiv:1612.03836](#).
- [290] **IceCube** Collaboration, R. Abbasi et al., *Search for Dark Matter from the Galactic Halo with the IceCube Neutrino Observatory*, *Phys. Rev.* **D84** (2011) 022004, [[arXiv:1101.3349](#)].
- [291] B. Dasgupta and R. Laha, *Neutrinos in IceCube/KM3NeT as probes of Dark Matter Substructures in Galaxy Clusters*, *Phys. Rev.* **D86** (2012) 093001, [[arXiv:1206.1322](#)].



- [292] **IceCube** Collaboration, M. G. Aartsen et al., *IceCube Search for Dark Matter Annihilation in nearby Galaxies and Galaxy Clusters*, *Phys. Rev.* **D88** (2013) 122001, [[arXiv:1307.3473](#)].
- [293] **IceCube** Collaboration, M. G. Aartsen et al., *Multipole analysis of IceCube data to search for dark matter accumulated in the Galactic halo*, *Eur. Phys. J.* **C75** (2015), no. 99 20, [[arXiv:1406.6868](#)].
- [294] A. Moline, A. Ibarra, and S. Palomares-Ruiz, *Future sensitivity of neutrino telescopes to dark matter annihilations from the cosmic diffuse neutrino signal*, *JCAP* **1506** (2015), no. 06 005, [[arXiv:1412.4308](#)].
- [295] C. Rott, K. Kohri, and S. C. Park, *Superheavy dark matter and IceCube neutrino signals: Bounds on decaying dark matter*, *Phys. Rev.* **D92** (2015), no. 2 023529, [[arXiv:1408.4575](#)].
- [296] C. El Aisati, M. Gustafsson, and T. Hambye, *New Search for Monochromatic Neutrinos from Dark Matter Decay*, *Phys. Rev.* **D92** (2015), no. 12 123515, [[arXiv:1506.02657](#)].
- [297] M. Chianese, G. Miele, S. Morisi, and E. Vitagliano, *Low energy IceCube data and a possible Dark Matter related excess*, *Phys. Lett.* **B757** (2016) 251–256, [[arXiv:1601.02934](#)].
- [298] S. M. Boucenna, M. Chianese, G. Mangano, G. Miele, S. Morisi, O. Pisanti, and E. Vitagliano, *Decaying Leptophilic Dark Matter at IceCube*, *JCAP* **1512** (2015), no. 12 055, [[arXiv:1507.01000](#)].
- [299] **IceCube** Collaboration, M. G. Aartsen et al., *All-flavour Search for Neutrinos from Dark Matter Annihilations in the Milky Way with IceCube/DeepCore*, [arXiv:1606.00209](#).
- [300] J. Kumar and P. Sandick, *Searching for Dark Matter Annihilation to Monoenergetic Neutrinos with Liquid Scintillation Detectors*, *JCAP* **1506** (2015), no. 06 035, [[arXiv:1502.02091](#)].
- [301] **LENA** Collaboration, M. Wurm et al., *The next-generation liquid-scintillator neutrino observatory LENA*, *Astropart. Phys.* **35** (2012) 685–732, [[arXiv:1104.5620](#)].

- [302] M. Kachelriess and P. D. Serpico, *Model-independent dark matter annihilation bound from the diffuse  $\gamma$  ray flux*, *Phys. Rev.* **D76** (2007) 063516, [[arXiv:0707.0209](#)].
- [303] N. F. Bell, J. B. Dent, T. D. Jacques, and T. J. Weiler, *Electroweak Bremsstrahlung in Dark Matter Annihilation*, *Phys. Rev.* **D78** (2008) 083540, [[arXiv:0805.3423](#)].
- [304] N. F. Bell, J. B. Dent, T. D. Jacques, and T. J. Weiler, *Dark Matter Annihilation Signatures from Electroweak Bremsstrahlung*, *Phys. Rev.* **D84** (2011) 103517, [[arXiv:1101.3357](#)].
- [305] N. F. Bell, J. B. Dent, A. J. Galea, T. D. Jacques, L. M. Krauss, and T. J. Weiler, *W/Z Bremsstrahlung as the Dominant Annihilation Channel for Dark Matter, Revisited*, *Phys. Lett.* **B706** (2011) 6–12, [[arXiv:1104.3823](#)].
- [306] M. Cirelli, G. Corcella, A. Hektor, G. Hutsi, M. Kadastik, P. Panci, M. Raidal, F. Sala, and A. Strumia, *PPPC 4 DM ID: A Poor Particle Physicist Cookbook for Dark Matter Indirect Detection*, *JCAP* **1103** (2011) 051, [[arXiv:1012.4515](#)]. [Erratum: *JCAP*1210,E01(2012)].
- [307] K. Murase, R. Laha, S. Ando, and M. Ahlers, *Testing the Dark Matter Scenario for PeV Neutrinos Observed in IceCube*, *Phys. Rev. Lett.* **115** (2015), no. 7 071301, [[arXiv:1503.04663](#)].
- [308] A. Esmaili and P. D. Serpico, *Gamma-ray bounds from EAS detectors and heavy decaying dark matter constraints*, *JCAP* **1510** (2015), no. 10 014, [[arXiv:1505.06486](#)].
- [309] D. Chowdhury, A. M. Iyer, and R. Laha, *Constraints on dark matter annihilation to fermions and a photon*, [arXiv:1601.06140](#).
- [310] F. S. Queiroz, C. E. Yaguna, and C. Weniger, *Gamma-ray Limits on Neutrino Lines*, *JCAP* **1605** (2016), no. 05 050, [[arXiv:1602.05966](#)].
- [311] A. D. Avrorin et al., *Sensitivity of the Baikal-GVD neutrino telescope to neutrino emission toward the center of the galactic dark matter halo*, *JETP Lett.* **101** (2015), no. 5 289–294, [[arXiv:1412.3672](#)].
- [312] K. Abe et al., *Letter of Intent: The Hyper-Kamiokande Experiment — Detector Design and Physics Potential* —, [arXiv:1109.3262](#).

- [313] E. G. Speckhard, K. C. Y. Ng, J. F. Beacom, and R. Laha, *Dark Matter Velocity Spectroscopy*, *Phys. Rev. Lett.* **116** (2016), no. 3 031301, [[arXiv:1507.04744](#)].
- [314] D. Powell, R. Laha, K. C. Y. Ng, and T. Abel, *The Doppler effect on indirect detection of dark matter using dark matter only simulations*, *Phys. Rev.* **D95** (2017), no. 6 063012, [[arXiv:1611.02714](#)].
- [315] C. Biggio, M. Blennow, and E. Fernandez-Martinez, *General bounds on non-standard neutrino interactions*, *JHEP* **0908** (2009) 090, [[arXiv:0907.0097](#)].
- [316] T. Ohlsson, *Status of non-standard neutrino interactions*, *Rept. Prog. Phys.* **76** (2013) 044201, [[arXiv:1209.2710](#)].
- [317] O. G. Miranda and H. Nunokawa, *Non standard neutrino interactions: current status and future prospects*, *New J. Phys.* **17** (2015), no. 9 095002, [[arXiv:1505.06254](#)].
- [318] **Super-Kamiokande** Collaboration, G. Mitsuka et al., *Study of Non-Standard Neutrino Interactions with Atmospheric Neutrino Data in Super-Kamiokande I and II*, *Phys.Rev.* **D84** (2011) 113008, [[arXiv:1109.1889](#)].
- [319] J. Salvado, O. Mena, S. Palomares-Ruiz, and N. Rius, *Non-standard interactions with high-energy atmospheric neutrinos at IceCube*, [arXiv:1609.03450](#).
- [320] **IceCube** Collaboration, M. Aartsen et al., *Search for Nonstandard Neutrino Interactions with IceCube DeepCore*, *Phys. Rev.* **D97** (2018), no. 7 072009, [[arXiv:1709.07079](#)].
- [321] M. Blennow, P. Coloma, P. Huber, and T. Schwetz, *Quantifying the sensitivity of oscillation experiments to the neutrino mass ordering*, *JHEP* **1403** (2014) 028, [[arXiv:1311.1822](#)].
- [322] G. Fogli, E. Lisi, A. Marrone, D. Montanino, and A. Palazzo, *Getting the most from the statistical analysis of solar neutrino oscillations*, *Phys.Rev.* **D66** (2002) 053010, [[hep-ph/0206162](#)].
- [323] E. Ma, *Gauged  $B - 3L(\tau)$  and radiative neutrino masses*, *Phys. Lett.* **B433** (1998) 74–81, [[hep-ph/9709474](#)].
- [324] H.-S. Lee and E. Ma, *Gauged  $B - x_i L$  origin of  $R$  Parity and its implications*, *Phys. Lett.* **B688** (2010) 319–322, [[arXiv:1001.0768](#)].

- [325] P. Langacker, *The Physics of Heavy  $Z'$  Gauge Bosons*, *Rev. Mod. Phys.* **81** (2009) 1199–1228, [[arXiv:0801.1345](#)].
- [326] R. Foot, *New Physics From Electric Charge Quantization?*, *Mod. Phys. Lett.* **A6** (1991) 527–530.
- [327] R. Foot, G. C. Joshi, H. Lew, and R. R. Volkas, *Charge quantization in the standard model and some of its extensions*, *Mod. Phys. Lett.* **A5** (1990) 2721–2732.
- [328] X.-G. He, G. C. Joshi, H. Lew, and R. Volkas, *Simplest Z-prime model*, *Phys. Rev.* **D44** (1991) 2118–2132.
- [329] R. Foot, X. G. He, H. Lew, and R. R. Volkas, *Model for a light Z-prime boson*, *Phys. Rev.* **D50** (1994) 4571–4580, [[hep-ph/9401250](#)].
- [330] A. S. Joshipura and S. Mohanty, *Constraints on flavor dependent long range forces from atmospheric neutrino observations at super-Kamiokande*, *Phys. Lett.* **B584** (2004) 103–108, [[hep-ph/0310210](#)].
- [331] A. Bandyopadhyay, A. Dighe, and A. S. Joshipura, *Constraints on flavor-dependent long range forces from solar neutrinos and kamland*, *Phys. Rev. D* **75** (May, 2007) 093005.
- [332] J. Grifols and E. Masso, *Neutrino oscillations in the sun probe long range leptonic forces*, *Phys. Lett.* **B579** (2004) 123–126, [[hep-ph/0311141](#)].
- [333] S. S. Chatterjee, A. Dasgupta, and S. K. Agarwalla, *Exploring Flavor-Dependent Long-Range Forces in Long-Baseline Neutrino Oscillation Experiments*, *JHEP* **12** (2015) 167, [[arXiv:1509.03517](#)].
- [334] J. Williams, X. Newhall, and J. Dickey, *Relativity parameters determined from lunar laser ranging*, *Phys. Rev.* **D53** (1996) 6730–6739.
- [335] J. G. Williams, S. G. Turyshev, and D. H. Boggs, *Progress in lunar laser ranging tests of relativistic gravity*, *Phys. Rev. Lett.* **93** (2004) 261101, [[gr-qc/0411113](#)].
- [336] E. G. Adelberger, B. R. Heckel, and A. E. Nelson, *Tests of the gravitational inverse square law*, *Ann. Rev. Nucl. Part. Sci.* **53** (2003) 77–121, [[hep-ph/0307284](#)].

- [337] A. Dolgov, *Long range forces in the universe*, *Phys.Rept.* **320** (1999) 1–15.
- [338] T. Lee and C.-N. Yang, *Conservation of Heavy Particles and Generalized Gauge Transformations*, *Phys.Rev.* **98** (1955) 1501.
- [339] L. Okun, *Leptons and photons*, *Phys. Lett.* **B382** (1996) 389–392, [[hep-ph/9512436](#)].
- [340] L. B. Okun, *On muonic charge and muonic photons*, *Yad. Fiz.* **10** (1969) 358–362.
- [341] J. Grifols, E. Masso, and S. Peris, *Supernova neutrinos as probes of long range nongravitational interactions of dark matter*, *Astropart.Phys.* **2** (1994) 161–165.
- [342] J. Grifols, E. Masso, and R. Toldra, *Majorana neutrinos and long range forces*, *Phys.Lett.* **B389** (1996) 563–565, [[hep-ph/9606377](#)].
- [343] R. Horvat, *Supernova MSW effect in the presence of leptonic long range forces*, *Phys.Lett.* **B366** (1996) 241–247.
- [344] M. Gonzalez-Garcia, P. de Holanda, E. Masso, and R. Zukanovich Funchal, *Probing long-range leptonic forces with solar and reactor neutrinos*, *JCAP* **0701** (2007) 005, [[hep-ph/0609094](#)].
- [345] A. Samanta, *Long-range Forces : Atmospheric Neutrino Oscillation at a magnetized Detector*, *JCAP* **1109** (2011) 010, [[arXiv:1001.5344](#)].
- [346] S. K. Agarwalla, Y. Kao, and T. Takeuchi, *Analytical approximation of the neutrino oscillation matter effects at large  $\theta_{13}$* , *JHEP* **1404** (2014) 047, [[arXiv:1302.6773](#)].
- [347] J. N. Bahcall, *Neutrino Astrophysics*. Cambridge University Press, Cambridge, England, 1989.
- [348] A. M. Dziewonski and D. L. Anderson, *Preliminary reference earth model*, *Physics of the Earth and Planetary Interiors* **25** (1981) 297–356.